学位論文

Search for top squarks in events with one lepton

in pp collisions at $\sqrt{s}$ = 13 TeV

（重心系エネルギー13 TeV の陽子・陽子衝突における

１レプトン事象を用いたトップ・スクォークの探索）

平成２８年１２月博士（理学）申請

東京大学大学院理学系研究科

物理学専攻

森　達哉

Search for top squarks in events with one lepton

in pp collisions at $\sqrt{s} = 13$ TeV

Tatsuya Mori

Department of Physics, Faculty of Science & Graduate School of Science, The University of Tokyo

December, 2016

Abstract

This thesis presents the results of a search for the top squark (stop), the supersymmetric partner of the top quark, in events with one lepton. The search uses the datasets of the 2015 and 2016 LHC pp collisions at $\sqrt{s} = 13$ TeV recorded by the ATLAS detector, which amount to an integrated luminosity of 28.0 fb^{-1}. The analysis targets a direct pair production of stops where each stop decays into the top quark and the lightest neutralino ($\tilde{t}_1 \to t\tilde{\chi}_1^0$), the W boson from one of the two top quarks decays to an electron or muon (either directly or via a τ lepton), and the W boson from the other top quark decays hadronically. Since the signal event topology highly depends on the mass difference between the stop and the lightest neutralino, three analyses are performed which are optimized to *Boosted*, *Resolved*, and *Diagonal* topologies of the signal events. In *Boosted* topology ($\Delta m(\tilde{t}_1, \tilde{\chi}_1^0) \gtrsim 3m_t$), top quarks are highly boosted so that bqq' from hadronic top decay forms one large-R jet. In *Resolved* topology ($\Delta m(\tilde{t}_1, \tilde{\chi}_1^0) \sim 2m_t$), the hadronic top decay products are not merged into one large-R jet but resolved into three smaller-radius jets because p_{T} of top quark is relatively medium. In *Diagonal* topology ($\Delta m(\tilde{t}_1, \tilde{\chi}_1^0) \sim m_t$), the behavior of hadronic top decay is the same as *Resolved* region but $\tilde{\chi}_1^0$ and t from $\tilde{t}_1$ decay are nearly collinear with respect to $\tilde{t}_1$ momentum. The detector signature of the signal events is similar to that of a top quark pair produced in association with large missing transverse momentum, which is highly suppressed by dedicated variables in *Boosted* and *Resolved* analyses and precisely estimated by a 2-dimensional shape fit in *Diagonal* analysis.

No significant excess from the Standard Model background-only hypothesis is observed, and exclusion limits on a plane of stop and lightest neutralino masses are set at 95% confidence level. The results extend the ATLAS and the CMS exclusion limits for stop pair production model obtained with data of 13.2 fb^{-1}. The *Resolved* result doesn't newly exclude but enlarges the expected CL$_s$ contour up to $(m_{\tilde{t}_1}, m_{\tilde{\chi}_1^0}) \sim (700 - 800, 400)$ GeV. The *Boosted* result newly excludes the $\tilde{t}_1 \to t\tilde{\chi}_1^0$ model with the $m_{\tilde{t}_1} \lesssim 980$ GeV for $m_{\tilde{\chi}_1^0} \lesssim 300$ GeV and $(m_{\tilde{t}_1}, m_{\tilde{\chi}_1^0}) = (900, 350)$ GeV. The *Diagonal* result is reinterpreted to set exclusion limits on the model where stop decays to bottom quark, W-boson, and lightest neutralino ($\tilde{t}_1 \to bW\tilde{\chi}_1^0$), and newly excludes the $\tilde{t}_1 \to t\tilde{\chi}_1^0$ and $\tilde{t}_1 \to bW\tilde{\chi}_1^0$ models with 200 GeV $< m_{\tilde{\chi}_1^0} <$ 240 GeV and $(m_{\tilde{t}_1}, m_{\tilde{\chi}_1^0}) \sim (430, 250)$ GeV near a *Diagonal* line of $m_{\tilde{t}_1} = m_t + m_{\tilde{\chi}_1^0}$.

Contents

Chapter 1

Introduction

The final goal of elementary particle physics is to discovery an ultimate law of nature that is the origin of all physics phenomena in the universe. As one of the steps, elementary particle physicists have constructed the Standard Model (SM), successfully describing physics of elementary particles in a high energy scale called electroweak scale (around W/Z-boson mass, 100 GeV). However, the SM is not perfect and has many problems. One of the most important problems is 'hierarchy problem', which points out why the electroweak scale is much different from the grand unification theory (GUT) scale (10^{16} GeV) or Planck scale (10^{19} GeV). The difference results in an extremely large quantum correction to the Higgs mass. The other problem is that there is no appropriate candidate for dark matter in the SM. Furthermore, the grand unification cannot be derived from the SM.

These problems can be solved by introducing 'supersymmetry', one of the most compelling extension of the SM. If supersymmetry is true, there should be superpartner of top quark named top squarks (or stops). Since the stop mass is the most important key to solve the hierarchy problem, searching for stop could be a powerful test of supersymmetry. Furthermore, if the hierarchy problem is solved by supersymmetry, then stop mass is predicted ~ 1 TeV at maximum, which is small enough to be searched for in the LHC-ATLAS experiment. This thesis presents a search for top squarks (stops) using pp-collisions data of 28.0 fb^{-1} in the LHC-ATLAS experiment.

In this Chapter 1, the SM and supersymmetry are briefly overviewed to support the following sections where motivations of stop search and outline of the analysis are introduced.

1.1 The Standard Model

The Standard Model (SM) [1] is essentially based on three types of elementary particles (leptons, quarks, and gauge-bosons). Figure 1.1 and 1.2 show all the particles and possible interactions in the SM. Interaction of fermions (leptons or quarks) via photon, W/Z-boson and gluon are called electromagnetic, weak and strong interaction, respectively.

The electrically neutral part of the SM Higgs field is a complex scalar ϕ with a classical potential:

$$V = \frac{1}{2}\mu^2|\phi|^2 + \frac{1}{4}\lambda|\phi|^4. \tag{1.1}$$

Figure 1.3 illustrates the global Higgs potential before/after electroweek spontaneous symmetry breaking (EWSB). Above a certain extremely high energy, energy on ground state of the global
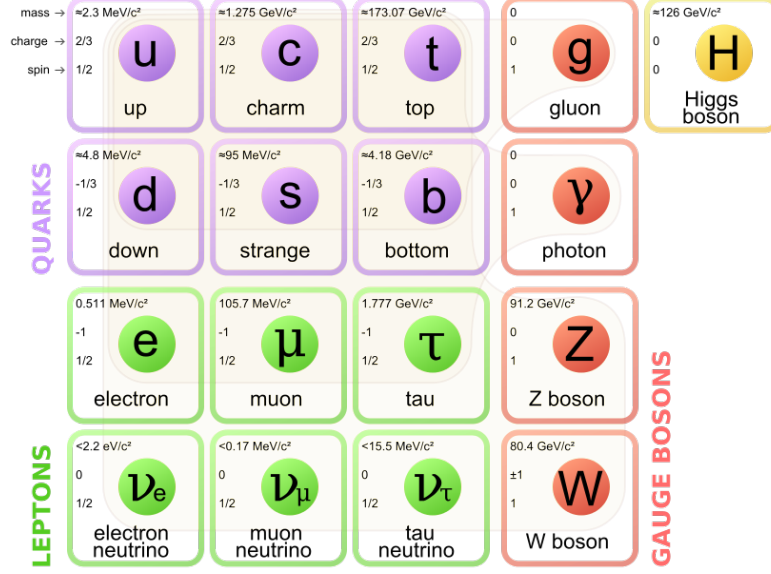
Figure 1.1: All particles described in the Standard Model [1]. In each block for each particle, its mass, spin, and electro-charge are shown.

Higgs field or vacuum expectation value (VEV, v) is considered zero (left of Figure 1.3), and below the high energy threshold, the EWSB happens and then $v \to \sqrt{\frac{-\mu^2}{\lambda}}$, experimentally known as approximately 246 GeV (right of Figure 1.3)[1]. After the EWSB, the transformation from the global to the local Higgs field (H) is denoted by $\phi = \frac{v+H}{\sqrt{2}}$, and then a mass term of the local Higgs field can be expressed with λ, v or μ:

$$\frac{m_H^2}{2}H^2 = \lambda v^2 H^2 = -\mu^2 H^2 \tag{1.2}$$

1.2 Hierarchy Problem

In the SM, each fermion that couples to the Higgs field has a Yukawa coupling λ_f. The interaction term between fermion and Higgs is denoted by:

$$\mathcal{L}_{\text{Yukawa}} = -\lambda_f \bar{f} H f$$

where f is the Dirac Field. The mass of a fermion after the EWSB is deduced to:

$$m_f = \frac{v}{\sqrt{2}}\lambda_f \tag{1.3}$$

Equation 1.3 means that the Higgs boson is most likely to couple to the heaviest fermion, namely top quark, with $\lambda_t \sim 1$. Then if one considers the loop-correction to the Higgs mass shown in Figure 1.4(a) and the following Equation 1.4, the most significant correction comes from top quark:

$$\Delta m_H^2 = -\frac{|\lambda_f|^2}{8\pi^2}\Lambda_{\text{UV}}^2 + ... \tag{1.4}$$

where Λ_{UV} is an ultraviolet momentum cutoff used to regulate the loop integral, which should be interpreted as at least the threshold of energy scale above which the SM is not valid and new physics appears.

---

[1] The mass of W-boson, M_W, after the EWSB can be expressed by $\frac{ve}{2\sin\theta_w}$, where $\frac{e^2}{4\pi} \sim \frac{1}{137}$ and $\cos\theta_w = \frac{M_W}{M_Z}$. All the parameters to calculate v have been measured and therefore v can be determined $\sim$246 GeV.
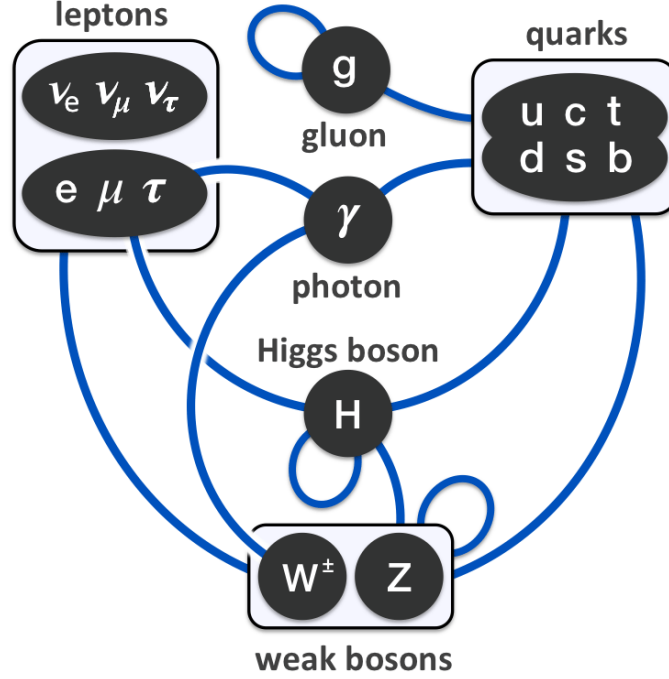
Figure 1.2: Possible interactions between particles in the SM [1].

The problem is that if Λ_{UV} is at the order of the grand unification energy scale 10^{16} GeV, where electromagnetic, weak, and strong forces are unified into one force, this quantum correction to m_H^2 is some 24 orders of magnitude larger than the value of $m_H^2 = -(125 \text{ GeV})^2$. This is called 'hierarchy problem' [2–6]. The hierarchy problem is just for the Higgs boson mass. Indeed the quantum corrections to fermion and gauge boson masses do not have the quadratic term of Λ_{UV} because of symmetries.

In addition, since the Higgs mass is a parameter determined only through measurement at least in the SM, the problem can be also interpreted as a criterion that a future theory of particle physics, where the Higgs mass will be calculable, must be constructed without any excessive fine-tunings of the Higgs mass.

1.3   Supersymmetry

SM Particle Type	Particle	Symbol	Spin	R-Parity	Superpartner	Symbol	Spin	R-parity
Fermions	Quark	q	$\frac{1}{2}$	+1	Squark	$\tilde{q}$	0	-1
	Lepton	ℓ	$\frac{1}{2}$	+1	Slepton	$\tilde{\ell}$	0	-1
Bosons	W	W	1	+1	Wino	$\tilde{W}$	$\frac{1}{2}$	-1
	B	B	1	+1	Bino	$\tilde{B}$	$\frac{1}{2}$	-1
	Gluon	g	1	+1	Gluino	$\tilde{g}$	$\frac{1}{2}$	-1
Higgs bosons	Higgs	$H_u,\ H_d$	0	+1	Higgsino	$\tilde{H}_u,\ \tilde{H}_d$	$\frac{1}{2}$	-1

Table 1.1: The SM particles and their superpartners introduced by the supersymmetry. Symbol, Spin and R-Parity of each particle are shown.
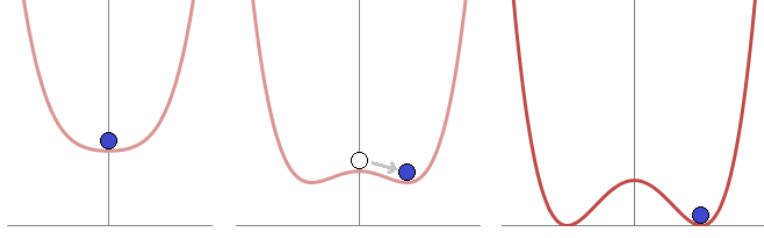
Figure 1.3: Illustration of the Higgs potential. The left/right figure shows the Higgs potential before/after electroweek spontaneous symmetry breaking (EWSB) and the center shows the transition. The parameters are $\lambda > 0$ and $\mu^2 > 0$ before the EWSB, and $\lambda > 0$ and $\mu^2 < 0$ after the EWSB.
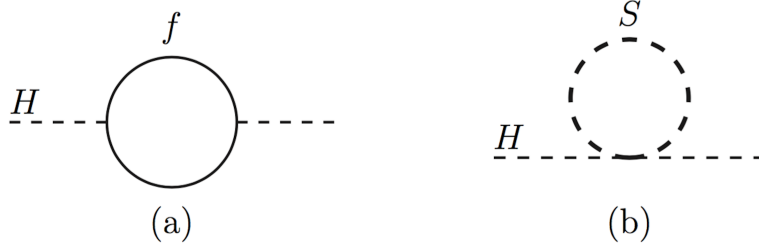

Figure 1.4: Feynman diagrams for loop correction to the Higgs mass m_H^2 from a fermion (a) and the correction from a scalar (b)

Supersymmetry (SUSY) or Supersymmetric Standard Model [6–12] is a well motivated extension of the SM that provides a natural solution [13, 14] to the hierarchy problem.

The supersymmetry assumes that there exists a symmetry between fermions and bosons by introducing an operator Q carrying spin angular momentum $1/2$ that transforms from a bosonic state into a fermionic state, and vice versa such as:

$$Q\,|\text{Boson}\rangle = |\text{Fermion}\rangle\,,\ Q\,|\text{Fermion}\rangle = |\text{Boson}\rangle \tag{1.5}$$

A minimal incorporation of the supersymmetry into the SM requires that there should exist supersymmetric partner (superpartner) particles to each of the SM particles as shown in Table 1.1, respectively. The superpartner of fermion is a scalar particle with spin 0 (Sfermion), and the superpartner of boson is a fermion particle with spin $\frac{1}{2}$ (Bosino). Each superpartner particle has the same mass as its partner unless the supersymmetry be broken. Each sfermion also has the same multiplet structure of its partner, $SU(3)_C \otimes SU(2)_L \otimes U(1)_Y$, so there are also left- and right-handed spinors for each sfermion. This extension of fermion multiplet is called 'chiral supermultiplet' and summarized in Table 1.2.

Furthermore, the couplings of fermion and sfermion to the Higgs are assumed to be exactly the same, namely $\lambda_S = |\lambda_f|^2$, where λ_S is a Yukawa coupling constant for sfermion. Therefore, the Feynman diagram of the loop correction from the sfermion to the Higgs mass is described as shown in Figure 1.4(b) and the correction is denoted by:

$$\Delta m_H^2 = 2 \times \left[\frac{\lambda_S}{16\pi^2} \Lambda_{\text{UV}}^2 - 2m_S^2 \ln\left(\Lambda_{\text{UV}}/m_S\right)... \right], \tag{1.6}$$

7

Names	Spinor Notation	spin 0	spin 1/2	$SU(3)_C,\ SU(2)_L,\ U(1)_Y$
squarks, quarks	Q	$\begin{pmatrix} \tilde{u}_L\ \tilde{d}_L \end{pmatrix}$	$(u_L\ d_L)$	$(\mathbf{3},\ \mathbf{2},\ \frac{1}{6})$
($\times 3$ families)	$\bar{u}$	$\tilde{u}_R^*$	$u_R^\dagger$	$(\bar{\mathbf{3}},\ \mathbf{1},\ -\frac{2}{3})$
	$\bar{d}$	$\tilde{d}_R^*$	$d_R^\dagger$	$(\bar{\mathbf{3}},\ \mathbf{1},\ \frac{1}{3})$
sleptons, leptons	L	$(\tilde{\nu}_L\ \tilde{e}_L)$	$(\nu_L\ e_L)$	$(\mathbf{1},\ \mathbf{2},\ -\frac{1}{2})$
($\times 3$ families)	$\bar{e}$	$\tilde{e}_R^*$	$e_R^\dagger$	$(\mathbf{1},\ \mathbf{1},\ 1)$

Table 1.2: Chiral supermultiplet and notation of left- and right-handed spinors for each fermion and each sfermion.

where m_S is mass of a sfermion. A remarkable thing is that the correction is positive[2] and completely cancels the huge loop correction from fermion to the Higgs mass in Equation 1.4. However, since the sfermion cancellation also leaves its own logarithmic correction proportional to m_S^2 (the second term in Equation 1.6), the mass of the sfermion with the largest Yukawa coupling must be, at most, at the order of ~ 1 TeV so that Δm_H^2 does not become too large.

This series of extensions of the SM is called Minimal Supersymmetric Standard Model (MSSM) and its logic or property to solve the hierarchy problem is called 'naturalness'.

In the MSSM, baryon number and lepton number get no longer conserved by all of the renormalizable couplings, but this conservation breaking must be very small in order not to conflict with the experimental upper limit on the proton life time [15]. To solve this, the MSSM requires that 'R-parity' should be conserved in the MSSM interactions. The R-parity is defined by:

$$P_R = (-1)^{3(B-L)+2s} \tag{1.7}$$

where B and L are baryon and lepton number and s is spin, respectively. As shown in Table 1.1, $P_R = +1$ for the SM particles and $P_R = -1$ for the superpartners. If R-parity conservation is true, this provides three important phenomenological consequences [16]:

- The lightest sparticle (LSP) with $P_R = -1$ must be stable. If the LSP is electrically neutral, it interacts only weakly with ordinary matter. Then the LSP can be an attractive candidate for the 'Dark Matter' [17, 18].

- Each sparticle except for the LSP must eventually decay into a state that contains an odd number of LSPs (usually just one).

- In collider experiments, sparticles can only be produced in even numbers at one collision (usually two at one collision).

In addition to naturalness and dark matter, 'gauge coupling unification' is also one of the theoretical motivations of the MSSM. By introducing the supersymmetric particles, it modifies the energy dependence of the three running coupling constants, making possible their perfect convergence at the scale of grand unification theory (GUT), $\Lambda_{\mathrm{GUT}} \sim 10^{16}$ GeV [6, 19–21]. Figure 1.5 shows the three running coupling constants in the SM and MSSM.

---

[2]This is due to a spin-statistics theorem meaning that fermions will have a negative contribution and bosons a positive contribution.
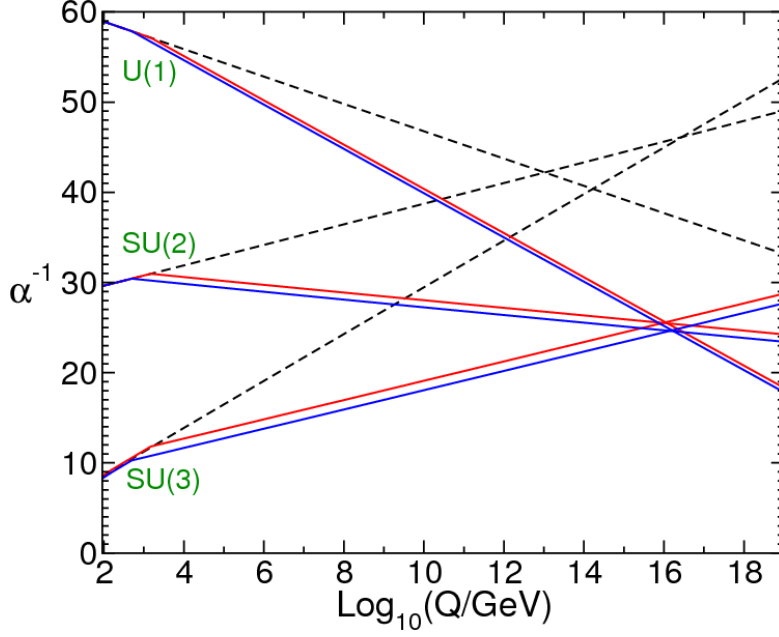
Figure 1.5: Two-loop renormalization group evolution of the inverse gauge couplings $\alpha_a^{-1}(Q)$ in the SM (dashed lines) and the MSSM (solid lines) [6]. The dependency on the threshold energy of transition from the SM to the MSSM is indicated by blue line (500 GeV) and red line (1.5 TeV).

1.4 Top Squark

Up to the present time, a superpartner particle that has the same mass as its normal partner has not been discovered, hence the supersymmetry breaking must occur so that superpartner particles get heavier than their normal partners.

Unlike the light-flavor squarks in the first and second generation, the stop has a non-negligible left-right mixing due to its large Yukawa coupling [22] [3]. The left-right mixing is described by a hermitian 2×2 mass matrix:

$$\mathcal{L}_M^{\tilde{t}} = -(\tilde{t}_L^*, \tilde{t}_R^*) \begin{pmatrix} M_{\tilde{t}_{LL}}^2 & M_{\tilde{t}_{LR}}^2 \\ M_{\tilde{t}_{RL}}^2 & M_{\tilde{t}_{RR}}^2 \end{pmatrix} \begin{pmatrix} \tilde{t}_L \\ \tilde{t}_R \end{pmatrix}, \tag{1.8}$$

with

$$\begin{aligned}
M_{\tilde{t}_{LL}}^2 &= M_{\tilde{Q}_3}^2 + (T_t^3 - Q_t \sin^2 \theta_W) \cos 2\beta \, m_Z^2 + m_t^2 \\
M_{\tilde{t}_{RR}}^2 &= M_{\tilde{t}}^2 + Q_t \sin^2 \theta_W \cos 2\beta \, m_Z^2 + m_t^2 \\
M_{\tilde{t}_{RL}}^2 &= (M_{\tilde{t}_{LR}}^2)^* = m_t \left(A_{\tilde{t}} - \mu^* (\tan \beta)^{-2T_t^3} \right)
\end{aligned} \tag{1.9}$$

where m_t, Q_t and T_t^3 are the mass, electric charge and weak isospin of top quark, respectively. θ_W denotes the weak mixing angle, $\tan \beta = v_u/v_d$ with v_u (v_d) being the vacuum expectation value of the Higgs field H_u^0 (H_d^0). $M_{\tilde{Q}_3}$ is the mass of left-handed squark spinor of third generation ($\tilde{Q}_3 = \left(\tilde{t}_L, \, \tilde{b}_L \right)$), and $M_{\tilde{t}}$ is the mass of right-handed spinor of stop. $A_{\tilde{t}}$ is a trilinear coupling constant of stop. In case parameters μ and $A_{\tilde{t}}$ are complex, the off-diagonal elements $M_{\tilde{t}_{RL}}^2 = (M_{\tilde{t}_{LR}}^2)^*$ are also complex with a phase of

$$\phi_{\tilde{t}} = \arg \left[M_{\tilde{t}_{RL}}^2 \right] = \arg \left[A_t - \mu^* (\tan \beta)^{-2T_t^3} \right]. \tag{1.10}$$

---

[3]The sbottom also has a non-negligible left-right mixing in the same way.

9

Finally, the stops in the mass eigenstates are written such as

$$\tilde{t}_1 = e^{i\phi_{\tilde{t}}} \cos\theta_{\tilde{t}}\tilde{t}_L + \sin\theta_{\tilde{t}}\tilde{t}_R$$
$$\tilde{t}_2 = -\sin\theta_{\tilde{t}}\tilde{t}_L + e^{-i\phi_{\tilde{t}}}\cos\theta_{\tilde{t}}\tilde{t}_R \tag{1.11}$$

where

$$\cos\theta_{\tilde{t}} = \frac{-\left|M^2_{\tilde{t}_{LR}}\right|}{\sqrt{\left|M^2_{\tilde{t}_{LR}}\right|^2 + \left(m^2_{\tilde{t}_1} - M^2_{\tilde{t}_{LL}}\right)^2}}, \; \sin\theta_{\tilde{t}} = \frac{M^2_{\tilde{t}_{LL}} - m^2_{\tilde{t}_1}}{\sqrt{\left|M^2_{\tilde{t}_{LR}}\right|^2 + \left(m^2_{\tilde{t}_1} - M^2_{\tilde{t}_{LL}}\right)^2}}. \tag{1.12}$$

Then the mass eigenvalues can be deduced to:

$$m^2_{\tilde{t}_{1,2}} = \frac{1}{2}\left(\left(M^2_{\tilde{t}_{LL}} + M^2_{\tilde{t}_{RR}}\right) \mp \sqrt{\left(M^2_{\tilde{t}_{LL}} - M^2_{\tilde{t}_{RR}}\right)^2 + 4\left|M^2_{\tilde{t}_{LR}}\right|^2}\right) \tag{1.13}$$

where $m_{\tilde{t}_1} < m_{\tilde{t}_2}$.

1.5 Neutralino

The higgsinos and electroweak gauginos mix each other because of the effects of the EWSB. The neutral higgsinos ($\tilde{H}^0_u$ and $\tilde{H}^0_d$) and the neutral gauginos ($\tilde{B}$, $\tilde{W}^0$) are combined to form four mass eigenstates called 'neutralinos'. The neutralino mass eigenstates are denoted by $\tilde{\chi}^0_{1,2,3,4}$. By convention, they are labeled in ascending order; $m_{\tilde{\chi}^0_1} < m_{\tilde{\chi}^0_2} < m_{\tilde{\chi}^0_3} < m_{\tilde{\chi}^0_4}$. The lightest neutralino $\tilde{\chi}^0_1$ is usually assumed to be the LSP or the dark matter candidate.

In the gauge-eigenstate basis $\psi^0 = (\tilde{B}, \tilde{W}^0, \tilde{H}^0_d, \tilde{H}^0_u)$, the neutralino mass term of the Lagrangian is

$$\mathcal{L}_{\text{neutralino mass}} = \frac{1}{2}(\psi^0)^T \boldsymbol{M}_{\tilde{\chi}^0}\psi^0 + \text{c.c.}, \tag{1.14}$$

where

$$\boldsymbol{M}_{\tilde{\chi}^0} = \begin{pmatrix} M_1 & 0 & -c_\beta s_W m_Z & s_\beta s_W m_Z \\ 0 & M_2 & c_\beta c_W m_Z & -s_\beta c_W m_Z \\ -c_\beta s_W m_Z & c_\beta c_W m_Z & 0 & -\mu \\ s_\beta s_W m_Z & -s_\beta c_W m_Z & -\mu & 0 \end{pmatrix}. \tag{1.15}$$

M_1 and M_2 are bino and wino mass, μ is higgsino mass, and $s_\beta = \sin\beta$, $c_\beta = \cos\beta$, $s_W = \sin\theta_W$, and $c_W = \cos\theta_W$. The mass matrix $\boldsymbol{M}_{\tilde{\chi}^0}$ can be diagonalized by a unitary matrix $\boldsymbol{N}$ to obtain mass eigenstates:

$$\tilde{\chi}^0{}_i = \boldsymbol{N}_{ij}\psi^0_j \tag{1.16}$$

so that

$$\boldsymbol{N}^*\boldsymbol{M}_{\tilde{\chi}^0}\boldsymbol{N}^{-1} = \begin{pmatrix} m_{\tilde{\chi}^0_1} & 0 & 0 & 0 \\ 0 & m_{\tilde{\chi}^0_2} & 0 & 0 \\ 0 & 0 & m_{\tilde{\chi}^0_3} & 0 \\ 0 & 0 & 0 & m_{\tilde{\chi}^0_4} \end{pmatrix} \tag{1.17}$$

has real positive values on the diagonal. Although $\tilde{\chi}^0_1$ (and $\tilde{\chi}^0_2$, $\tilde{\chi}^0_3$, $\tilde{\chi}^0_4$) is basically a mixture of $\tilde{B}$, $\tilde{W}^0$, $\tilde{H}^0_d$, $\tilde{H}^0_u$, $\tilde{\chi}^0_1$ could be in a pure state, such as:

- Pure Bino: $M_1 \ll M_2, \mu \Longrightarrow \tilde{\chi}^0_1 \approx \tilde{B}$

- Pure Wino: $M_2 \ll M_1, \mu \Longrightarrow \tilde{\chi}^0_1 \approx \tilde{W}^0$

- Pure Higgsino: $\mu \ll M_1, M_2 \Longrightarrow \tilde{\chi}^0_1 \approx \frac{\left(\tilde{H}^0_u \pm \tilde{H}^0_d\right)}{\sqrt{2}}$

1.6   Stop Search

This thesis aims at searching for the lighter stop ($\tilde{t}_1$). As described in Section 1.3, if the naturalness is true, the sfermion with the largest Yukawa coupling, namely stop, must have the mass of the order of ~ 1 TeV [23, 24]. This mass range can be explored sufficiently in the LHC, a hadron collider providing pp collisions at $\sqrt{s} = 13$ TeV. Stops can be produced through strong interactions and therefore can be produced in pp collisions. Because of the R-parity conservation, two stops are directly produced at one collision.

(a) stop two-body decay ($\tilde{t}_1 \rightarrow t\tilde{\chi}_1^0$)   (b) stop three-body decay ($\tilde{t}_1 \rightarrow bW\tilde{\chi}_1^0$)
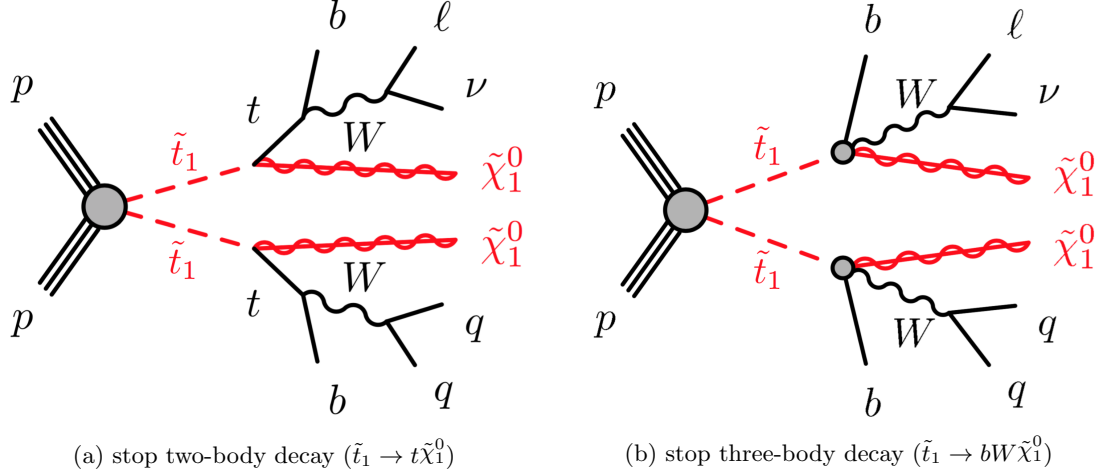
Figure 1.6: Feynman diagram of the direct pair production of $\tilde{t}_1$ particles and their two types of decays, $\tilde{t}_1 \rightarrow t\tilde{\chi}_1^0$ (a) and $\tilde{t}_1 \rightarrow bW\tilde{\chi}_1^0$ (b). For simplicity, no distinction is made between particles and antiparticles. The $\tilde{t}_1 \rightarrow t\tilde{\chi}_1^0$ and $\tilde{t}_1 \rightarrow bW\tilde{\chi}_1^0$ decay modes can be allowed if $m_{\tilde{t}_1} - m_{\tilde{\chi}_1^0} \equiv \Delta m(\tilde{t}_1, \tilde{\chi}_1^0) > m_t$ and $m_t > \Delta m(\tilde{t}_1, \tilde{\chi}_1^0) > m_W$, respectively.

The stop can decay into a variety of final states, depending on the SUSY particle mass spectrum, in particular on the masses of the stop and lightest neutralino. The analysis presented in this thesis targets $\tilde{t}_1 \rightarrow t\tilde{\chi}_1^0$ decay mode illustrated in Figure 1.6(a) where $m_{\tilde{t}_1} - m_{\tilde{\chi}_1^0} \equiv \Delta m(\tilde{t}_1, \tilde{\chi}_1^0) > m_t$, and focuses on the events with one lepton, where each $\tilde{t}_1$ decays as $\tilde{t}_1 \rightarrow t\tilde{\chi}_1^0$, the W boson from one of the two top quarks decays to an electron or muon (either directly or via a τ lepton) and the W boson from the other top quark decays hadronically. The final state can be denoted by $\tilde{t}_1\tilde{t}_1 \rightarrow [bqq\tilde{\chi}_1^0][b\ell\nu\tilde{\chi}_1^0]$ (with no distinction between particles and antiparticles). Thus, the dominant SM background events are:

- $t\bar{t}$

- a top quark and a W boson (single top, Wt)

- $t\bar{t} + Z(\rightarrow \nu\bar{\nu})$

- W bosons and jets (W+jets)

- two bosons (diboson)

In the analysis, the contribution of multijet events is found to be negligible from an data-driven estimation using a fake-factor method [25, 26]. In addition, since the $\tilde{t}_1 \rightarrow t\tilde{\chi}_1^0$ search is somewhat

sensitive to $\tilde{t}_1 \to bW\tilde{\chi}_1^0$ decay mode shown in Figure 1.6(b) where $m_t > \Delta m(\tilde{t}_1, \tilde{\chi}_1^0) > m_W$, the results are also interpreted in the $\tilde{t}_1 \to bW\tilde{\chi}_1^0$ decay mode scenario.

The signal kinematic topology highly depends on the model parameter $\Delta m(\tilde{t}_1, \tilde{\chi}_1^0)$, therefore there are three analyses individually optimized to three types of kinematic topologies, *Boosted* ($\Delta m(\tilde{t}_1, \tilde{\chi}_1^0) \gtrsim 3m_t$), *Resolved* ($\Delta m(\tilde{t}_1, \tilde{\chi}_1^0) \sim 2m_t$), and *Diagonal* ($\Delta m(\tilde{t}_1, \tilde{\chi}_1^0) \sim m_t$). Figure 1.7 and 1.8 illustrate the three topologies and territories of the three topologies in a $(m_{\tilde{t}_1}, m_{\tilde{\chi}_1^0})$ plane. For a scenario of $\Delta m(\tilde{t}_1, \tilde{\chi}_1^0) \gtrsim 3m_t$, the topology would be *Boosted* (Figure 1.7(a)), where the three jets from the t decay forms one large-R jet and a significantly large missing transverse energy (E_T^{miss}) arises from the two $\tilde{\chi}_1^0$'s with very high p_T. For a scenario of $\Delta m(\tilde{t}_1, \tilde{\chi}_1^0) \sim 2m_t$, the topology would be *Resolved* (Figure 1.7(b)), where the three jets are not merged into one large-R jet but resolved and a large E_T^{miss} arises from the two $\tilde{\chi}_1^0$'s. For a scenario of $\Delta m(\tilde{t}_1, \tilde{\chi}_1^0) \sim m_t$, the topology would be *Diagonal* (Figure 1.7(c)), where the three jets are resolved and $\tilde{\chi}_1^0$ and t from $\tilde{t}_1$ decay are nearly collinear with respect to $\tilde{t}_1$ momentum. The latter tendency results in a large cancellation of E_T^{miss} contributions from the two $\tilde{\chi}_1^0$'s.

In a preceding study using the data of 13.2 fb^{-1}, which uses events with one lepton in the final state, there were some excesses of CL$_b$ = 2.2 σ − 3.3 σ in several signal regions which are somewhat kinematically overlapped with each other [27]. The search in this thesis covers a part of the phase spaces with the excesses. For this reason, *Resolved* and *Boosted* analyses in this thesis are similar to those of Ref. [27]. The originality in this thesis is that a new analysis is developed and performed to search a stop mass region, named *Diagonal*, which is very important to solve the hierarchy problem naturally. The key technique newly developed for *Diagonal* analysis is a background estimation using '2-dimensional shape fit', which greatly expands the search region of *Diagonal*. In the following sections, *Boosted*, *Resolved*, and *Diagonal* analysis strategies are outlined.
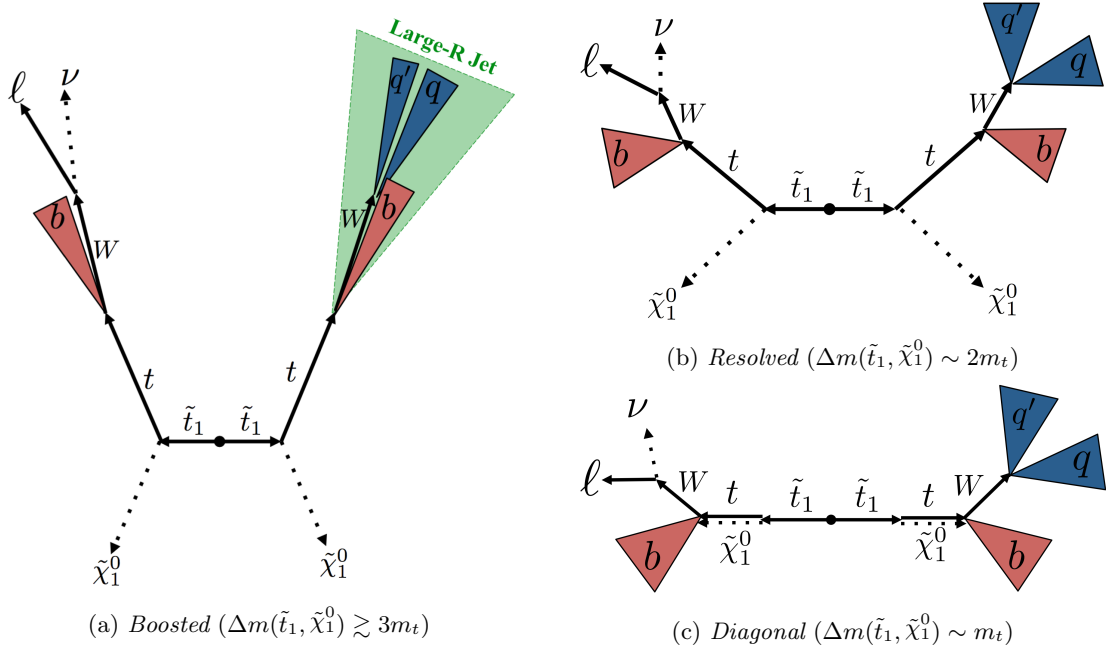

Figure 1.7: Illustration of three types of the signal kinematic topologies, *Boosted*, *Resolved*, and *Diagonal*, categorized by $\Delta m(\tilde{t}_1, \tilde{\chi}_1^0)$. The dashed lines indicate particles completely invisible to ATLAS detector. The cones indicate jets. The detail is explained in the main text.
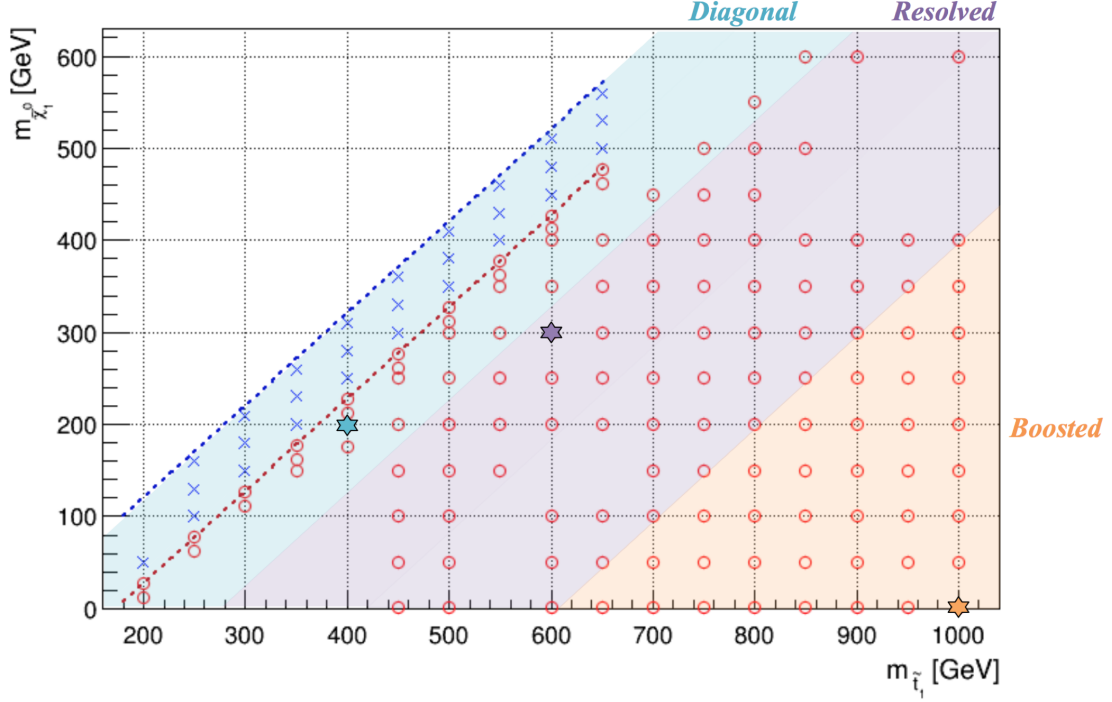
Figure 1.8: Illustration of all the mass points used in the analysis with categorization of the signal kinematic topologies. The red circle and the blue cross indicate the decay modes, $\tilde{t}_1 \to t\tilde{\chi}_1^0$ and $\tilde{t}_1 \to bW\tilde{\chi}_1^0$, respectively. The red and blue dashed lines are the boundaries of the decay modes. The cyan, purple, and orange regions are generally *Diagonal*, *Resolved*, and *Boosted* topology, respectively. The benchmark mass points to optimize *Diagonal*, *Resolved*, and *Boosted* analyses are indicated by cyan, purple, and orange stars, respectively.

1.6.1   *Boosted*

Boosted analysis aims at signal events with $\Delta m(\tilde{t}_1, \tilde{\chi}_1^0) \gtrsim 3m_t$ as indicated by the orange region in Figure 1.8. The benchmark mass point to optimize *Boosted* analysis is $(m_{\tilde{t}_1}, m_{\tilde{\chi}_1^0}) = (1000, 1)$ GeV.

In *Boosted* region, as shown in Figure 1.7(a), top quarks are highly boosted so that bqq' from hadronic top decay forms one large-R jet. If one approximates its ΔR by ΔR of W and b from top decay, then it can be written as the following equation;

$$\Delta R \approx \frac{2m_t}{p_T}, \tag{1.18}$$

where p_T is for top quark. In *Boosted* region, the top quark p_T can be approximately deduced to $p_T \sim \frac{m_{\tilde{t}_1}^2 - m_t^2}{2m_{\tilde{t}_1}}$, hence p_T in *Boosted* region is typically more than ~ 300 GeV and therefore ΔR of the large-R jet is less than ~ 1.2. Figure 1.9 shows distribution of ΔR between the W and b from top quark decay as a function of the top quark p_T and indicates that ΔR for top quarks with $p_T = 300$ GeV is mostly less than 1.2. From this fact and an optimization study, a reclustering jet algorithm is used in *Boosted* analysis that reconstructs large-R jets from small-R jets using anti-k_T algorithm with a jet radius parameter $R = 1.2$ [28]. Section 4.8 describes the algorithm in detail.

The $\tilde{\chi}_1^0$'s p_T is also very high and thus *Boosted* topology tends to provide larger missing

transverse energy (E_T^{miss}, see Section 4.6) than *Resolved* and *Diagonal* topologies and the SM events. The dominant background remaining after a large E_T^{miss} requirement is $t\bar{t}$ and $t\bar{t} + Z(\nu\nu)$ event.
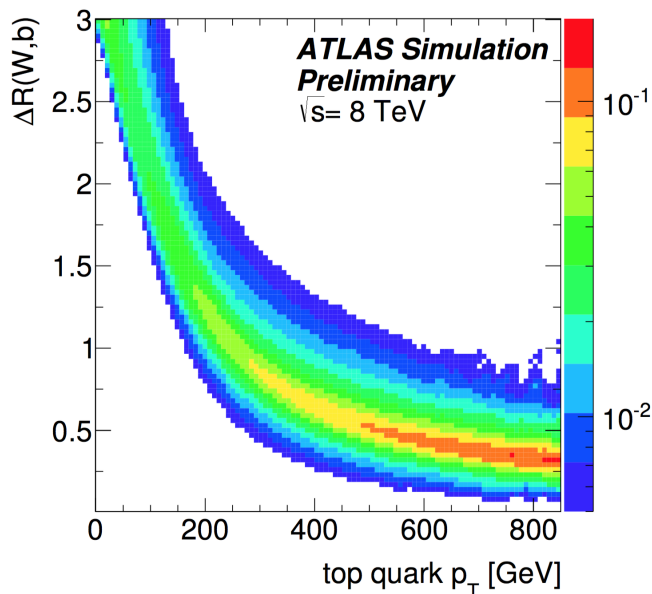
Figure 1.9: ΔR between the W and b from top quark decay as a function of the top quark p_T [29]. The distributions in every p_T bins are normalized to 1. the color coding corresponds to the fraction of considered top quarks at a p_T bin. The distribution corresponds to the particle information at the generator level after the emission of initial and final state radiation and are obtained from $t\bar{t}$ decays in pp collisions at $\sqrt{s} = 8$ TeV simulated using POWHEG +PYTHIA.

1.6.2 *Resolved*

Resolved analysis aims at signal events with $\Delta m(\tilde{t}_1, \tilde{\chi}_1^0) \sim 2m_t$ as indicated by the purple region in Figure 1.8. The benchmark mass point to optimize *Resolved* analysis is $(m_{\tilde{t}_1}, m_{\tilde{\chi}_1^0}) = (600, 300)$ GeV.

In *Resolved* region, as shown in Figure 1.7(b), the hadronic top decay products are not merged into one large-R jet but resolved into three smaller-radius jets because p_T of top quark is relatively medium. Since the $\tilde{\chi}_1^0$'s p_T is also relatively medium, *Resolved* topology tends to provide larger E_T^{miss} than *Diagonal* topology and the SM events. The dominant background remaining after a large E_T^{miss} requirement is $t\bar{t} \rightarrow [b\ell\nu][b\ell_{lost}\nu]$ event where ℓ_{lost} is a lost lepton due to outside acceptance, and thus contributes to increase E_T^{miss}. Section 5.2 describes an event selection to suppress the $t\bar{t} \rightarrow [b\ell\nu][b\ell_{lost}\nu]$ event and the other backgrounds.

1.6.3 *Diagonal*

Diagonal analysis aims at signal events with $\Delta m(\tilde{t}_1, \tilde{\chi}_1^0) \sim m_t$ as indicated by the cyan region in Figure 1.8. In Figure 1.8, $\Delta m(\tilde{t}_1, \tilde{\chi}_1^0) = m_{top}$ is equivalent to the red dashed line of the transition from $\tilde{t}_1 \rightarrow t\tilde{\chi}_1^0$ to $\tilde{t}_1 \rightarrow bW\tilde{\chi}_1^0$ decay mode, and thus it is called '(top-mass) diagonal line'. *Diagonal* analysis is also sensitive to $\tilde{t}_1 \rightarrow bW\tilde{\chi}_1^0$ scenario because it is similar to the

$\tilde{t}_1 \to t\tilde{\chi}_1^0$ event topology, although the analysis is optimized just only to $\tilde{t}_1 \to t\tilde{\chi}_1^0$ scenario. The benchmark mass point to optimize *Diagonal* analysis is $(m_{\tilde{t}_1}, m_{\tilde{\chi}_1^0}) = (400, 200)$ GeV.

In the region near the diagonal line, as shown in Figure 1.7(c), the behavior of hadronic top decay is the same as *Resolved* region. Figure 1.7(c) also indicates that $\tilde{\chi}_1^0$ and t from $\tilde{t}_1$ decay are nearly collinear with respect to $\tilde{t}_1$ momentum, because momenta of t and $\tilde{\chi}_1^0$ at the center of mass system of $\tilde{t}_1 \to t\tilde{\chi}_1^0$ are nearly 0. In addition, since $\tilde{t}_1$ pair is produced typically back-to-back, the directions of the two $\tilde{\chi}_1^0$'s also tend to be almost back-to-back. This results in a large cancellation of $E_{\mathrm{T}}^{\mathrm{miss}}$ contributions from the two $\tilde{\chi}_1^0$'s, and therefore *Diagonal* topology tends to provide a little bit larger $E_{\mathrm{T}}^{\mathrm{miss}}$ than the SM events[4].

Since the difference between *Diagonal* topology and $t\bar{t}$ event topology is smaller than *Boosted* and *Resolved*, the dominant background is $t\bar{t}$ event and it is very challenging to suppress them by event selection. For this reason, *Diagonal* analysis exploits a 2-dimensional ($E_{\mathrm{T}}^{\mathrm{miss}}$, m_{T}) shape fit that provides a precise background estimation, which is described in Section 6.4.

In the following chapters, the *Boosted*, *Resolved*, and *Diagonal* analyses are described in detail. Chapter 2 introduces outlines of the LHC and the ATLAS detector. Chapter 3 describes dataset and Monte Carlo samples used in the analyses. Chapter 4 defines physics objects and Chapter 5 defines event selections using the physics objects. Chapter 6 describes background estimations. Chapter 7 introduces hypothesis test procedures used to provide quantitative results of stop search. Chapter 8 describes systematic uncertainties used in the background estimations. Chapter 9 presents the stop search results. Chapter 10 is the conclusion of this thesis.

---

[4] If there is an initial or final state radiation from $pp \to \tilde{t}_1\tilde{t}_1$ process, the two $\tilde{\chi}_1^0$'s are not in back-to-back state and then a relatively large $E_{\mathrm{T}}^{\mathrm{miss}}$ also can arise.

Chapter 2

ATLAS Experiment

2.1 Large Hadron Collider

The Large Hadron Collider (LHC) [30] at the European Organization for Nuclear research (CERN) is a circular proton-proton (*pp*) collider. It is located in a tunnel with a 27 km circumference at a depth below ground of between 45 m (around lake Geneva) - 170 m (at the foot of the Jura mountains), which was excavated in the 1980s. In 8.33 T magnetic fields provided by superconducting dipole electromagnets, the proton beams circulate in opposite direction in two separate beam pipes in an ultra-high vacuum. Before being injected into the LHC, proton beams pass through a chain of pre-accelerators shown in Figure 2.1. First of all, the hydrogen atoms
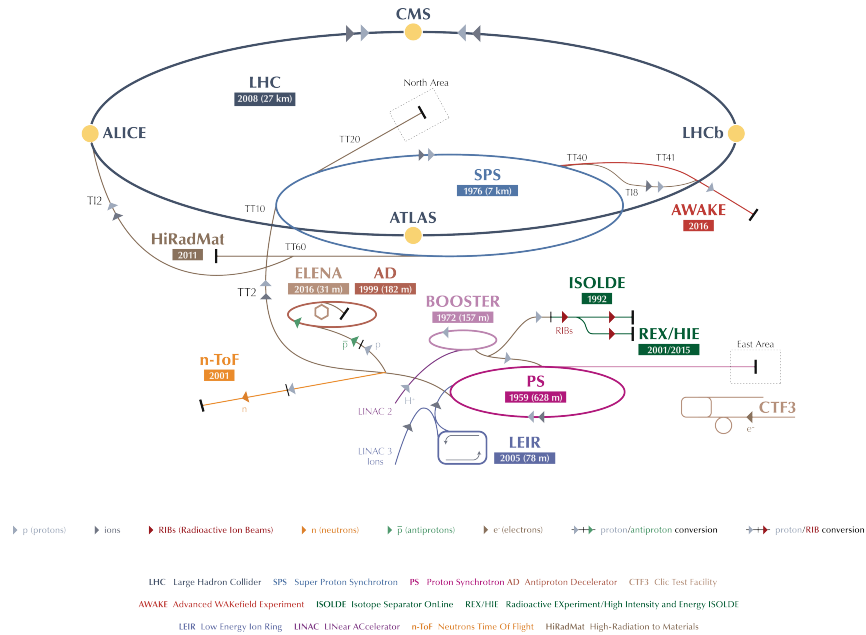
Figure 2.1: The CERN accelerator complex [31]. The LHC is the last ring (dark blue line) in a complex chain of particle accelerators.

with valence electrons stripped off are accelerated in the linear accelerator 2 (LINAC2) up to 50 MeV, and are injected afterwards into the Proton Synchrotron Booster (PSB). This first circular pre-accelerator increases the energy of the protons up to 1.4 GeV. After that, the protons are

accelerated to 25 GeV in the Proton Synchrotron (PS) and then injected into the Super Proton Synchrotron (SPS), where they are accelerated up to 450 GeV and then piped to the LHC. At the LHC, the protons are further accelerated up to the maximum achievable energy and are then collided at each of the four interaction points where the four main LHC experiments are hosted, the ATLAS, CMS, ALICE and LHCb experiments.

In the physics runs from 2010 to 2012 (Run-1), the center of mass energy of pp collisions $\sqrt{s}$ was 7-8 TeV. From 2015, LHC started with approximately 2 times higher energy $\sqrt{s} = 13$ TeV (Run-2). Figure 2.2 shows the peak and average instantaneous luminosity as a function of date in 2016. The max peak instantaneous luminosity in 2016 was $13.7 \times 10^{33} \mathrm{cm}^{-2} \mathrm{s}^{-1}$. The frequency of the bunch crossing is 40 MHz (in other words, the time between colliding bunches is 25 ns). The number of average interactions per bunch crossing is measured as shown in Figure 2.3. Since the instantaneous luminosity gradually increased during 2016, the number of the average interactions in 2016 is larger than 2015.
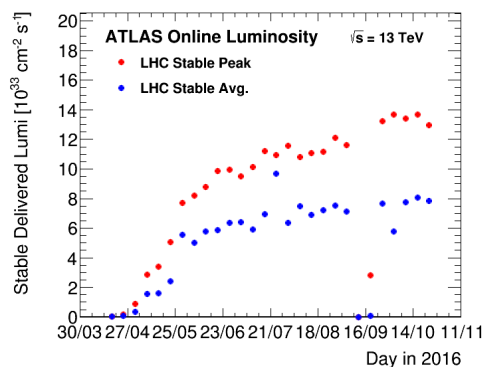
Figure 2.2: Peak and average instantaneous luminosity as a function of date in 2016.
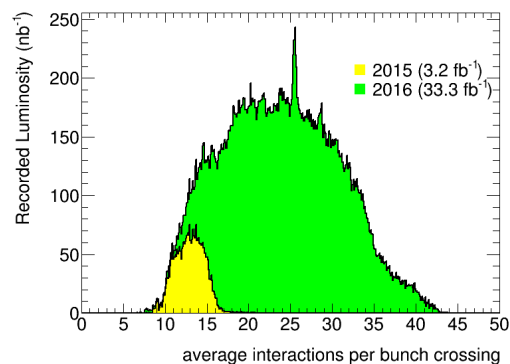
Figure 2.3: Observed number of the average interactions per bunch crossing. The 2015 dataset (3.2 fb^{-1}) and the 2016 dataset (33.3 fb^{-1}) are shown in the plot (amount to 36.5 fb^{-1}).

2.2 ATLAS Detector

ATLAS (A Toroidal LHC ApparatuS) detector [32] is a multipurpose particle physics detector with nearly 4π coverage in solid angle at the collision point.

In the ATLAS experiment, a right-handed coordinate system where the reference point is set at the nominal interaction point in the center of the detector and the z-axis is set along the beam pipe. The x-axis is set to point from the interaction point to the center of the LHC ring, and the y-axis points upward vertically. Cylindrical coordinates (r, ϕ) are also used in the x-y plane, where ϕ is the azimuthal angle around the z-axis. The pseudorapidity is defined using the polar angle θ as $\eta = -\ln \tan(\theta/2)$. ϕ and η are also used to measure angular distance defined as $\Delta R \equiv \sqrt{(\Delta\eta)^2 + (\Delta\phi)^2}$.

From inside to outside, particles traverse the inner detector (tracking of charged particles), the electromagnetic calorimeter (measuring energies of electron and photon), the hadronic calorimeter (measuring energies of hadrons), and the muon spectrometer (identifying muon and measuring its momentum) as illustrated in Figure 2.4 and 2.5.
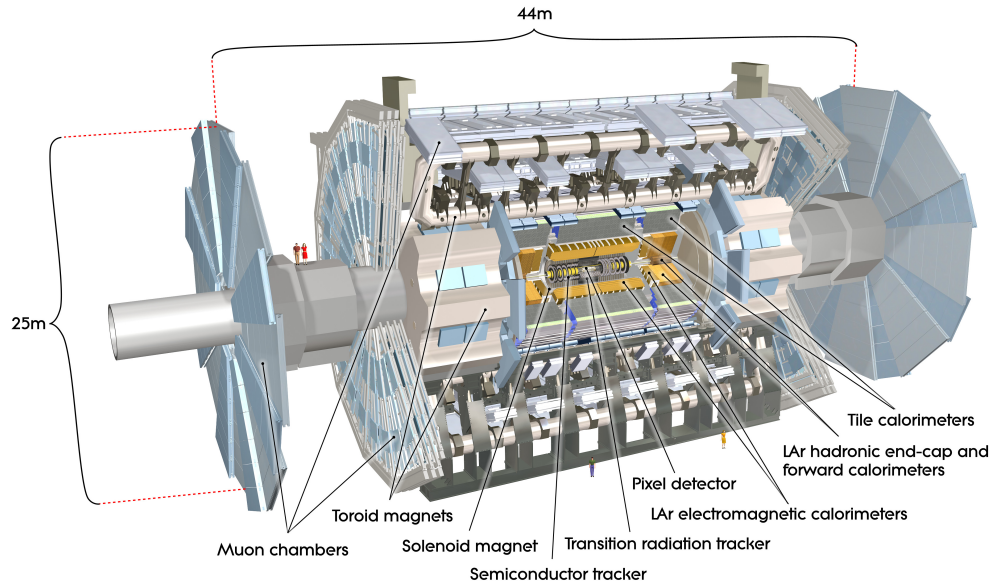
Figure 2.4: Cut-away view of the ATLAS detector [32]. The dimensions of the detector are 25 m in height and 44 m in length. The overall weight of the detector is approximately 7000 tonnes.
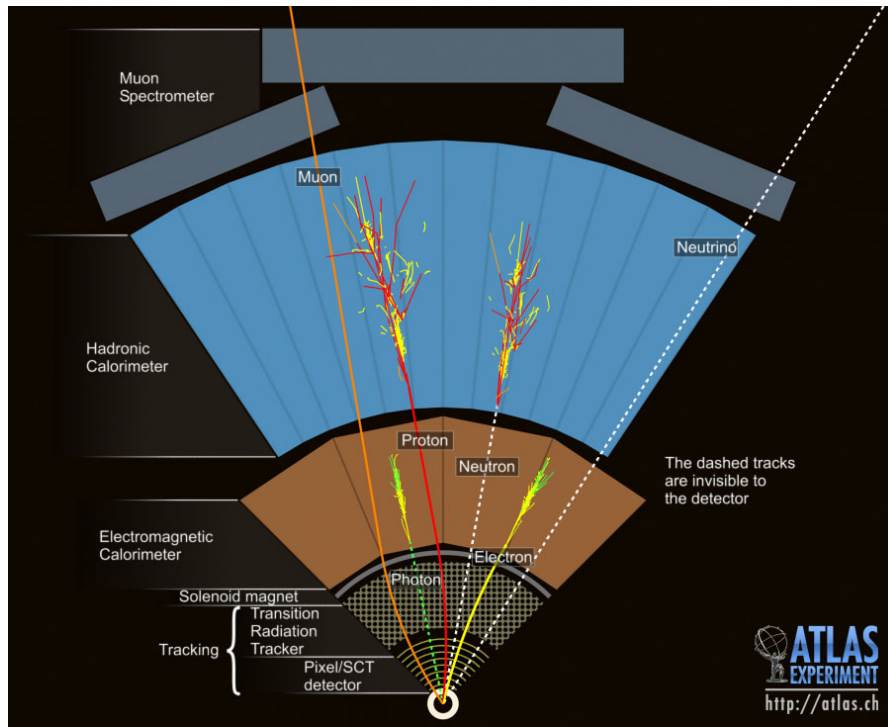
Figure 2.5: Illustration of particle detection in the sub-detectors of the ATLAS detector in R-ϕ cut-away view. From inside to outside, particles traverse the inner tracking detector, the electromagnetic calorimeter, the hadronic calorimeter, and the muon spectrometer. Trajectories indicated by dashed lines are invisible to the sub-detectors. For example, photons are invisible to the inner tracking detector but visible to the electromagnetic calorimeter. Neutrinos are invisible to all the sub-detectors.

2.2.1 Inner Detector
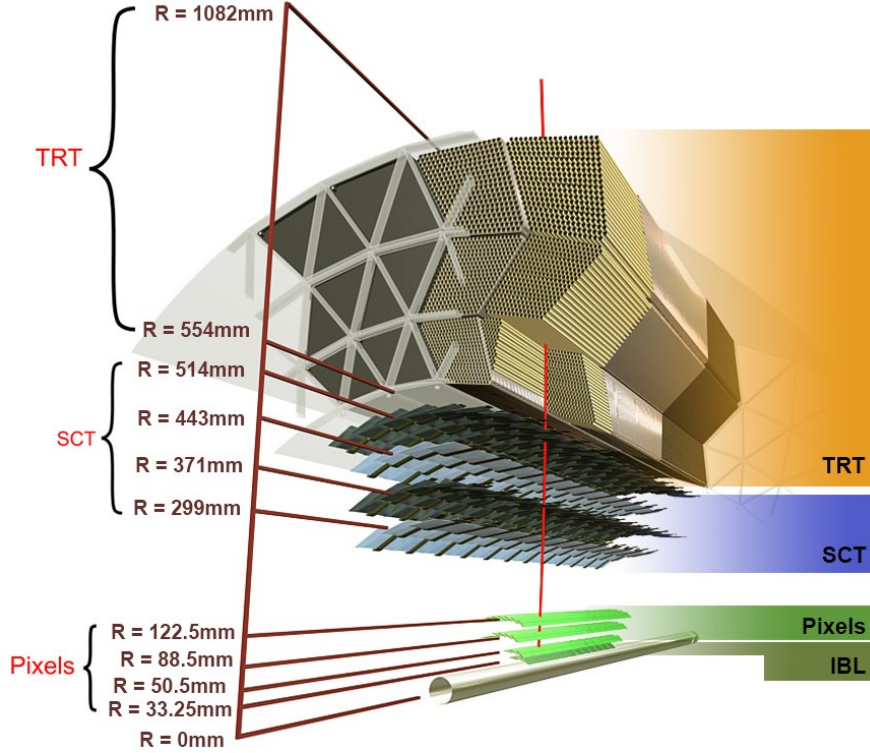
Figure 2.6: R-ϕ cross-sectional view of barrel part of the ATLAS inner detector, including the new insertable B-layer (IBL) [33]. The distances to the interaction point are also shown.

Approximately 1000 particles are produced from the collision point every 25 ns within $|\eta| <$ 2.5, and make a very high track density in the detector. The inner detector (ID) is designed to achieve robust track-pattern recognition and precision measurements of tracks and vertices. Figure 2.6 and 2.7 show the R-ϕ cross-sectional view of the ID barrel part and the R-z cross-sectional view of the ID, respectively. The ID is immersed in a uniform 2 T magnetic field generated by the central solenoid, which extends over a length of 5.3 m with a diameter of 2.5 m. The ID consists of 4 discrete sub-detectors, from inside to outside, silicon pixel detector (Pixel), semi-conductor tracker (SCT), and transition radiation tracker (TRT).

The precision tracking detectors (Pixel and SCT) cover the region $|\eta| <$ 2.5. In the barrel region, Pixel and SCT are arranged on concentric cylinders around the beam axis. In the end-cap regions, Pixel and SCT are located on disks perpendicular to the beam axis.

The Pixel achieves the high granularity around the vertex region. The Pixel layers are located such that each track typically crosses four pixel layers. The innermost layer, named insertable B-layer (IBL) [33], consists of 14 staves equipped with planar and 3D silicon pixel sensor technology that are arranged in turbine-like fashion. The pixel size of the IBL is $50 \times 250 \ \mu\text{m}^2$ in R-$\phi \times z$. The pixel sensors in the three outer layers have a minimum pixel size of $50 \times 400 \ \mu\text{m}^2$ in R-ϕ $\times z$. The intrinsic accuracies in the barrel are 10 μm (R-ϕ) and 115 μm (z) and in the disks are 10 μm (R-ϕ) and 115 μm (R).

For the SCT, eight strip layers are crossed by each track and reconstruct four space points. In the barrel region, the SCT uses small-angle (40 mrad) stereo strips and locate one set of strips
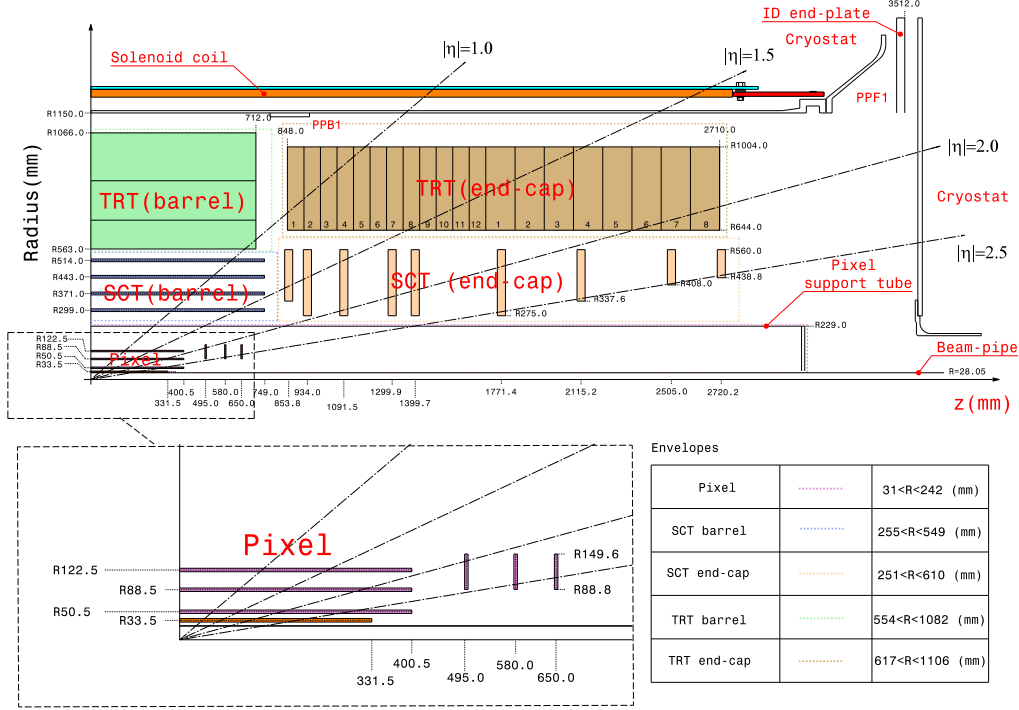
Figure 2.7: *R-z* cross-sectional view of the layout of the ATLAS Inner Detector for Run-2 [34]. The top panel shows the whole Inner Detector, whereas the bottom panel shows a magnified view of the Pixel detector region.

in each layer parallel to the beam axis in order to measure R-ϕ coordinates. The layers consist of two 6.4 cm long daisy-chained sensors with a strip pitch of 80 μm. In the end-cap region, the SCT has a set of strips running radially and a set of (40 mrad) stereo strips. The average pitch of the strips is approximately 80 μm. The intrinsic accuracies in the barrel are 17 μm (R-ϕ) and 580 μm (z) and in the disks are 17 μm (R-ϕ) and 580 μm (R).

The TRT provides typically 36 hits per track by its 4 mm diameter straw tubes and covers $|\eta| < 2.0$. The TRT only provides R-ϕ information and the intrinsic accuracy is 130 μm per straw. In the barrel region, the straws are 144 cm long and are parallel to the beam axis. In the end-cap region, the straws are 37 cm long and are arranged radially in wheels. The combination of the Pixel and the SCT with the TRT gives very robust pattern recognition and very high precision in both R-ϕ and z coordinates. The TRT contribute significantly to the momentum measurement because of the large number of measurements and the longer measured track length.

In order to identify electron, the tracking measurements in the ID system are also used with the precision measurements of the electromagnetic calorimeter. The electron identification capabilities are enhanced by the detection of transition-radiation photons in the xenon-based gas mixture of the TRT straw tubes. The Pixel and SCT also allow impact parameter measurements and vertexing for b-jet and τ lepton tagging. The performance of secondary vertex measurement is enhanced by the innermost layer of the Pixel at a radius of 33.5 mm.

21

2.2.2 Electromagnetic Calorimeter and Hadronic Calorimeter
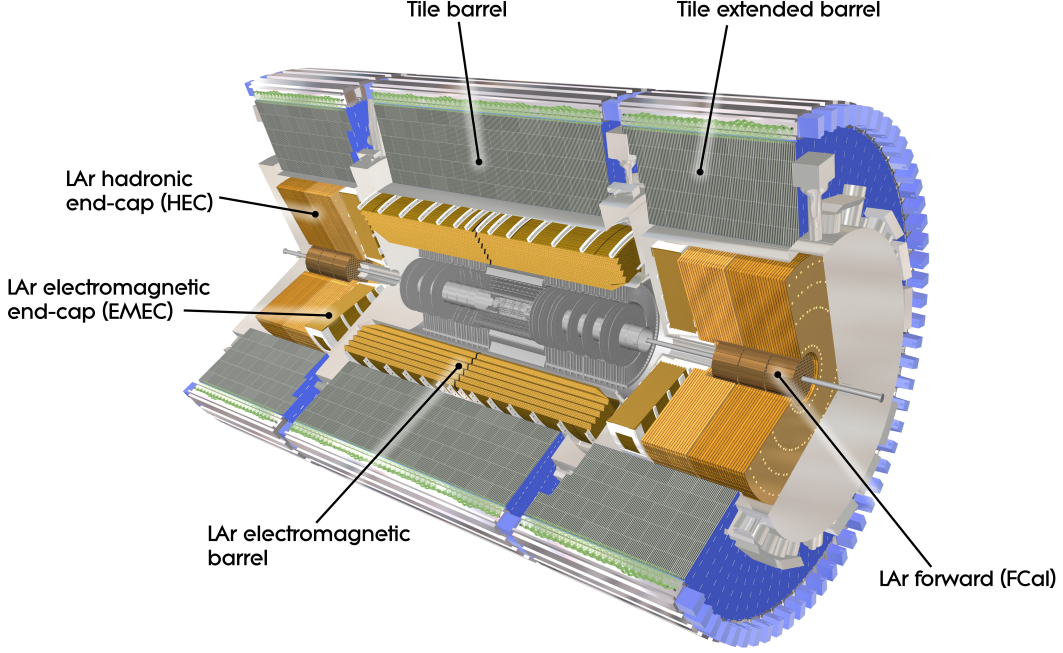
Figure 2.8: A cut-away view of the ATLAS calorimeter [35].

Figure 2.8 shows a cut-away view of the calorimeters. These calorimeters cover the range $|\eta|$ < 4.9, using different techniques suited to the various requirements of the physics processes of interest and of the radiation environment over this large η-range. Over the η region matched to the inner detector, $|\eta| < 2.5$, the fine granularity of the electromagnetic (EM) calorimeter is ideally suited for precision measurements of electrons and photons. The coarser granularity of the rest of the calorimeter is enough to satisfy the physics requirements for jet reconstruction and missing transverse energy measurements. Table 2.1 shows granularity versus $|\eta|$ of all the calorimeters.

Calorimeters are required to stop electromagnetic and hadronic showers in themselves, and suppress punch-through into the muon system. The total thickness of the EM calorimeter is at least 22 radiation lengths (X_0) in the barrel and at least 24 X_0 in the end-caps. The approximate 9.7 nuclear interaction lengths (λ) of hadronic calorimeter in the barrel (10 λ in the end-caps) are adequate to provide good resolution for high energy jets, $\sigma_E/E = 50\%/\sqrt{E/\mathrm{GeV}} \oplus 3\%$. The total thickness (including 1.3 λ from the outer support) is 11 λ at $|\eta| = 0$ and is enough to reduce punch-through of jets significantly (although muons can pass). This thickness also ensures a good missing transverse energy measurement, which is important for many physics analyses especially for SUSY particle searches. Figure 2.9 and 2.10 summarize radiation and interaction lengths of the ATLAS calorimeters.

The ATLAS Calorimeter consists of 4 types of calorimeters:

Liquid Argon (LAr) Calorimeter

It is a lead-LAr detector with accordion-shaped kapton electrodes and lead absorber plates. The accordion geometry provides complete ϕ symmetry without azimuthal cracks. The

EM Calorimeter			
	Barrel	End-cap	
Granularity $\Delta\eta \times \Delta\phi$ versus $|\eta|$			
Presampler	0.025×0.1 $\qquad |\eta| < 1.52$	0.025×0.1	$1.5 < |\eta| < 1.8$
Calorimeter 1st layer	$0.025/8 \times 0.1$ $\qquad |\eta| < 1.40$	0.050×0.1	$1.375 < |\eta| < 1.425$
	0.025×0.025 $\quad 1.40 < |\eta| < 1.475$	0.025×0.1	$1.425 < |\eta| < 1.5$
		$0.025/8 \times 0.1$	$1.5 < |\eta| < 1.8$
		$0.025/6 \times 0.1$	$1.8 < |\eta| < 2.0$
		$0.025/4 \times 0.1$	$2.0 < |\eta| < 2.4$
		0.025×0.1	$2.4 < |\eta| < 2.5$
		0.1×0.1	$2.5 < |\eta| < 3.2$
Calorimeter 2nd layer	0.025×0.025 $\qquad |\eta| < 1.40$	0.050×0.025	$1.375 < |\eta| < 1.425$
	0.075×0.025 $\quad 1.40 < |\eta| < 1.475$	0.025×0.025	$1.425 < |\eta| < 2.5$
		0.1×0.1	$2.5 < |\eta| < 3.2$
Calorimeter 3rd layer	0.050×0.025 $\qquad |\eta| < 1.35$	0.050×0.025	$1.5 < |\eta| < 2.5$
LAr Hadronic End-cap (HEC)			
Granularity $\Delta\eta \times \Delta\phi$ versus $|\eta|$			
Calorimeter 1st layer		0.1×0.1	$1.5 < |\eta| < 2.5$
Calorimeter 2nd layer		0.1×0.1	$1.5 < |\eta| < 2.5$
Calorimeter 3rd layer		0.2×0.2	$2.5 < |\eta| < 3.2$
Calorimeter 4th layer		0.2×0.2	$2.5 < |\eta| < 3.2$
LAr Forward Calorimeter (FCal)			
Granularity $\Delta x \times \Delta y$ (cm) versus $|\eta|$			
Calorimeter 1st layer		3.0×2.6	$3.15 < |\eta| < 4.30$
		$\sim$ four times finer	$3.10 < |\eta| < 3.15$
			$4.30 < |\eta| < 4.83$
Calorimeter 2nd layer		3.3×4.2	$3.24 < |\eta| < 4.50$
		$\sim$ four times finer	$3.20 < |\eta| < 3.24$
			$4.50 < |\eta| < 4.81$
Calorimeter 3rd layer		5.4×4.7	$3.32 < |\eta| < 4.60$
		$\sim$ four times finer	$3.29 < |\eta| < 3.32$
			$4.60 < |\eta| < 4.75$
Scintillator Tile Calorimeter			
Granularity $\Delta\eta \times \Delta\phi$ versus $|\eta|$			
	Barrel	Extended Barrel	
Calorimeter 1st layer	0.1×0.1 $\qquad |\eta| < 1.0$	0.1×0.1	$0.8 < |\eta| < 1.7$
Calorimeter 2nd layer	0.1×0.1 $\qquad |\eta| < 1.0$	0.1×0.1	$0.8 < |\eta| < 1.7$
Calorimeter 3rd layer	0.2×0.1 $\qquad |\eta| < 1.0$	0.2×0.1	$0.8 < |\eta| < 1.7$

Table 2.1: Granularity versus $|\eta|$ in each layer of each calorimeters.
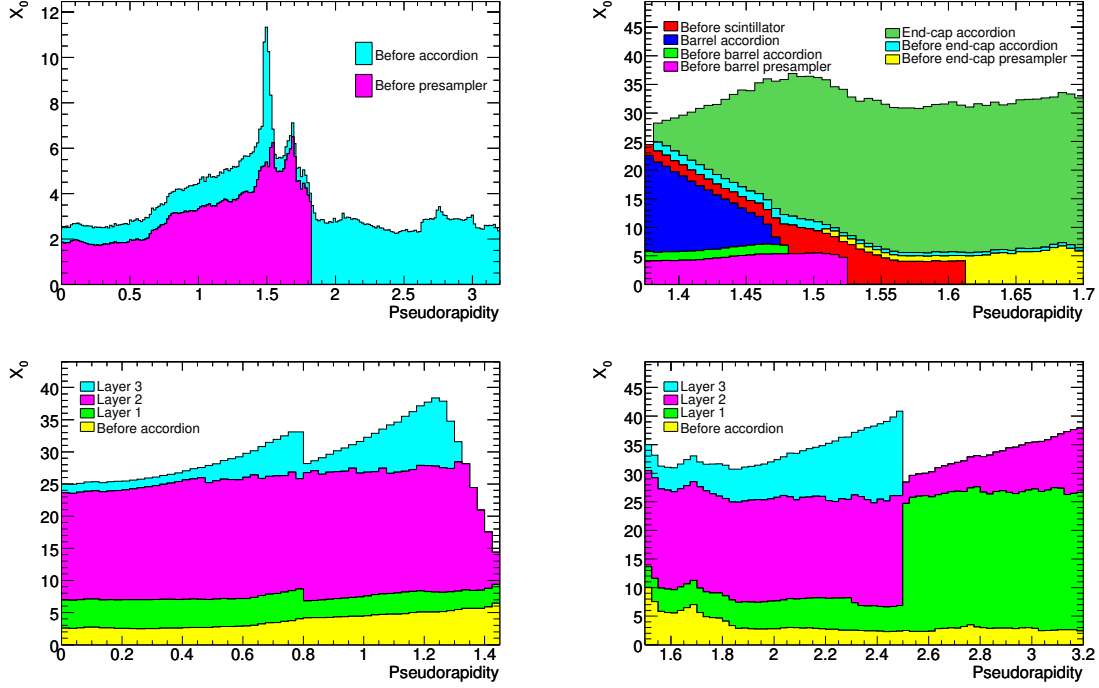
Figure 2.9: Cumulative amounts of material in front of and in the electromagnetic calorimeters, in units of radiation length X_0, as a function of $|\eta|$. The top left-hand plot shows separately the total amount of material in front of the presampler layer and in front of the accordion for the full η-coverage. The top right-hand plot shows the details of the crack region between the barrel and endcap cryostats. The two bottom figures show the thicknesses of each accordion layer as well as the amount of material in front of the accordion, for the barrel (left) and end-cap (right) part, respectively.

lead thickness in the absorber plates has been optimized as a function of η in terms of EM calorimeter performance in energy resolution. The EM calorimeter is divided into a barrel part ($|\eta| < 1.475$) and two end-cap components ($1.375 < |\eta| < 3.2$). The barrel calorimeter consists of two identical half-barrels, separated by a small gap (4 mm) at $z = 0$. Each end-cap calorimeter is mechanically divided into two coaxial wheels; an outer wheel covering the region $1.375 < |\eta| < 2.5$, and an inner wheel covering the region $2.5 < |\eta| < 3.2$. Over the region devoted to precision physics ($|\eta| < 2.5$), the EM calorimeter is segmented in three sections in depth. Furthermore, in the region of $|\eta| < 1.8$, a presampler detector is used to correct for the energy lost by electrons and photons upstream of the calorimeter. The presampler consists of only an active LAr layer of thickness 1.1 cm (0.5 cm) in the barrel (end-cap) region. Figure 2.11 and 2.12 show a module in the barrel and the accordion-shaped structure. With Run-1 full datasets, the energy resolution for electron and photon has been studied and is shown in Figure 2.13.

Tile Calorimeter

It is a hadronic calorimeter located just outside the EM calorimeter envelope. Its barrel covers the region $|\eta| < 1.0$, and its two extended barrels $0.8 < |\eta| < 1.7$. It is a sampling calorimeter using steel as the absorber and scintillating tiles as the active material.
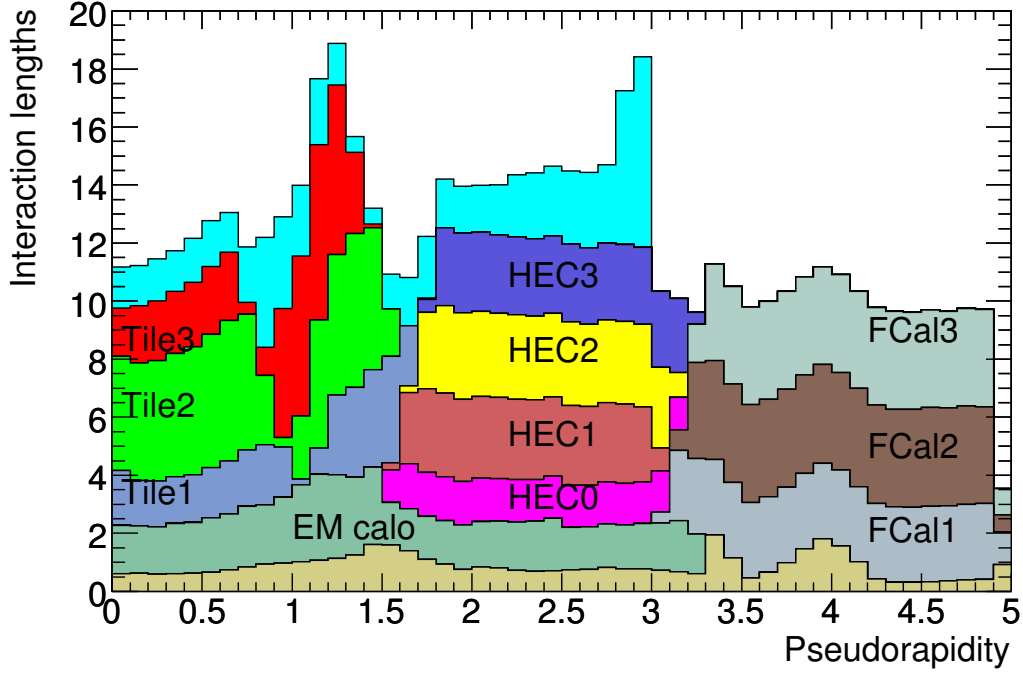
Figure 2.10: Cumulative amount of material, in units of interaction length, as a function of $|\eta|$. The total amount of material in front of the electromagnetic calorimeters and in front of the first active layer of the muon spectrometer (up to $|\eta| < 3.0$) are also shown (dusty yellow and light blue respectively).

Figure 2.14 shows structure of a barrel module of the tile calorimeter. The barrel and extended barrels are divided azimuthally into 64 modules. Radially, the tile calorimeter extends from an inner radius of 2.28 m to an outer radius of 4.25 m. It is segmented in depth in three layers, approximately 1.5, 4.1 and 1.8 nuclear interaction lengths (λ) for the barrel and 1.5, 2.6, and 3.3 λ for the extended barrel. The total detector thickness at the outer edge of the tile-instrumented region is 9.7 λ at $|\eta| = 0$.

LAr Hadronic End-cap Calorimeter (HEC)

It consists of two independent wheels per end-cap located behind the end-cap electromagnetic calorimeter. The HEC covers the range $1.5 < |\eta| < 3.2$.

LAr Forward Calorimeter (FCal)

It covers $3.1 < |\eta| < 4.9$. In order to reduce the amount of neutrons in the inner detector cavity, the front face of the FCal is 1.2 m behind the EM calorimeter front face as shown in Figure 2.15. This severely limits the depth of the calorimeter and therefore calls for a high-density design. The FCal is approximately 10 interaction lengths deep, and consists of three modules in each end-cap; the first, made of copper, is optimized for electromagnetic measurements, while the other two, made of tungsten, measure mainly the energy of hadronic interactions. As shown in Figure 2.16, each module consists of a metal matrix, with regularly spaced longitudinal channels filled with the electrode structure consisting of concentric rods and tubes parallel to the beam axis. The LAr in the gap between the rod and the tube is the sensitive medium.
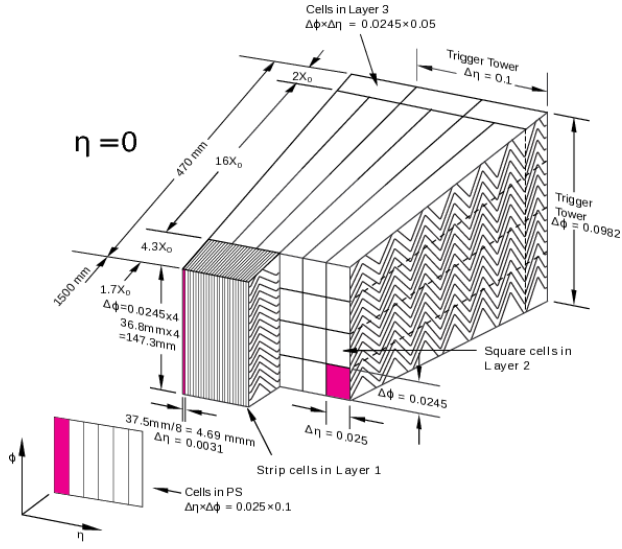
Figure 2.11: Sketch of a barrel module in the LAr calorimeter where the different layers are clearly visible with the accordion-shaped kapton electrodes [36]. The granularity in $\Delta\eta \times \Delta\phi$ of the cells of each of the three layers is also shown.
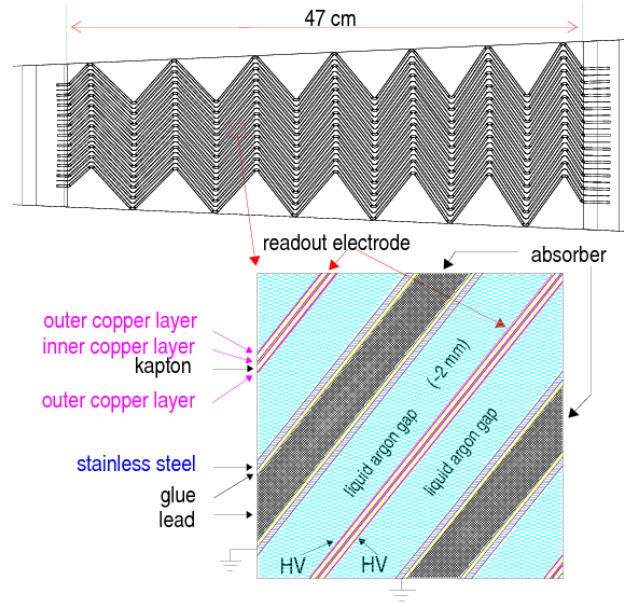
Figure 2.12: Accordion structure of the barrel [36]. The top figure is a view of a small sector of the barrel calorimeter in R-ϕ plane.
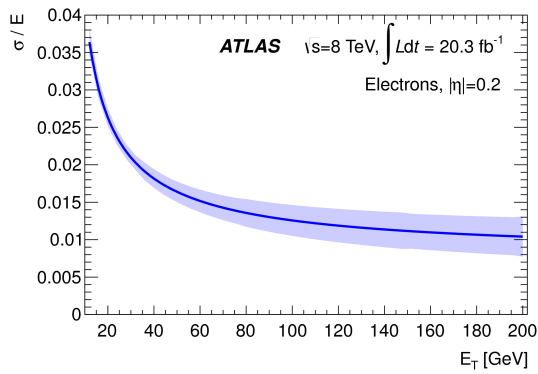
(a) Energy resolution for electron
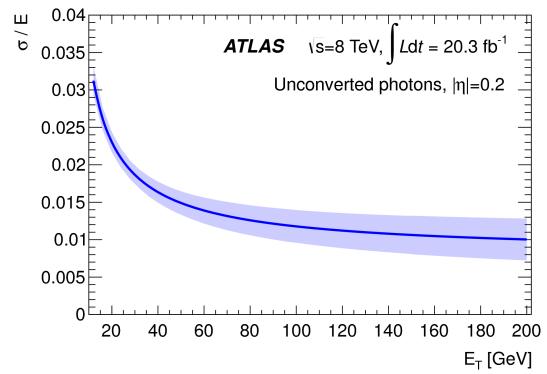
(b) Energy resolution for photon

Figure 2.13: Energy resolution for electron and photon as function of E_T [37].
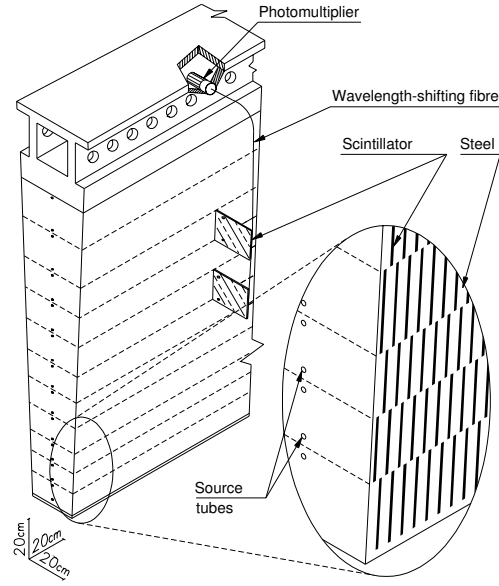
Figure 2.14: Sketch of a barrel module of the tile calorimeter.
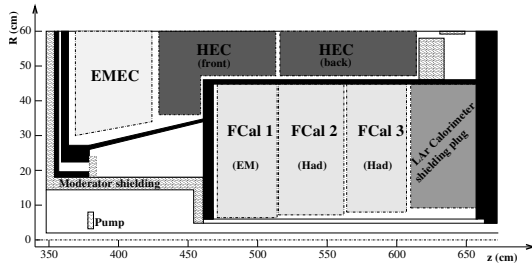
Figure 2.15: A schematic diagram showing the three FCal modules located in the end-cap cryostat. The material in front of the FCal and the shielding plug behind it are also shown. The black regions are structural parts of the cryostat. For clarity, the vertical scale is enlarged in the diagram.
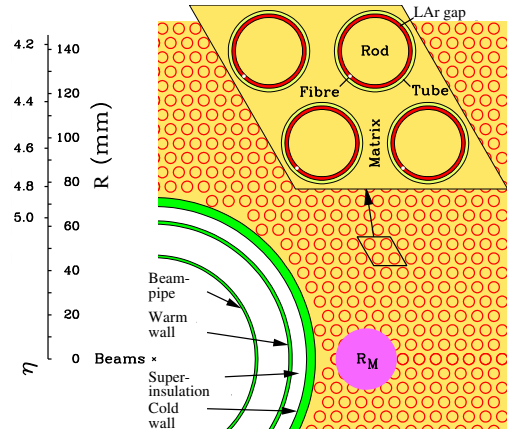
Figure 2.16: Electrode structure of the FCal 1st layer with the matrix of copper plates and the copper tubes and rods with the LAr gap for the electrodes. The Moliere radius, R_M, is represented by the solid disk.

2.2.3 Muon Spectrometer
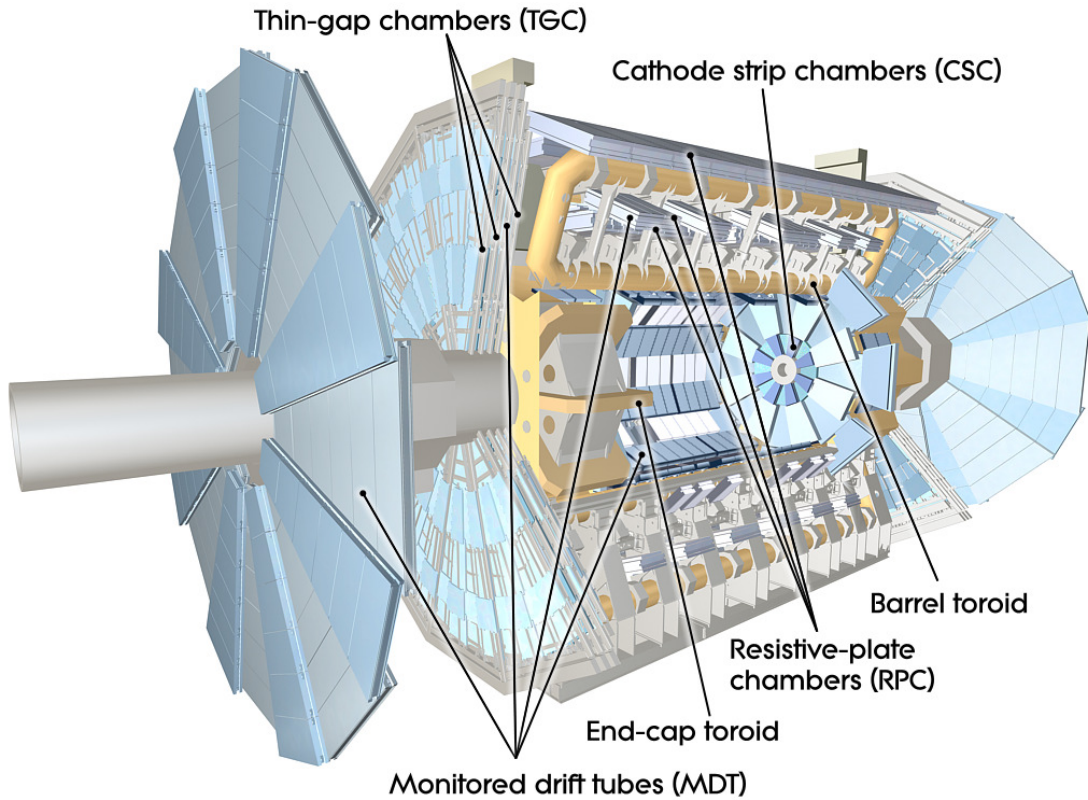
Figure 2.17: Cut-away view of the ATLAS muon system.

The Muon Spectrometer (MS) is the outermost and largest part of the ATLAS detector as shown in Figure 2.17. The MS is based on the magnetic deflection of muon tracks in the large superconducting air-core toroid magnets and consists of separate trigger and high-precision tracking chambers. Figure 2.18 shows geometry of the air-core toroid magnets. The use of air-core toroid magnets can minimize the degradation of resolution due to multiple scattering. Figure 2.19 shows a R-z cross-sectional view of the MS. For $|\eta| < 1.4$, magnetic bending is provided by the large barrel toroid. For $1.6 < |\eta| < 2.7$, muon tracks are bent by two smaller end-cap magnets which are inserted into both ends of the barrel toroid. The range of $1.4 < |\eta| < 1.6$ is usually referred to as the transition region where magnetic deflection is provided by a combination of barrel and end-cap fields and the field is mostly orthogonal to the muon trajectories.

For $|\eta| < 2.7$, a precision measurement of the track coordinates is provided by Monitored Drift Tubes (MDT's). The mechanical separation in the drift tubes of each sense wire from its neighbors assures a robust and reliable operation. For $2.0 < |\eta| < 2.7$, Cathode Strip Chambers (CSC's) are used, which are multiwire proportional chambers with cathodes segmented into strips with higher granularity.

The trigger system of the MS covers the pseudorapidity range $|\eta| < 2.4$. As trigger chambers, Resistive Plate Chambers (RPC's) are used in the barrel and Thin Gap Chambers (TGC's) are used in the end-cap regions. The trigger chambers provide bunch-crossing identification, provide well-defined p_T thresholds, and measure the muon momentum in z-axis.
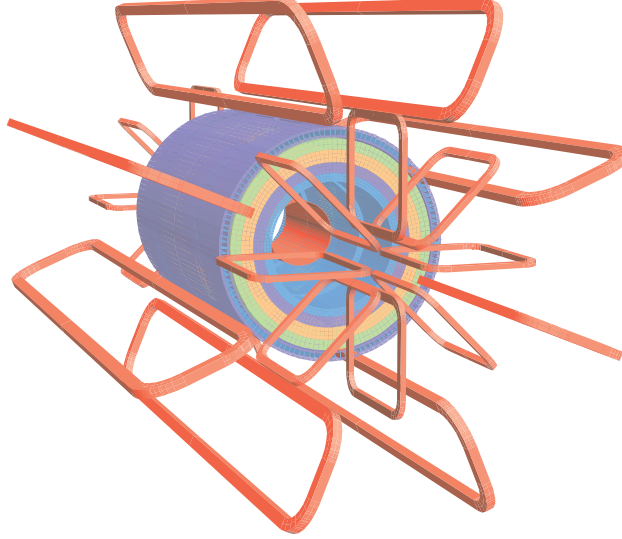
Figure 2.18: Geometry of air-core toroid magnets. The Tile calorimeter steel is also shown as a reference. The eight barrel toroid coils and the end-cap coils inserted into both ends of the barrel toroid are visible.
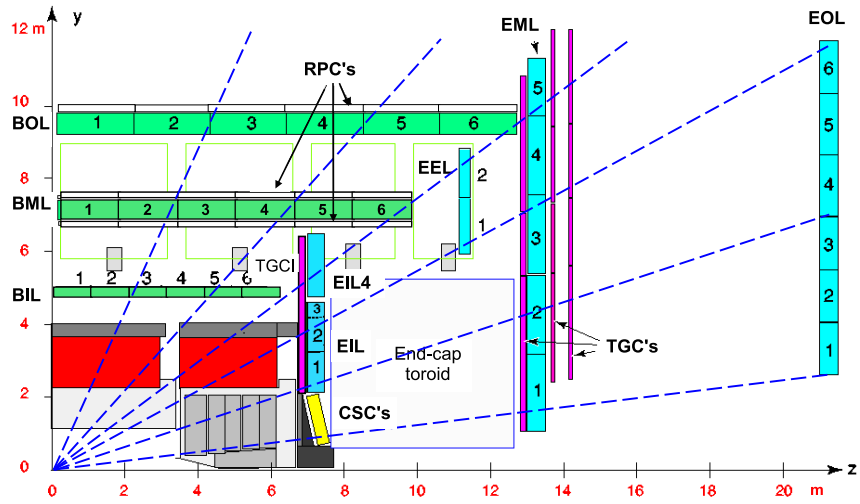
Figure 2.19: $R\text{-}z$ cross-sectional view of the muon system. Infinite-momentum muons would propagate along straight trajectories which are illustrated by the dashed lines and typically traverse three muon stations.

2.3 Trigger and Data Acquisition

pp collisions in the LHC produce too many events to record all of them, most of which are not interesting in physics analyses, for example, low p_T multi-jet events. The cross section of these events is about 100 mb while that of new physics events is typically at the order of 1 fb. Therefore, by using a two-level trigger system, the only interesting events are recorded as many as possible with rejecting unimportant events. Figure 2.20 shows a schematic of the trigger and data acquisition (TDAQ) system. The first level is a hardware-based system named 'Level 1 Trigger (L1)' and uses information of the calorimeter[1] and the the muon spectrometer to reduce the accepted rate to 100 kHz. The second level is a software-based system named 'High Level Trigger (HLT)' that reduces the rate of event records to 1 kHz. There are many types of triggers for several physics purposes [38], which are called "trigger menus". The trigger menu must be changed depending on the instantaneous luminosity.
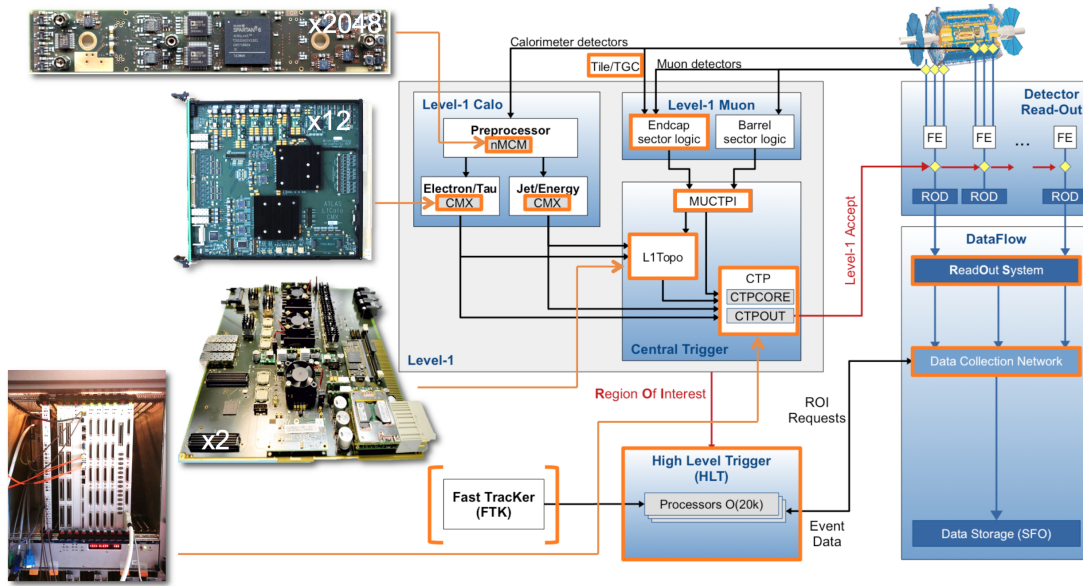
Figure 2.20: The ATLAS trigger and data acquisition (TDAQ) system in Run-2 [39]. New features with respect to the Run-1 system are indicated with orange boxes.

---

[1] There is a long-term project of upgrading trigger readout of the calorimeter, which is aimed at 'High-Luminosity LHC (HL-LHC)' that will start from 2024 with an ultimate peak instantaneous luminosity of $\mathcal{L} \sim 5 \times 10^{34}$ cm^{-2}s^{-1}. See Appendix D.

Chapter 3

Data and Monte Carlo Samples

This chapter introduces datasets and Monte Carlo (MC) samples used in the analysis. The datasets are described in Section 3.1 with the detail of triggers used in the analysis. MC samples are used to model events of the SM background and signal processes in ATLAS. The MC samples are summarized in Section 3.2.

3.1   Data and Trigger

In this thesis, ATLAS data collected in proton-proton (pp) collisions at a center-of-mass energy of $\sqrt{s} = 13$ TeV in 2015 and 2016 are used. The data is required to have been recorded in the state of stable beam and stable detector operation with no issue. In 2016, data taking has continued until 26 October and finally amounts to 33.3 fb^{-1}. In this thesis, the 2015 data (3.2 fb^{-1}) and the data taken until 9 September in 2016 (24.8 fb^{-1}) are used, and therefore the total amount is 28.0 fb^{-1}.

Resolved and *Boosted* analyses use events recorded by a $E_{\mathrm{T}}^{\mathrm{miss}}$ trigger that accepts events with an $E_{\mathrm{T}}^{\mathrm{miss}}$ threshold at trigger level 80 GeV for the 2015 dataset and 100 and 110 GeV for an early and a late part of 2016 dataset, respectively[1].

Diagonal analysis uses events recorded by the same $E_{\mathrm{T}}^{\mathrm{miss}}$ trigger as the *Resolved* and *Boosted* case, three single-electron triggers, or two single-muon triggers. If $E_{\mathrm{T}}^{\mathrm{miss}}$ reconstructed at the offline level (see Section 4.6) is larger than 200 GeV, the $E_{\mathrm{T}}^{\mathrm{miss}}$ trigger and the single-electron and the single-muon triggers are considered; otherwise only those lepton triggers are considered. The three single-electron triggers record an event if an electron has p_{T} at the trigger level larger than 24, 60, and 120 GeV for the 2015 dataset and 26, 60, and 140 GeV for the 2016 dataset. The two single-muon triggers record an event if a muon has p_{T} at the trigger level larger than 20 and 50 GeV for the 2015 dataset and 26 and 50 GeV for the 2016 dataset. The single-electron and single-muon triggers with lower p_{T} threshold impose tighter electron and muon quality requirements. Table 3.1 summarizes the trigger configurations for *Resolved*, *Boosted*, and *Diagonal*.

---

[1] As the instantaneous luminosity increases, pileup events increase so that trigger thresholds must be tighten to keep the total L1 trigger rate 100 kHz.

Trigger	Threshold	2015	early-2016	late-2016
For *Resolved*, *Boosted*, and *Diagonal*				
MET	80 GeV	◯		
	100 GeV		◯	
	110 GeV			◯
For *Diagonal* Only				
Single Electron	24 GeV + Medium ID	◯		
	26 GeV + Tight ID + Loose Isolation		◯	◯
	60 GeV + Medium ID	◯	◯	◯
	120 GeV + Loose ID	◯		
	140 GeV + Loose ID		◯	◯
Single Muon	20 GeV + Loose Isolation	◯		
	26 GeV + Medium Isolation		◯	◯
	50 GeV	◯	◯	◯

Table 3.1: Trigger configurations for *Resolved*, *Boosted*, and *Diagonal*. For *Diagonal*, events are recorded by the $E_\mathrm{T}^\mathrm{miss}$ or the single-lepton triggers, and the $E_\mathrm{T}^\mathrm{miss}$ triggers are used only when offline $E_\mathrm{T}^\mathrm{miss} > 200$ GeV; otherwise single-lepton triggers are used only. The single-electron and single-muon triggers with lower p_T threshold impose tighter electron and muon quality and/or isolation requirements.

3.2 Monte Carlo Samples

The nominal MC samples used in this analysis are summarized in Table 3.2. All samples, except for the signal and $t\bar{t} + \gamma$ sample, are processed with the full simulation of the ATLAS detector [40] based on GEANT4 [41]. The signal samples and the $t\bar{t} + \gamma$ sample are processed with a fast simulation [42] of the ATLAS detector, where a parameterized shower simulation is used for the calorimeter and other parts are the same as the full simulation.

The signal, $t\bar{t} + W/Z$ (for *Resolved* and *Boosted*), and $t\bar{t} + \gamma$ sample that are generated at leading order (LO), while other samples and $t\bar{t} + W/Z$ (for *Diagonal*) are generated at next-to-leading order (NLO). To simulate these events more realistically, additional radiations are generated by PYTHIA 8 in the parton showering process.

All samples are produced with varying the number of minimum-bias events following the expected pileup distributions, where the minimum-bias events simulated from PYTHIA 8 are added to a hard-scattering simulated event to account for pileup from multiple pp interactions in the same or nearby bunch crossings. Then, the number of average interactions per bunch crossing is reweighted to match the distributions in data. In addition, all the MC samples are reweighted to account for small differences in the efficiencies of physics-object reconstruction and identification with respect to those measured in data.

The detail of the nominal MC sample is described in the following sections, while the setups to estimate and model the impact of theoretical uncertainties are discussed in Chapter 8.

Process	ME generator	ME PDF	decay, PS, and Hadronization	UE tune	Cross-section order
$t\bar{t}$	POWHEG-BOX v2	CT10	PYTHIA 6	P2012	NNLO+NNLL [43–48]
Single top	POWHEG-BOX v1/v2	CT10	PYTHIA 6	P2012	NNLO+NNLL [49–51]
W/Z+jets	SHERPA 2.2	NNPDF3.0 NNLO	SHERPA	SHERPA	NNLO [52]
Diboson	SHERPA 2.1.1	CT10	SHERPA	SHERPA	NLO
$t\bar{t} + W/Z$	MG5_AMC@NLO 2.2.2	NNPDF2.3	PYTHIA 8	A14	NLO [53]
$t\bar{t} + \gamma$	MG5_AMC@NLO 2.2.3	CTEQ6L1	PYTHIA 8	A14	NLO [53]
Signal	MG5_AMC@NLO 2.2.2	NNPDF2.3	PYTHIA 8	A14	NLO+NLL [54]

Table 3.2: Summary of setups of the nominal MC samples. All the MC samples are normalized to the highest-order (in α_S) cross section available as indicated in the last column.

3.2.1 Signal

The signal samples are based on a simplified model [55, 56], assuming that the branching ratio of $\tilde{t}_1 \to t\tilde{\chi}_1^0$ is 100%. The $\tilde{\chi}_1^0$ is taken to be a pure bino as a benchmark model. The signal samples are generated at LO with MG5_AMC@NLO 2.2.2 [53] as a matrix element (ME) generator of $pp \to \tilde{t}_1\tilde{t}_1$ process, accompanied by NNPDF2.3 [57] PDF (Parton Distribution Function) set along with the A14 [58] set of underlying-event tuned parameters (UE tune). For decay, parton shower (PS), and hadronization, PYTHIA 8 [59] generator is used. Since the kinematics of signal events highly depend on the masses of $\tilde{t}_1$ and $\tilde{\chi}_1^0$, the signal samples are generated in a grid across the plane of $\tilde{t}_1$ and $\tilde{\chi}_1^0$ masses (from $(m_{\tilde{t}_1}, m_{\tilde{\chi}_1^0}) = (200,12)$ GeV to $(1000,600)$ GeV) with a spacing of 50 GeV for most of the plane. The grid spacing around the '*Diagonal*' region where $m_{\tilde{t}_1}$ approaches $m_t + m_{\tilde{\chi}_1^0}$ is finer. All the mass points produced are shown in Figure 1.8. The produced samples are normalized to the cross sections at NLO also including resummation of soft gluon emission up to next-to-leading logarithmic (NLL), which are shown in Figure 3.1.
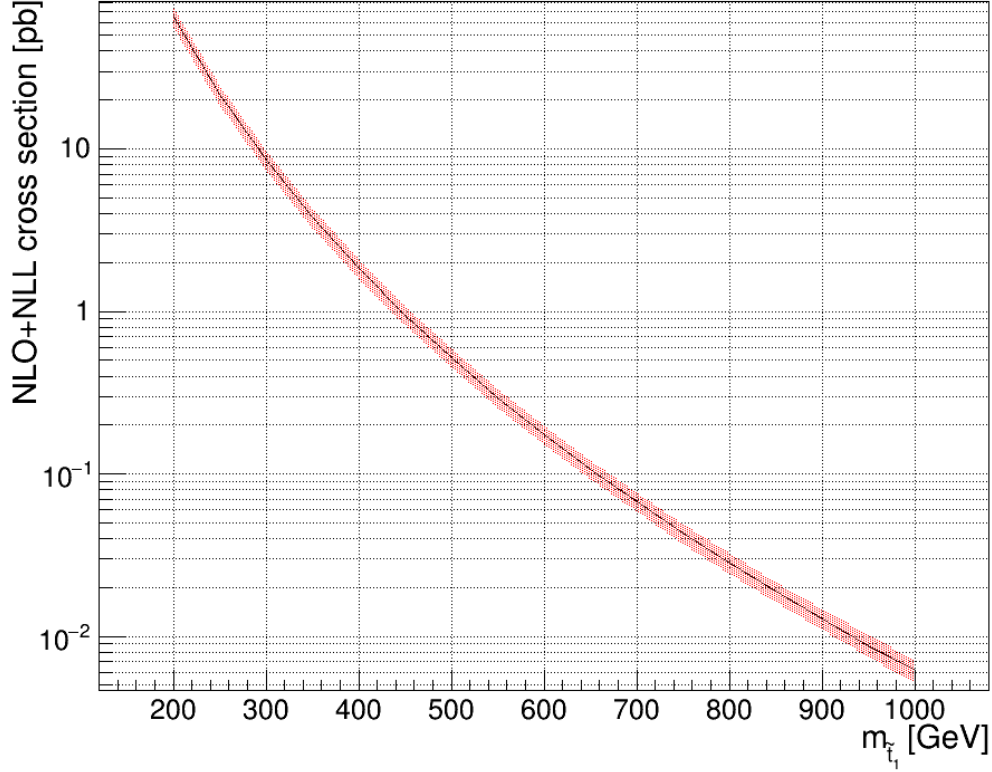
Figure 3.1: NLO and NLL cross section of the signal event as a function of $m_{\tilde{t}_1}$ [54], to which all signal samples are normalized. The cross section just only depends on $m_{\tilde{t}_1}$ and not depend on either $m_{\tilde{\chi}_1^0}$ or decay mode ($\tilde{t}_1 \to t\tilde{\chi}_1^0$ or $\tilde{t}_1 \to bW\tilde{\chi}_1^0$). The band indicates theoretical uncertainty taken from an envelopment of systematic error on PDF sets and factorization and renormalization scales, as described in [60].

3.2.2 $t\bar{t}$

$t\bar{t}$ samples are generated at NLO with POWHEG-BOX v2 [61–65] as ME generator, accompanied by CT10 [66] NLO PDF set along with the P2012 [67] set of UE-tuned parameters. For PS and hadronization, PYTHIA 6 [68] generator is used. The cross section is normalized to the cross section at NNLO and NNLL, 831.78 pb [43–48]. More details can be seen in [69].

3.2.3 Single Top

Figure 3.2 shows 3 types of single top events, s-channel, t-channel, and Wt associated production. Single top samples are produced with the same generator combination as $t\bar{t}$ sample, except that ME generator for electroweak t-channel single top events is POWHEG-BOX v1 generator instead of POWHEG-BOX v2 generator. The cross section is normalized to the cross section at NNLO and NNLL, 145.45 pb (s-channel: 3.35 pb, t-channel: 70.43 pb, Wt associated production: 71.67 pb) [49–51]. More details can be seen in [69]. The dominant remaining process after event selections is Wt channel because its event topology is similar to the signal.

34
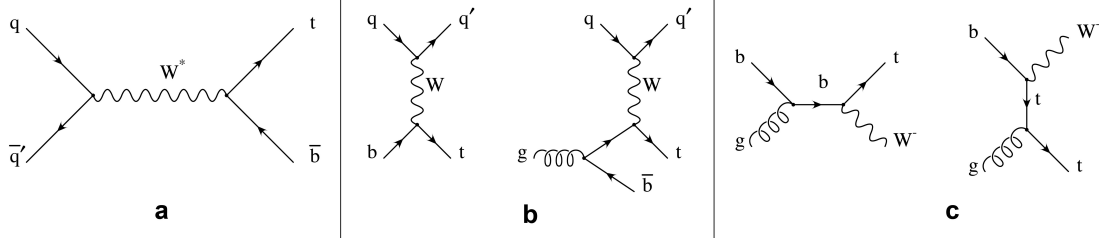
Figure 3.2: Feynman diagrams of s-channel (a), t-channel (b), and Wt associated production (c) of single top events.

3.2.4 W/Z+jets

W/Z+jets samples are generated at NLO by SHERPA 2.2 [70] ME generator along with Comix [71] and OpenLoops [72] ME generators. For W/Z+jets samples, a simplified scale setting prescription in the multi-parton matrix elements is used to improve the event generation speed. A theory-based re-weighting of the jet multiplicity distribution is applied event by event that is derived from event generation with a strict scale prescription [73]. The PDF set is NNPDF 3.0 NNLO [74] along with the default UE tune provided by the authors of SHERPA. SHERPA is also used as decay, PS, and hadronization generator [75]. The cross sections are normalized to the cross sections at NNLO, 60180.48 pb and 17662.80 pb for W+jets and Z+jets, respectively [52]. More details can be seen in [76]. Since Z+jets process provides two leptons, it can be highly reduced by requiring exact one lepton. Therefore, mainly W+jets remains after event selections.

3.2.5 $t\bar{t} + W/Z$

Figure 3.3(a)-3.3(d) shows $t\bar{t} + W/Z$ events. $t\bar{t} + W/Z$ samples are generated with at LO for *Resolved* and *Boosted* and at NLO for *Diagonal*. with MG5_AMC@NLO 2.2.2 [53] as ME generator, accompanied by NNPDF2.3 [57] PDF set along with the A14 [58] set of UE tune. For decay, PS, and hadronization, PYTHIA 8 [59] generator is used. For LO samples, the cross sections is normalized to the cross sections at NLO, 0.61 pb and 0.87 pb for $t\bar{t}$ +W and $t\bar{t}$ +Z, respectively [53]. More details can be seen in [77]. The dominant remaining process after event selections is $t\bar{t} + Z(\to \nu\bar{\nu})$ channel (its NLO cross section produced by its branching ratio is 0.17 pb) because its event topology is similar to the signal.

3.2.6 $t\bar{t} + \gamma$

$t\bar{t} + \gamma$ samples are generated at LO with the same configuration as $t\bar{t} + W/Z$ samples except that MG5_AMC@NLO 2.2.3 and CTEQ6L1 [78] LO PDF set are used. The cross section is normalized to the cross sections at NLO, 4.38 pb [53]. More details can be seen in [69]. $t\bar{t} + \gamma$ events are used to estimate $t\bar{t} + Z(\to \nu\nu)$ background by regarding γ as the $Z \to \nu\bar{\nu}$ branch shown in Figure 3.3(b)-3.3(d)[2]. The detail and the systematic uncertainty of the estimation are described in Section 6.2 and Section 8.6.

---

[2] For *Diagonal*, $t\bar{t} + \gamma$ is not used and $t\bar{t} + Z(\to \nu\bar{\nu})$ is predicted by MC only.

(a) $t\bar{t} + W$

(b) $t\bar{t} + Z(\to \nu\bar{\nu})$ (1/3)

(c) $t\bar{t} + Z(\to \nu\bar{\nu})$ (2/3)

(d) $t\bar{t} + Z(\to \nu\bar{\nu})$ (3/3)
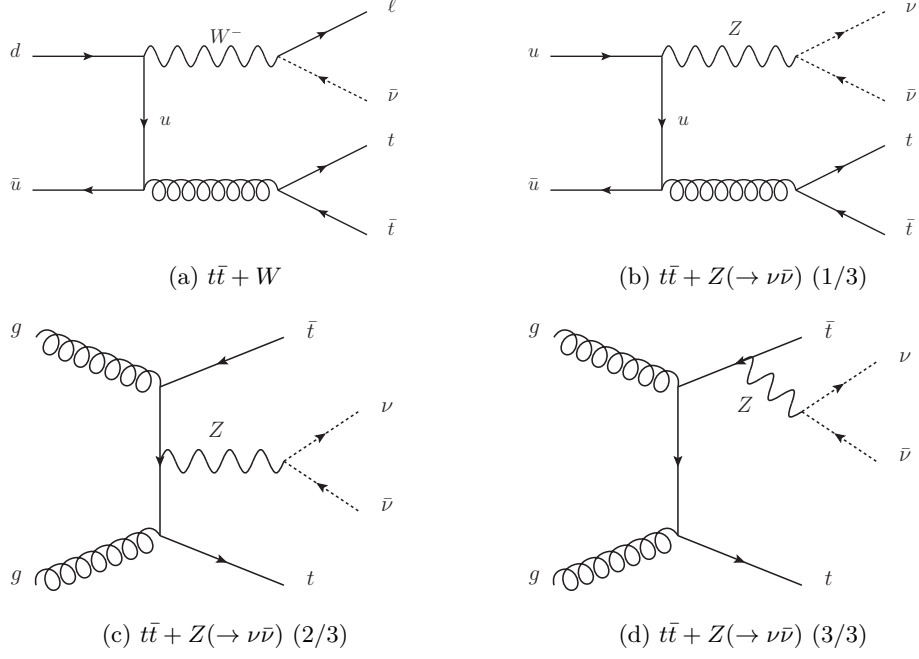
Figure 3.3: Feynman diagrams of $t\bar{t} + W(\to \ell\nu)$ (a), $t\bar{t} + Z(\to \nu\bar{\nu})$ (b)-(d).

3.2.7 Diboson

Diboson samples (WW, WZ, ZZ) are generated at NLO by SHERPA 2.1.1 [70] ME generator along with Comix [71] and OpenLoops [72] ME generators. The off-shell bosons are also considered in the generation. The PDF set is CT10 [66] NLO PDF set along with the UE tune provided by authors of SHERPA. SHERPA is also used as PS and hadronization generator [75]. The cross section at NLO provided by the generator, 136.78 pb, is used. More details can be seen in [79].

Chapter 4

Physics Object Definition

This chapter introduces definition of physics objects, which is commonly used in *Boosted*, *Resolved*, and *Diagonal* analyses. In this thesis, 'physics object' means a reconstructed particle (or a reconstructed 4-momentum) with a label like electron, muon, photon, jet, b-jet, τ-jet, etc. Since the reconstruction and the labeling are based on measurements with a limited detector acceptance in a high-density environment, for example, an electron in a signal event is sometimes not reconstructed due to outside acceptance or a b from W decay is sometimes labeled as not b-jet but jet due to a limitation of b-tagging algorithm. These effects are not negligible and therefore considered in the definitions of physics objects and event selections.

In the analysis, electrons and muons from W-boson decay must be reconstructed and labeled correctly, but electrons and muons from the other sources not. For example, leptons from c/b-jet are not important. To distinguish them, generally the former is called isolated lepton and the latter is called non-isolated lepton. To pick up only isolated ones, electron and muon definitions in the analysis include 'isolation' requirement [80] as described in Section 4.2 and 4.3.

In the labeling of physics objects, there are two levels called *baseline* and *signal*. The *signal-level* physics objects are defined by the tighter requirements than *baseline-level* physics objects, thus the efficiency of baseline-level labeling is higher than signal-level labeling, but the fake rate of signal-level labeling is lower than baseline-level labeling. Therefore, baseline objects are used to compute the missing transverse momentum and to apply a second-lepton veto to suppress events with $t\bar{t}$ dileptonic event. Because of the reliability of signal-level labeling, signal objects are mostly used in the event selection.

Since there is no priority among all the labeling (identification) algorithms by default, sometimes physics objects could have more than one label. To avoid physics objects to have more than one label, an overlap removal procedure described in Section 4.7 is applied just after all the reconstruction and the labeling. All baseline and signal objects are also required to survive the overlap removal procedure.

Section 4.1 introduces the definition of a primary vertex, which is used for definitions of the other physics objects. Section 4.2-4.6 introduce the definitions of electron, muon, photon, jet, and missing transverse momentum. Section 4.7 describes the overlap removal procedure. Section 4.8 explains the definition of a large-R jet.

4.1   Primary Vertex

The primary vertex is defined by a reconstructed vertex with the highest $\sum_{i \in T} p_{\mathrm{T}i}^2$, where T is a set of all tracks used to reconstruct the vertex. Furthermore, the primary vertex is required to have at least two tracks with $p_{\mathrm{T}} > 400$ MeV. In order to confirm that there is at least one hard pp collision in an event, all events are required to have at least one primary vertex. The primary vertex is also used as a reference point of impact parameters of electron and muon candidates.

4.2   Electron

Electron candidates are reconstructed from electromagnetic calorimeter cell clusters that are matched to tracks reconstructed in the ID system. Baseline electrons are required to have $p_{\mathrm{T}} > 7$ GeV, $|\eta| < 2.47$, and satisfy 'VeryLoose' likelihood identification criteria described in [81].

Signal electrons in *Resolved* and *Boosted* are required to pass all baseline requirements and have $p_{\mathrm{T}} > 25$ GeV, satisfy 'Loose' likelihood identification criteria [81], and have impact parameters with respect to the reconstructed primary vertex along the beam axis (z_0) and in the transverse plane (d_0) that satisfy $|z_0 \sin\theta| < 0.5$ mm and $|d_0|/\sigma_{d_0} < 5$, where σ_{d_0} is the uncertainty of d_0. Furthermore, the signal electrons in *Resolved* and *Boosted* must pass 'Loose-TrackOnly' isolation criteria. The LooseTrackOnly isolation criteria use track-based information to obtain a 99% efficiency that is independent of p_{T}. These values are estimated from $Z \to \ell\ell$ MC samples and confirmed in data [80].

Signal electrons in *Diagonal* are required to pass all baseline requirements and also have $p_{\mathrm{T}} > 27$ GeV, satisfy 'Tight' likelihood identification criteria [81], and have the same impact parameter requirements as the signal electrons in *Resolved* and *Boosted*. Furthermore, the signal electrons in *Diagonal* must pass 'GradientLoose' isolation criteria. The GradientLoose isolation criteria use both caloriemter-cell and track-based information to obtain a 95(99)% efficiency at $p_{\mathrm{T}} = 25(60)$ GeV. These values are estimated from $Z \to \ell\ell$ MC samples and confirmed in data [80].

The reason why the signal electrons in *Diagonal* are more tightly defined than *Resolved* and *Boosted* is that single electron triggers are used in *Diagonal* strategy and not used in *Resolved* or *Boosted*. Therefore, a little bit tighter definition is required to use the triggers introduced in Section 3.1.

4.3   Muon

Typically, a muon is reconstructed from a track reconstructed by combining two tracks in the ID and the MS. In order to improve the muon reconstruction efficiency, a track in the ID matched to a track segment in the MS, a track in the MS not matched to any tracks in the ID, or a track in the ID matched to an energy deposit in the calorimeter compatible with a minimum-ionizing particle (referred to as calo-tagged muon) [82] is also used to reconstruct a muon. Baseline muons are required to have $p_{\mathrm{T}} > 6$ GeV, $|\eta| < 2.6$, and satisfy 'Loose' identification criteria described in [82].

Signal muons must pass all baseline requirements and also have $p_{\mathrm{T}} > 25$ GeV, and have

impact parameters $|z_0 \sin\theta| < 0.5$ mm and $|d_0|/\sigma_{d_0} < 3$. Furthermore, the signal muons must pass 'LooseTrackOnly' isolation criteria like the signal electrons.

4.4 Photon

Photon identification is not used in the main event selection, and therefore photons are labeled as extra jet or electron candidates. Photons are identified only when the $t\bar{t} + \gamma$ sample is used for the data-driven estimation of the $t\bar{t} + Z$ background in *Resolved* and *Boosted*[1]. In this case, photons are reconstructed from calorimeter cell clusters and must have $p_{\mathrm{T}} > 145$ GeV and $|\eta| < 2.37$, excluding the barrel-endcap calorimeter transition in the range $1.37 < |\eta| < 1.52$. Photons are also required to satisfy 'Tight' identification criteria described in [83] and 'Tight' isolation criteria based on both track and calorimeter information. For recording $t\bar{t} + \gamma$ events, a single photon trigger is used that records events with a photon passing Loose identification criteria with $p_{\mathrm{T}} > 140$ GeV. The photon definition is tighter than the trigger requirements, hence all events with at least one photon defined here are $\sim100\%$ recorded by the trigger.

4.5 Jet

Jets are reconstructed from topological clusters [84, 85] in the calorimeters using the anti-k_t algorithm with angular distance parameter of $R = 0.4$ [28]. Jets are corrected for contamination from pileup events using the jet area method [86–88], and then jet energy calibration to account for the detector response [89, 90] is performed. Furthermore, jets in data are calibrated based on *in situ* measurements of the jet energy scale. Baseline jets are required to have $p_{\mathrm{T}} > 20$ GeV and $|\eta| < 4.9$ to precisely reconstruct missing transverse momentum described in Section 4.6. Signal jets must have $p_{\mathrm{T}} > 25$ GeV and $|\eta| < 2.5$. For signal jets with $p_{\mathrm{T}} < 60$ GeV, 'Jet Vertex Tagger (JVT)' criteria is applied to them, which is designed to reject jets stemmed from pileup events using vertex information [88]. Events containing a jet that does not pass specific jet quality criteria are rejected in the analysis to suppress detector noise and non-collision backgrounds [91, 92].

Jets resulting from b-quarks (called b-jets) are identified using the MV2c10 b-tagging algorithm, which exploits one of machine learning techniques, boosted decision tree (BDT) [93], and uses quantities such as impact parameters and distances between primary and secondary vertices [94–96]. This algorithm outputs a b-jet likelihood score (or b-tagging weight), and then jets exceeding a threshold of the weight are b-tagged. In the analysis, the threshold is relatively loose in order to increase b-tagging efficiency, resulting in 77% b-tagging efficiency and fake rates of $\sim1/134$ for light-quark flavors and gluons and $\sim1/6$ for c-jets in simulated $t\bar{t}$ events.

In the event selections of *Resolved* and *Boosted*, some variables such as m_{top}^{χ}, am_{T2}, and *topness* require at least 2 b-jets by definition. Even if there is only one b-tag jet in an event, anti-b-tag jet with the second highest b-tagging weight is temporarily regarded as the second b-tag jet in the calculation.

Hadronically decaying τ leptons are identified by using a BDT [93] technique which uses quantities such as number of tracks in a jet and shape of the jet. The analysis uses the 'Loose'

---

[1] The photon candidates are not used in *Diagonal* and $t\bar{t} + Z$ background is estimated with MC only in *Diagonal*

criteria described in [97, 98] which provides 60% and 50% efficiencies for identifying τ leptons decaying into one and three charged pions, respectively. For τ candidates, a dedicated energy calibration [98] is applied. The τ candidates must have $p_\mathrm{T} > 20$ GeV, $|\eta| < 2.5$, and one or three tracks with total electric charge opposite to that of the signal lepton.

In this thesis, if 'jet' is mentioned without any specification such as '(anti-) b-tag', the two types of jets are implicitly included in the context. For example, the word 'number of signal jets' means number of signal anti-b-tag jets and signal b-tag jets. In this thesis, τ candidates are categorized as τ, not jet. However, the analysis doesn't remove overlap between τ candidate and the parent jet, and therefore τ object and the parent jet object are used independently in the analysis. As described in Section 5.1, the analysis rejects events with at least one tau candidate that fail in m_T2^τ criteria. In some of the events passing the criteria, the tau candidates are regarded as not τ. Since the tau candidate should be regarded as jet in the case, the overlap between τ candidate and jet is not removed although this is confusing.

4.6 Missing Transverse Momentum

The missing transverse momentum, $\vec{p}_\mathrm{T}^{\,\mathrm{miss}}$ (or $E_\mathrm{T}^\mathrm{miss} \equiv |\vec{p}_\mathrm{T}^{\,\mathrm{miss}}|$), is defined by the negative vector sum of the transverse momenta of baseline leptons, baseline jets, and a *soft-term* which is built from high-quality tracks associated with the primary vertex but not with the baseline objects [99, 100]. The norm of missing transverse momentum is called missing transverse energy denoted by $E_\mathrm{T}^\mathrm{miss}$. Basically, photons and hadronically decaying τ leptons contribute to $\vec{p}_\mathrm{T}^{\,\mathrm{miss}}$ as jets or electrons or via the soft-term. In the event selections requiring photons, transverse momenta of the photons[2] are also added to $\vec{p}_\mathrm{T}^{\,\mathrm{miss}}$.

4.7 Overlap Removal

To avoid physics objects to have more than one label, an overlap removal procedure is applied after all the reconstruction and the labeling. The procedure is optimized to this analysis by simulation. Table 4.1 summarizes the procedure. Given a set of objects passing at least baseline definition[3], the procedure checks for overlap based on either a shared track, ghost-matching [87], or a minimal distance ΔR between objects. For example, if ΔR between a baseline electron and a baseline jet is less than 0.2, then the electron is retained (as indicated in the 'Precedence' row) and the jet is discarded, unless the jet is b-tagged (as indicated in the 'Condition' row) in which case the electron is expected to originate from a heavy-flavor decay and then discarded while the b-tagged jet is retained. If the matching requirement in Table 4.1 is not satisfied, the both objects are kept. The procedure shown in the columns in Table 4.1 is executed from left to right. The second (ej) and the third (μj) steps of the procedure ensure that ΔR between leptons and jets is at least 0.2. Therefore, the fourth step (ℓj) is considered only for $\Delta R > 0.2$. The steps involving a photon are applied only for the event selection requiring photons. All baseline objects are required to survive the overlap removal procedure, and all signal objects are the survivors that also pass signal definition.

---

[2] There is no baseline/signal labeling for photon as described in Section 4.4.

[3] Therefore, some of them may pass signal requirements, but the overlap removal procedure does not check whether objects pass signal definition or not.

Object 1	e	e	μ	ℓ	γ	γ	τ
Object 2	μ	j	j	j	j	e	e
Matching criteria	shared track	$\Delta R < 0.2$	ghost-matched and $\Delta R < 0.2$	$\Delta R < \min\left(0.4, 0.04 + \frac{10}{p_T^\ell/\mathrm{GeV}}\right)$	$\Delta R < 0.2$	$\Delta R < 0.1$	$\Delta R < 0.1$
Condition	calo-tagged μ	j not b-tagged	(j not b-tagged) and $\left(n_{\mathrm{track}}^j < 3 \text{ or } \frac{p_T^\mu}{p_T^j} > 0.7\right)$	−	−	−	−
Precedence	e	e	μ	j	γ	e	e

Table 4.1: A summary of overlap removal procedure. The procedure is executed from left to right. The first two rows (Object 1, Object 2) indicate the types of overlapping objects: electrons (e), muons (μ), electron or muon (ℓ), jets (j), photons (γ), and hadronically decaying τ lepton (τ). The procedure is applied only to baseline objects except for γ and τ where there is no distinction between baseline and signal definition. The third row (Matching criteria) defines the criteria to consider that an object pair is overlapping. If there is the overlap, the object shown in the last row (Precedence) is retained and the other is discarded. If a condition is described in the fourth row (Condition) and if the condition is not satisfied, then the precedence is inversed.

4.8 Large-Radius Jet

Large-radius jets are used only in *Boosted* that are clustered from all signal jets using the anti-k_t algorithm with $R = 1.2$. To reduce the impact of soft radiation and pileup events, the large-radius jets are groomed using reclustered jet trimming, where the constituent signal jets with p_T less than 5% of the ungroomed jet p_T are removed [101–104]. Leptons are not included in the reclustering procedure, because it was found that including them increases the background acceptance more than the signal efficiency. Since the signal jets pass the overlap removal procedure by definition, the large-radius jets are not used in the overlap removal procedure. The *Boosted* analysis uses a large-radius jet mass reconstructed from four-vectors of the constituent signal jets.

Chapter 5

Event Selection

This chapter introduces definition of event selection that specifies a phase space where the signal events are enhanced and the SM backgrounds are suppressed so that the signal contribution can be seen explicitly in the number of the observed event if stop truly exists. The specified phase space is named 'signal region' (SR), and the number of observed events in SR is used to precisely determine (or measure) the parameter of interest $\mu_{\rm sig}$ (Chapter 7). Event selection is a series of requirements using dedicated variables discriminating signal and backgrounds, which are also explained. Section 5.1 introduces an event preselection commonly used in *Resolved*, *Boosted*, and *Diagonal*. Section 5.2 and 5.3 describe the event selections of SR for *Resolved* and *Boosted*. Since *Diagonal* strategy exploits a shape fit for background estimation described in Chapter 6, there are multiple SRs for *Diagonal* topology. For this reason, Section 5.4 describes a base event selection for the shape fit in *Diagonal*.

5.1 Event Preselection

The topology of the signal events as explained in Section 1.6 is as follows.

- one lepton

- 4 jets including 2 b-jets

- missing energy (due to neutrinos and $\tilde{\chi}_1^0$'s)

To ensure a basic topology of the signal event, all the SRs for *Resolved*, *Boosted*, and *Diagonal* commonly require events to have one signal lepton, no additional baseline lepton, at least four signal jets, where at least one of them should be b-tag jet. After this selection, events with hadronically decaying tau lepton (τ_h), especially $t\bar{t} \to [b\ell\nu][b\tau_h\nu]$ events[1], still remain and thus they are suppressed by using $m_{\rm T2}^\tau$ variable, which is introduced in Section 5.1.1.

5.1.1 Stransverse Mass

m_{T2}^τ is a type of 'stransverse mass', $m_{\rm T2}$ [105], which targets a topology where there are two branches of particle decay chains labeled here as a and b in an event. Figure 5.1(a) illustrates

---

[1] Only hadronically decaying tau lepton is considered because it is very challenging to suppress events with leptonically decaying tau lepton (τ_ℓ) because of its short lifetime in the ATLAS experiment.

the $t\bar{t}$ event topologies targeted by m^{τ}_{T2}. In each branch, there are visible (measured) and invisible (unmeasured) particles. The vector sum of the measured momenta in branch $i \in \{a, b\}$ is denoted by $p_i = (E_i, \vec{p}_{\mathrm{T}i}, p_{zi})$ and the vector sum of the unmeasured momenta is denoted by $q_i = (F_i, \vec{q}_{\mathrm{T}i}, q_{zi})$. With $m^2_{p_i} = E^2_i - \vec{p}^{\,2}_i$ and $m^2_{q_i} = F^2_i - \vec{q}^{\,2}_i$, the m_{T} of the particles in branch i is given by

$$m^2_{\mathrm{T}i} = \left(\sqrt{p^2_{\mathrm{T}i} + m^2_{p_i}} + \sqrt{q^2_{\mathrm{T}i} + m^2_{q_i}} \right)^2 - \left(\vec{p}_{\mathrm{T}i} + \vec{q}_{\mathrm{T}i} \right)^2. \tag{5.1}$$

The stransverse mass, m_{T2}, is defined as a minimum quantity of the maximum of m_{Ta} and m_{Tb} over the allocation of $\vec{p}^{\,\mathrm{miss}}_{\mathrm{T}}$ between $\vec{q}_{\mathrm{T}a}$ and $\vec{q}_{\mathrm{T}b}$;

$$m_{\mathrm{T2}} \equiv \min_{\vec{q}_{\mathrm{T}a} + \vec{q}_{\mathrm{T}b} = \vec{p}^{\,\mathrm{miss}}_{\mathrm{T}}} \{ \max(m_{\mathrm{T}a}, m_{\mathrm{T}b}) \} \tag{5.2}$$

where an assumption of m_{q_a} and m_{q_b} is required in the computation of m_{Ta} and m_{Tb}. The result of the minimization is the minimum parent mass which doesn't kinematically contradict the observed event topology.

For m^{τ}_{T2}, the configuration is as follows;

Branch Start Points:

- Branch a: W-boson decaying as $W \to \tau_h \nu$.
- Branch b: W-boson decaying as $W \to \ell \nu$.

Measured particles:

- Branch a: the τ candidate defined in Section 4.5.
- Branch b: the signal lepton.

Unmeasured particles:

- Branch a: the two neutrinos from $W \to \tau_h \nu$ and from $\tau_h \to \nu + \mathrm{jet}$.
- Branch b: the neutrino.

Input masses:

- Branch a: $m_{q_a} = 0$ GeV.
- Branch b: $m_{q_b} = m_{\nu} = 0$ GeV.

For $t\bar{t} \to [b\ell\nu][b\tau_h\nu]$ events, the endpoint of m^{τ}_{T2} is the W boson mass, whereas the signal events can exceed this bound.

Events with τ_h are vetoed exploiting the m^{τ}_{T2} variable in the following way;

1. Not veto events which do not have a reconstructed τ that passes the 'Loose' identification criteria with $p_{\mathrm{T}} > 20$ GeV, 1 or 3 tracks, $\Delta R > 0.1$ from the signal lepton and charge opposite to the signal lepton.

2. Otherwise, veto events if the leading[2] τ candidate results in $m^{\tau}_{T2} < 80$ GeV.

---

[2] 'Leading' means that the physics object has the highest p_{T} among physics objects with the same label in the event.
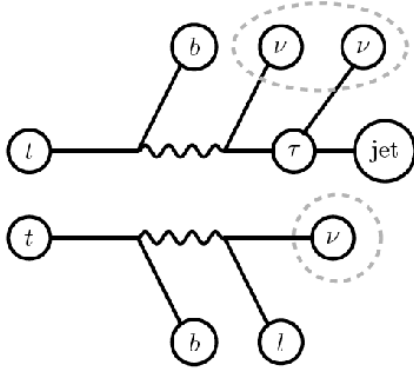
(a) $t\bar{t} \to [b\ell\nu][b\tau_h\nu]$ event targeted by m_{T2}^{τ} (b) $t\bar{t} \to [b\ell\nu][b\ell_{\mathrm{lost}}\nu]$ event targeted by am_{T2}
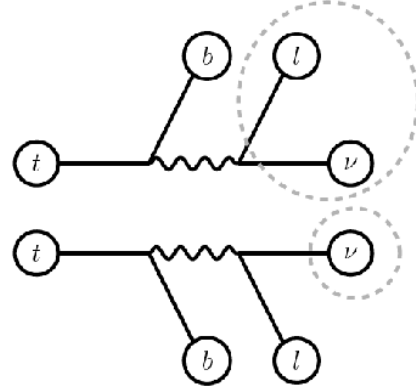
Figure 5.1: Illustration of of m_{T2}^{τ} (left) and am_{T2} (right) variables, which are used to discriminate against $t\bar{t} \to [b\ell\nu][b\tau_h\nu]$ event (left) and $t\bar{t} \to [b\ell\nu][b\ell_{\mathrm{lost}}\nu]$ where ℓ_{lost} is an undetected (lost) lepton or τ_h due to outside acceptance. The objects surrounded by the dashed lines are assumed to be undetected (lost) in the calculation of the two variables.

Figure 5.2 shows the m_{T2}^{τ} distribution. In this thesis, $t\bar{t}$ events are categorized into the following final states;

1. $t\bar{t} \to [b\ell\nu][b\ell\nu]$ (2L),

2. $t\bar{t} \to [b\ell\nu][bqq]$ (1L),

3. $t\bar{t} \to [b\ell\nu][b\tau_h\nu]$ or $[b\tau_\ell\nu][b\tau_h\nu]$ (1L1τ_h),

4. $t\bar{t} \to$ others (Other).

τ_h and τ_ℓ denote hadronically and leptonically decaying taus, respectively. From the top to the bottom, they are labeled as 2L, 1L, 1L1τ_h, and Other. As shown in Figure 5.2, most $t\bar{t}$ (1L1τ_h) events cannot exceed W-boson mass. Most of the surviving $t\bar{t}$ (1L1τ_h) events have no τ_h candidate because the τ_h's are undetected (lost) due to outside acceptance, which are suppressed by dedicated variables in *Resolved* and *Boosted* (Section 5.2 and 5.3) or precisely estimated by a shape fit in *Diagonal* (Section 5.4).
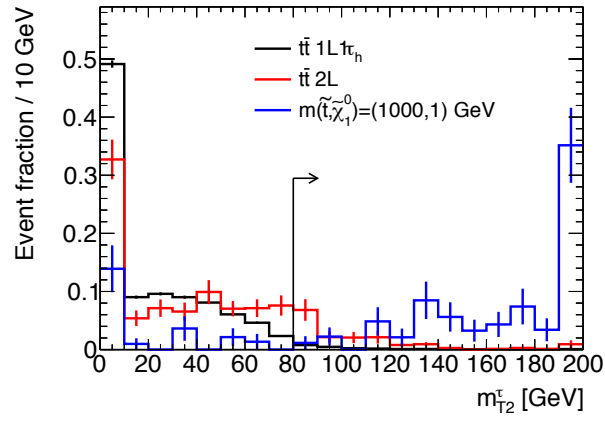
Figure 5.2: m_{T2}^{τ} distribution after the event preselection without $m_{\mathrm{T2}}^{\tau} > 80$ GeV requirement (Section 3.1). Each event is normalized to one and required to have a τ candidate that passes the 'Loose' identification criteria with $p_{\mathrm{T}} > 20$ GeV, 1 or 3 tracks, $\Delta R > 0.1$ from the signal lepton and charge opposite to the signal lepton. Events passing the m_{T2}^{τ} requirement are indicated by the arrow.

5.2 *Resolved* Signal Region

As described in Section 3.1, the E_T^{miss} trigger is used. Since the momenta of jets in the signal events are harder than the backgrounds, the leading to fourth leading jets ordered by p_T are required to have p_T of at least 80, 50, 40, 40 GeV, respectively. As shown in Figure 5.3 shows E_T^{miss} distribution, the signal events make larger E_T^{miss} than the backgrounds, and thus E_T^{miss} is required to be larger than 260 GeV. To enhance the signal events, $H_{T,sig}^{miss}$, which is a signal-object-based missing transverse momentum divided by the per-event resolution, is defined by

$$H_{T,sig}^{miss} = \frac{|\vec{H}_T^{miss}| - M}{\sigma_{|\vec{H}_T^{miss}|}}, \tag{5.3}$$

where $\vec{H}_T^{miss}$ is the sum of the signal jets and signal lepton transverse momenta. The $\sigma_{|\vec{H}_T^{miss}|}$ is computed in a sampling method using jet energy resolution [106], while the lepton is assumed to be well-measured. The parameter M is a characteristic 'scale' of the background, which is fixed at 100 GeV determined by optimization studies [107, 108]. As shown in Figure 5.4, the signal events can provide higher $H_{T,sig}^{miss}$ than the backgrounds, and thus $H_{T,sig}^{miss}$ is required at least 14.
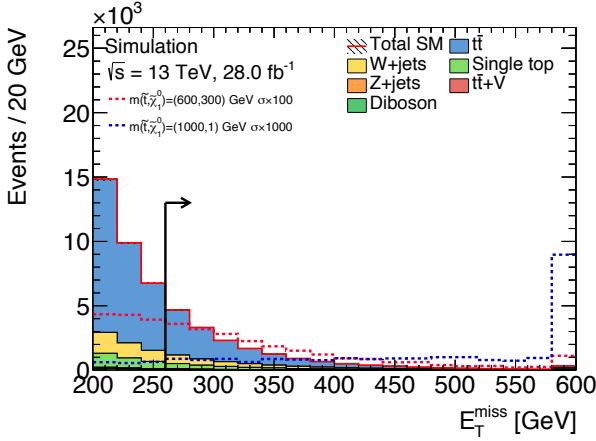
Figure 5.3: E_T^{miss} distribution after the event preselection described in Section 5.1 plus $E_T^{miss} > 200$ GeV precut and the E_T^{miss} trigger requirement. Events passing the $E_T^{miss} > 260$ GeV requirement are indicated by the arrow. For comparison, the cross sections of signal events with $(m_{\tilde{t}_1}, m_{\tilde{\chi}_1^0}) = (600, 300)$ GeV (red dashed-line) and (1000, 1) GeV (blue dashed-line) are scaled up by a factor of 100 and 1000, respectively.
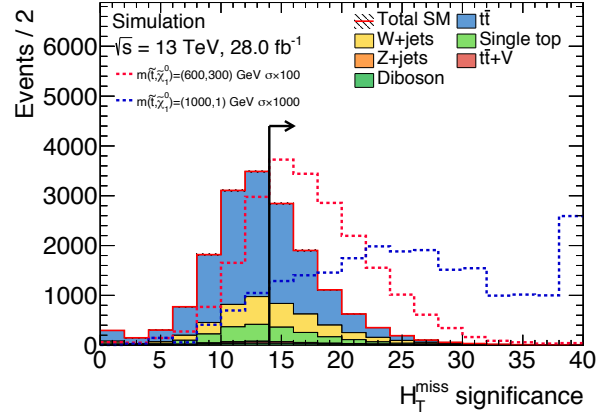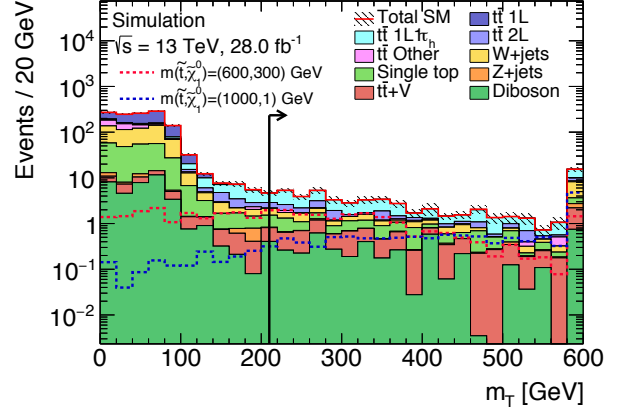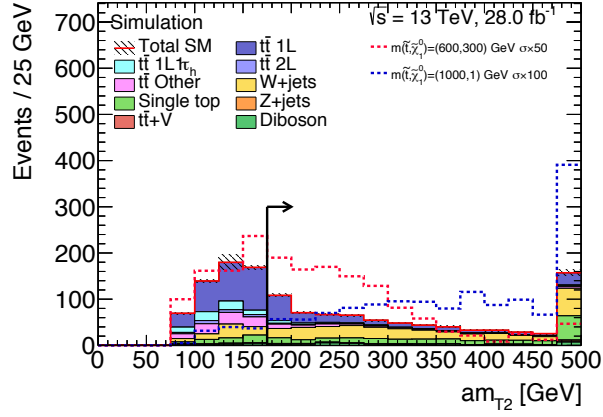
Figure 5.4: $H_{T,sig}^{miss}$ distribution after the event preselection described in Section 5.1 plus $E_T^{miss} > 260$ GeV and the E_T^{miss} trigger requirement. Events passing the $H_{T,sig}^{miss} > 14$ requirement are indicated by the arrow. For comparison, the cross sections of signal events with $(m_{\tilde{t}_1}, m_{\tilde{\chi}_1^0}) = (600, 300)$ GeV (red dashed-line) and (1000, 1) GeV (blue dashed-line) are scaled up by a factor of 100 and 1000, respectively.

To suppress events providing large E_T^{miss} due to mis-measurement of jet energy, $|\Delta\phi(\text{jet}_i, \vec{p}_T^{miss})|$ for $i \in \{1, 2\}$ are required larger than 0.4. As shown in Figure 5.5, $\Delta R(b, \ell)$, where b is the leading b-jet in the event, discriminates W+jets events from the signal events. To suppress W+jets events, $\Delta R(b, \ell)$ are required smaller than 3.0.

To suppress $t\bar{t}$ (1L) and W+jets events, a 'transverse mass' denoted by m_T is used. m_T is a reconstructed mass using the signal lepton transverse momenta $\vec{p}_T^\ell$ and $\vec{p}_T^{miss}$, defined by

$$m_T = \sqrt{2 \cdot p_T^\ell \cdot E_T^{miss} \left(1 - \cos\Delta\phi(\vec{p}_T^\ell, \vec{p}_T^{miss})\right)}. \tag{5.4}$$

As shown in Figure 5.6, for $t\bar{t}$ (1L) and W+jets events, m_T tends to be below the W boson mass. For events with more than one invisible particle like the signal event, m_T can go above the W boson mass. Therefore, m_T is required larger than 170 GeV.
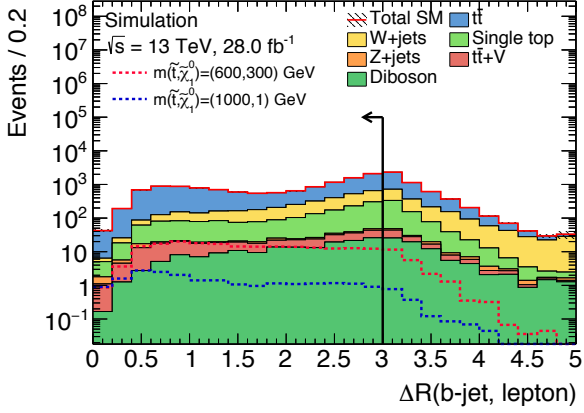
Figure 5.5: $\Delta R(b,\ell)$ distribution after the event preselection described in Section 5.1 plus the $E_\mathrm{T}^\mathrm{miss} >$ 260 GeV and the $E_\mathrm{T}^\mathrm{miss}$ trigger requirements. Events passing the $\Delta R(b,\ell) < 3.0$ requirement are indicated by the arrow.
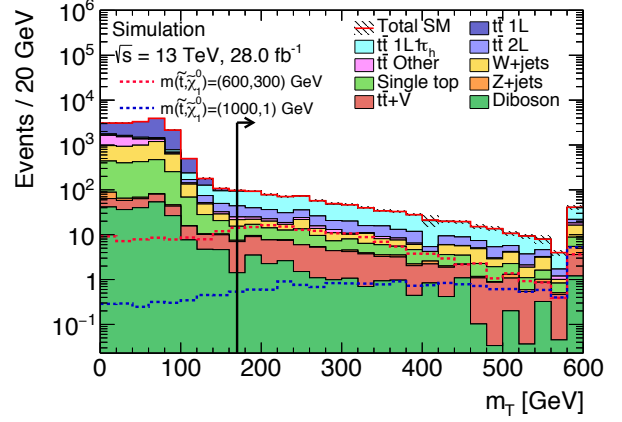
Figure 5.6: m_T distribution after the event preselection described in Section 5.1 plus the $E_\mathrm{T}^\mathrm{miss} >$ 260 GeV and the $E_\mathrm{T}^\mathrm{miss}$ trigger requirements. Events passing the $m_\mathrm{T} > 170$ GeV requirement are indicated by the arrow.

In order to ensure a hadronically decaying top in each event and to suppress events without hadronically decaying top, 3 jets are selected by the following χ^2 minimization;

$$\chi^2 = \frac{\left(m_{j_1,j_2,b_i} - m_\mathrm{top}\right)^2}{\sigma^2_{m_{j_1,j_2,b_i}}} + \frac{\left(m_{j_1,j_2} - m_W\right)^2}{\sigma^2_{m_{j_1,j_2}}}, \quad \text{where } i = 1 \text{ or } 2. \tag{5.5}$$

b_1 and b_2 are the two jets which have the highest b-tagging weights, j_1 and j_2 are jets with the highest p_T in the event excluding b_1 and b_2, and

$$\sigma^2_{m_{j_1,j_2,b_i}} = m^2_{j_1,j_2,b_i}(r^2_{j_1} + r^2_{j_2} + r^2_{b_i})$$
$$\sigma^2_{m_{j_1,j_2}} = m^2_{j_1,j_2}(r^2_{j_1} + r^2_{j_2}).$$

r_i is the fractional p_T resolution for jet i determined by dedicated studies [106]. Especially, the mass of this χ^2-base hadronic top, m_{j_1,j_2,b_i}, is denoted by m^χ_top in this thesis. m^χ_top is required smaller than 270 GeV. Figure 5.7 shows m^χ_top distribution.

In order to suppress $t\bar{t}$ (2L) and (1L1τ_h) events where one lepton or one τ_h from one W decay is undetected (lost) due to outside acceptance, am_T2, another type of stransverse mass shown in Figure 5.1(b), is exploited. am_T2 is an asymmetric form of m_T2 [109–111] where one of the two W bosons is considered invisible because its lepton or τ_h is assumed lost due to outside acceptance (denoted by ℓ_lost). Then the parameters for am_T2 are determined as follows;

Branch Start Points:

- Branch a: top quark decaying as $t \to bW \to b\ell_\mathrm{lost}\nu$
- Branch b: top quark decaying as $t \to bW \to b\ell\nu$

Measured particles

- Branch a: the b-jet.

- Branch b: the b-jet and the signal lepton.

The two b-jets are identified based on the highest b-tagging weights. Since there are two combination in the b-jet assignment to branches a and b, m_{T2} is calculated for each and the minimum one is used as the final discriminant.

Unmeasured particles

- Branch a: the W boson decaying as $W \to \ell_{\text{lost}}\nu$.

- Branch b: the neutrino.

Input masses

- Branch a: $m_{q_a} = m_W = 80$ GeV.

- Branch b: $m_{q_b} = m_\nu = 0$ GeV.

For the $t\bar{t}$ (2L) and (1L1τ_h) events with one ℓ_{lost}, am_{T2} is mostly smaller than the top quark mass, while for the signal events, am_{T2} can exceed the top quark mass as shown in Figure 5.8. In case the ℓ_{lost} is an electron, its energy deposit is included in the E_T^{miss} calculation as a jet. Then am_{T2} in $t\bar{t}$ events can be larger than the top quark mass, but this variable is still useful to distinguish between signal and background. Therefore, am_{T2} is required larger than 175 GeV.
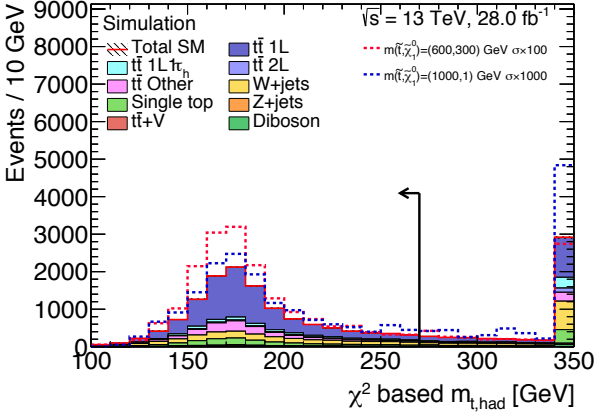
Figure 5.7: m_{top}^χ distribution after the event preselection described in Section 5.1 plus $E_T^{\text{miss}} > 260$ GeV and the E_T^{miss} trigger requirements. Events passing the $m_{\text{top}}^\chi < 270$ GeV requirement are indicated by the arrow. For comparison, the cross sections of signal events with $(m_{\tilde{t}_1}, m_{\tilde{\chi}_1^0}) = (600, 300)$ GeV (red dashed-line) and (1000, 1) GeV (blue dashed-line) are scaled up by a factor of 100 and 1000, respectively.
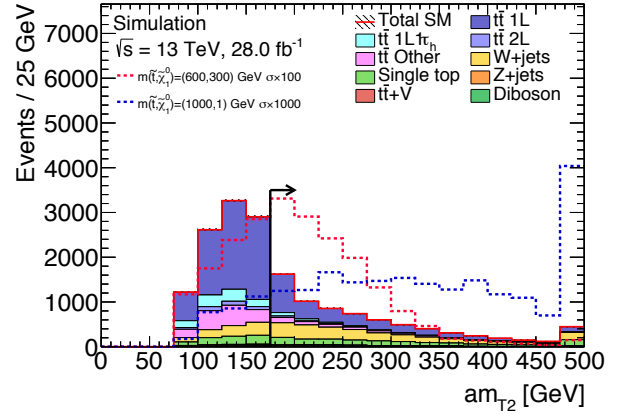
Figure 5.8: am_{T2} distribution after the event preselection described in Section 5.1 plus $E_T^{\text{miss}} > 260$ GeV and the E_T^{miss} trigger requirements. Events passing the $am_{T2} > 175$ GeV requirement are indicated by the arrow. For comparison, the cross sections of signal events with $(m_{\tilde{t}_1}, m_{\tilde{\chi}_1^0}) = (600, 300)$ GeV (red dashed-line) and (1000, 1) GeV (blue dashed-line) are scaled up by a factor of 100 and 1000, respectively.

For the further suppression of the $t\bar{t}$ (2L) and (1L1τ_h) events, *topness* is defined [112]. The *topness* is a χ^2 function which indicates the similarity of the event to $t\bar{t}$ (2L) and (1L1τ_h) events with one lepton (including τ_h) assumed lost like the am_{T2} variable. The *topness* is defined as

$\ln(\min S)$, where S is a χ^2 function defined as

$$
S(p_{W,x}, p_{W,y}, p_{W,z}, p_{\nu,z}) = \frac{\left(m_W^2 - (p_\ell + p_\nu)^2 \right)^2}{a_W^4} + \frac{\left(m_t^2 - (p_{b_1} + p_\ell + p_\nu)^2 \right)^2}{a_t^4}
$$
$$
+ \frac{\left(m_t^2 - (p_{b_2} + p_W)^2 \right)^2}{a_t^4} + \frac{\left(4\, m_t^2 - (\Sigma_i p_i)^2 \right)^2}{a_{\mathrm{CM}}^4}.
$$
(5.6)

$p_{W,x}$, $p_{W,y}$, and $p_{W,z}$ are the 3-momentum of the invisible W boson. $p_{\nu,z}$ is the longitudinal momentum of the neutrino from the other W boson decay where the lepton is not lost. $\Sigma_i p_i$ is the sum of 4-vectors of all the 5 assumed final state particles. a_W, a_t and a_{CM} are the constant values suggested by the authors [112]; $a_W = 5$ GeV, $a_t = 15$ GeV, $a_{\mathrm{CM}} = 1$ TeV. The four arguments of S are varied to find the minimum of S. The minimization is constrained such that the observed missing transverse momentum is assumed to stem from the unobserved W boson (decaying into a lost lepton and a neutrino) and a neutrino from the other top decay branch. To find all four arguments of S, the neutrinos and the invisible W boson are assumed to be on-shell. Two combination of b-jets are evaluated in this minimization. If there is only one b-tagged jet, the leading or subleading anti-b-tagged jet is temporarily regarded as the second b-jet (in this case, a total of four possible jet assignments is evaluated). Figure 5.9 shows *topness* distribution and indicates that the lower *topness* region is populated by the $t\bar{t}$ events and the signal events are enhanced at the higher *topness* region. Therefore, *topness* is required larger than 6.5. All the selection described is summarized in Table 6.1. After all the *Resolved* selections, numbers of the benchmark signal events with $(m_{\tilde{t}_1}, m_{\tilde{\chi}_1^0}) = (600, 300)$ GeV and the total SM-background events are 38 (efficiency $= 0.77\%$) and 46 events, respectively, for the data of 28.0 fb^{-1}. The dominant background in the SR is $t\bar{t}$ which occupies 37% of the total background events. For the detail of background yields, see Table 9.1.
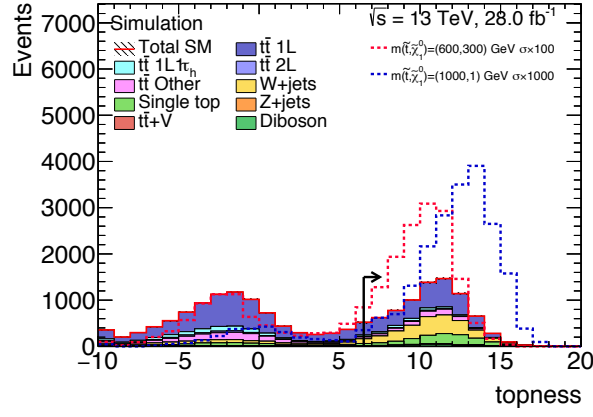
Figure 5.9: *topness* distribution after the event prese-
lection described in Section 5.1 plus $E_T^{miss} > 260$ GeV
and the E_T^{miss} trigger requirements. Events passing
the *topness* > 6.5 requirement are indicated by the
arrow. For comparison, the cross sections of sig-
nal events with $(m_{\tilde{t}_1}, m_{\tilde{\chi}_1^0}) = (600, 300)$ GeV (red
dashed-line) and (1000, 1) GeV (blue dashed-line) are
scaled up by a factor of 100 and 1000, respectively.

5.3 *Boosted* Signal Region

Compared to *Resolved* topology, *Boosted* topology provides larger E_T^{miss} as shown in Figure 5.10. Therefore, *Boosted* signal region requires the tighter cut, $E_T^{\mathrm{miss}} > 450$ GeV. As described in Section 3.1, the E_T^{miss} trigger is used. Since the momenta of jets in the signal events are larger than the backgrounds, the leading to fourth leading jets ordered by p_T are required to have p_T of at least 120, 80, 50, 25 GeV, respectively. To enhance the signal events, $H_{T,\mathrm{sig}}^{\mathrm{miss}}$ described in Section 5.2 is required at least 22. Figure 5.11 shows $H_{T,\mathrm{sig}}^{\mathrm{miss}}$ distribution.
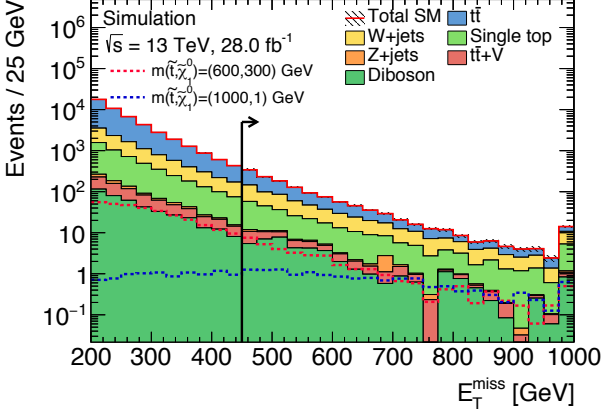
Figure 5.10: E_T^{miss} distribution after the event preselection described in Section 5.1 plus $E_T^{\mathrm{miss}} > 200$ GeV precut and the E_T^{miss} trigger requirement. Events passing the $E_T^{\mathrm{miss}} > 450$ GeV requirement are indicated by the arrow.
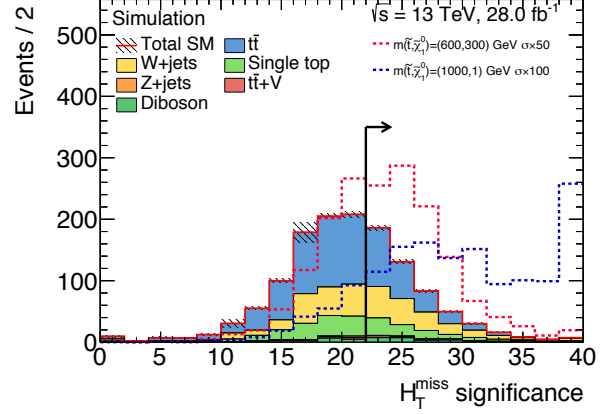
Figure 5.11: $H_{T,\mathrm{sig}}^{\mathrm{miss}}$ distribution after the event preselection described in Section 5.1 plus $E_T^{\mathrm{miss}} > 450$ GeV and the E_T^{miss} trigger requirements. Events passing the $H_{T,\mathrm{sig}}^{\mathrm{miss}} > 22$ requirement are indicated by the arrow. For comparison, the cross sections of signal events with $(m_{\tilde{t}_1}, m_{\tilde{\chi}_1^0}) = (600, 300)$ GeV (red dashed-line) and (1000, 1) GeV (blue dashed-line) are scaled up by a factor of 50 and 100, respectively.

For suppressing events with large E_T^{miss} due to mis-measurement of jet energy, $|\Delta\phi(\mathrm{jet}_i, \vec{p}_T^{\mathrm{miss}})|$ for $i \in \{1, 2\}$ are required larger than 0.4. Since the leptonically decaying top in *Boosted* topology is highly boosted, $\Delta R(b, \ell)$ of *Boosted* topology tends to be smaller than $t\bar{t}$, W+jets, and single top events as shown in Figure 5.12. To enhance the signal events, $\Delta R(b, \ell)$ are required smaller than 2.4. In order to suppress $t\bar{t}$ (1L) and W+jets events, m_T described in Section 5.2 is required larger than 210 GeV. Figure 5.13 shows m_T distribution.

In order to suppress $t\bar{t}$ (2L) and ($1L1\tau_h$) events with one ℓ_{lost}, am_{T2} described in Section 5.2 is required larger than 175 GeV. Figure 5.14 shows am_{T2} distribution.

To ensure the *Boosted*-specific event topology, at least one large-R jet with $p_T > 290$ GeV and mass > 70 GeV is required. The p_T of 290 GeV is nearly the threshold for a hadronically decaying top to form large-R jet with $R = 1.2$ as described in Section 1.6.1, and then the mass of 70 GeV is used because the selected large-R jet should come from a top or at least a W-boson from a top decay. Figure 5.15 and 5.16 show p_T and mass distributions of the leading large-R jet.

Furthermore, a perpendicular missing transverse energy, $E_{T,\perp}^{\mathrm{miss}}$, is used to suppress $t\bar{t}$ (1L) events surviving from all the criteria described up to here. A schematic view of $E_{T,\perp}^{\mathrm{miss}}$ is shown
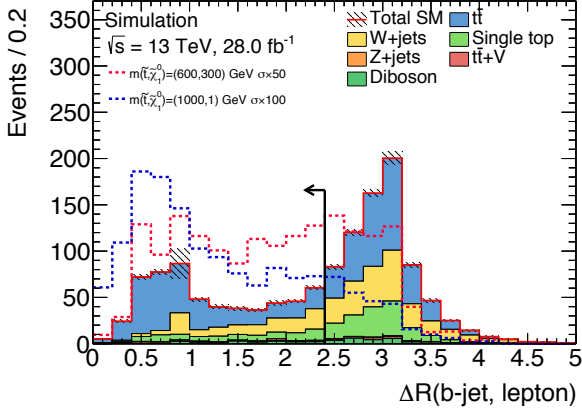
Figure 5.12: $\Delta R(b, \ell)$ distribution after the event preselection described in Section 5.1 plus $E_{\mathrm{T}}^{\mathrm{miss}} > 450$ GeV and the $E_{\mathrm{T}}^{\mathrm{miss}}$ trigger requirements. Events passing the $\Delta R(b, \ell)$ requirement are indicated by the arrow. For comparison, the cross sections of signal events with $(m_{\tilde{t}_1}, m_{\tilde{\chi}_1^0}) = (600, 300)$ GeV (red dashed-line) and $(1000, 1)$ GeV (blue dashed-line) are scaled up by a factor of 50 and 100, respectively.

Figure 5.13: m_{T} distribution after the event preselection described in Section 5.1 plus $E_{\mathrm{T}}^{\mathrm{miss}} > 450$ GeV and the $E_{\mathrm{T}}^{\mathrm{miss}}$ trigger requirements. Events passing the $m_{\mathrm{T}} > 210$ GeV requirement are indicated by the arrow. For comparison, the cross sections of signal events with $(m_{\tilde{t}_1}, m_{\tilde{\chi}_1^0}) = (600, 300)$ GeV (red dashed-line) and $(1000, 1)$ GeV (blue dashed-line) are scaled up by a factor of 50 and 100, respectively.

in Figure 5.17. In the $t\bar{t}$ background passing a series of the stringent cuts, the boost of the leptonic top tends to align the neutrino with the leptonic top direction. After reconstructing the hadronic top through the χ^2 minimization described in Section 5.2, the remaining b-jet and the signal lepton are used to reconstruct the leptonic top[3]. After boosting the leptonic top and $E_{\mathrm{T}}^{\mathrm{miss}}$ into the $t\bar{t}$ rest frame, the perpendicular component of the $E_{\mathrm{T}}^{\mathrm{miss}}$ with respect to the leptonic top is calculated. This $E_{\mathrm{T},\perp}^{\mathrm{miss}}$ is expected to be smaller for the $t\bar{t}$ background because the dominant contribution to $E_{\mathrm{T}}^{\mathrm{miss}}$ is the neutrino in this case. From optimization studies [27], $E_{\mathrm{T},\perp}^{\mathrm{miss}}$ is set to be larger than 180 GeV. Figure 5.18 shows $E_{\mathrm{T},\perp}^{\mathrm{miss}}$ distribution. All the selection described is summarized in Table 6.1. After all the *Boosted* selections, numbers of the benchmark signal events with $(m_{\tilde{t}_1}, m_{\tilde{\chi}_1^0}) = (1000, 1)$ GeV and the total SM-background events are 7 (efficiency = 4.1%) and 7 events, respectively, for the data of 28.0 fb^{-1}. The dominant background in the SR is $t\bar{t} + Z(\rightarrow \nu\nu)$ which occupies 36% of the total background events. For the detail of background yields, see Table 9.2.

---

[3] The contribution of neutrino from the leptonic top decay is ignored here. The reconstructed 4-momentum of leptonic top is just the sum of 4-momenta of the remaining b-jet and the signal lepton.

Figure 5.14: am_{T2} distribution after the event preselection described in Section 5.1 plus $E_T^{miss} > 450$ GeV and the E_T^{miss} trigger requirements. Events passing the $am_{T2} > 175$ GeV requirement are indicated by the arrow. For comparison, the cross sections of signal events with $(m_{\tilde{t}_1}, m_{\tilde{\chi}_1^0}) = (600, 300)$ GeV (red dashed-line) and (1000, 1) GeV (blue dashed-line) are scaled up by a factor of 50 and 100, respectively.
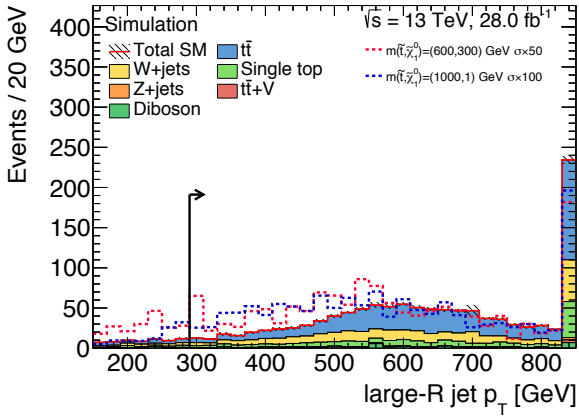
Figure 5.15: p_T distribution of the leading large-R jet after the event preselection described in Section 5.1 plus $E_T^{miss} > 450$ GeV and the E_T^{miss} trigger requirements. Events passing the $p_T > 290$ GeV requirement are indicated by the arrow. For comparison, the cross sections of signal events with $(m_{\tilde{t}_1}, m_{\tilde{\chi}_1^0}) = (600, 300)$ GeV (red dashed-line) and (1000, 1) GeV (blue dashed-line) are scaled up by a factor of 50 and 100, respectively.
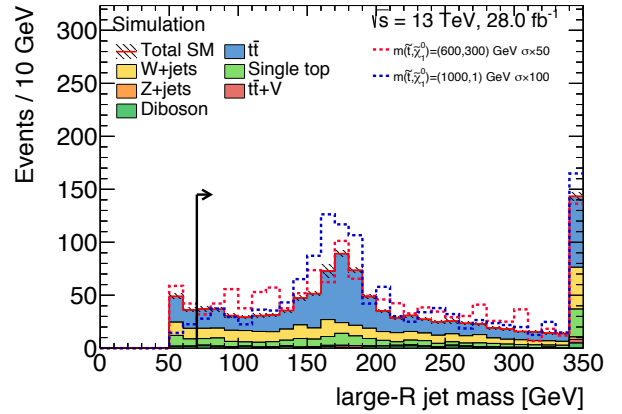
Figure 5.16: mass distribution of the leading large-R jet after the event preselection described in Section 5.1 plus $E_T^{miss} > 450$ GeV, the E_T^{miss} trigger, and the leading large-R jet $p_T > 290$ GeV requirements. Events passing the $m > 70$ GeV requirement are indicated by the arrow. For comparison, the cross sections of signal events with $(m_{\tilde{t}_1}, m_{\tilde{\chi}_1^0}) = (600, 300)$ GeV (red dashed-line) and (1000, 1) GeV (blue dashed-line) are scaled up by a factor of 50 and 100, respectively.

(a) SM $t\bar{t}$ decay
(b) $\tilde{t}\tilde{t}^*$ decay
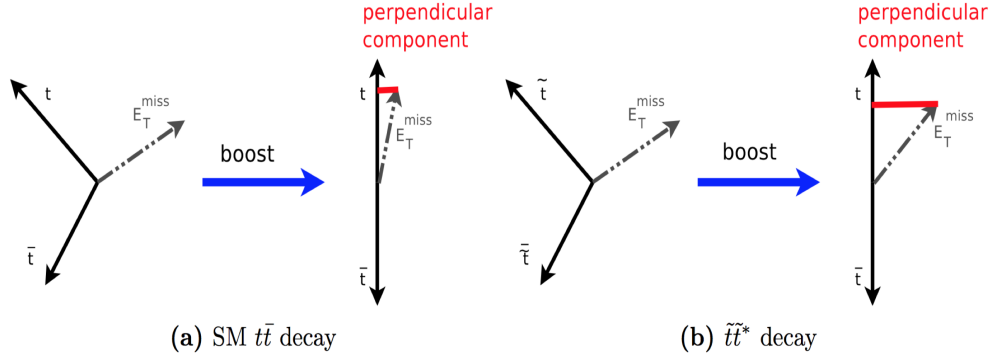
Figure 5.17: The schematic view of $E_{\mathrm{T},\perp}^{\mathrm{miss}}$ variable. (a) In the $t\bar{t}$ (1L) events, the neutrino ($E_{\mathrm{T}}^{\mathrm{miss}}$) is orientated in the same direction as the leptonically decaying top quark when it gets boosted. (b) In the stop events, the neutralinos also contribute to the $E_{\mathrm{T}}^{\mathrm{miss}}$ and they are not collinear to the leptonically decaying top quark, thus the perpendicular component tends to be larger than the ones in $t\bar{t}$ events.
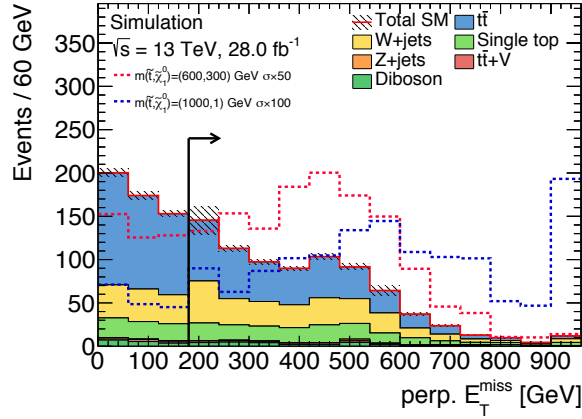
Figure 5.18: $E_{\mathrm{T},\perp}^{\mathrm{miss}}$ distribution after the event preselection described in Section 5.1 plus $E_{\mathrm{T}}^{\mathrm{miss}} > 450$ GeV and the $E_{\mathrm{T}}^{\mathrm{miss}}$ trigger requirements. Events passing the $E_{\mathrm{T},\perp}^{\mathrm{miss}} > 180$ GeV requirement are indicated by the arrow. For comparison, the cross sections of signal events with $(m_{\tilde{t}_1}, m_{\tilde{\chi}_1^0}) = (600, 300)$ GeV (red dashed-line) and $(1000, 1)$ GeV (blue dashed-line) are scaled up by a factor of 50 and 100, respectively.

54

5.4 *Diagonal* Base Event Selection

Variable	Selection
Trigger	$E_\mathrm{T}^\mathrm{miss}$ OR lepton trigger
Lepton	exactly one signal lepton (e, μ), no additional baseline leptons
Number of (jets, b-tags)	$(\geq 4, \geq 1)$
Hadronic τ veto	veto events with a hadronic τ decay and $m_\mathrm{T2}^\tau < 80$ GeV
1st to 4th Jet $p_\mathrm{T} >$ [GeV]	(60 60 40 25)
$E_\mathrm{T}^\mathrm{miss}$ [GeV]	$> 100^*$
m_T [GeV]	$> 60^*$
$E_\mathrm{T}^\mathrm{miss}/\sqrt{H_\mathrm{T}}$	> 5
$\lvert\Delta\phi(\mathrm{jet}_i, \vec{p}_\mathrm{T}^\mathrm{miss})\rvert$ for $i \in \{1, 2\}$	> 0.4

Table 5.1: Summary table of the base event selection for *Diagonal*. (*) indicates the lowest edge of the $(E_\mathrm{T}^\mathrm{miss}, m_\mathrm{T})$ shape fit (see Figure 6.24).

As described in Section 1.6.3, the dominant background is $t\bar{t}$ event and it is very challenging to suppress them by event selection, because the difference between *Diagonal* topology and $t\bar{t}$ event topology is smaller than *Resolved* and *Boosted*. Therefore, the base event selection is designed to just ensure a basic topology of the signal event. Table 5.1 summarizes the selection for *Diagonal*.

Since events with $E_\mathrm{T}^\mathrm{miss} < 200$ GeV are also utilized to improve background estimation in *Diagonal* described in Section 6.4, $E_\mathrm{T}^\mathrm{miss}$ trigger and lepton trigger are used as described in Section 3.1. Since the momenta of jets in the signal events are harder than the backgrounds, the leading to fourth leading jets ordered by p_T are required to have p_T of at least 60, 60, 40, 25 GeV, respectively. $E_\mathrm{T}^\mathrm{miss}$ and m_T is required at least 100 GeV and 60 GeV to ensure a basic signal topology, respectively. Figure 5.19 and 5.20 show $E_\mathrm{T}^\mathrm{miss}$ and m_T distributions. The bump at $E_\mathrm{T}^\mathrm{miss} = 200$ GeV in Figure 5.19 arises because $E_\mathrm{T}^\mathrm{miss}$ trigger is also used if offline $E_\mathrm{T}^\mathrm{miss} > 200$ GeV (see Section 3.1). As shown in Figure 5.20, the main background in high-m_T region is $t\bar{t}$ (1L1τ_h) event. As shown in Figure 5.21, the number of $t\bar{t}$ (1L1τ_h) events passing m_T2^τ requirement (Section 5.1) is around 10000, most of which comes from the first bin of the m_T2^τ distribution where there is no τ_h candidate to calculate m_T2^τ. The reason is that τ_h tends to be undetected due to outside acceptance. However, since most events failing in the m_T2^τ requirement are also $t\bar{t}$ (1L1τ_h) events, those events are used for the background estimation (explained in Section 6.4).

For suppressing events with large $E_\mathrm{T}^\mathrm{miss}$ due to mis-measurement of jet energy, $\lvert\Delta\phi(\mathrm{jet}_i, \vec{p}_\mathrm{T}^\mathrm{miss})\rvert$ for $i \in \{1, 2\}$ are required larger than 0.4. Because of the same reason, $E_\mathrm{T}^\mathrm{miss}$ significance denoted by $E_\mathrm{T}^\mathrm{miss}/\sqrt{H_\mathrm{T}}$ is used. The denominator is approximately the resolution of $E_\mathrm{T}^\mathrm{miss}$ and is expected to be smaller if the main contribution to $E_\mathrm{T}^\mathrm{miss}$ comes from $E_\mathrm{T}^\mathrm{miss}$ resolution. Therefore, $E_\mathrm{T}^\mathrm{miss}/\sqrt{H_\mathrm{T}}$ is required at least 5 and larger.
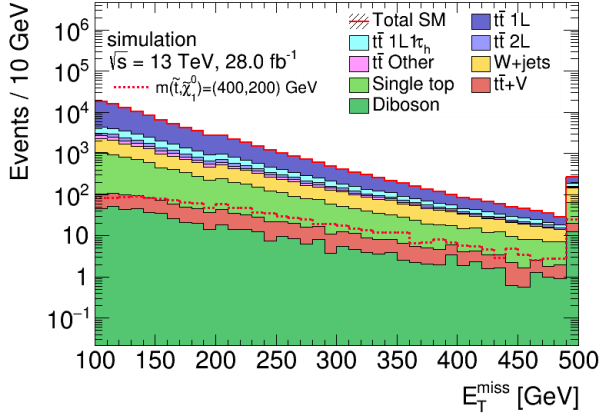
Figure 5.19: E_T^{miss} distribution after *Diagonal* base event selection.
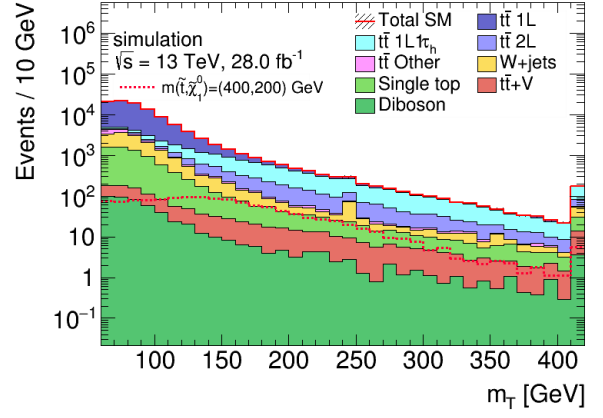
Figure 5.20: m_T distribution after *Diagonal* base event selection.
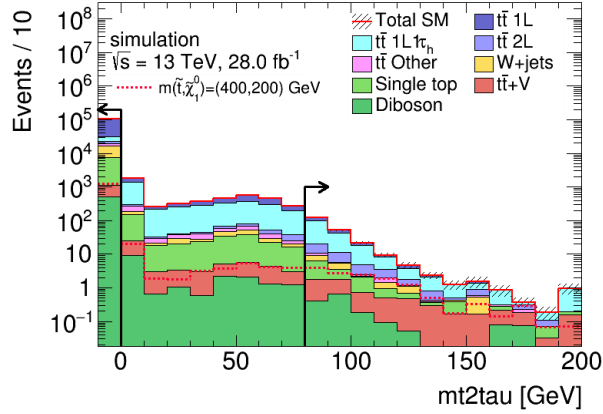
Figure 5.21: m_{T2}^{τ} distribution after *Diagonal* base event selection without $m_{T2}^{\tau} > 80$ GeV requirement. In events at the first bin, there are no τ candidate to calculate m_{T2}^{τ}. Events passing the m_{T2}^{τ} requirement are indicated by the arrows.

Chapter 6

Background Estimation

This chapter introduces background estimations in the SRs. Background estimation is mainly based on a simultaneous fit of numbers of events in SR and in the other phase spaces near SR. The phase space near SR is named 'control region' (CR). CRs are kinematically similar to the SRs, but a few key requirements are changed in order to significantly enhance the yield and purity of a specific background event and to reduce signal contamination. In case each background is significantly enhanced in each CR, the simultaneous fit can measure the normalization of background from data and the uncertainties on the normalization can become smaller than those evaluated by MC samples. As explained in Section 7.3, the fitted parameters are total normalization scale factors[1], μ_{sig} and $\boldsymbol{\mu_{\mathbf{bkg}}}$ for signal and backgrounds, respectively. Each μ-parameter scales up or down its total yield over SR and all CRs by its value, while all the yield ratios between SR and CRs are unchanged. For example, if μ_{ttbar} ($\in \boldsymbol{\mu_{\mathbf{bkg}}}$) is fitted to 1.1, each of $t\bar{t}$ yields in SR and all CRs is scaled up by 1.1 from the nominal yield expected by MC. Since each CR includes each background with higher purity and statistics than SR, $\boldsymbol{\mu_{\mathbf{bkg}}}$ are precisely determined from the statistical constrait of CRs in the simultaneous fit, and then the background contamination in SR can be estimated from the fitted $\boldsymbol{\mu_{\mathbf{bkg}}}$.

To check validity of the simultaneous fit before checking data at SRs, validation regions (VRs) are prepared, which are not overlapped with either CRs or SRs. Number of events in a VR, expected by $\boldsymbol{\mu_{\mathbf{bkg}}}$ fitted in a 'background-only fit', is compared to the observed one to confirm there is no significant problem in the procedure of background estimation. The background-only fit is a fit with a background-only model (μ_{sig} is fixed to 0) and using only CRs, not SRs. VRs never contribute to the background-only fit result (or never affect the likelihood used in the fit), hence VRs provide a statistically independent test of the background estimation with the CRs. In the background-only fit, number of the observed events at SRs had been blinded until it has been concluded by checking the VRs that the fit configuration and modeling are fine. The VRs are prepared for *Resolved* and *Boosted* in this analysis.

The background estimation for *Diagonal* analysis exploits a 2-dimensional ($E_{\mathrm{T}}^{\mathrm{miss}}$,$m_{\mathrm{T}}$) shape fit. Since suppression of $t\bar{t}$ events is very challenging as discussed in Section 5.4, the *Diagonal* analysis gains signal sensitivity with a very precise background estimation achieved by the 2-D shape fit. Since the ($E_{\mathrm{T}}^{\mathrm{miss}}$,$m_{\mathrm{T}}$) shapes of signal and backgrounds are quite different, the shape fit can be stable and background can be estimated with small uncertainties. In *Diagonal*, instead of

---

[1] Parameters of systematic uncertainties ($\boldsymbol{\alpha}$) are also fitted but not explained in this section. See Chapter 7.
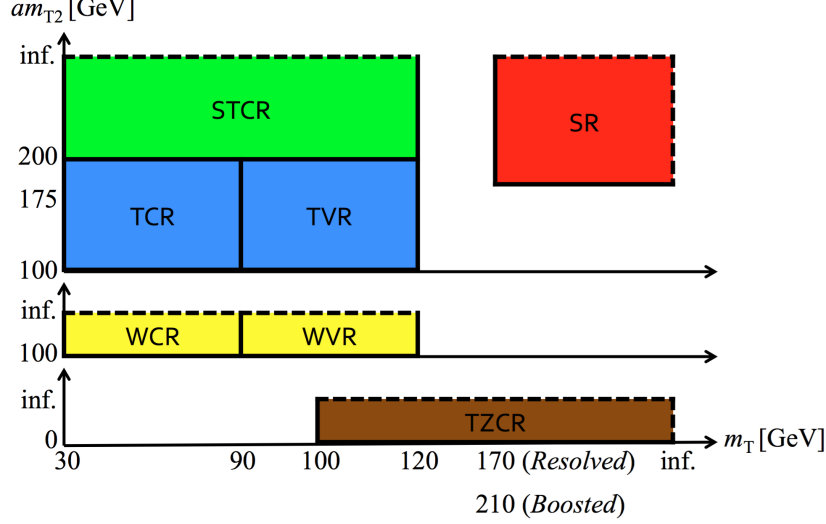
Figure 6.1: A schematic diagram of the signal regin (SR), control region (CR), and validation region (VR) used in *Resolved* and *Boosted*. Solid lines are boundaries of $m_{\rm T}$ and $am_{\rm T2}$ while dashed lines indicate that there is no upper boundary for the region. The initials of the regions, T, ST, W, and TZ, mean $t\bar{t}$, single top, W+jets, and $t\bar{t} + Z$, respectively. The low $m_{\rm T}$ edge of SR is 170 GeV and 210 GeV for *Resolved* and *Boosted*.

preparing VRs, a test fit is used to validate the 2-D shape fit, which is described in Appendix A.

Section 6.1 describes CRs used for *Resolved* and *Boosted* with showing data/MC distributions after the background-only fit. Section 6.2 is dedicated to the description of $t\bar{t} + Z(\rightarrow \nu\nu)$ CR (TZCR) for *Resolved* and *Boosted* and shows distributions after the background-only fit. Section 6.3 describes VRs used for *Resolved* and *Boosted* with showing distributions after the background-only fit. Section 6.4 is dedicated to *Diagonal* background estimation and describes the $(E_{\rm T}^{\rm miss}, m_{\rm T})$ shape fit with showing data/MC distributions without any fit.

6.1 *Resolved* and *Boosted* Control Regions

Figure 6.1 illustrates SR and CRs for *Resolved* and *Boosted*. CRs for $t\bar{t}$, W+jets, single top, and $t\bar{t} + V$ backgrounds are prepared for *Resolved* and *Boosted*, labeled as TCR, WCR, STCR, and TZCR, respectively. SRs, TCR, WCR and STCR are summarized in Table 6.1 while TZCR is explained in Section 6.2. The TCRs and WCRs are prepared by changing the $m_{\rm T}$ selection to be a window, upper edge of which is near the W boson mass. A requirement of $am_{\rm T2} = [100, 200]$ GeV is also applied to the TCRs to enhance $t\bar{t}$ events and to be separated from the STCRs. The STCRs requires $am_{\rm T2}$ larger than 200 GeV to strongly reduce $t\bar{t}$ events. Some other requirements are removed or loosened to enhance the background yields in the CRs. The WCRs are the same as the TCRs except that b-jet requirement changes into a b-jet veto and the $am_{\rm T2}$ requirement is loosened to increase the statistics of the WCR.

The STCRs also require at least two b-tagged jets to reduce the W+jets contamination. Furthermore, the STCRs require $\Delta R(b_1, b_2) > 1.2$ where b_1 and b_2 are the two highest-$p_{\rm T}$ b-tagged jets. This is because the $t\bar{t}$ events can exceed the $am_{\rm T2}$ kinematic bound when one of the two b-tagged jets used in the calculation of $am_{\rm T2}$ is a charm quark from the W decay misidentified

as a b-tagged jet, but $\Delta R(b_1, b_2)$ in those events tends to be smaller than Wt events.

Figure 6.4-6.11 show variables after the background-only fit in CRs compared to the observed data.

Common event selection	
Trigger	E_T^miss trigger
Lepton	exactly one signal lepton (e, μ), no additional baseline leptons
Jets	at least four signal jets, and $|\Delta\phi(\text{jet}_i, \vec{p}_\text{T}^\text{miss})| > 0.4$ for $i \in \{1, 2\}$
Hadronic τ veto	veto events with a hadronic τ decay and $m_\text{T2}^\tau < 80$ GeV

Resolved			
Variable	SR	TCR / WCR	STCR
1st to 4th Jet $p_\text{T} >$ [GeV]	(80 50 40 40)	(80 50 40 40)	(80 50 40 40)
E_T^miss [GeV]	> 260	> 200	> 200
$H_\text{T,sig}^\text{miss}$	> 14	> 5	> 5
m_T [GeV]	> 170	[30,90]	[30,120]
am_T2 [GeV]	> 175	$[100, 200]$ / > 100	> 200
topness	> 6.5	> 6.5	> 6.5
m_top^χ [GeV]	< 270	< 270	< 270
$\Delta R(b, \ell)$	< 3.0	–	–
$\Delta R(b_1, b_2)$	–	–	> 1.2
Number of b-tags	≥ 1	≥ 1 / $= 0$	≥ 2

Boosted			
Variable	SR	TCR / WCR	STCR
1st to 4th Jet $p_\text{T} >$ [GeV]	(120 80 50 25)	(120 80 50 25)	(120 80 50 25)
E_T^miss [GeV]	> 450	> 300	> 250
$E_\text{T,}^\text{miss}{}_\perp$ [GeV]	> 180	> 160	> 160
$H_\text{T,sig}^\text{miss}$	> 22	> 15	> 10
m_T [GeV]	> 210	[30,90]	[30,120]
am_T2 [GeV]	> 175	$[100, 200]$ / > 100	> 200
$\Delta R(b, \ell)$	< 2.4	–	–
$\Delta R(b_1, b_2)$	–	–	> 1.2
Number of b-tags	≥ 1	≥ 1 / $= 0$	≥ 2
Leading large-R jet p_T [GeV]	> 290	> 290	> 290
Leading large-R jet mass [GeV]	> 70	> 70	> 70

Table 6.1: Summary of the signal region (SR) and the $t\bar{t}$ (TCR), W+jets (WCR), and Wt (STCR) control regions each for *Resolved* and *Boosted*. TZCRs are described in Section 6.2 because TZCRs are very different from the other CRs,
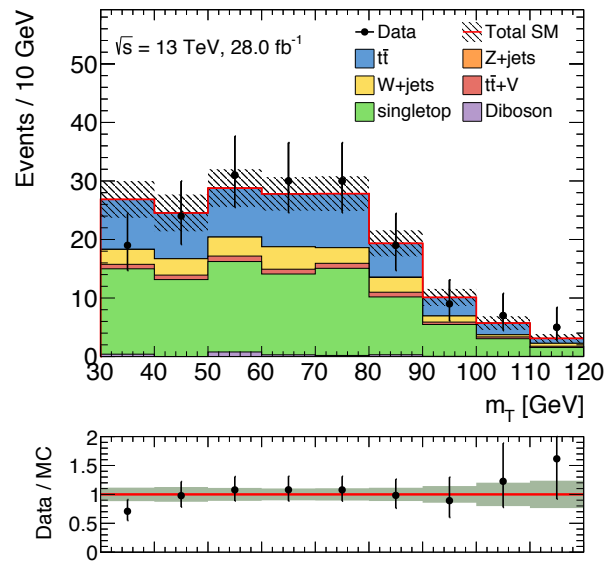
Figure 6.2: m_T distributions at TCR (top), WCR (middle), and STCR (bottom), respectively. The left and right columns correspond to *Resolved* and *Boosted*, respectively. The background-only fit results are applied to the distributions. The uncertainty band includes statistical and systematic error.
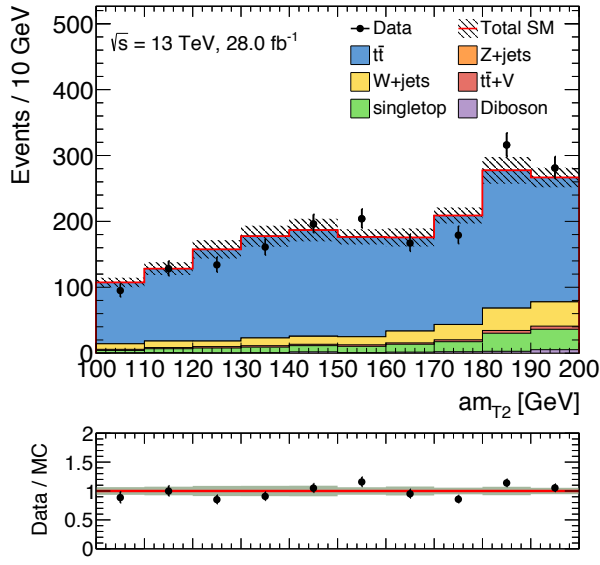
(a) am_{T2} at TCR of *Resolved*
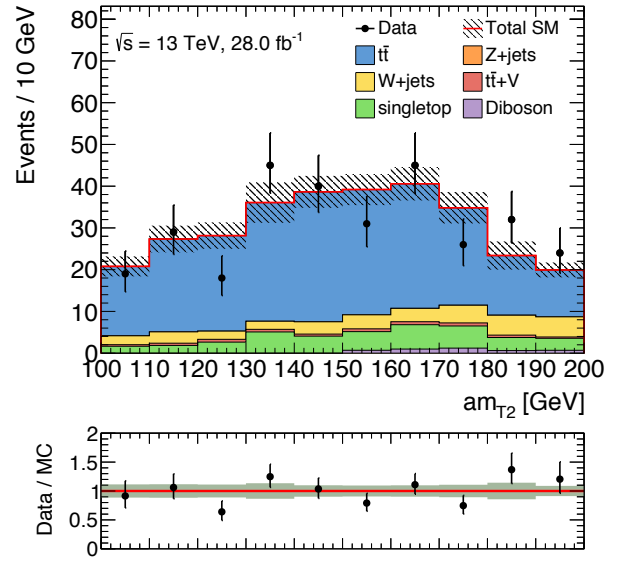
(b) am_{T2} at TCR of *Boosted*
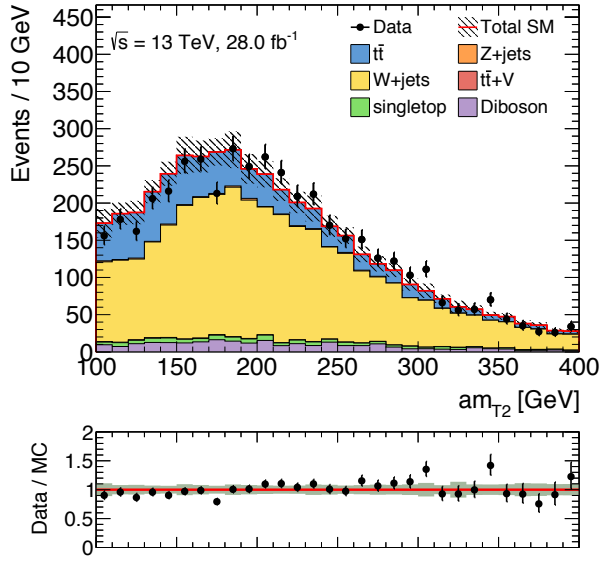
(c) am_{T2} at WCR of *Resolved*
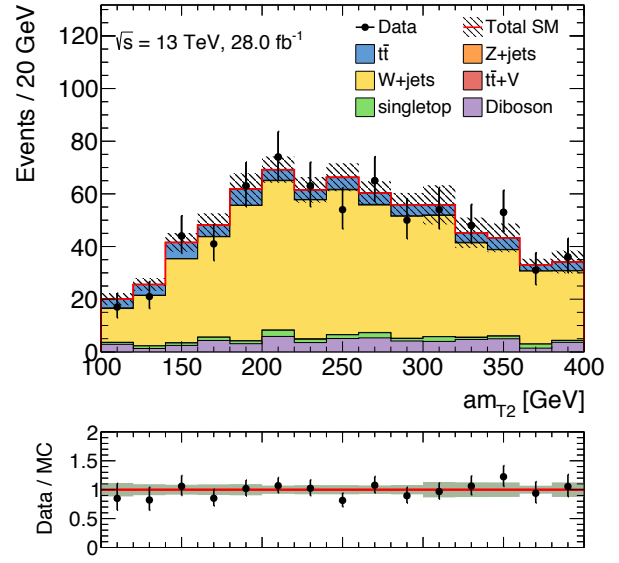
(d) am_{T2} at WCR of *Boosted*
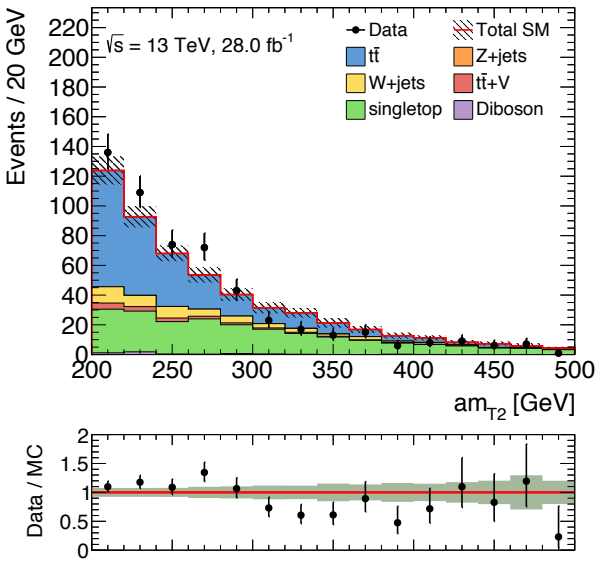
(e) am_{T2} at STCR of *Resolved*
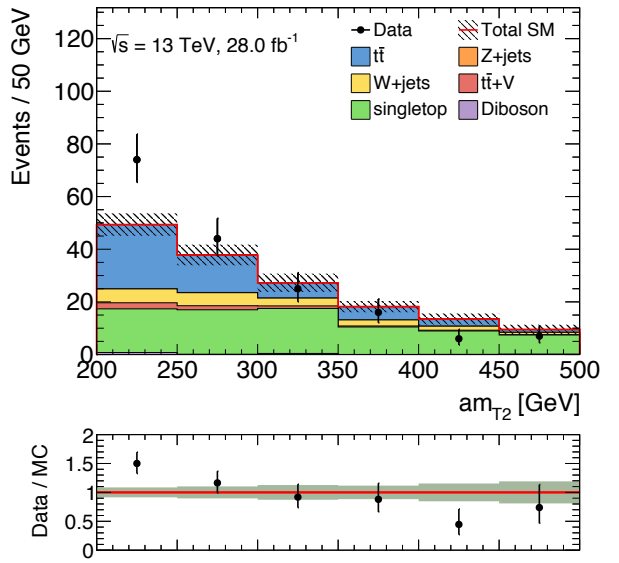
(f) am_{T2} at STCR of *Boosted*
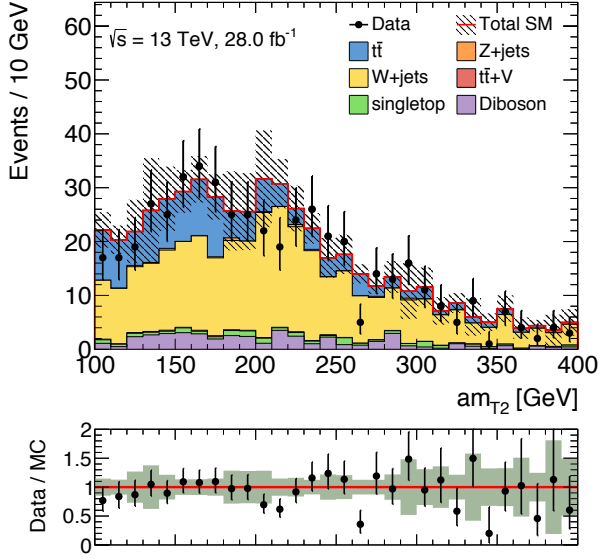
Figure 6.3: am_{T2} distributions at TCR (top), WCR (middle), and STCR (bottom), respectively. The left and right columns correspond to *Resolved* and *Boosted*, respectively. The background-only fit results are applied to the distributions. The uncertainty band includes statistical and systematic error.
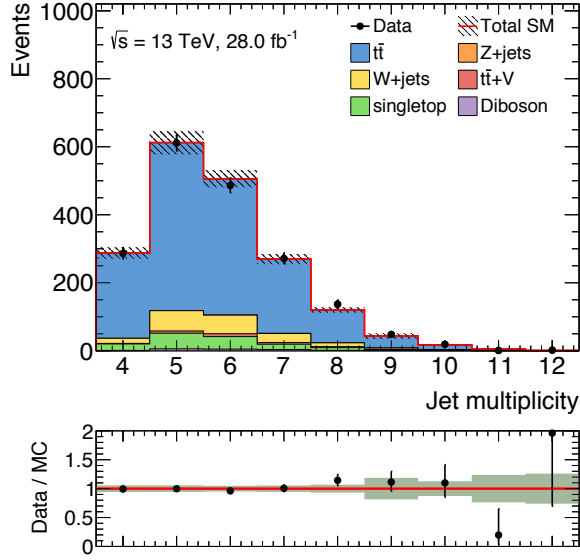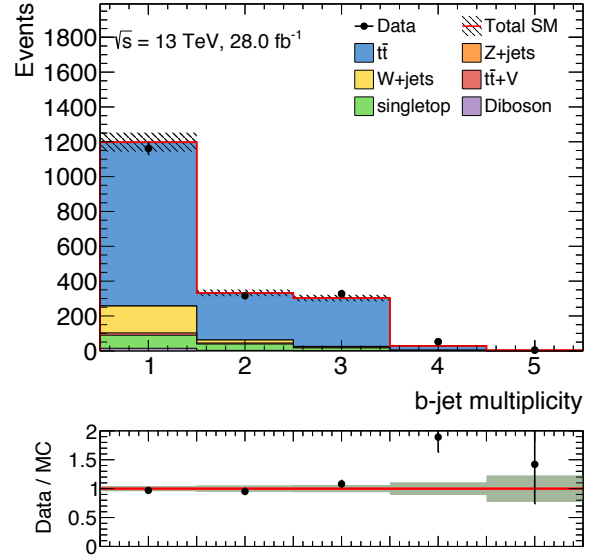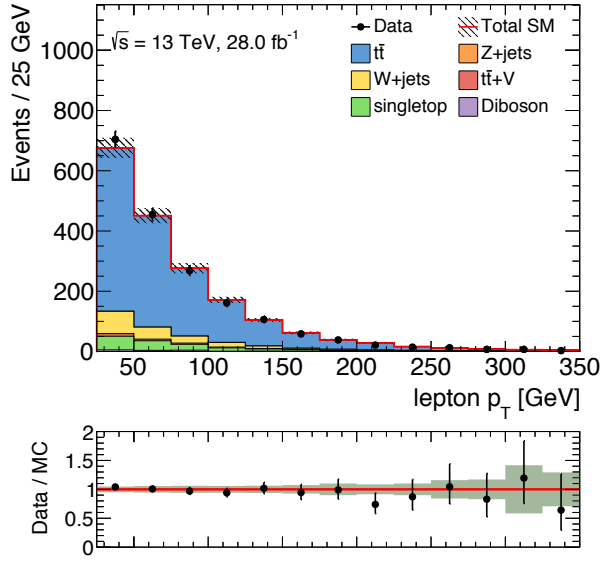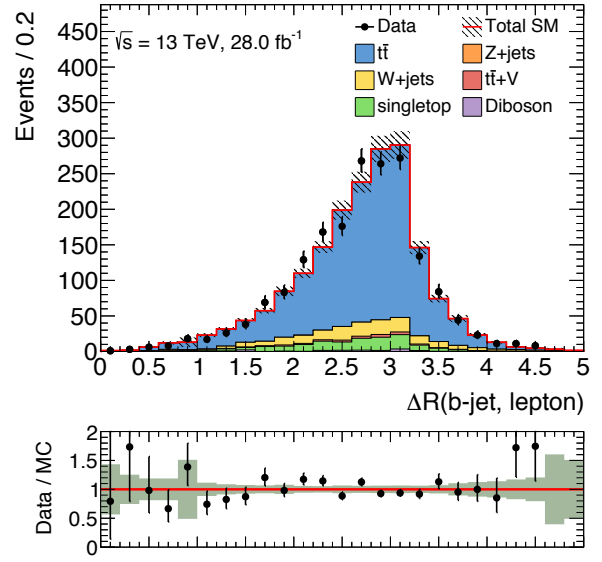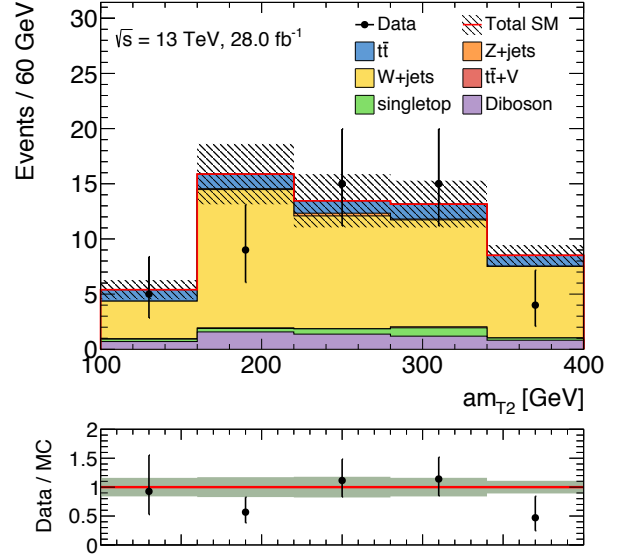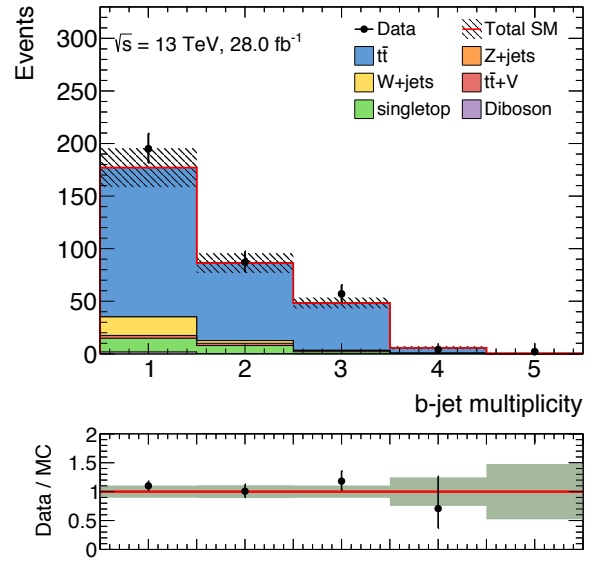
Figure 6.4: Jet and b-jet multiplicity, signal lepton p_{T}, and $\Delta R(b, \ell)$ distributions at TCR of *Resolved* after the background-only fit. The uncertainty band includes statistical and systematic error.

(a) $E_{\mathrm{T}}^{\mathrm{miss}}$

(b) $H_{\mathrm{T,sig}}^{\mathrm{miss}}$

(c) m_{top}^{χ}

(d) *topness*

Figure 6.5: $E_{\mathrm{T}}^{\mathrm{miss}}$, $H_{\mathrm{T,sig}}^{\mathrm{miss}}$, m_{top}^{χ}, and *topness* distributions at TCR of *Resolved* after the background-only fit. The uncertainty band includes statistical and systematic error.
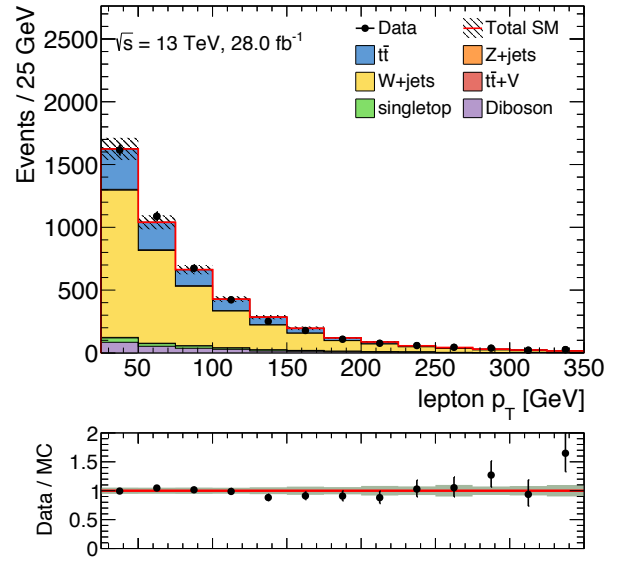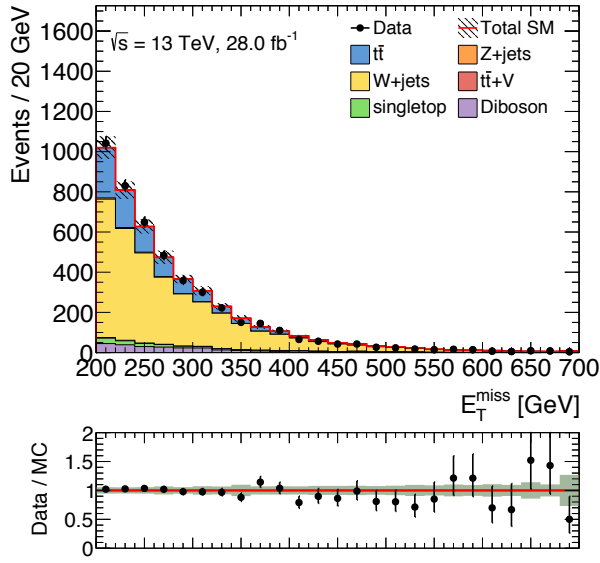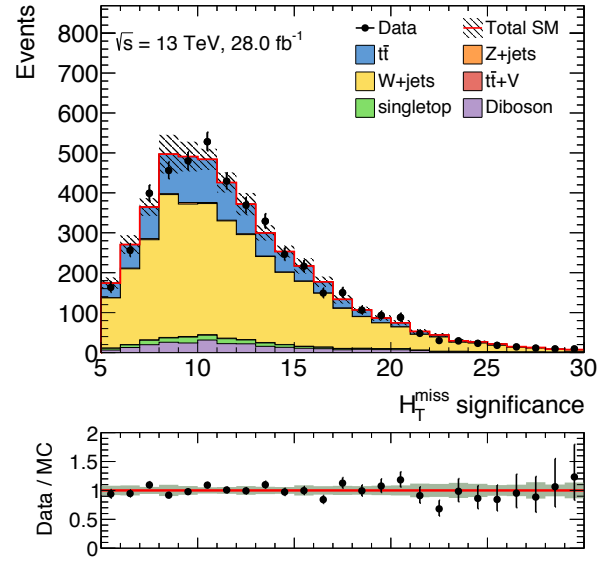
Figure 6.6: jet multiplicity, signal lepton p_T, E_T^{miss}, $H_{T,sig}^{miss}$, m_{top}^{χ}, and *topness* distributions at WCR of *Resolved* after the background-only fit. The uncertainty band includes statistical and systematic error.

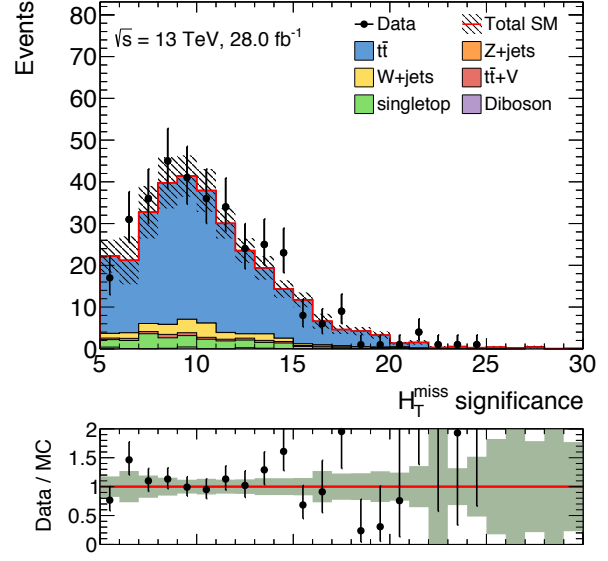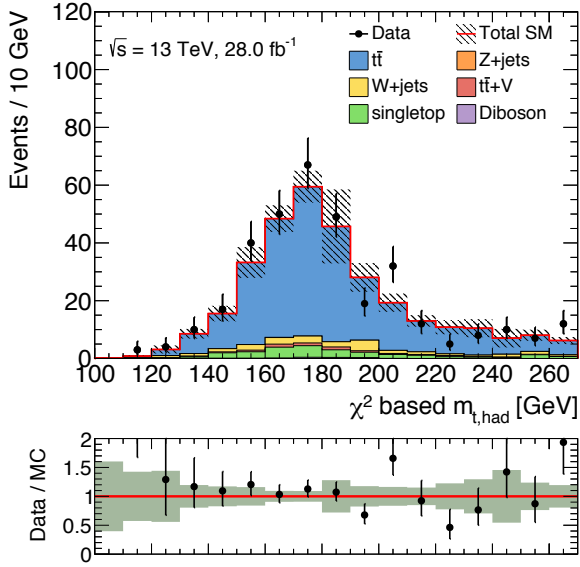Figure 6.7: Jet and b-jet multiplicity, signal lepton p_T, and $\Delta R(b, \ell)$ distributions at STCR of *Resolved* after the background-only fit. The uncertainty band includes statistical and systematic error.
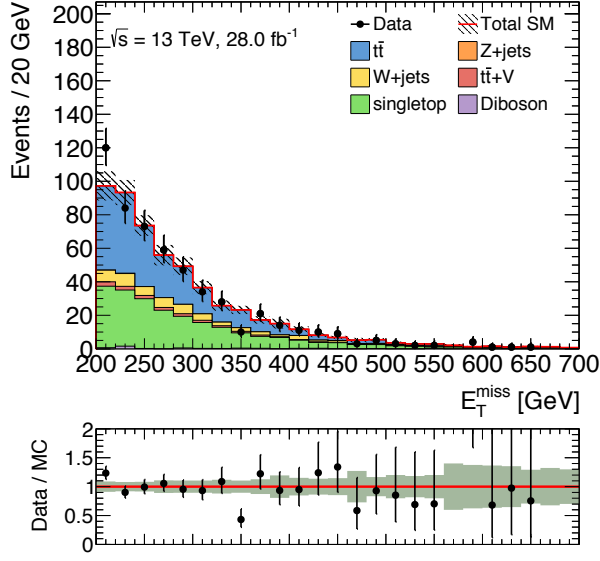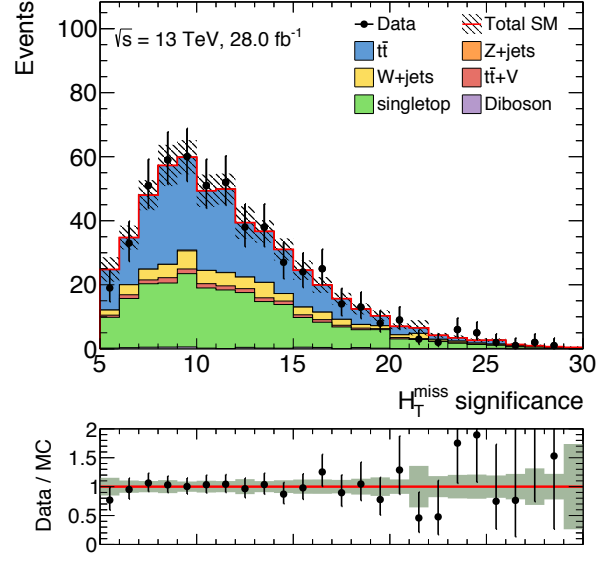
(a) $E_{\mathrm{T}}^{\mathrm{miss}}$
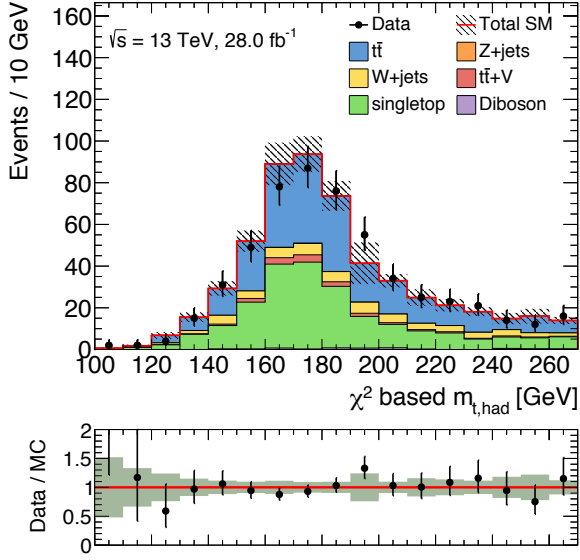
(b) $H_{\mathrm{T,sig}}^{\mathrm{miss}}$

(c) m_{top}^{χ}
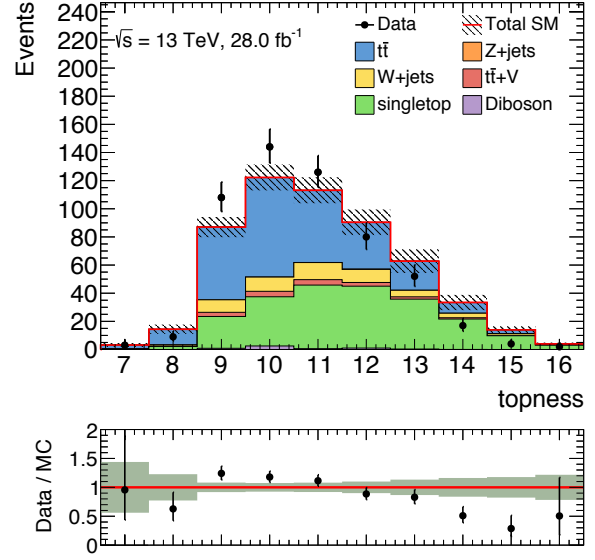
(d) *topness*

Figure 6.8: $E_{\mathrm{T}}^{\mathrm{miss}}$, $H_{\mathrm{T,sig}}^{\mathrm{miss}}$, m_{top}^{χ}, and *topness* distributions at STCR of *Resolved* after the background-only fit. The uncertainty band includes statistical and systematic error.
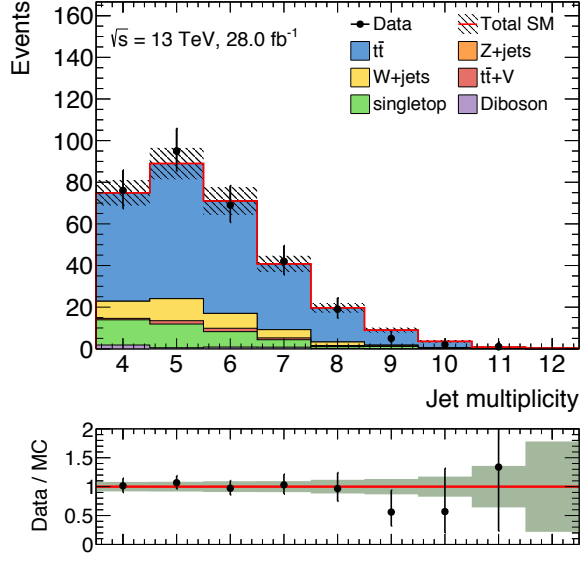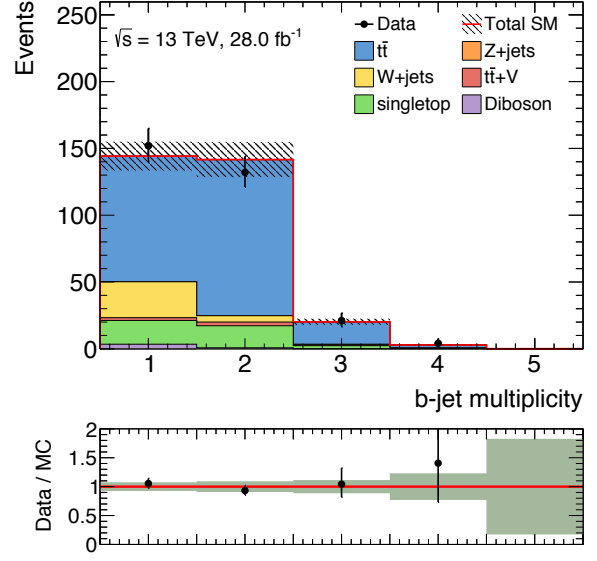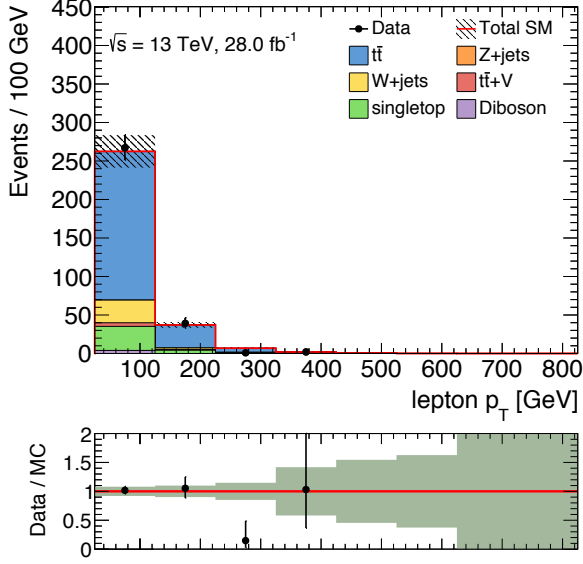
Figure 6.9: Jet and b-jet multiplicity, signal lepton p_{T}, and $\Delta R(b, \ell)$ distributions at TCR of *Boosted* after the background-only fit. The uncertainty band includes statistical and systematic error.
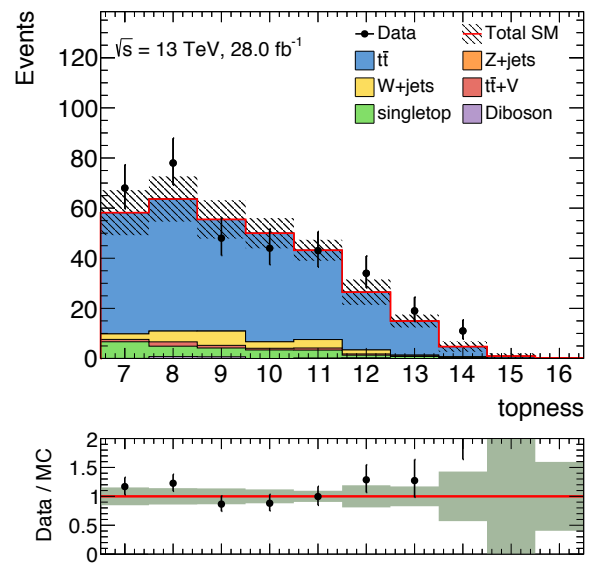
(a) $E_{\mathrm{T}}^{\mathrm{miss}}$

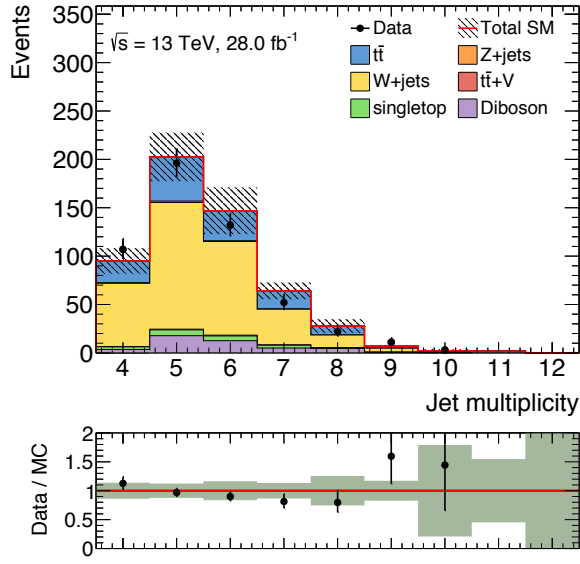(b) $H_{\mathrm{T,sig}}^{\mathrm{miss}}$

(c) $m_{\text{large-R jet}}$

(d) $p_{\mathrm{T\,large\text{-}R\,jet}}$

Figure 6.10: $E_{\mathrm{T}}^{\mathrm{miss}}$, $H_{\mathrm{T,sig}}^{\mathrm{miss}}$, and large-R jet mass and p_{T} distributions at TCR of *Boosted* after the background-only fit. The uncertainty band includes statistical and systematic error.

Figure 6.11: Jet multiplicity, signal lepton p_T, E_T^{miss}, $H_{T,sig}^{miss}$, and large-R jet mass and p_T distributions at WCR of *Boosted* after the background-only fit. The uncertainty band includes statistical and systematic error.

Figure 6.12: Jet and b-jet multiplicity, signal lepton p_T, and $\Delta R(b, \ell)$ distributions at STCR of *Boosted* after the background-only fit. The uncertainty band includes statistical and systematic error.
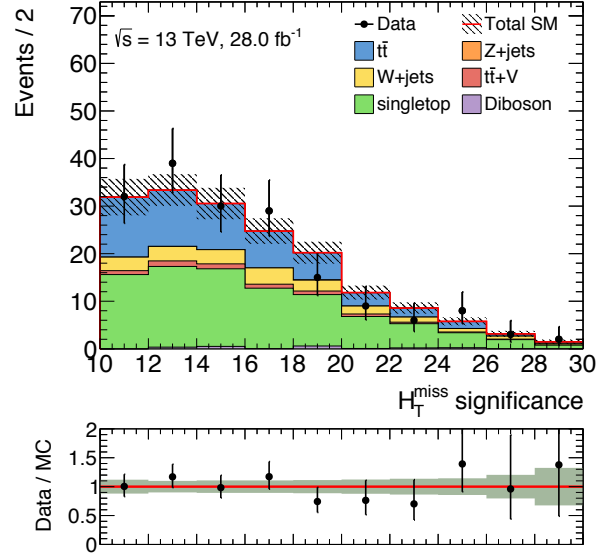
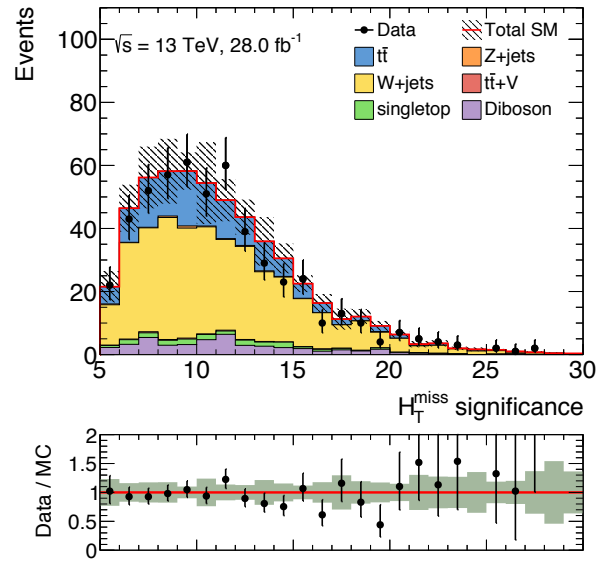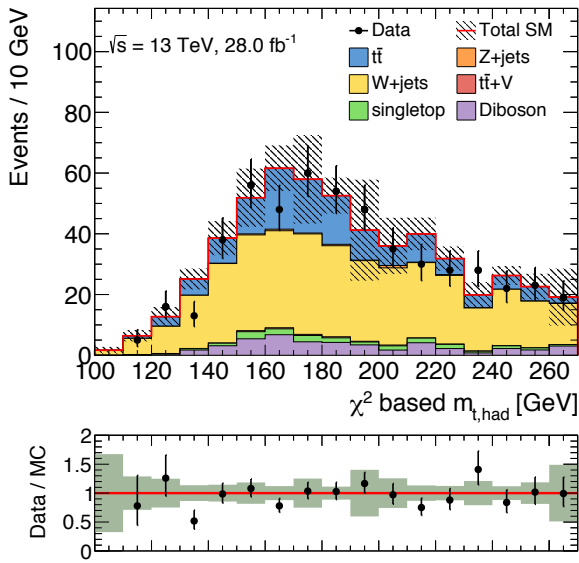(a) $E_{\mathrm{T}}^{\mathrm{miss}}$
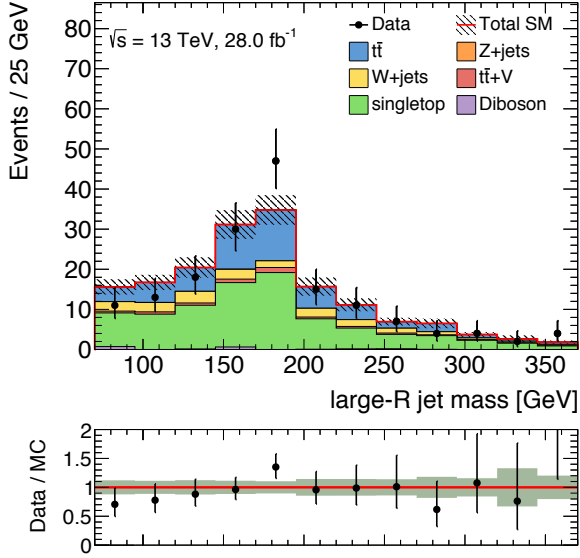
(b) $H_{\mathrm{T,sig}}^{\mathrm{miss}}$
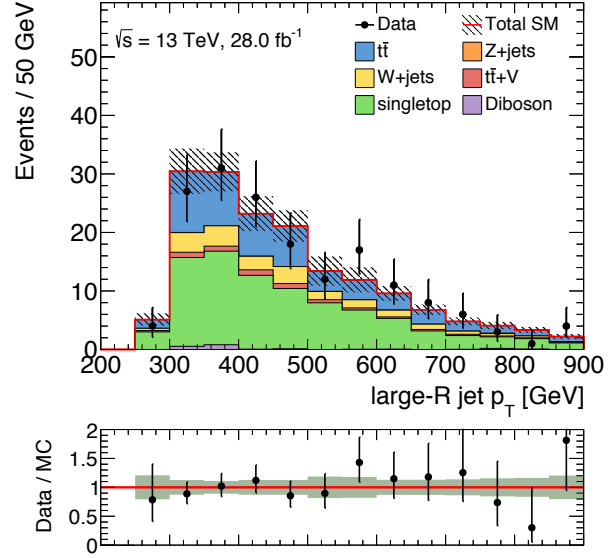
(c) $m_{\text{large-R jet}}$

(d) $p_{\mathrm{T\,large\text{-}R\,jet}}$

Figure 6.13: $E_{\mathrm{T}}^{\mathrm{miss}}$, $H_{\mathrm{T,sig}}^{\mathrm{miss}}$, and large-R jet mass and p_{T} distributions at STCR of *Boosted* after the background-only fit. The uncertainty band includes statistical and systematic error.

6.2 *Resolved* and *Boosted* Control Regions For $t\bar{t} + Z$

Control regions for $t\bar{t} + Z$ (TZCRs) are prepared for *Resolved* and *Boosted* in a dedicated way different from the other CRs. $t\bar{t}$ production with radiation of a Z boson decaying into neutrinos is an irreducible background[2].

A CR using Z boson decays to charged leptons doesn't work well because of the limited data statistics due to the small branching ratio to leptons. Instead, a CR using $t\bar{t} + \gamma$ events is used where the Z boson is emulated by the γ. The CR is defined to minimize the differences between $t\bar{t} + Z$ and $t\bar{t} + \gamma$ processes to reduce the theoretical uncertainties in the emulation of $t\bar{t} + Z$. The main difference arises from the fact that the Z boson mass is much larger than γ mass. This causes difference in kinematic distributions. Furthermore, at LHC energies, the bremsstrahlung rate of Z boson from top quark is lower than that of γ from top quark and its decay products.

These differences can be reduced if the boson p_T is larger than the Z boson mass. In the limit, the kinematical impact of the mass difference on the phase space is reduced, and the bremsstrahlung rate of photon is suppressed [113]. For this reason, photon objects are required to have p_T larger than 145 GeV as described in Section 4.4. In this condition, the uncertainty from photon radiations has turned out to be subdominant compared to the uncertainties described in Section 8.6 and therefore can be neglected [26].

The event selection for the TZCRs requires at least one photon, exactly one signal lepton, no additional baseline lepton, and at least four signal jets, at least one of which must be b-tagged. Furthermore, the TZCRs are required to have the same jet p_T thresholds as the corresponding SRs. To emulate the $Z \to \nu\bar{\nu}$ decay, the photon with the highest p_T is vectorially added to $\vec{p}_\mathrm{T}^{\mathrm{miss}}$ and this sum is used to construct an emulated $E_\mathrm{T}^{\mathrm{miss}}$ denoted by $\tilde{E}_\mathrm{T}^{\mathrm{miss}} \equiv |\vec{p}_\mathrm{T}^{\mathrm{miss}} + \vec{p}_\mathrm{T}^{\gamma}|$. Then, $\tilde{m}_\mathrm{T}$ and $\tilde{H}_{\mathrm{T,sig}}^{\mathrm{miss}}$ are also calculated by regarding $\tilde{E}_\mathrm{T}^{\mathrm{miss}}$ as the normal missing transverse energy. In order to make the region kinematically closer to the SRs, event in the TZCRs must satisfy $\tilde{E}_\mathrm{T}^{\mathrm{miss}} > 120$ GeV, $\tilde{m}_\mathrm{T} > 100$ GeV, and $\tilde{H}_{\mathrm{T,sig}}^{\mathrm{miss}} > 5$. Finally, $E_\mathrm{T}^{\mathrm{miss}} < 200$ GeV is required to make the TZCR statistically orthogonal to the other CRs and SRs.

Figure 6.14-6.15 show variables after the background-only fit in CRs compared to the observed data.

---

[2] The expected yields of $t\bar{t} + W$ in the SRs are less than 10% of the expected yields of $t\bar{t} + Z$, and hence the two processes are combined in the analysis.

(a) E_T^{miss}

(b) $\tilde{m}_T$
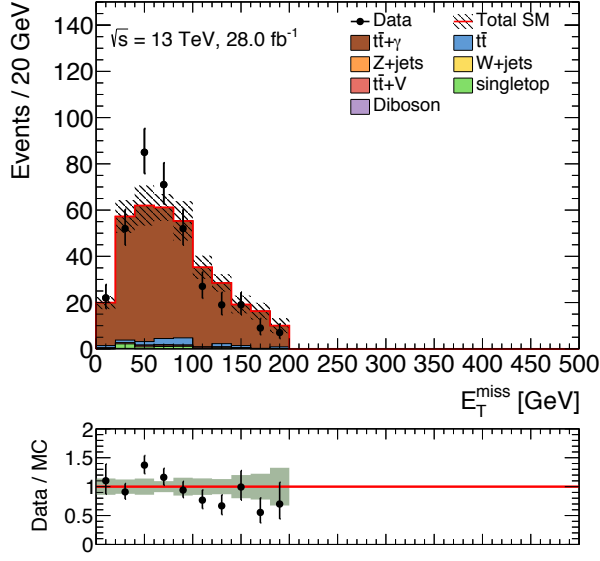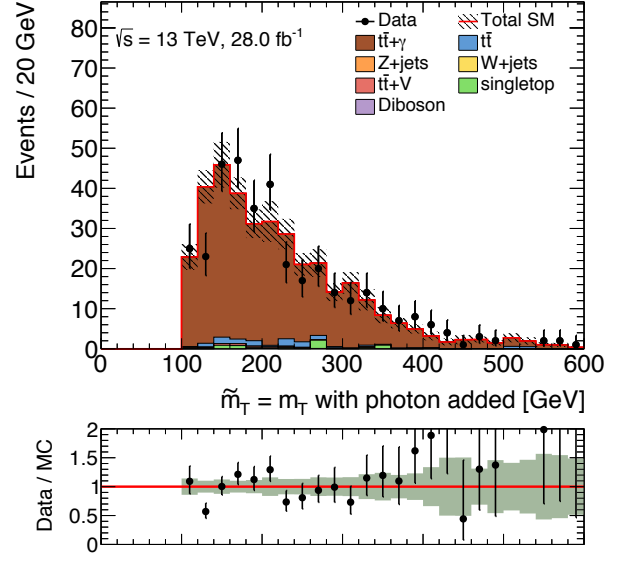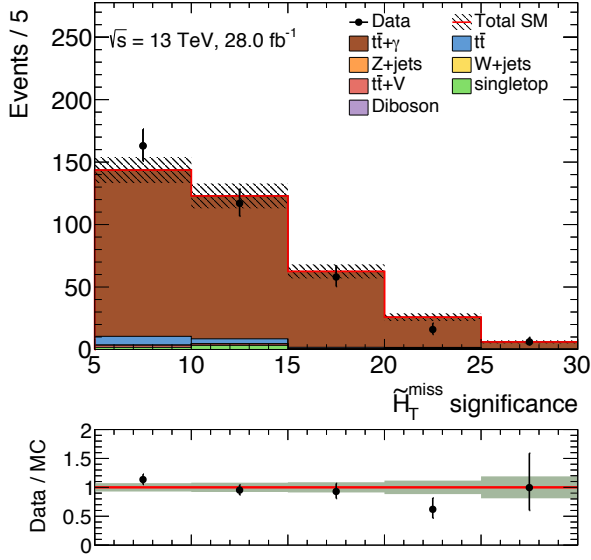
(c) $\tilde{H}_{T,sig}^{miss}$
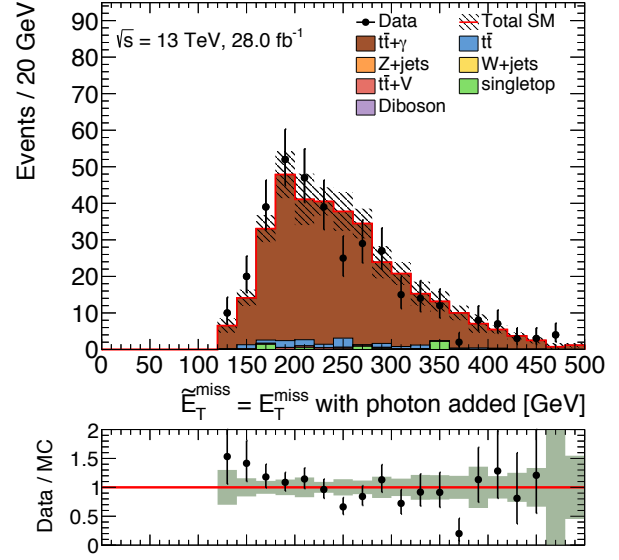
(d) $\tilde{E}_T^{miss}$

Figure 6.14: E_T^{miss}, $\tilde{m}_T$, $\tilde{H}_{T,sig}^{miss}$, and $\tilde{E}_T^{miss}$ distributions at TZCR of *Resolved* after the background-only fit. The uncertainty band includes statistical and systematic error.

(a) E_T^{miss}

(b) $\tilde{m}_T$
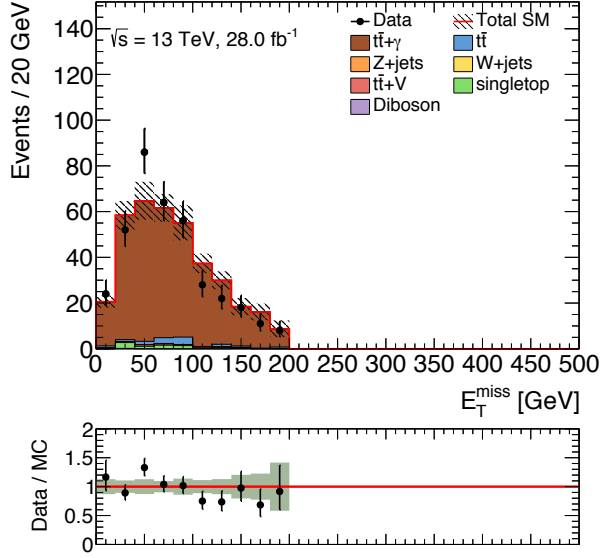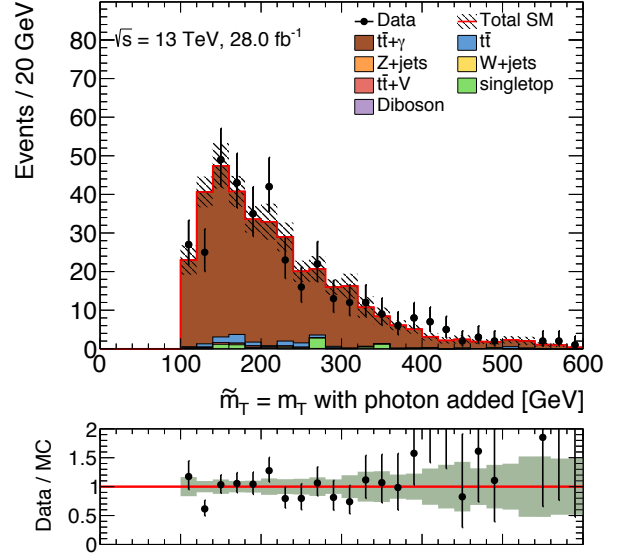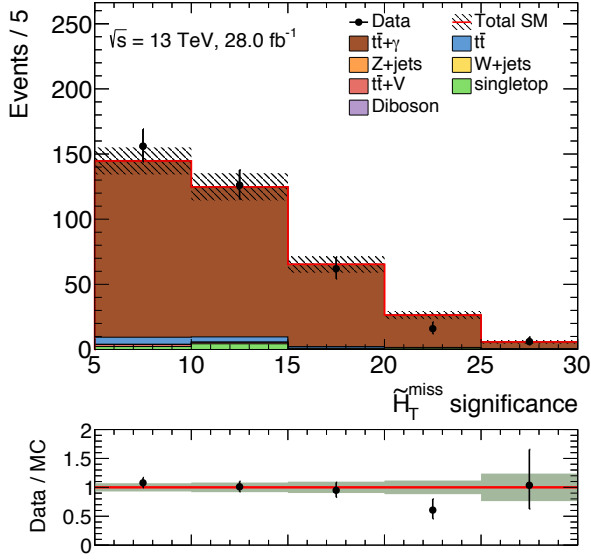
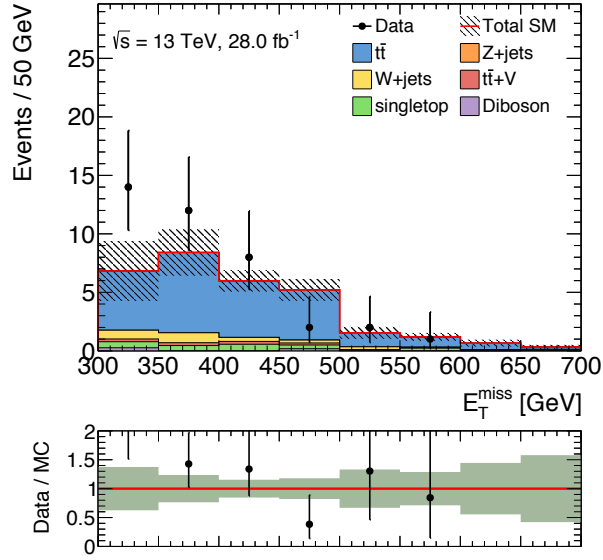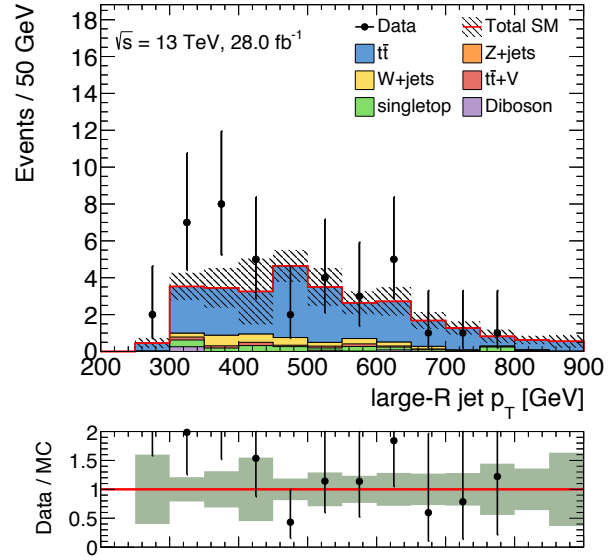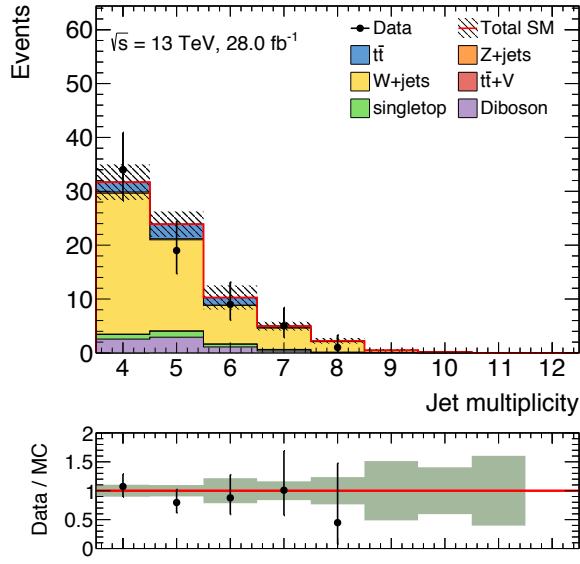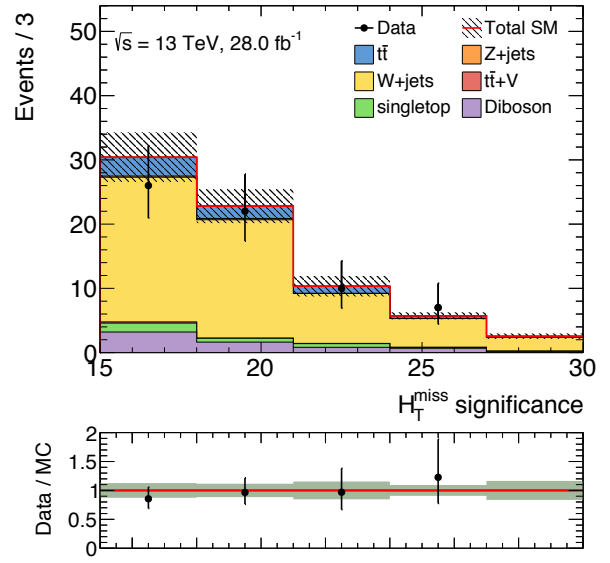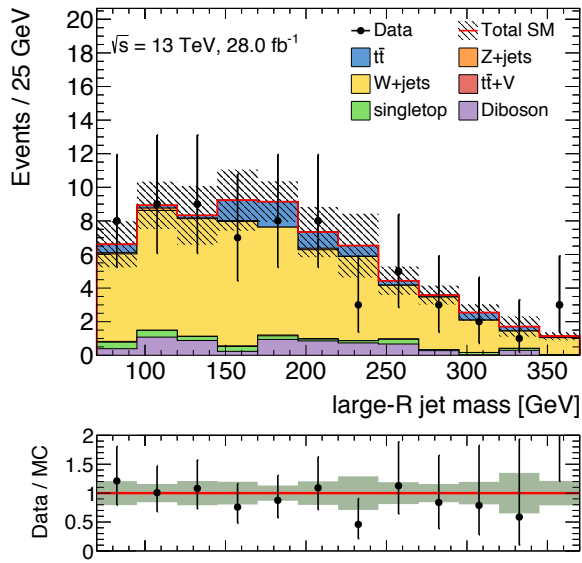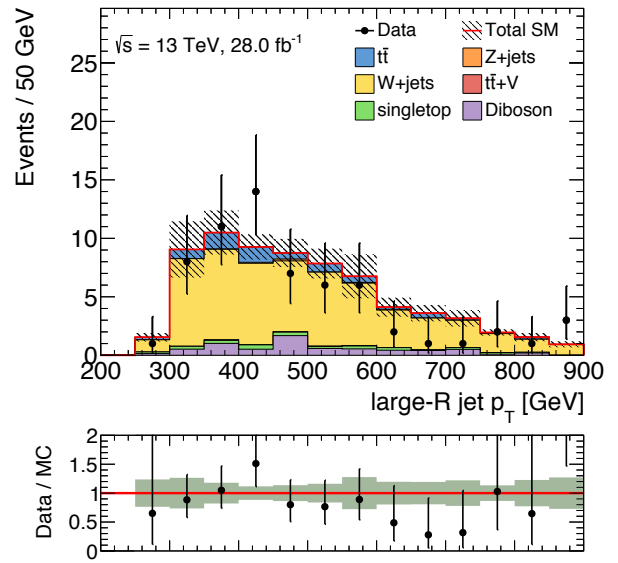(c) $\tilde{H}_{T,sig}^{miss}$
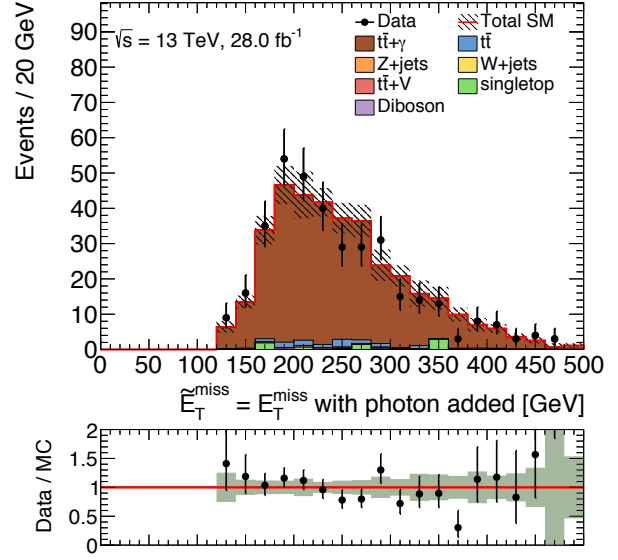
(d) $\tilde{E}_T^{miss}$

Figure 6.15: E_T^{miss}, $\tilde{m}_T$, $\tilde{H}_{T,sig}^{miss}$, and $\tilde{E}_T^{miss}$ distributions at TZCR of *Boosted* after the background-only fit. The uncertainty band includes statistical and systematic error.

6.3 *Resolved* and *Boosted* Validation Regions

Each SR has two VRs, TVR ($t\bar{t}$) and WVR (W+jets). These are constructed with the same selection as the TCR and the WCR except that m_T is required to be between 90 and 120 GeV[3]. The signal contamination in the VRs is checked for all the signal mass points shown in Figure 1.8, and found to be negligible. Figure 6.18-6.23 show variables after the background-only fit in VRs compared to the observed data. These VR plots show that there is no significant problem in the background estimation procedure developed in this section.

---

[3] Since the m_T range in the STCR is already extended upward to 120 GeV to increase statistics, a Wt VR is not defined.
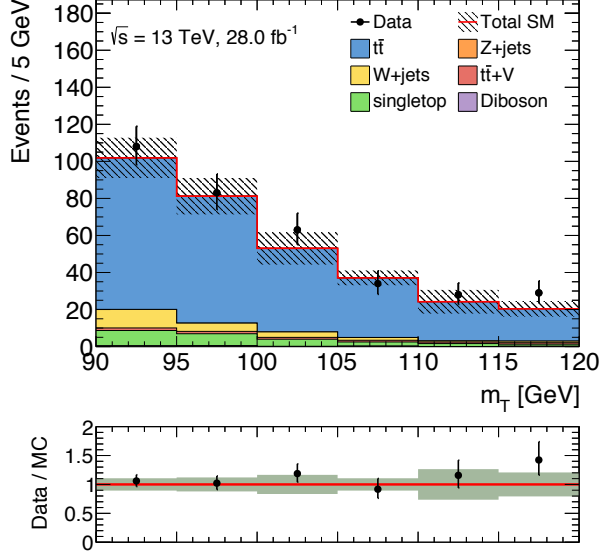
(a) m_T at TVR of *Resolved*
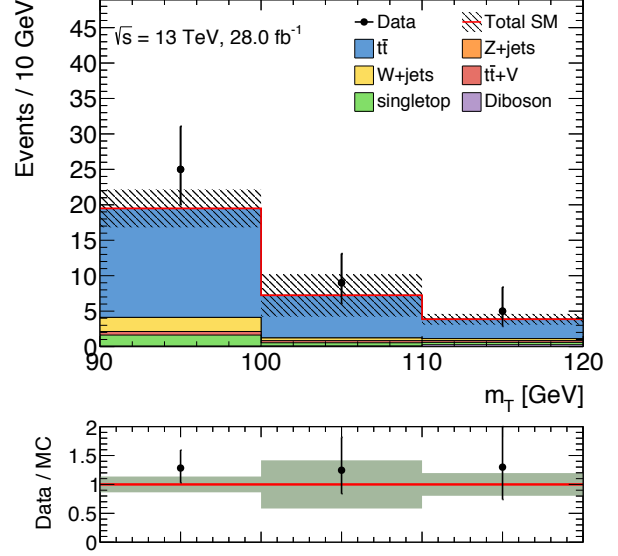
(b) m_T at TVR of *Boosted*
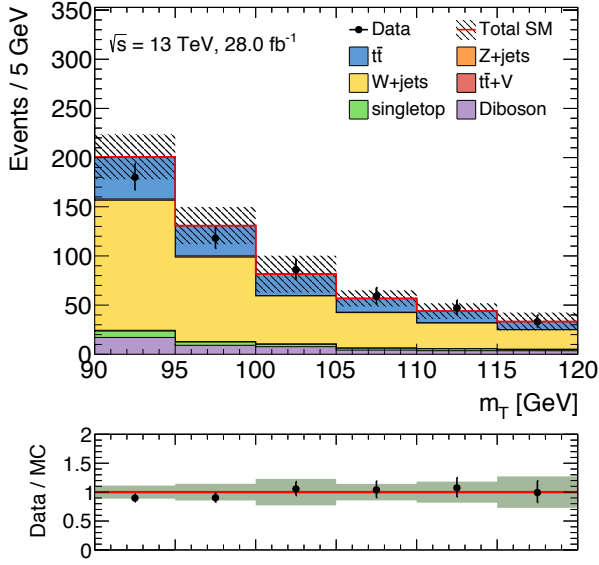
(c) m_T at WVR of *Resolved*
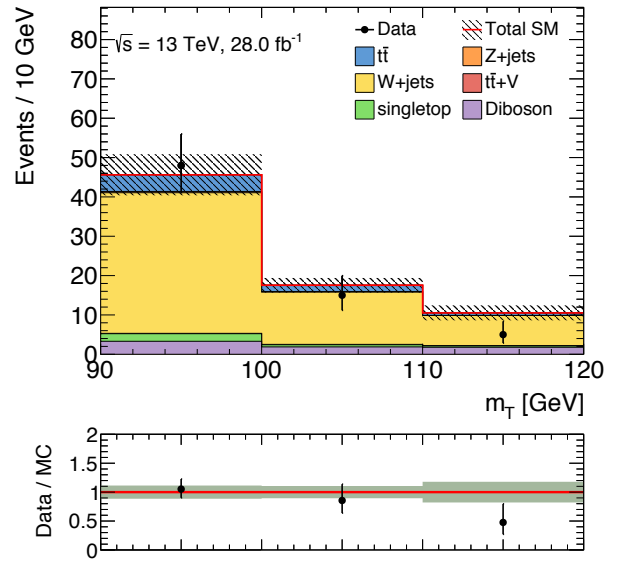
(d) m_T at WVR of *Boosted*

Figure 6.16: m_T distributions at TVR (top) and WVR (bottom), respectively. The left and right columns correspond to *Resolved* and *Boosted*, respectively. The background-only fit results are applied to the distributions. The uncertainty band includes statistical and systematic error.
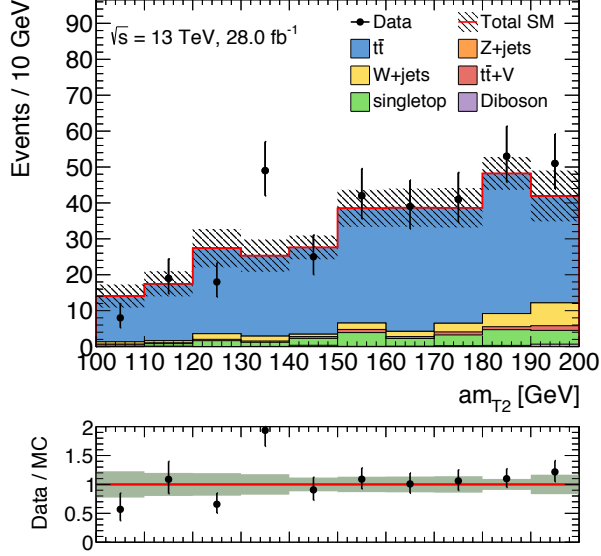
(a) am_{T2} at TVR of *Resolved*
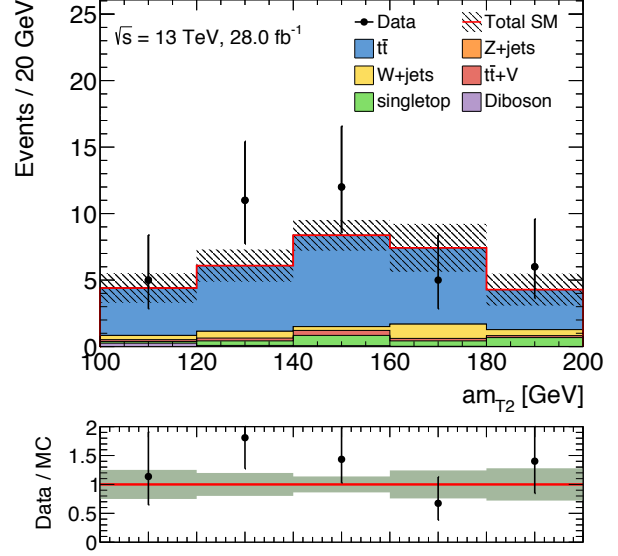
(b) am_{T2} at TVR of *Boosted*

(c) am_{T2} at WVR of *Resolved*

(d) am_{T2} at WVR of *Boosted*

Figure 6.17: am_{T2} distributions at TVR (top) and WVR (bottom), respectively. The left and right columns correspond to *Resolved* and *Boosted*, respectively. The background-only fit results are applied to the distributions. The uncertainty band includes statistical and systematic error.
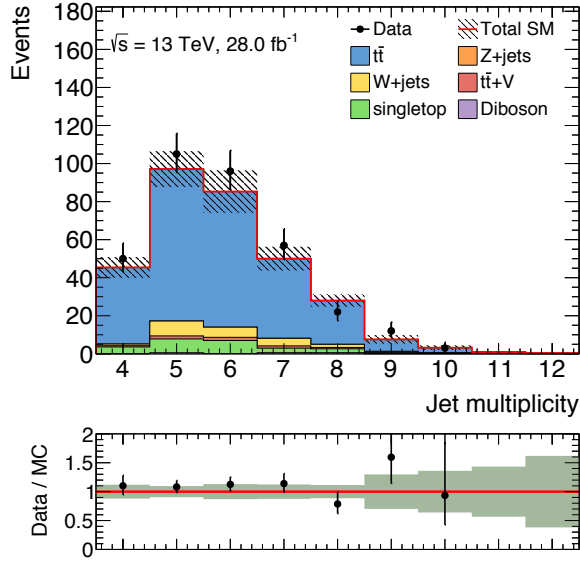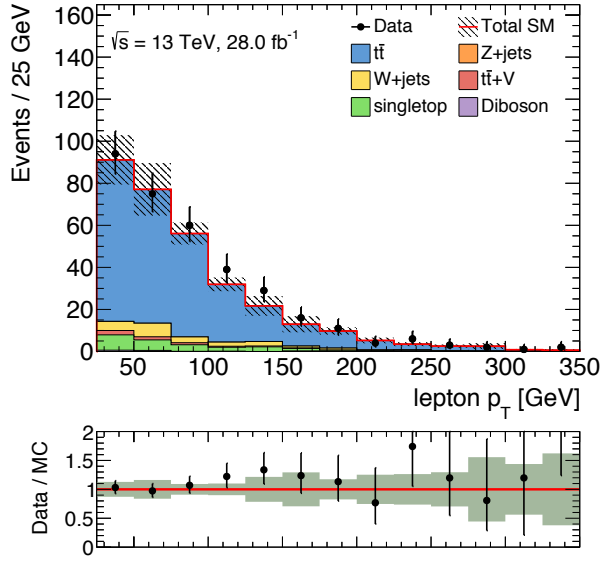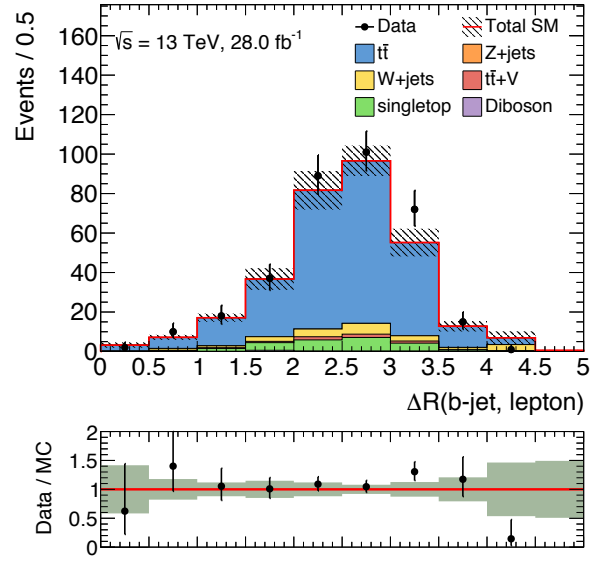
Figure 6.18: Jet and b-jet multiplicity, signal lepton p_T, and $\Delta R(b, \ell)$ distributions at TVR of *Resolved* after the background-only fit. The uncertainty band includes statistical and systematic error.
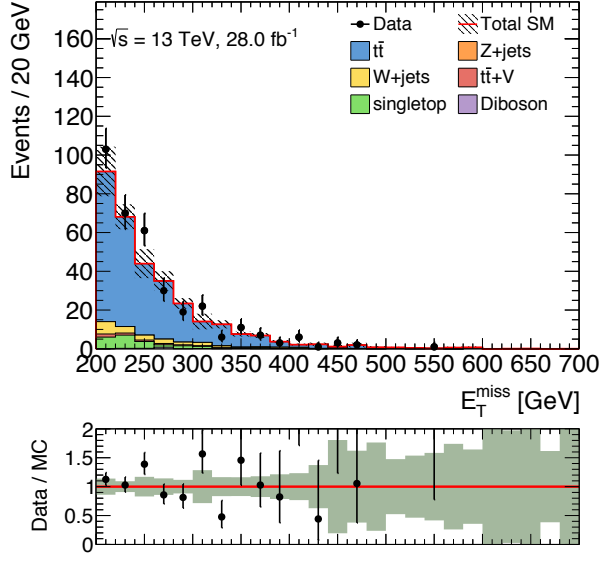
(a) $E_{\mathrm{T}}^{\mathrm{miss}}$

(b) $H_{\mathrm{T,sig}}^{\mathrm{miss}}$

(c) m_{top}^{χ}

(d) *topness*

Figure 6.19: $E_{\mathrm{T}}^{\mathrm{miss}}$, $H_{\mathrm{T,sig}}^{\mathrm{miss}}$, m_{top}^{χ}, and *topness* distributions at TVR of *Resolved* after the background-only fit. The uncertainty band includes statistical and systematic error.
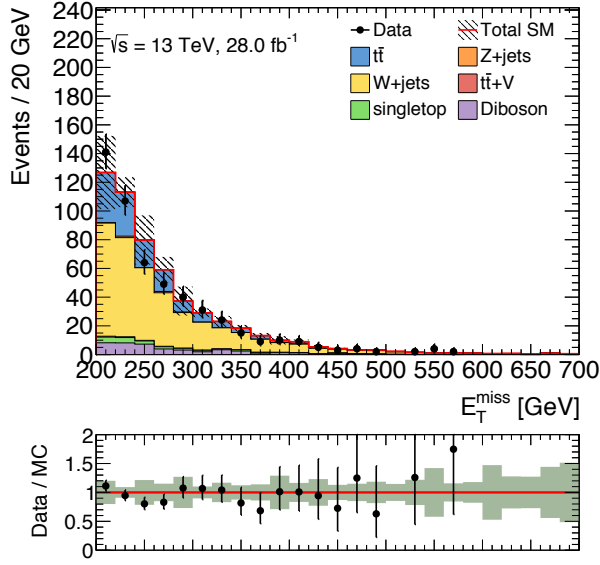
Figure 6.20: Jet multiplicity, signal lepton p_T, E_T^{miss}, $H_{T,\text{sig}}^{\text{miss}}$, m_{top}^{χ}, and *topness* distributions at WVR of *Resolved* after the background-only fit. The uncertainty band includes statistical and systematic error.
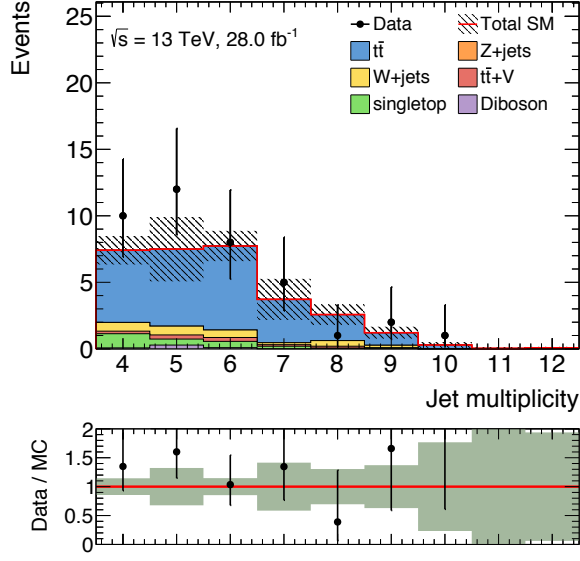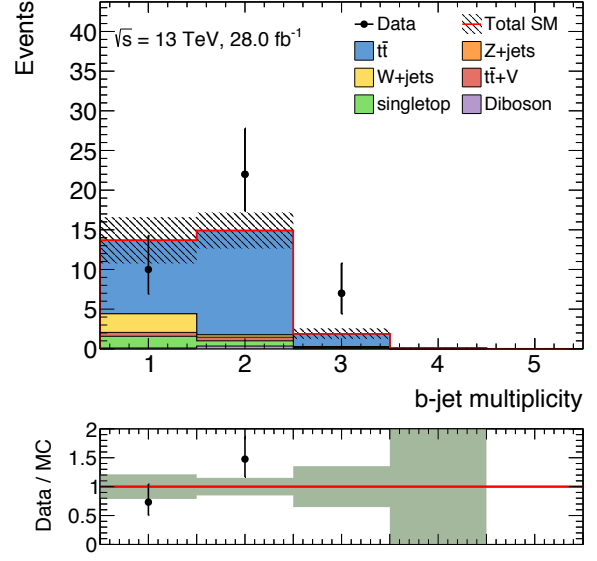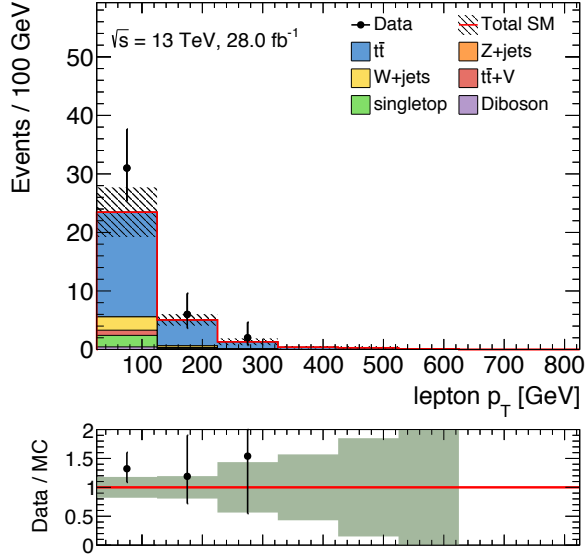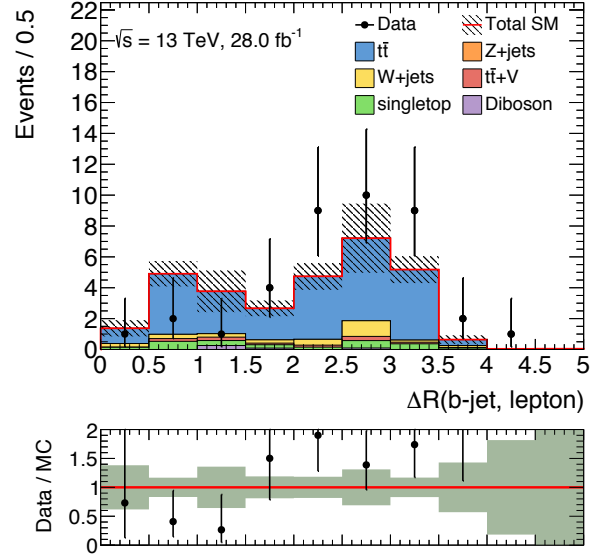
Figure 6.21: Jet and b-jet multiplicity, signal lepton p_T, and $\Delta R(b, \ell)$ distributions at TVR of *Boosted* after the background-only fit. The uncertainty band includes statistical and systematic error.
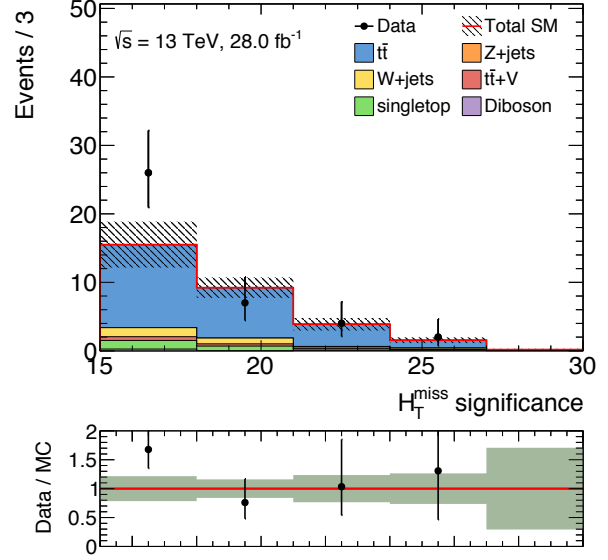
(a) $E_{\mathrm{T}}^{\mathrm{miss}}$
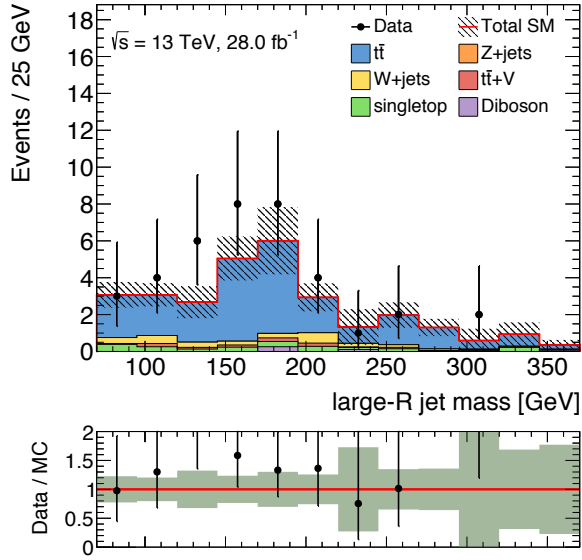
(b) $H_{\mathrm{T,sig}}^{\mathrm{miss}}$

(c) $m_{\text{large-R jet}}$

(d) $p_{\mathrm{T\,large\text{-}R\,jet}}$

Figure 6.22: $E_{\mathrm{T}}^{\mathrm{miss}}$, $H_{\mathrm{T,sig}}^{\mathrm{miss}}$, and large-R jet mass and p_{T} distributions at TVR of *Boosted* after the background-only fit. The uncertainty band includes statistical and systematic error.
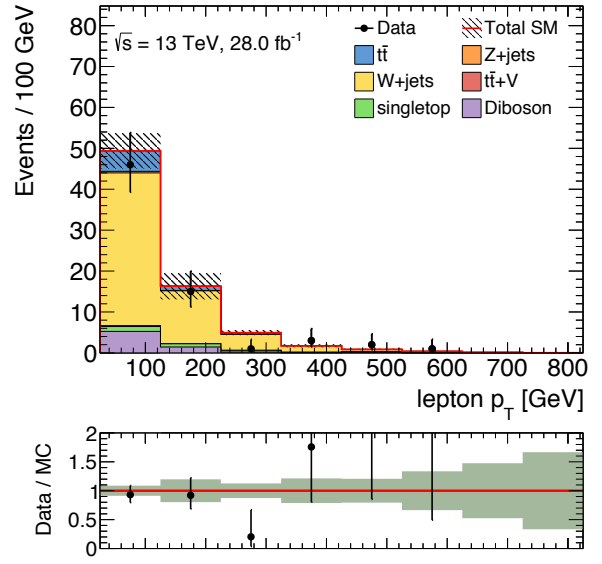
(a) jet multiplicity

(b) $p_{\mathrm{T}\ell}$
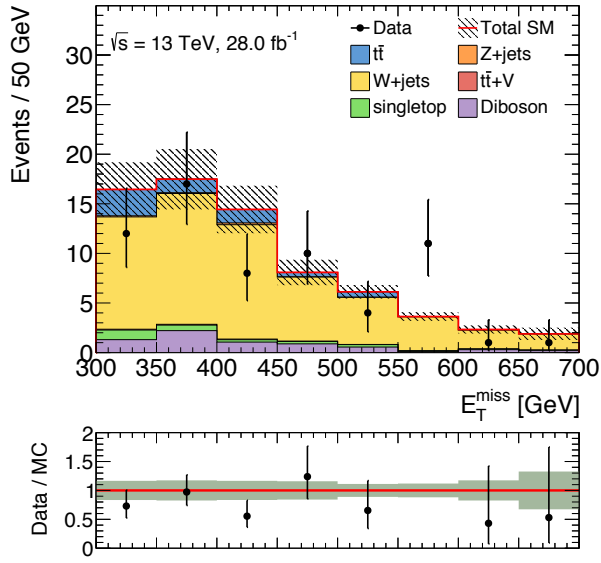
(c) $E_{\mathrm{T}}^{\mathrm{miss}}$

(d) $H_{\mathrm{T,sig}}^{\mathrm{miss}}$

(e) $m_{\text{large-R jet}}$

(f) $p_{\mathrm{T}\,\text{large-R jet}}$

Figure 6.23: Jet multiplicity, signal lepton p_{T}, $E_{\mathrm{T}}^{\mathrm{miss}}$, $H_{\mathrm{T,sig}}^{\mathrm{miss}}$, and large-R jet mass and p_{T} distributions at WVR of *Boosted* after the background-only fit. The uncertainty band includes statistical and systematic error.

6.4 2-D Shape Fit for *Diagonal*
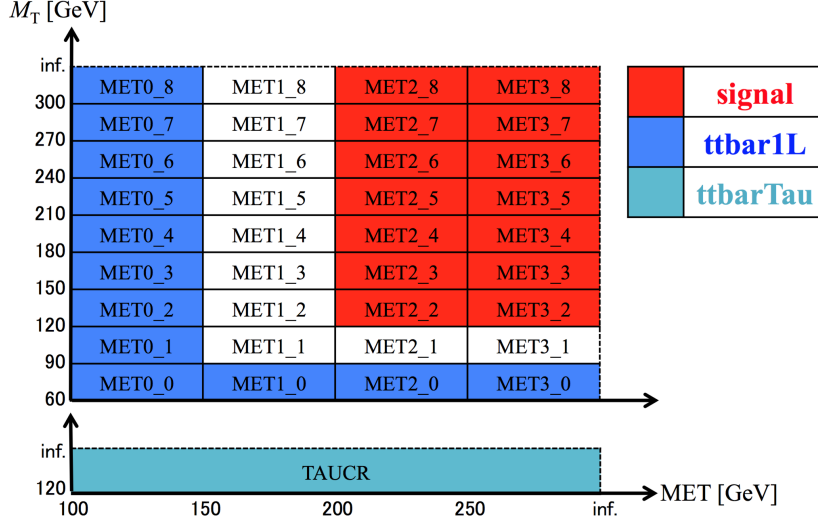
Figure 6.24: Binning configuration for the 2-dimensional (E_T^{miss}, m_T) binned shape fit in the *Diagonal* analysis. Each yield at each bin is used in the binned maximum likelihood fit. Colored bins indicate that they enhance a specific process to control its normalization. (red:signal, blue:$t\bar{t} \to [b\ell\nu][bqq]$, cyan:$t\bar{t} \to 1\ell 1\tau_h$).

After the base event selection described in Section 5.4, the selected events are divided into 4 E_T^{miss} slices, [100, 150], [150, 200], [200, 250], [250, inf] GeV, and subsequently divided into 9 m_T slices, [60, 90], [90, 120], [120, 150], [150, 180], [180, 210], [210, 240], [240, 270], [270, 300], [300, inf] GeV. The binning configuration of the 2-dimensional (E_T^{miss},m_T) shape fit is shown in Figure 6.24.

Figure 6.25 shows each m_T distribution at each E_T^{miss} slice. To show how well the background MC samples can describe data, Figure 6.25 also shows data points while those in the region where $E_T^{miss} > 150$ GeV and $m_T > 120$ GeV are blinded. The signal events are enriched in the high-E_T^{miss} and high-m_T region, where, however, $1L1\tau_h$ events are also enriched and become the dominant background. The hadronically decaying tau in $1L1\tau_h$ events after the base selection tends to be outside acceptance and thus contributes to E_T^{miss} and m_T as an invisible object like neutrino. Therefore $1L1\tau_h$ events have also high m_T. To precisely estimate the $1L1\tau_h$ events, 'TAUCR' is prepared, which enriches $1L1\tau_h$ events by requiring events to pass the base selection with the tau-veto requirement 'inversed' and have $m_T > 120$ GeV. Figure 6.26 shows each m_T distribution at TAUCR at each E_T^{miss} slice. TAUCR is not divided into E_T^{miss} and m_T slices but remains just one bin in the fit because it is enough for $1L1\tau_h$ to be controlled well and because of simplicity of the fit. The subdominant background is 1L events, which can be precisely estimated by m_T shape at low-E_T^{miss} slice. All other small backgrounds are determined from simulation and normalized to the most accurate theoretical cross-section available.

Instead of preparing VRs like *Resolved* and *Boosted*, the 2-D shape fit has been validated by a test fit, called 'validation fit', in which bins in the region where $E_T^{miss} > 150$ GeV and $m_T > 120$ GeV are not used and blinded as shown in Figure A.1. The purpose of the validation fit is to assure that the SM-background model can describes data at background-enhanced regions

well without any significant issues. As a goodness of fit, CL_b has been calculated and the result is 0.436 (0.160σ). The result has concluded that there is no insanity in the fit configuration and modeling. For the validation studies, see Appendix A. After confirming by the tests that there is no significant issue in the fit configuration and modeling, the 'unblind' fit has been done and the results are shown in Section 9.2.
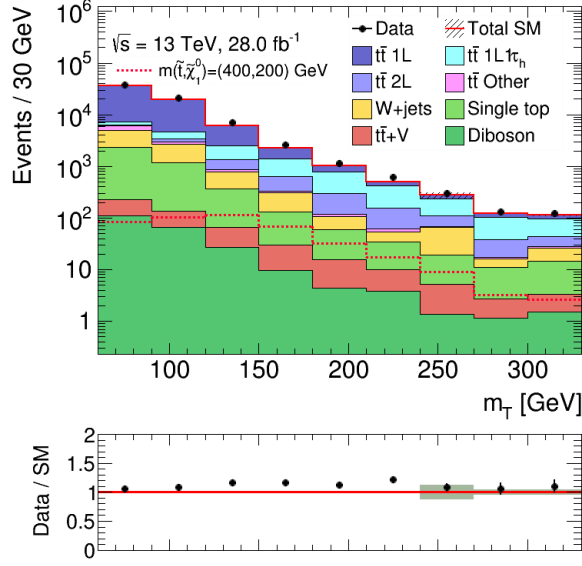
(a) m_T at $E_T^{miss} = [100,\ 150]$ GeV.
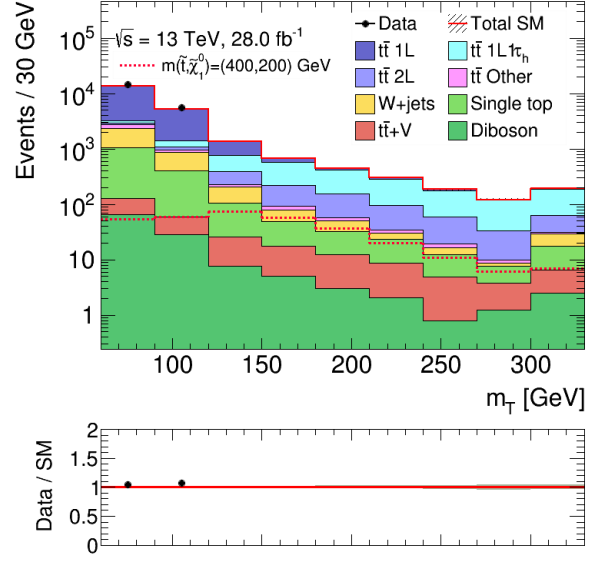
(b) m_T at $E_T^{miss} = [150,\ 200]$ GeV.
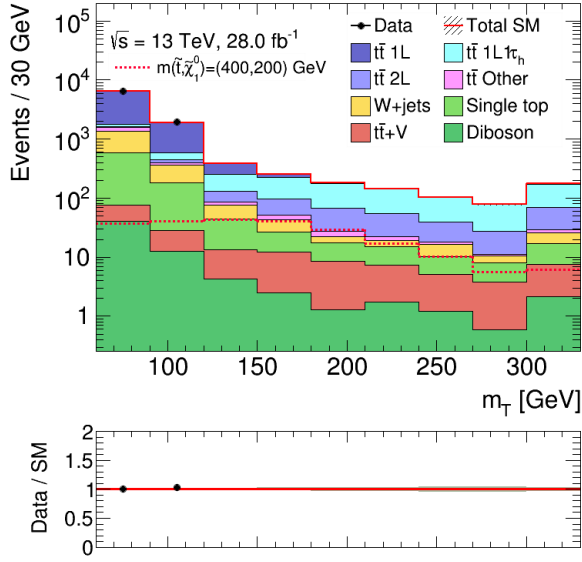
(c) m_T at $E_T^{miss} = [200,\ 250]$ GeV.
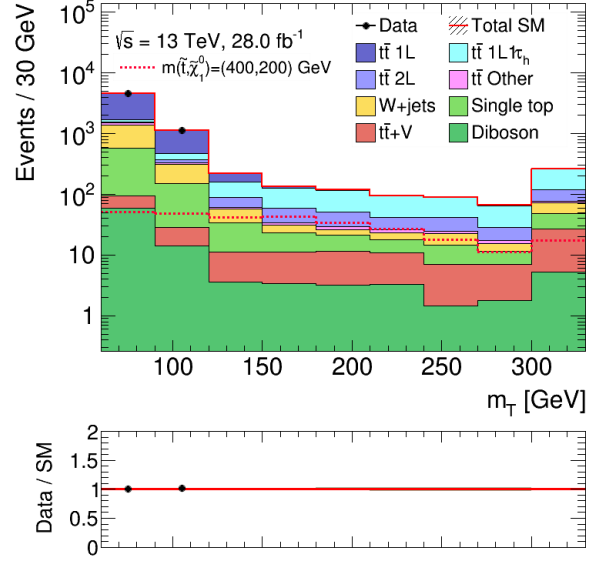
(d) m_T at $E_T^{miss} = [250,\ inf]$ GeV.

Figure 6.25: m_T distributions at each E_T^{miss} slice. Data points are blinded in the region where $E_T^{miss} > 150$ GeV and $m_T > 120$ GeV. The uncertainty band includes statistical error.
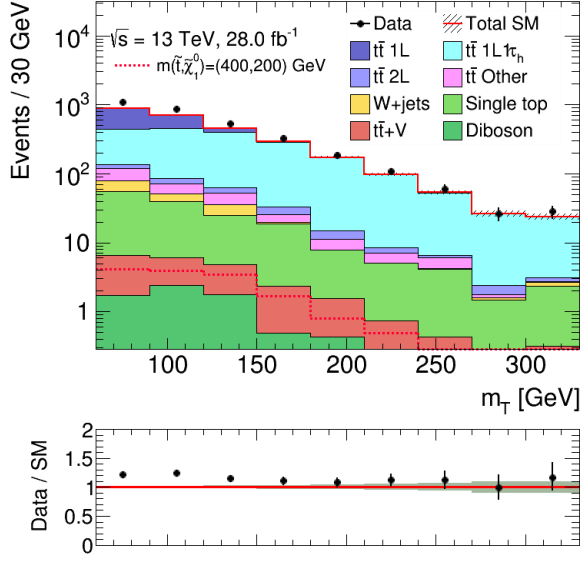
(a) m_T at TAUCR at $E_\mathrm{T}^\mathrm{miss} = [100,\ 150]$ GeV.
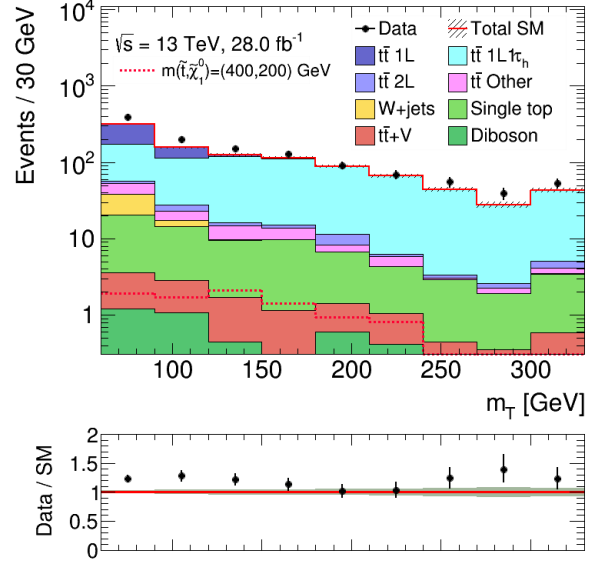
(b) m_T at TAUCR at $E_\mathrm{T}^\mathrm{miss} = [150,\ 200]$ GeV.
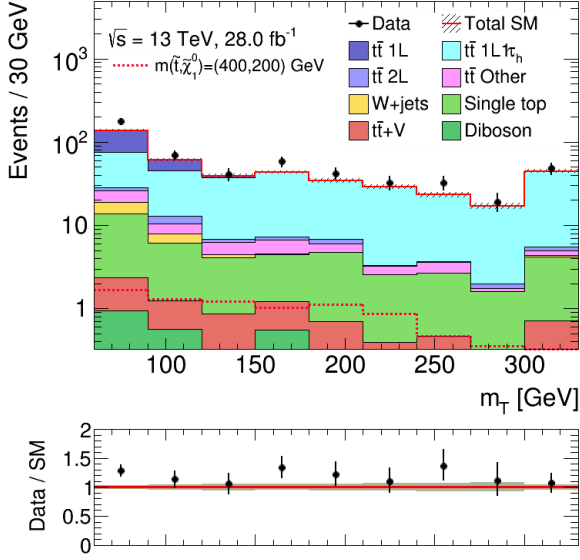
(c) m_T at TAUCR at $E_\mathrm{T}^\mathrm{miss} = [200,\ 250]$ GeV.
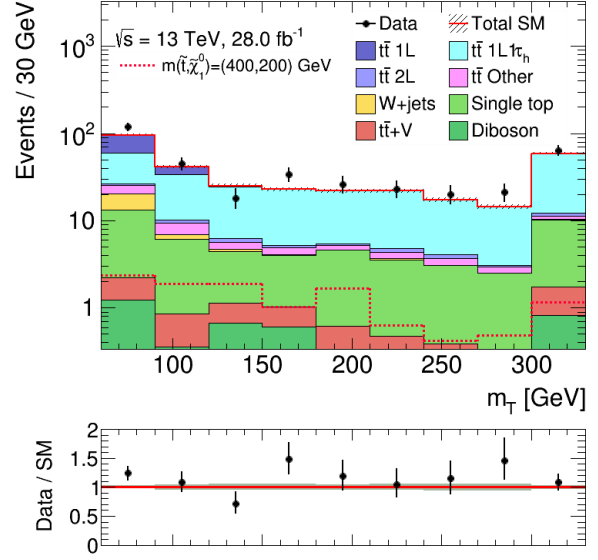
(d) m_T at TAUCR at $E_\mathrm{T}^\mathrm{miss} = [250,\ \mathrm{inf}]$ GeV.

Figure 6.26: m_T distributions at TAUCR at each $E_\mathrm{T}^\mathrm{miss}$ slice. The $m_\mathrm{T} > 120$ GeV requirement is not applied in the plots. The uncertainty band includes statistical error.

Chapter 7

Hypothesis Test Procedures

In this chapter, hypothesis test procedures used in the analysis are introduced. Section 7.1 outlines hypothesis test dedicated to new particle search in high energy physics. Section 7.2 introduces a maximum binned likelihood fit with a description of likelihood form used in the fit to determine a parameter of interest and nuisance parameters. This is needed to calculate a test statistic used in the analysis, profile likelihood ratio, introduced in Section 7.4. This likelihood fit is applied at signal and control regions as shown in Chapter 6 and 9.

Section 7.3 describes the actual likelihood form for each strategies, *Resolved*, *Boosted*, and *Diagonal*. Section 7.4 introduces calculation of probability distribution of the test statistic by asymptotic formulae instead of a traditional MC sampling method. The probability distribution is needed to calculate p-values used to quantitatively declare discovery or exclusion of new theory.

7.1 Hypothesis Test for New Particle Search

In high energy physics, to declare discovery of a new particle and exclusion of its existence, a hypothesis test is used that compares two hypotheses: a new particle doesn't exists (called null-hypothesis) and truly exists (called alternative-hypothesis). The hypothesis test provides p-values, quantitative measures about how well null-hypothesis or alternative-hypothesis are matched to observed data. To do the hypothesis test, first one must calculate posterior probability each for the two hypotheses, and then must construct probability distributions of a test statistic in each assumption that either null- or alternative-hypothesis is actually true. The test statistic is a variable as a function of observed data that indicates which hypothesis is plausible, so the test statistic should be chosen to be highly sensitive to null- or alternative-hypothesis. Then, the probability distribution of the test statistic is integrated to calculate p-value. In the recent high energy experiments, mainly two types of p-values are used, called CL_b and CL_s [114], which are used for discovery and exclusion declaration of new theory, respectively.

CL_b is defined as:

$$\mathrm{CL}_b = \int_{t_\mathrm{obs}}^{\infty} Prob(t|\mu_\mathrm{sig} = 0)dt, \tag{7.1}$$

where t is a test statistic, t_obs is the one for observed data, $Prob(t|\mu_\mathrm{sig} = 0)$ is a probability density as function of t in the assumption that null-hypothesis is true, which is denoted by $\mu_\mathrm{sig}=0$, and μ_sig is a scale factor of signal cross section. When $\mu_\mathrm{sig} = 1$, it indicates that nominal signal cross section predicted by a new theory is assumed, and when $\mu_\mathrm{sig} = 0$, it indicates signal cross

section is assumed 0 (in other words assumes there is no new particle), so CL_b is a probability indicating how often the observation could happen if null-hypothesis is true. In high energy and cosmological physics experiments, when one obtains $\mathrm{CL}_b < 2.87 \times 10^{-7}$ from a hypothesis test, it is conventionally called 'discovery' of a new particle because the value indicates that the observed data happened with an unnatural probability just only 2.87×10^{-7} if null-hypothesis is true. Since the value 2.87×10^{-7} is sometimes inconvenient, p-value is conventionally transformed to z-value. z-value is a quaintly of standard Gaussian distribution and p-value is expressed with z-value as follows:

$$p = \int_z^\infty \frac{1}{\sqrt{2\pi}} e^{-\frac{x^2}{2}} dx \qquad (7.2)$$

For p-value $(\mathrm{CL}_b) = 2.87 \times 10^{-7}$, z-value $= 5\ \sigma$, called $5\ \sigma$ discovery.

When observed CL_b is relatively large (typically around 0.5), the null-hypothesis is considered to be reasonable. Then, CL_s value [114] is used to quantitatively declare how much alternative-hypothesis could be realistic, which is defined as:

$$\mathrm{CL}_s = \frac{\mathrm{CL}_{s+b}}{1 - \mathrm{CL}_b}, \qquad (7.3)$$

where CL_{s+b} is a posterior probability for the alternative-hypothesis defined as:

$$\mathrm{CL}_{s+b} = \int_{-\infty}^{t_{\mathrm{obs}}} Prob(t|\mu_{\mathrm{sig}} = 1) dt. \qquad (7.4)$$

In earlier times, CL_{s+b} was a standard measure of exclusion of new theories, but this is not a good measure when observed data has downward fluctuation with respect to background expectation and the signal expectation is relatively smaller than the background. CL_s can be robust to the issue although CL_s somewhat sacrifices the characteristic as probability in a mathematical sense. When $\mathrm{CL}_s < 0.05$ is observed, one can declare that the alternative-hypothesis, the new theory is excluded with 95% confidence level. The z-value for $\mathrm{CL}_s = 0.05$ corresponds to $1.64\ \sigma$.

Since μ_{sig} is a parameter that represents which hypothesis is assumed, it is called parameter of interest (POI). All parameters in the test statistic except for POI, called 'nuisance parameters', must be determined or marginalized by, for example, a profiling technique (see Section 7.4), otherwise p-values cannot be calculated.

7.2 Binned Maximum Likelihood Fit

In the analysis, the observable is a set of number of events at each bin[1], and the observable is modeled to consist of the SM events (backgrounds) and the signal events from a new theory. Then, a binned likelihood form for the observable, which is frequently used in the analysis, is denoted by

$$L(\boldsymbol{n}|\mu_{\mathrm{sig}}, \boldsymbol{\mu_{\mathrm{bkg}}}, \boldsymbol{\alpha}) = \prod_{b \in \text{all histogram bins}} P(n_b|\nu_b(\mu_{\mathrm{sig}}, \boldsymbol{\mu_{\mathrm{bkg}}}, \boldsymbol{\alpha})) \times \prod_{i \in \boldsymbol{\alpha}} \Phi_{\mathrm{syst}}(\alpha_i), \qquad (7.5)$$

where $\boldsymbol{n}$ is a vector of each number of observed events at each bins (n_b is b-th component of the $\boldsymbol{n}$), $\boldsymbol{\alpha}$ is a vector of the systematic parameters[2], $\boldsymbol{\mu_{\mathrm{bkg}}}$ is a vector of each scale factors of

---

[1] For *Resolved* and *Boosted*, the observable is a set of number of events at SR, TCR, WCR, STCR, TZCR. For *Diagonal*, it is a set of number of events at each bin, all of which constitute the 2-dimensional ($E_{\mathrm{T}}^{\mathrm{miss}}$, m_{T}) distribution.

[2] The systematic parameters are standardized as $\alpha_i = \frac{(\alpha_i^{\mathrm{raw}} - \alpha_i^{\mathrm{raw,mean}})}{\sigma_{\alpha_i^{\mathrm{raw}}}}$.

each background cross section, $P(n_b|\nu_b(\mu_{\text{sig}}, \boldsymbol{\mu_{\text{bkg}}}, \boldsymbol{\alpha}))$ is a poisson distribution of number of events with the expected mean $\nu_b(\mu_{\text{sig}}, \boldsymbol{\mu_{\text{bkg}}}, \boldsymbol{\alpha})$ at b-th bin, and $\Phi_{\text{syst}}(\boldsymbol{\alpha})$ is a standard gaussian distribution.

To perform a maximum likelihood fit to the observed data, 'MINUIT' [115] is used in the analysis. The error and correlation of fitted parameters are calculated from hessian matrix of the log likelihood[3]. One remarkable thing is that the uncertainty from the systematic effect is automatically propagated into the POI μ_{sig} with consideration of correlation among systematic parameters.

Another important characteristic of fit with the likelihood is that systematic parameter α_i is included in both its gaussian term and poisson term, meaning that systematic parameters can be also correlated with observed number of events and thus can be constrained by not only its gaussian term but also the poisson term. If a systematic effect estimated before fit is statistically too large compared to the observation, then the poisson term reduces the likelihood score drastically, resulting in a narrower error width of a systematic parameter after fit than before fit. This effect is called 'profile effect'[4] and gets larger as the expected number of events increases, so it can be interpreted such that the systematic effect estimated before fit[5] is more precisely estimated by measurement (fit) with higher statistics.

7.3 Model Parameterization

In this section, the actual form of $\nu_b(\mu_{\text{sig}}, \boldsymbol{\mu_{\text{bkg}}}, \boldsymbol{\alpha})$ in Equation 7.5 each for *Resolved*, *Boosted*, and *Diagonal* is introduced. For *Resolved* and *Boosted*, $\nu_b(\mu_{\text{sig}}, \boldsymbol{\mu_{\text{bkg}}}, \boldsymbol{\alpha})$ can be explicitly written down such as

$$
\begin{aligned}
\nu_b = \nu_b^{\text{sig}} \quad &\times \prod_{i \in \boldsymbol{\alpha}} \eta_{i,b}^{\text{sig}}(\alpha_i) \quad &\times \mu_{\text{sig}} \\
+ \nu_b^{\text{ttbar}} \quad &\times \prod_{i \in \boldsymbol{\alpha}} \eta'^{\text{ttbar}}_{i,b}(\alpha_i) \quad &\times \mu_{\text{ttbar}} \\
+ \nu_b^{\text{wjets}} \quad &\times \prod_{i \in \boldsymbol{\alpha}} \eta'^{\text{wjets}}_{i,b}(\alpha_i) \quad &\times \mu_{\text{wjets}} \\
+ \nu_b^{\text{singletop}} \quad &\times \prod_{i \in \boldsymbol{\alpha}} \eta'^{\text{singletop}}_{i,b}(\alpha_i) \quad &\times \mu_{\text{singletop}} \\
+ \nu_b^{\text{ttV}} \quad &\times \prod_{i \in \boldsymbol{\alpha}} \eta'^{\text{ttV}}_{i,b}(\alpha_i) \quad &\times \mu_{\text{ttV}} \\
+ \nu_b^{\text{zjets}} \quad &\times \prod_{i \in \boldsymbol{\alpha}} \eta_{i,b}^{\text{zjets}}(\alpha_i) \quad & \\
+ \nu_b^{\text{diboson}} \quad &\times \prod_{i \in \boldsymbol{\alpha}} \eta_{i,b}^{\text{diboson}}(\alpha_i) \quad &
\end{aligned}
\tag{7.6}
$$

---

[3] In the assumption that likelihood can be approximated by a multivariate gaussian distribution, $\log[L] \propto -\frac{1}{2}(\boldsymbol{\theta} - \hat{\boldsymbol{\theta}})^T \text{H}(\boldsymbol{\theta} - \hat{\boldsymbol{\theta}})$, where $\boldsymbol{\theta}$ is a vector of all model parameters and $\text{H} = -\left. \frac{\partial^2 \log L(\boldsymbol{n}|\boldsymbol{\theta})}{\partial \boldsymbol{\theta}}^2 \right|_{\boldsymbol{\theta} = \hat{\boldsymbol{\theta}}}$, one can estimate the covariance matrix of parameters, $\hat{\text{V}} = \text{H}^{-1}$. The numerical calculation of hessian is done by 'HEESE' implemented in MINUIT [115].

[4] In a different context, the word 'profile' is also used for a marginalization of all parameters except for POI in a test statistic, described in Section 7.4.

[5] Typically, the systematic effect has been estimated with an early dataset that has lower statistics than the data stored up to now. It is also estimated with an extrapolation from measurement with Run-1 $\sqrt{s} = 7$, 8 TeV dataset but tends to have large uncertainty due to the extrapolation. The systematic parameters estimated in these ways tend to be profiled.

for any $b \in$ SR, TVR, WCR, STCR, and just for TZCR:

$$
\begin{aligned}
\nu_{\text{TZCR}} = \nu_{\text{TZCR}}^{\text{sig}} \quad & \times \prod_{i \in \boldsymbol{\alpha}} \eta_{i,\text{TZCR}}^{\text{sig}}(\alpha_i) \quad && \times \mu_{\text{sig}} \\
+ \nu_{\text{TZCR}}^{\text{ttbar}} \quad & \times \prod_{i \in \boldsymbol{\alpha}} \eta'^{\text{ttbar}}_{i,\text{TZCR}}(\alpha_i) \quad && \times \mu_{\text{ttbar}} \\
+ \nu_{\text{TZCR}}^{\text{wjets}} \quad & \times \prod_{i \in \boldsymbol{\alpha}} \eta'^{\text{wjets}}_{i,\text{TZCR}}(\alpha_i) \quad && \times \mu_{\text{wjets}} \\
+ \nu_{\text{TZCR}}^{\text{singletop}} \quad & \times \prod_{i \in \boldsymbol{\alpha}} \eta'^{\text{singletop}}_{i,\text{TZCR}}(\alpha_i) \quad && \times \mu_{\text{singletop}} \\
+ \nu_{\text{TZCR}}^{\text{ttgamma}} \quad & \times \prod_{i \in \boldsymbol{\alpha}} \eta'^{\text{ttgamma}}_{i,\text{TZCR}}(\alpha_i) \quad && \times \mu_{\text{ttV}} \\
+ \nu_{\text{TZCR}}^{\text{zjets}} \quad & \times \prod_{i \in \boldsymbol{\alpha}} \eta_{i,\text{TZCR}}^{\text{zjets}}(\alpha_i) && \\
+ \nu_{\text{TZCR}}^{\text{diboson}} \quad & \times \prod_{i \in \boldsymbol{\alpha}} \eta_{i,\text{TZCR}}^{\text{diboson}}(\alpha_i) &&
\end{aligned}
\tag{7.7}
$$

where

$$
\begin{aligned}
\sum_{b \in \text{SR, TVR, WCR, STCR, TZCR}} \eta'^{\text{ttbar}}_{i,b}(\alpha_i) &= 1 \\
\sum_{b \in \text{SR, TVR, WCR, STCR, TZCR}} \eta'^{\text{wjets}}_{i,b}(\alpha_i) &= 1 \\
\sum_{b \in \text{SR, TVR, WCR, STCR, TZCR}} \eta'^{\text{singletop}}_{i,b}(\alpha_i) &= 1 \\
\sum_{b \in \text{SR, TVR, WCR, STCR}} \eta'^{\text{ttV}}_{i,b}(\alpha_i) + \eta'^{\text{ttgamma}}_{i,\text{TZCR}}(\alpha_i) &= 1
\end{aligned}
\tag{7.8}
$$

for any $i \in \boldsymbol{\alpha}$. Each of ν_b^{sig}, ν_b^{ttbar}, ν_b^{wjets}, $\nu_b^{\text{singletop}}$, ν_b^{ttV}, ν_b^{diboson} is an expected mean yield for the event at b bin, which is estimated with each MC sample. Each of μ_{sig}, μ_{ttbar}, μ_{wjets}, $\mu_{\text{singletop}}$, μ_{ttV} is a scale factor shared at all bins for each event type[6]. Each of $\eta_{i,b}^{\text{sig}}(\alpha_i)$, $\eta'^{\text{ttbar}}_{i,b}(\alpha_i)$, $\eta'^{\text{wjets}}_{i,b}(\alpha_i)$, $\eta'^{\text{singletop}}_{i,b}(\alpha_i)$, $\eta'^{\text{ttV}}_{i,b}(\alpha_i)$, $\eta_{i,b}^{\text{diboson}}(\alpha_i)$ is a scale factor at b bin for the event as a function of a standardized systematic parameter α_i shared at all bins. The $\eta_{i,b}(\alpha_i)$ function is modeled continuously with respect to α_i by using an interpolation among three points: $\eta_{i,b}(\alpha_i = +1)$, $\eta_{i,b}(\alpha_i = 0)$, $\eta_{i,b}(\alpha_i = -1)$, which can be estimated by preparing three MC samples in each condition of $\alpha_i = 0$, $\alpha_i = -1$, and $\alpha_i = +1$. The interpolation used in the analysis is implemented in HistFactory [116]. Figure 7.1 shows four types of interpolation implemented in HistFactory, and a combination of polynomial interpolation (inside ± 1 σ) and exponential extrapolation (outside ± 1 σ) is used in the analysis (green line in Figure 7.1).

Equation 7.8 means that each systematic variation of $t\bar{t}$, W+jets, singletop, and $t\bar{t} + V/\gamma$ samples never changes total yield (sum of yields at all bins) of the sample by itself. Although systematic effects of course could change the total yield of the event, those changes are absorbed (or integrated) into the μ-parameters of the samples. This μ-absorption also reduces local minima in the likelihood and makes fit more stable, so if precise measurement of total normalization of a sample (or a bin that strongly constrains it) is possible, this μ-parameter technique should be used[7]. For *Resolved* and *Boosted*, TCR, WCR, STCR, and TZCR are prepared, and then

---

[6] Note that μ_{ttV} is also shared by $t\bar{t} + \gamma$ at TZCR.

[7] The reason why the signal term includes not only the scale factor μ_{sig} but also the unconserved systematic variations $\eta_{i,b}^{\text{sig}}(\alpha_i)$, not the conserved one, is that if systematic effects on total yield of the signal are integrated into μ_{sig}, then there is no way to invert the signal cross section from μ_{sig} and the hypothesis test doesn't make sense in the case.
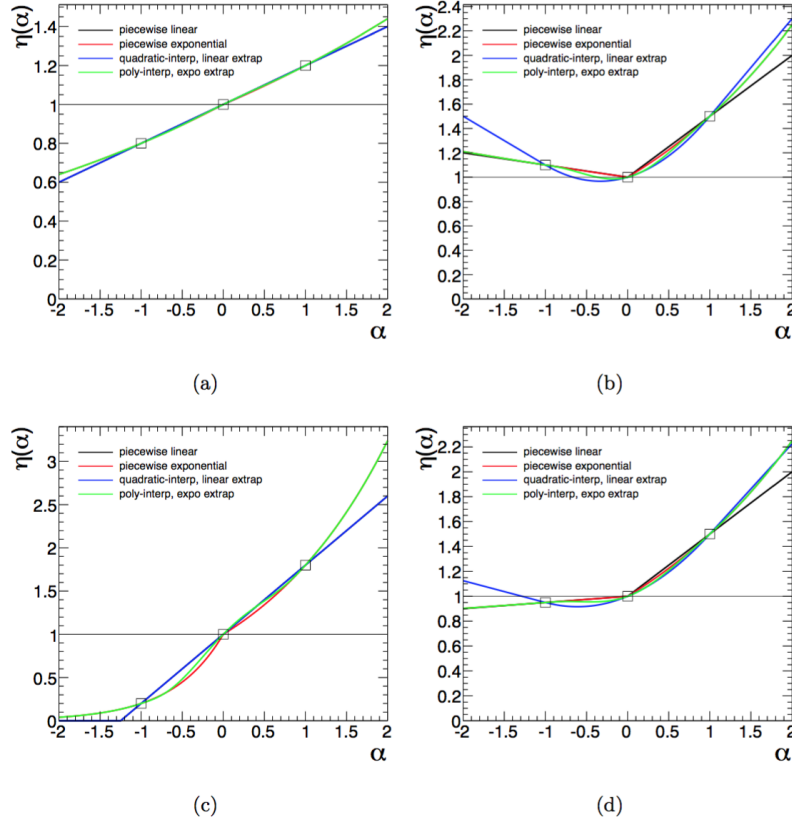
Figure 7.1: Comparison of the four interpolation options implemented in HistFactory [116] for four different models (a)-(d). $\eta(\alpha)$ is a scale factor of expected mean of number of events at a histogram bin as function of a standardized systematic parameter α. The given (modeled) sets of $\eta(\pm 1)$ before the interpolation are (a) $\eta(-1) = 0.8$, $\eta(+1) = 1.2$, (b) $\eta(-1) = 1.1$, $\eta(+1) = 1.5$, (c) $\eta(-1) = 0.2$, $\eta(+1) = 1.8$, (d) $\eta(-1) = 0.95$, $\eta(+1) = 1.5$. In this analysis, the combination of polynomial-interpolation and exponential-extrapolation (green line) is used.

μ_{ttbar}, μ_{wjets}, $\mu_{\text{singletop}}$, μ_{ttV} are available. For diboson and Z+jets, it is a little bit difficult to prepare their control regions, but their contribution is very small, and hence their μ-parameters are not provided.

In the same context, the model Parameterization for *Diagonal* can also be written down such as:

$$
\begin{aligned}
\nu_b = &\ \nu_b^{\text{sig}} & &\times \prod_{i \in \boldsymbol{\alpha}} \eta_{i,b}^{\text{sig}}(\alpha_i) & &\times \mu_{\text{sig}} \\
&+ \nu_b^{\text{ttbar1L}} & &\times \prod_{i \in \boldsymbol{\alpha}} \eta'^{\text{ttbar1L}}_{i,b}(\alpha_i) & &\times \mu_{\text{ttbar1L}} \\
&+ \nu_b^{\text{ttbarTau}} & &\times \prod_{i \in \boldsymbol{\alpha}} \eta'^{\text{ttbarTau}}_{i,b}(\alpha_i) & &\times \mu_{\text{ttbarTau}} \\
&+ \nu_b^{\text{wjets}} & &\times \prod_{i \in \boldsymbol{\alpha}} \eta_{i,b}^{\text{wjets}}(\alpha_i) & & \\
&+ \nu_b^{\text{singletop}} & &\times \prod_{i \in \boldsymbol{\alpha}} \eta_{i,b}^{\text{singletop}}(\alpha_i) & & \\
&+ \nu_b^{\text{ttV}} & &\times \prod_{i \in \boldsymbol{\alpha}} \eta_{i,b}^{\text{ttV}}(\alpha_i) & & \\
&+ \nu_b^{\text{diboson}} & &\times \prod_{i \in \boldsymbol{\alpha}} \eta_{i,b}^{\text{diboson}}(\alpha_i) & &
\end{aligned}
\tag{7.9}
$$

for any $b \in$ all histogram bins

where

$$
\begin{aligned}
\sum_{b \in \text{all histogram bins}} \eta'^{\text{ttbar1L}}_{i,b}(\alpha_i) = 1 \\
\sum_{b \in \text{all histogram bins}} \eta'^{\text{ttbarTau}}_{i,b}(\alpha_i) = 1
\end{aligned}
\tag{7.10}
$$

for any $i \in \boldsymbol{\alpha}$

As discussed in Section 6.4, the dominant and subdominant backgrounds are $t\bar{t} \to [b\ell\nu][bqq]$ and $t\bar{t} \to [b\ell\nu][b\tau_h\nu]$, and their total normalizations can be determined precisely by TAUCR and the m_{T} shape at low $E_{\text{T}}^{\text{miss}}$ slices. Therefore there are μ_{ttbar1L} and μ_{ttbarTau} for $t\bar{t} \to [b\ell\nu][bqq]$ and $t\bar{t} \to [b\ell\nu][b\tau_h\nu]$[8]. In *Diagonal*, μ_{wjets} is dropped off because from the fit tests with μ_{wjets} configuration with WCR-like bins, it has turned out that the sensitivity doesn't change with or without μ_{wjets}. This can be interpreted such as the contribution of W+jets events are very small in the signal-enhanced bins, and then the reduction of W+jets yield uncertainty by the measurement (or fit) of μ_{wjets} is negligible. The contribution of singletop and $t\bar{t} + V$ events are also small in *Diagonal*, hence they are also not let have their μ scale factors. For *Diagonal*, the contribution of Z+jets is ignorable and thus dropped off.

For implementation of the model described until here, HistFitter [117] has been used, which provides a human-friendly interface to HistFactory [116] and RooStats [118]. The model building is based on HistFactory, and the hypothesis test is based on RooStats.

---

[8] The contributions of the other $t\bar{t}$ decay modes is small, but their ($E_{\text{T}}^{\text{miss}}$, m_{T}) shapes are relatively similar to $t\bar{t} \to [b\ell\nu][b\tau_h\nu]$. Therefore, although the notation of 'ttbarTau' is used also for ν and η-parameter, they are modeled by $t\bar{t}$ samples excluding $t\bar{t} \to [b\ell\nu][bqq]$ decay mode.

7.4 Profile Likelihood Ratio as Test Statistic

In the case where one compares just only two hypotheses each of which has neither unknown nor undetermined parameters, choosing as a test statistic a ratio of 'likelihood for the alternative-hypothesis ($\mu_{\text{sig}} = 1$)' to 'likelihood for the null-hypothesis ($\mu_{\text{sig}} = 0$)' is justified by Neyman-Pearson lemma [119] that assures that such a test statistic has the highest power for the test:

$$\lambda = \frac{L\left(\boldsymbol{n}|\mu_{\text{sig}} = 1\right)}{L\left(\boldsymbol{n}|\mu_{\text{sig}} = 0\right)}. \tag{7.11}$$

Although including undetermined nuisance parameters in the likelihoods is required to model the observable and therefore the likelihood ratio cannot be directly applied in the analysis, the undetermined nuisance parameters can be marginalized by using 'profile likelihood ratio (PLR)' defined as:

$$\lambda(\mu_{\text{sig}}) = \frac{L\left(\boldsymbol{n}\left|\mu_{\text{sig}}, \hat{\hat{\boldsymbol{\mu}}}_{\text{bkg}}(\mu_{\text{sig}}), \hat{\hat{\boldsymbol{\alpha}}}(\mu_{\text{sig}})\right.\right)}{L\left(\boldsymbol{n}\left|\hat{\mu}_{\text{sig}}, \hat{\boldsymbol{\mu}}_{\text{bkg}}, \hat{\boldsymbol{\alpha}}\right.\right)}. \tag{7.12}$$

where parameters with single-hat mean that they are simply the best fitted values in the likelihood (Equation 7.5) and parameters with double hats mean that they are the best fitted values in a condition that μ_{sig} is fixed to a given value in the fit, practically 0 or 1. For a protection against the unphysical $\hat{\mu}_{\text{sig}}$, a modified PLR is defined as:

$$\tilde{\lambda}(\mu_{\text{sig}}) = \begin{cases} \dfrac{L\left(\boldsymbol{n}\left|\mu_{\text{sig}}, \hat{\hat{\boldsymbol{\mu}}}_{\text{bkg}}(\mu_{\text{sig}}), \hat{\hat{\boldsymbol{\alpha}}}(\mu_{\text{sig}})\right.\right)}{L\left(\boldsymbol{n}\left|0, \hat{\hat{\boldsymbol{\mu}}}_{\text{bkg}}(0), \hat{\hat{\boldsymbol{\alpha}}}(0)\right.\right)} & (\hat{\mu}_{\text{sig}} < 0) \\[2em] \dfrac{L\left(\boldsymbol{n}\left|\mu_{\text{sig}}, \hat{\hat{\boldsymbol{\mu}}}_{\text{bkg}}(\mu_{\text{sig}}), \hat{\hat{\boldsymbol{\alpha}}}(\mu_{\text{sig}})\right.\right)}{L\left(\boldsymbol{n}\left|\hat{\mu}_{\text{sig}}, \hat{\boldsymbol{\mu}}_{\text{bkg}}, \hat{\boldsymbol{\alpha}}\right.\right)} & (\hat{\mu}_{\text{sig}} \geq 0) \end{cases} \tag{7.13}$$

Probability distribution of the modified PLR can be analytically deduced from 'asymptotic formulae [120]', which doesn't need a traditional MC sampling method, so called Toy MC. In Appendix B, the deduction of probability distribution from the asymptotic formulae is summarized. Finally, the probability distribution of the modified PLR is used in Equation 7.1 and 7.4 to calculate CL_b and CL_{s+b}, and then CLs in Equation 7.3 is also calculated.

Chapter 8

Systematic Uncertainties

This chapter introduces systematic uncertainties. Systematic uncertainties in the signal and the SM-background models arise from experimental and theoretical sources. Those systematic uncertainties are included as nuisance parameters in the likelihood fits as described in Section 7.2. Practically, the systematic uncertainties are incorporated into the analysis by modeling η-functions in Equation 7.6, 7.7, and 7.9 using MC samples with α parameters varied to ± 1 one by one. In this chapter, systematic effects are directly indicated by η-functions for *Resolved* and *Boosted* SRs. Since *Diagonal* analysis exploits the shape fit, in other words, multiple SR-like bins, this chapter only picks up a η-function for MET3_3 bin (E_T^{miss}:[250, inf] GeV, m_T:[150, 180] GeV) indicated in Figure 6.24, which is the most sensitive bin to the benchmark signal model, $(m_{\tilde{t}_1}, m_{\tilde{\chi}_1^0}) = (400, 200)$ GeV. The detailed descriptions on η-function modeling for *Diagonal* are shown in Appendix C.

Since *Resolved* and *Boosted* analyses use only five regions (one SR and four CRs) and the expected number of events in the regions are relatively small, constraints on systematic uncertainties via profile effect is small as described in Section 7.2. From this reason, systematic sources with small effects on the observable are integrated into one enveloped systematic source[1]. This envelopment simplifies the fit and reduces numerical calculation cost.

Compared to *Resolved* and *Boosted* strategies, *Diagonal* strategy exploits 2-D shape fit to data with relatively high statistics, and therefore some systematic uncertainties could be reduced via the profile effect described in Section 7.2. For exploiting the profile effect properly, the envelopment of systematic sources is avoided as much as possible in *Diagonal* strategy.

For the estimation of theoretical uncertainties, the MC samples without detector simulation are produced to determine η-functions at $0, \pm 1$ because of limitation of computing resources. For *Diagonal*, the MC samples for $t\bar{t}$, single top, and W+jets events could be processed with detector simulation thanks to some technical updates. Basically, $\eta(\alpha = \pm 1)$ for theoretical uncertainties are symmetrized, but only $t\bar{t}$ theoretical uncertainties for *Diagonal* are not symmetrized[2].

MC statistical uncertainty on total expected events at each bin is also considered in the fit. For a detailed description of the implementation, see Ref. [116].

---

[1] The 'enveloped' systematic uncertainty is defined to be sum of systematic uncertainties in quadrature.

[2] There are two technical reasons for symmetrization of theoretical uncertainties. For theoretical uncertainties evaluated using samples without detector simulation, the larger deviation from $\eta(\alpha = 0)$ is taken to make a symmetrized $\eta(\alpha = \pm 1)$ for conservativeness. For relatively small systematic uncertainties, they are also symmetrized in the same way to avoid having local minima in the fit.

Section 8.1 describes uncertainties arising from experimental sources. Section 8.2-8.7 describes theoretical uncertainties specific to $t\bar{t}$, single top, W+jets, diboson, $t\bar{t}+V$, and the signal events, respectively. For theoretical uncertainties specific to $t\bar{t}$ and single top, the estimation is based on a dedicated study [69].

8.1 Experimental Sources

The dominant experimental uncertainties stem from imperfect knowledge of the jet energy scale (JES) and jet energy resolution (JER) [90], calibrations of the b-tagging efficiencies for b, c and light-flavor jets [121, 122], and the contribution of the E_T^{miss} soft term, which is composed of tracks not associated with any reconstructed objects and not identified as originating from pileup.

For JES, there are 77 nuisance parameters (NPs) mainly arising from differences among in-situ JES measurements [89, 90]:

- 65 NPs for in-situ JES measurements using Z+jet, γ+jet, and multijet events.

- 3 NPs for pseudorapidity calibration.

- 1 NP for the behavior of high-p_T jets in propagation of single hadron to jet.

- 4 NPs for pileup.

- 1 NP for b-jet response.

- 1 NP for lighter-flavor-jet response.

- 1 NP for lighter-flavor-jet composition.

- 1 NP for punch-through of jet.

For *Diagonal*, the 12 NPs described from the second to the last items are directly used, but the 65 NPs in the first item are enveloped and formed into 7 NPs (5 dominant eigenvectors and 2 residual terms). Furthermore, for *Resolved* and *Boosted*, these 77 NPs are combined into 4 NPs as discussed in [123].

For JER, there are 9 NPs mainly arising from extrapolation from Run-1 JER measurements to estimate Run-2 JER [90]:

- 1 enveloped NP from in-situ JER measurements using di-jet and multijet events in Run-1.

- 7 NPs from Run-1 and Run-2 cross calibrations.

- 1 NP from Run-1 calibration of forward region.

For *Diagonal*, all the 9 NPs are directly used. For *Resolved* and *Boosted*, the 9 NPs are combined into 1 NP.

For calibrations of the b-tagging efficiency, there are 25 NPs enveloping efficiency measurements at each jet p_T bin as derived in [121, 122]:

- 5 NPs for efficiency for b-jet.

- 1 NP for extrapolated efficiency for high-p_T b-jet.

- 4 NPs for efficiency for c-jet.

- 1 NP for extrapolated efficiency for high-p_T c-jet.

- 14 NPs for efficiency for lighter-flavor-jet.

For *Diagonal*, all the 25 NPs are directly used. For *Resolved* and *Boosted*, 1 enveloped NP combining the 5 NPs for b-jet, 1 enveloped NP combining the 4 NPs for c-jet, and 1 enveloped NP combining the 14 NPs for lighter-flavor-jet are used, and the high-p_T b/c-jet NPs are directly used.

For E_T^miss soft term, there are 3 NPs:

- 1 NP for perpendicular resolution

- 1 NP for parallel resolution

- 1 NP for energy scale

For all the strategies, they are directly used. These experimental uncertainties for the dominant backgrounds, $t\bar{t}$ (*Resolved*), $t\bar{t} + Z$ (*Boosted*), and $t\bar{t}$ ($1\text{L}1\tau_h$) (*Diagonal*) events, are summarized in Table 8.1.

Other sources of experimental uncertainty are the modeling of lepton-related sources (efficiencies of reconstruction, identification, and isolation), photon identification, hadronic-tau-related sources (energy scale and efficiency of identification), and the uncertainty in the integrated luminosity. However, their impacts on the final results are found negligibly small. For *Diagonal*, they are still included while are not consider for *Resolved* and *Boosted*.

Table 8.1: η-functions with respect to JES, JER, b-tagging, and E_T^{miss} soft term uncertainties at $\alpha = \pm 1$ for dominant backgrounds, $t\bar{t}$ in *Resolved* SR, $t\bar{t} + Z$ in *Boosted* SR, and $t\bar{t}$ (1L1τ_h) event in *Diagonal* MET3_3 bin. The values are rounded off to three decimal places.

source	*Resolved* SR $t\bar{t}$ $\eta'(\alpha = \pm 1) - 1[\%]$	*Boosted* SR $t\bar{t} + Z$ $\eta'(\alpha = \pm 1) - 1[\%]$	*Diagonal* MET3_3 bin $t\bar{t}$ (1L1τ_h) $\eta'(\alpha = \pm 1) - 1[\%]$
JES			
Enveloped NP 1	-	-	$-1.40 \ / + 0.99$
Enveloped NP 2	-	-	$+2.25 \ / - 2.91$
Enveloped NP 3	-	-	$-0.49 \ / + 0.29$
Enveloped NP 4	-	-	$-0.79 \ / + 0.47$
Enveloped NP 5	-	-	$-0.02 \ / + 0.05$
Enveloped NP 6	-	-	$-0.04 \ / - 0.15$
Pseudorapidity Calibration 1	-	-	$-0.24 \ / + 0.29$
Pseudorapidity Calibration 2	-	-	$-0.18 \ / - 0.35$
Pseudorapidity Calibration 3	-	-	$-0.26 \ / + 0.01$
High-p_T Jet	-	-	$+0.00 \ / + 0.00$
Pileup 1	-	-	$-0.77 \ / + 0.48$
Pileup 2	-	-	$-0.29 \ / + 0.32$
Pileup 3	-	-	$+0.18 \ / + 0.05$
Pileup 4	-	-	$+0.16 \ / - 0.62$
B-Jet Response	-	-	$+0.00 \ / + 0.00$
Lighter-Flavor-Jet Response	-	-	$+0.37 \ / - 0.76$
Lighter-Flavor-Jet Composition	-	-	$-1.50 \ / + 1.48$
Punch Through	-	-	$+0.03 \ / - 0.09$
Strongly Enveloped NP 1	$+1.90 \ / + 4.04$	$+1.66 \ / - 0.75$	-
Strongly Enveloped NP 2	$-3.37 \ / + 3.43$	$+0.69 \ / + 1.90$	-
Strongly Enveloped NP 3	$-0.47 \ / + 2.74$	$+0.48 \ / + 1.41$	-
JER			
Enveloped NP	-	-	$+4.02 \ / - 0.39$
Cross Calibration 1	-	-	$-0.78 \ / - 0.44$
Cross Calibration 2	-	-	$+1.20 \ / + 0.47$
Cross Calibration 3	-	-	$-0.32 \ / + 0.44$
Cross Calibration 4	-	-	$-0.08 \ / + 0.15$
Cross Calibration 5	-	-	$+0.13 \ / - 0.64$
Cross Calibration 6	-	-	$+0.16 \ / + 0.17$
Cross Calibration 7	-	-	$-0.28 \ / + 0.74$
Forward Region	-	-	$+1.05 \ / - 0.34$
Strongly Enveloped NP	$+4.99 \ / - 5.27$	$+3.34 \ / - 3.50$	-
B-Tag			
B-Jet 1	-	-	$-0.34 \ / + 0.32$
B-Jet 2	-	-	$-0.14 \ / + 0.14$
B-Jet 3	-	-	$-0.10 \ / + 0.10$
B-Jet 4	-	-	$-0.08 \ / + 0.08$
B-Jet 5	-	-	$-0.00 \ / + 0.01$
Enveloped B-Jet	$+0.43 \ / - 0.03$	$+1.57 \ / - 1.64$	-

table continued on next page

source	Resolved SR	Boosted SR	Diagonal MET3_3 bin
	$t\bar{t}$	$t\bar{t} + Z$	$t\bar{t}$ (1L1τ_h)
	$\eta'(\alpha = \pm 1) - 1[\%]$	$\eta'(\alpha = \pm 1) - 1[\%]$	$\eta'(\alpha = \pm 1) - 1[\%]$
High-p_T B-Jet	+1.33 / − 0.71	+0.36 / − 0.24	+0.17 / − 0.17
C-Jet 1	-	-	−0.02 / + 0.01
C-Jet 2	-	-	+0.01 / − 0.01
C-Jet 3	-	-	+0.01 / − 0.01
C-Jet 4	-	-	−0.00 / + 0.00
Enveloped C-Jet	+0.18 / + 0.50	+0.26 / − 0.10	-
High-p_T C-Jet	+0.00 / + 0.68	+0.00 / + 0.17	+0.06 / − 0.06
Lighter-Flavor-Jet 1	-	-	+0.23 / − 0.24
Lighter-Flavor-Jet 2	-	-	−0.00 / + 0.00
Lighter-Flavor-Jet 3	-	-	−0.02 / + 0.02
Lighter-Flavor-Jet 4	-	-	−0.01 / + 0.01
Lighter-Flavor-Jet 5	-	-	−0.01 / + 0.01
Lighter-Flavor-Jet 6	-	-	+0.00 / − 0.00
Lighter-Flavor-Jet 7	-	-	+0.01 / − 0.00
Lighter-Flavor-Jet 8	-	-	+0.00 / − 0.00
Lighter-Flavor-Jet 9	-	-	−0.00 / + 0.00
Lighter-Flavor-Jet 10	-	-	+0.00 / − 0.00
Lighter-Flavor-Jet 11	-	-	+0.00 / − 0.00
Lighter-Flavor-Jet 12	-	-	+0.00 / − 0.00
Lighter-Flavor-Jet 13	-	-	+0.00 / + 0.00
Lighter-Flavor-Jet 14	-	-	+0.00 / + 0.00
Enveloped Lighter-Flavor-Jet	+1.84 / − 1.25	+0.10 / + 0.06	-
E_T^miss soft term			
Parallel Resolution	+0.49 / − 0.48	+0.37 / − 0.37	−0.49 / + 0.49
Perpendicular Resolution	+0.64 / − 0.63	+0.12 / − 0.12	−0.47 / + 0.46
Energy Scale	+0.25 / + 0.37	+0.32 / + 0.03	−0.48 / − 0.13

8.2 $t\bar{t}$

The uncertainty of radiation modeling is estimated by varying factorization scale, renormalization scale and resummation damping factor h_{damp} in Powheg-Box + Pythia6[3]. This uncertainty includes uncertainties due to missing higher order terms in NLO MC samples. The uncertainty of hadronization modeling is estimated by a comparison of the nominal configuration Powheg-Box + Pythia6 and Powheg-Box + Herwig++ sample. For Diagonal, this uncertainty is not taken into account because this effect is relatively smaller than others. The uncertainty of parton shower tuning and ME+PS matching is studied by comparing Powheg-Box + Pythia6 to Powheg-Box + Pythia8 samples. Table 8.2 shows η-functions of $t\bar{t}$ at $\alpha = \pm 1$ for *Resolved* and *Boosted* SRs and *Diagonal* MET3_3 bin.

source	*Resolved* SR	*Boosted* SR	*Diagonal* MET3_3 bin	
	$t\bar{t}$	$t\bar{t}$	$t\bar{t}$ (1L1τ_h)	$t\bar{t}$ (1L)
	$\eta'(\alpha=\pm1)-1[\%]$	$\eta'(\alpha=\pm1)-1[\%]$	$\eta'(\alpha=\pm1)-1[\%]$	$\eta'(\alpha=\pm1)-1[\%]$
Radiation	± 9.1	± 10.2	$+19.2\ /-4.5$	$+13.5\ /+4.5$
Hadronization	± 7.7	± 7.4	-	-
Parton Shower	-	-	$+1.3\ /-1.6$	$+4.4\ /-5.1$

Table 8.2: η-functions of $t\bar{t}$ at $\alpha = \pm 1$ for *Resolved* and *Boosted* SRs and *Diagonal* MET3_3 bin. The values are rounded off to three decimal places.

8.3 Single Top

Systematic uncertainties of radiation and hadronization tuning are estimated in the same way of $t\bar{t}$. Additionally, an uncertainty on interference between Wt and $t\bar{t}$ [124] is estimated by comparing the nominal $t\bar{t}$ and Wt sample with an $WWbb$ sample generated via MG5_AMC@NLO. Table 8.3 shows η-functions of single top at $\alpha = \pm 1$ for *Resolved* and *Boosted* SRs and *Diagonal* MET3_3 bin.

source	*Resolved* SR	*Boosted* SR	*Diagonal* MET3_3 bin
	$\eta'(\alpha=\pm1)-1[\%]$	$\eta'(\alpha=\pm1)-1[\%]$	$\eta(\alpha=\pm1)-1[\%]$
Radiation	± 9.2	± 25.2	± 3.3
Hadronization	± 9.0	± 11.2	-
Interference	± 34.6	± 62.2	± 69.5

Table 8.3: η-functions of single top at $\alpha = \pm 1$ for *Resolved* and *Boosted* SRs and *Diagonal* MET3_3 bin. The values are rounded off to three decimal places.

---

[3] For the low radiation tuning, factorization scale, renormalization scale, and an resummation damping factor h_{damp} are simultaneously varied by a factor of 2, 2, and 1, respectively, and for the high radiation tuning, 0.5, 0.5, and 2, respectively. h_{damp} controls the ME/PS matching in Powheg-Box and effectively regulates the high-p_{T} radiation and is set to m_{top} for the nominal samples. The configurations of the high/low radiation tunings are determined so that differences between data and MC can be explained by radiation tuning as discussed in Ref.[69].

8.4 W+jets

For W+jets, the samples to estimate systematic uncertainties have been generated with SHERPA. By varying renormalization scale, factorization scale, resummation scale and CKKW scale [4] by a factor of 2 and 0.5, respectively, these 4 systematic uncertainties are estimated. These 4 systematic uncertainties are integrated into one enveloped systematic uncertainty for *Resolved* and *Boosted*. Table 8.3 shows η-functions of W+jets at $\alpha = \pm 1$ for *Resolved* and *Boosted* SRs and *Diagonal* MET3_3 bin.

source	*Resolved* SR $\eta'(\alpha = \pm 1) - 1[\%]$	*Boosted* SR $\eta'(\alpha = \pm 1) - 1[\%]$	*Diagonal* MET3_3 bin $\eta(\alpha = \pm 1) - 1[\%]$
CKKW	± 1.4	± 0.8	± 13.4
Factorization	± 3.4	± 0.5	± 13.8
Renormalization	± 3.1	± 0.0	± 36.0
Resummation	± 0.7	± 0.4	± 11.5
Enveloped	± 4.9	± 1.0	-

Table 8.4: η-functions of W+jets at $\alpha = \pm 1$ for *Resolved* and *Boosted* SRs and *Diagonal* MET3_3 bin. The values are rounded off to three decimal places.

The W+jets background is normalized in WCR requiring b-veto in *Resolved* and *Boosted*. The W+heavy-flavor components are coherently scaled by the whole W+jets process modeled by MC. Therefore, an uncertainty on fraction of yields of W+light, $W + c(c)$ and $W + b(b)$ is additionally imposed for *Resolved* and *Boosted* because the b-veto region is used in these strategies. This uncertainty has been set to 30% on *Resolved* and *Boosted* SRs and is used independently of the enveloped uncertainty [126, 127].

8.5 Diboson

Diboson samples are generated via SHERPA, and uncertainties from renormalization, factorization and resummation scale are evaluated in the same way of W/Z+jets. Diboson samples are not normalized in a control region, but use the predicted cross section. Hence the cross section uncertainty 6% is considered, which has been estimated from a Run-1 measurement of cross-section [128]. For *Resolved* and *Boosted*, these uncertainties are integrated into one enveloped systematic uncertainty. Table 8.5 shows diboson theoretical uncertainties for all signal regions.

8.6 $t\bar{t} + V$

The method to estimate $t\bar{t} + Z$ background described here comes from a dedicated study [26]. Since the $t\bar{t}+Z$ background is normalized using $t\bar{t}+\gamma$ at the TZCR, the uncertainties are evaluated by simultaneously varying parameters of $t\bar{t}+\gamma$ and $t\bar{t}+Z$ samples. An uncertainty due to radiation tuning is estimated by simultaneously varying the renormalization and factorization scales of

---

[4] CKKW is a scheme of merging between matrix-element and parton-shower [125] used in SHERPA generator, and the parameter defines which phase-space regions are populated by matrix elements and which ones by parton showers

source	Resolved SR $\eta(\alpha = \pm 1) - 1[\%]$	Boosted SR $\eta(\alpha = \pm 1) - 1[\%]$	Diagonal MET3_3 bin $\eta(\alpha = \pm 1) - 1[\%]$
Factorization	±3.8	±6.7	±10.7
Renormalization	±19.1	±19.0	±26.8
Resummation	±9.3	±1.1	±7.3
Cross-section	±6.0	±6.0	±6.0
Enveloped	±22.4	±23.5	-

Table 8.5: η-functions of diboson at $\alpha = \pm 1$ for Resolved and Boosted SRs and Diagonal MET3_3 bin. The values are rounded off to three decimal places.

$t\bar{t} + Z$ and $t\bar{t} + \gamma$ events generated at LO by a factor of 2 and 0.5. The impact of the scale choices is different between $t\bar{t} + Z$ and $t\bar{t} + \gamma$ for high-p_{T} bosons, leading to a 10% uncertainty. Since the nominal samples are generated at LO, an uncertainty due to NLO corrections is estimated from a study of the kinematic dependency of the ratio between $t\bar{t} + Z$ and $t\bar{t} + \gamma$ cross-section factors. The kinematic dependency of the ratio is studied by calculating a cross-section factor for the $t\bar{t} + Z$ and $t\bar{t} + \gamma$ processes using MG5_AMC@NLO and SHERPA + OpenLoops as a function of the boson p_{T}, comparing the nominal generator setup with a series of variations, resulting in a 5% uncertainty. Comparing the results using the NNPDF and the CT14 [129] PDF varies ratio of the cross-section factor by less than 2%. An additional uncertainty due to an EW correction is 5%, which is estimated from a difference in two ratios of cross-section factor for $t\bar{t} + \gamma$ and $t\bar{t} + Z$ between MG5_AMC@NLO and SHERPA + OpenLoops when the same scale and PDF set is used.

These uncertainties are integrated into one enveloped uncertainty amount to 12% on Resolved and Boosted SRs ($\eta'(\alpha = \pm 1) - 1 = \pm 0.12$).

For Diagonal, $t\bar{t} + \gamma$ is not used to estimate $t\bar{t} + Z$ background. Therefore the theoretical uncertainty simply stems from $t\bar{t} + Z$ modeling. The uncertainty on radiation and factorization scales is estimated by varying a factor of 2 and 0.5, resulting in $\eta(\alpha = \pm 1) - 1 = \pm 5.80\%$ at Diagonal MET3_3 bin.

8.7   Signal

The signal cross-section uncertainties shown in Figure 3.1 are considered but not via η-functions. The hypothesis test is done three times with fixing cross-section at nominal, $+1\sigma$, and -1σ conditions, respectively. For the three conditions, three CL_s exclusion contours are drawn. For example, $\mathrm{CL}_s = 0.05$ contour with the $+1\sigma$ condition is drawn by interpolating CL_s values at all mass points which are calculated in the $+1\sigma$ condition.

Chapter 9

Results

This chapter presents results of *Resolved*, *Boosted*, and *Diagonal* analyses. For each analysis, the results of background-only fit described in Chapter 6 are shown in detail, and then CLs exclusion limits at 95% confidence level (95% CL) are presented in the $(m_{\tilde{t}_1}, m_{\tilde{\chi}_1^0})$ plane. Contours of 95% CL are derived by interpolating CL_s values evaluated at all the signal points shown in Figure 1.8

Section 9.1 describes *Resolved* and *Boosted* results. Section 9.2 presents *Diagonal* results. Section 9.3 shows CL_s limits combining *Resolved*, *Boosted*, and *Diagonal* results. Finally, Section 9.4 discusses future prospects of this study.

9.1 Results for *Resolved* and *Boosted*

The parameters and correlations after the background-only fit[1] in *Resolved* and *Boosted* are shown in Figure $9.1 - 9.4$. As indicated in Figure 9.1 and 9.3, there are no significant issue in the fitted parameters in *Resolved* and *Boosted*, that is, uncertainties obtained from the fit are almost the same as the input values and background normalization factor μ_{sig} are determined properly from CRs.

One thing to be noted is that the fitted μ_{ttV} is around 1.5. Although there are some correlations between μ_{ttV} and other parameters as shown in Figure 9.2 and 9.4, all the systematic parameters shown in Figure 9.1 and 9.3 are almost at 0, therefore such a large value could not be due to these parameters. Since there is no significant evidence of mis-modeling of the shapes of the various distributions and their deviations from the expectation are within uncertainties, this issue is not significant for the data with 28.0 fb^{-1}. but may be a future problem to be solved in an analysis with higher statistics.

The number of observed events for *Resolved* and *Boosted* are shown in Table 9.1 and 9.2, and the SRs with the VRs are also shown in Figure 9.5. The prediction of number of background events is obtained using the background-only fit configuration. In *Resolved* (*Boosted*) SR, 63 (8) events are observed and the mean of total number of background events predicted by the fit is 51 ± 7 (8 ± 3), and poisson upward/downward fluctuation from the mean is $+8/-7$ ($+4/-3$).

---

[1] As described in Chapter 6, the background-only fit is a fit with a background-only model (μ_{sig} is fixed to 0) and only CRs. The fit results are applied in the plots in Chapter 6 that shows distributions at CRs and VRs for *Resolved* and *Boosted*. As shown in Section 6.3, there is no significant insanity in distributions at VRs after the background-only fit and then it has concluded that the SRs can be unblinded.

Figure 9.6 shows m_T, $E_\mathrm{T}^\mathrm{miss}$, and am_T2 distributions at *Resolved* and *Boosted* SRs after the background-only fit.

To evaluate how plausible the prediction of the background-only fit is, CL_b and its z-value are calculated by a model independent discovery hypothesis test [117]. Since the choice of the (modified) PLR (Equation 7.13) as test statistic in the analysis requires the best fitted value of μ_sig ($\hat{\mu}_\mathrm{sig}$), a dummy signal model is used, which is defined to expect just one signal event at SR for $\mu_\mathrm{sig} = 1$. Since the dummy signal model is incorporated into the likelihood without any systematic uncertainties on the dummy signal model, the μ_sig is treated as a measure of a difference between data and the SM-only model at SR. From this context, it is called model-independent test. The model-independent test is only valid for CL_b calculation because of the dummy signal model. This cannot be applied to the shape fit of *Diagonal* (or a fit with more than two SRs) because it is impossible to define model-independent shape of a dummy signal model. The observed CL_b and its z-value obtained by the model independent discovery hypothesis test are 0.098 and 1.29 σ for *Resolved*, and 0.487 and 0.032 σ for *Boosted*. This concludes that there is no significant deviation from the SM-only model in *Resolved* and *Boosted* analyses.

To evaluate how much the signal models are excluded, CL_s exclusion limits at 95% CL are derived each from the *Resolved* and *Boosted* analyses, shown in Figure 9.7 and 9.9. In the exclusion test of *Resolved*, $\hat{\mu}_\mathrm{sig}$ for the benchmark mass point, $(m_{\tilde{t}_1}, m_{\tilde{\chi}_1^0}) = (600, 300)$ GeV, is 0.37 ± 0.28, and the CL_s value and the z-value are 0.0063 and 2.50 σ (excluded at 99.37% CL). In the exclusion test of *Boosted*, $\hat{\mu}_\mathrm{sig}$ for the benchmark mass point, $(m_{\tilde{t}_1}, m_{\tilde{\chi}_1^0}) = (1000, 1)$ GeV, is -0.01 ± 0.45, and the CL_s value and the z-value are 0.0619 and 1.54 σ (excluded at 93.81% CL). The mass points used to draw the contours are shown with the observed CL_s values in Figure 9.8 and 9.10. The mass points with stop mass lower than 400 GeV are not used for *Resolved* and *Boosted* but for *Diagonal*, because *Diagonal* analysis explicitly provides the better results around the region. For *Resolved* and *Boosted*, the observed CL_s limit is almost within the $\pm 1\sigma$ band of the expected CL_s. The *Resolved* result excludes up to $(m_{\tilde{t}_1}, m_{\tilde{\chi}_1^0}) = (700, 350)$ GeV, which is the excluded $\tilde{t}_1 \to t\tilde{\chi}_1^0$ model with the highest $\tilde{\chi}_1^0$ mass in *Resolved* region. The *Boosted* result excludes the $\tilde{t}_1 \to t\tilde{\chi}_1^0$ model with the $m_{\tilde{t}_1} \lesssim 980$ GeV for $m_{\tilde{\chi}_1^0} \lesssim 300$ GeV and $(m_{\tilde{t}_1}, m_{\tilde{\chi}_1^0}) = (900, 350)$ GeV,

Resolved channel	TCR	WCR	STCR	TZCR	TVR	WVR	SR
Observed events	1861	4664	545	363	345	523	63
Fitted bkg events	1860.99 ± 43.34	4663.72 ± 68.91	545.09 ± 23.30	362.94 ± 19.08	317.56 ± 29.69	546.52 ± 72.12	51.01 ± 5.38
Fitted $t\bar{t}$ events	1512.55 ± 54.36	915.39 ± 170.48	251.07 ± 23.47	12.55 ± 2.03	266.02 ± 28.35	128.43 ± 27.62	17.93 ± 2.79
Fitted W+jets events	174.39 ± 30.94	3327.66 ± 237.60	50.92 ± 11.51	0.17 ± 0.06	20.37 ± 4.98	349.10 ± 60.50	5.12 ± 2.07
Fitted single top events	129.10 ± 31.03	119.32 ± 46.30	220.41 ± 43.57	5.98 ± 1.85	22.92 ± 5.75	17.29 ± 6.93	6.21 ± 2.78
Fitted $t\bar{t} + Z$ events	25.94 ± 2.00	13.57 ± 2.73	16.73 ± 1.47	3.61 ± 0.31	6.14 ± 0.74	2.58 ± 0.68	17.94 ± 2.79
Fitted diboson events	17.49 ± 3.83	262.64 ± 55.44	5.30 ± 1.30	0.27 ± 0.06	2.00 ± 0.44	45.52 ± 9.84	2.55 ± 0.83
Fitted Z+jets events	1.52 ± 1.38	25.14 ± 22.39	0.65 ± 0.58	0.32 ± 0.29	0.11 ± 0.10	3.61 ± 3.30	1.25 ± 1.14
Fitted $t\bar{t} + \gamma$ events	0.00 ± 0.00	0.00 ± 0.00	0.00 ± 0.00	340.03 ± 19.23	0.00 ± 0.00	0.00 ± 0.00	0.00 ± 0.00
MC exp. SM events	1855.61 ± 72.04	5818.76 ± 270.24	548.06 ± 50.66	244.45 ± 13.50	312.14 ± 31.52	665.82 ± 93.62	46.01 ± 5.33
MC exp. $t\bar{t}$ events	1452.96 ± 51.28	879.58 ± 154.86	241.51 ± 26.83	12.06 ± 1.81	255.31 ± 28.03	123.28 ± 25.77	17.24 ± 2.65
MC exp. W+jets events	237.65 ± 25.78	4523.42 ± 138.70	69.48 ± 10.63	0.24 ± 0.07	27.75 ± 5.48	474.42 ± 72.34	6.98 ± 2.64
MC exp. single top events	128.96 ± 4.17	119.42 ± 20.81	220.14 ± 20.36	6.01 ± 1.62	22.94 ± 2.11	17.33 ± 3.58	6.20 ± 2.32
MC exp. $t\bar{t} + Z$ events	17.02 ± 0.54	8.91 ± 1.55	10.98 ± 0.79	2.37 ± 0.21	4.03 ± 0.35	1.70 ± 0.40	11.76 ± 1.60
MC exp. diboson events	17.52 ± 3.86	262.41 ± 55.79	5.30 ± 1.31	0.27 ± 0.06	2.00 ± 0.45	45.52 ± 9.90	2.56 ± 0.84
MC exp. Z+jets events	1.51 ± 1.39	25.02 ± 22.53	0.65 ± 0.59	0.31 ± 0.29	0.11 ± 0.10	3.57 ± 3.29	1.25 ± 1.15
MC exp. $t\bar{t} + \gamma$ events	0.00 ± 0.00	0.00 ± 0.00	0.00 ± 0.00	223.18 ± 11.41	0.00 ± 0.00	0.00 ± 0.00	0.00 ± 0.00

Table 9.1: Number of observed events and the mean of background yields predicted before and after fit in *Resolved* for an integrated luminosity of 28.0 fb^{-1}. The mean values are obtained from the associated control regions (TCR, WCR, STCR, TZCR) using the background-only fit. Uncertainties on the mean values are shown and calculated by linearly propagating uncertainties of all the model parameters (for fitted events, correlations calculated by the fit are also considered). Uncertainties on the fitted yields are symmetric by construction, where the negative error is truncated when reaching to zero event yield.

Boosted channel	TCR	WCR	STCR	TZCR	TVR	WVR	SR
Observed events	309	902	174	369	39	68	8
Fitted bkg events	309.05 ± 17.58	902.17 ± 30.12	174.04 ± 13.13	369.21 ± 19.24	30.60 ± 6.21	73.79 ± 18.33	8.11 ± 1.52
Fitted $t\bar{t}$ events	229.86 ± 26.35	73.38 ± 23.40	54.57 ± 10.22	11.22 ± 2.09	24.11 ± 5.66	6.44 ± 2.22	1.10 ± 0.44
Fitted W+jets events	32.12 ± 11.16	727.66 ± 50.20	19.58 ± 7.53	0.19 ± 0.06	2.65 ± 0.99	56.76 ± 18.35	0.78 ± 0.39
Fitted single top events	37.07 ± 16.57	26.45 ± 20.70	91.73 ± 20.06	8.09 ± 3.04	2.32 ± 1.94	2.85 ± 2.28	1.20 ± 0.89
Fitted $t\bar{t} + Z$ events	5.71 ± 0.81	2.09 ± 0.49	5.88 ± 0.93	3.44 ± 0.31	1.06 ± 0.22	0.28 ± 0.09	3.67 ± 0.69
Fitted diboson events	4.17 ± 1.33	69.44 ± 20.72	2.08 ± 0.72	0.27 ± 0.08	0.45 ± 0.23	6.96 ± 2.12	1.28 ± 0.56
Fitted Z+jets events	0.13 ± 0.12	3.15 ± 2.81	0.19 ± 0.18	0.31 ± 0.28	0.01 ± 0.00	0.51 ± 0.46	0.06 ± 0.06
Fitted $t\bar{t} + \gamma$ events	0.00 ± 0.00	0.00 ± 0.00	0.00 ± 0.00	345.69 ± 19.48	0.00 ± 0.00	0.00 ± 0.00	0.00 ± 0.00
MC exp. SM events	328.65 ± 20.76	1129.83 ± 58.04	161.76 ± 19.38	253.47 ± 13.58	32.58 ± 5.76	91.17 ± 24.03	6.95 ± 1.42
MC exp. $t\bar{t}$ events	249.96 ± 9.58	79.79 ± 22.56	59.40 ± 8.06	12.22 ± 1.65	26.17 ± 4.86	6.99 ± 2.12	1.20 ± 0.42
MC exp. W+jets events	42.22 ± 13.61	955.88 ± 37.74	25.77 ± 9.08	0.25 ± 0.07	3.48 ± 1.19	74.37 ± 23.23	1.02 ± 0.47
MC exp. single top events	28.32 ± 9.13	20.11 ± 13.21	70.37 ± 8.10	6.25 ± 1.69	1.76 ± 1.46	2.15 ± 1.52	0.91 ± 0.61
MC exp. $t\bar{t} + Z$ events	3.83 ± 0.51	1.40 ± 0.30	3.95 ± 0.60	2.31 ± 0.22	0.71 ± 0.14	0.19 ± 0.06	2.46 ± 0.42
MC exp. diboson events	4.19 ± 1.34	69.50 ± 20.87	2.08 ± 0.72	0.27 ± 0.08	0.45 ± 0.23	6.97 ± 2.13	1.29 ± 0.56
MC exp. Z+jets events	0.13 ± 0.12	3.14 ± 2.83	0.19 ± 0.18	0.31 ± 0.28	0.01 ± 0.00	0.50 ± 0.46	0.06 ± 0.06
MC exp. $t\bar{t} + \gamma$ events	0.00 ± 0.00	0.00 ± 0.00	0.00 ± 0.00	231.86 ± 11.45	0.00 ± 0.00	0.00 ± 0.00	0.00 ± 0.00

Table 9.2: Number of observed events and the mean of background yields predicted before and after fit in *Boosted* for an integrated luminosity of 28.0 fb^{-1}. The mean values are obtained from the associated control regions (TCR, WCR, STCR, TZCR) using the background-only fit. Uncertainties on the mean values are shown and calculated by linearly propagating uncertainties of all the model parameters (for fitted events, correlations calculated by the fit are also considered). Uncertainties on the fitted yields are symmetric by construction, where the negative error is truncated when reaching to zero event yield.
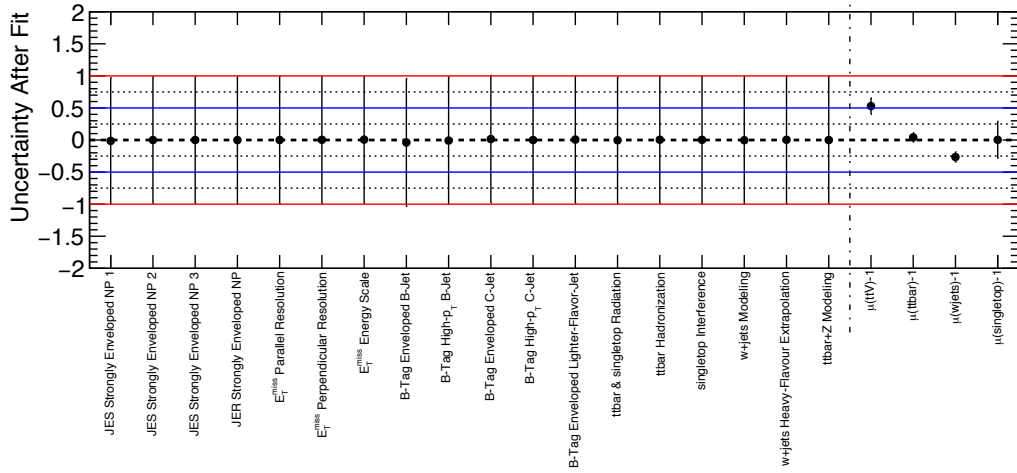
Figure 9.1: Model parameters and their uncertainties after the background-only fit for *Resolved*. The vertical dashed-dotted line divides into two categories: standardized systematic parameters (left) and normalization scale factors (right). The naming rule of systematic parameters follow Table 8.1−8.5. For the detailed explanation on the fit configuration, see Section 7.2.
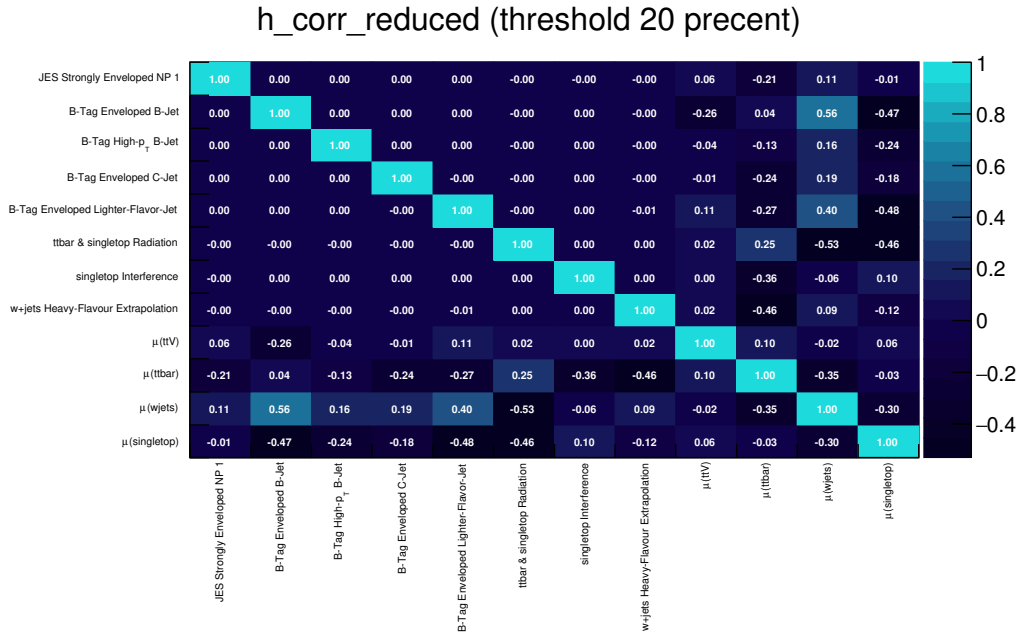
Figure 9.2: Correlations among model parameters after the background-only fit for *Resolved*. Only parameters with at least one correlation of more than 0.2 are shown. The naming rule of systematic parameters follow Table 8.1−8.5. For the detailed explanation on the fit configuration, see Section 7.2.
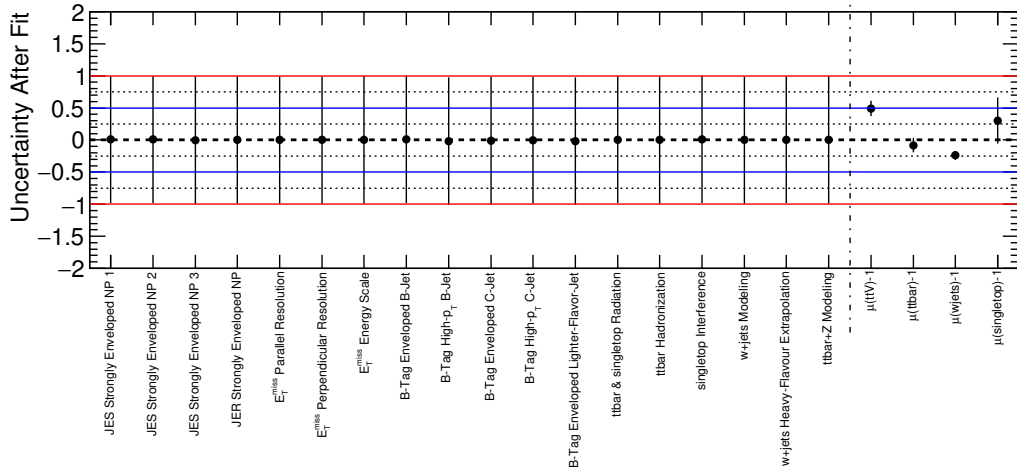
Figure 9.3: Model parameters and their uncertainties after the background-only fit for *Boosted*. The vertical dashed-dotted line divides into two categories: standardized systematic parameters (left) and normalization scale factors (right). The naming rule of systematic parameters follow Table 8.1−8.5. For the detailed explanation on the fit configuration, see Section 7.2.
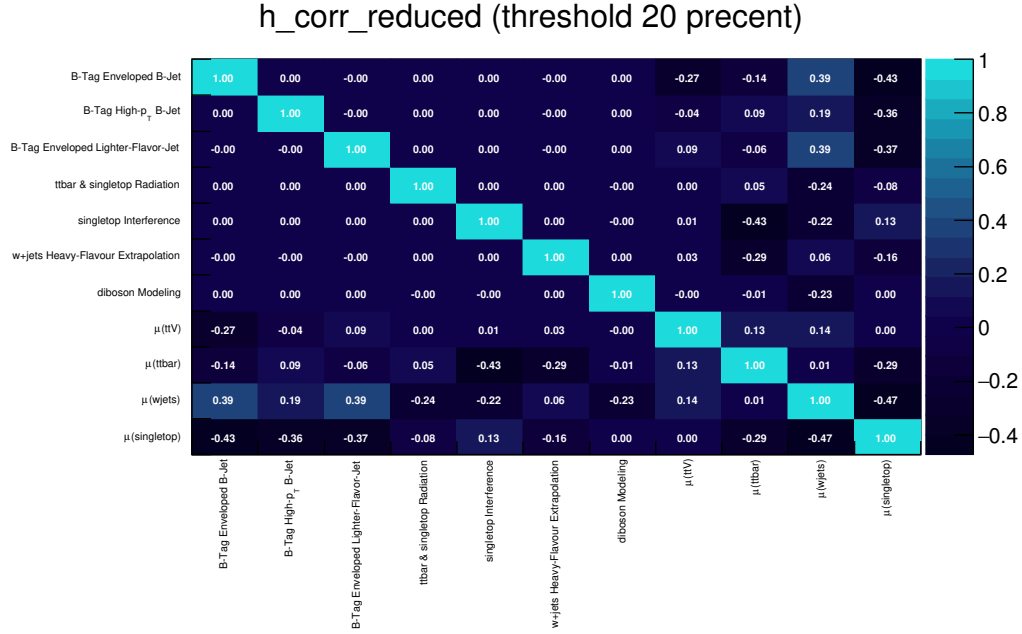
Figure 9.4: Correlations among model parameters after after the background-only fit for *Boosted*. Only parameters with at least one correlation of more than 0.2 are shown. The naming rule of systematic parameters follow Table 8.1−8.5. For the detailed explanation on the fit configuration, see Section 7.2.
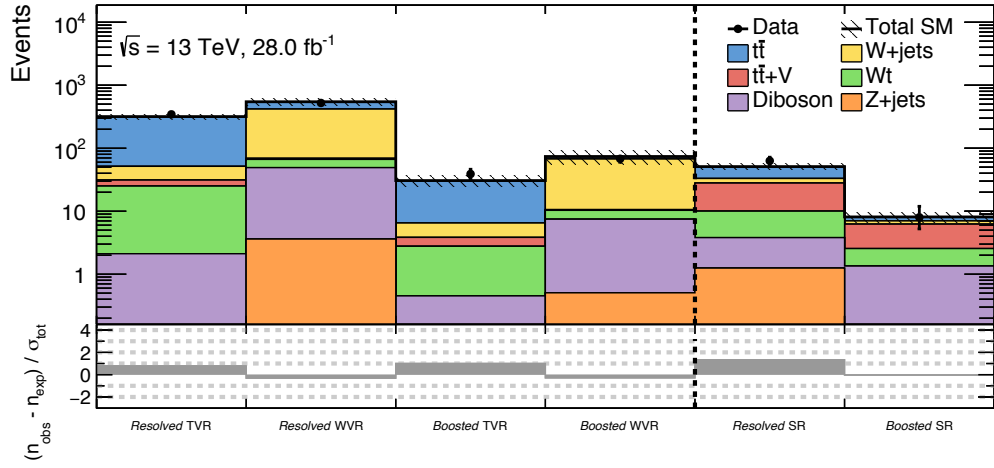
Figure 9.5: Comparison of the expected backgrounds (n_{exp}) with the observed data (n_{obs}) in the SRs and VRs. The n_{exp} is obtained by the background-only fit. The bottom plot shows significance of the difference between expected backgrounds and data. Here the significance is defined by $(n_{\text{obs}} - n_{\text{exp}})/\sigma_{\text{tot}}$, where σ_{tot} is sum of the model uncertainty shown in Table 9.1 and Table 9.2 and the poisson fluctuation from the mean number of events in quadrature.
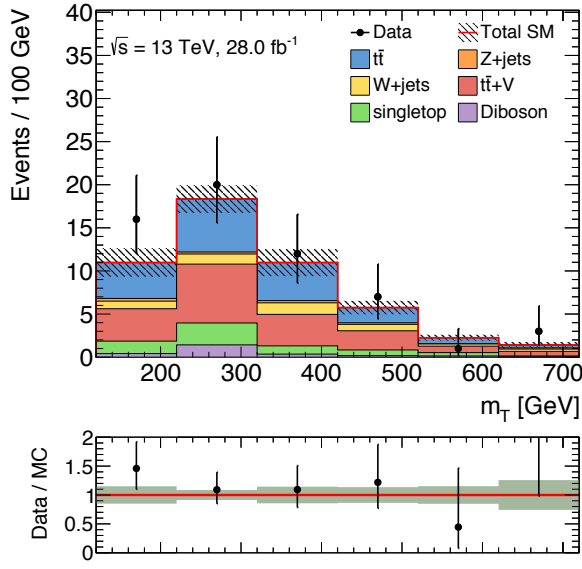
(a) m_T at SR of *Resolved*
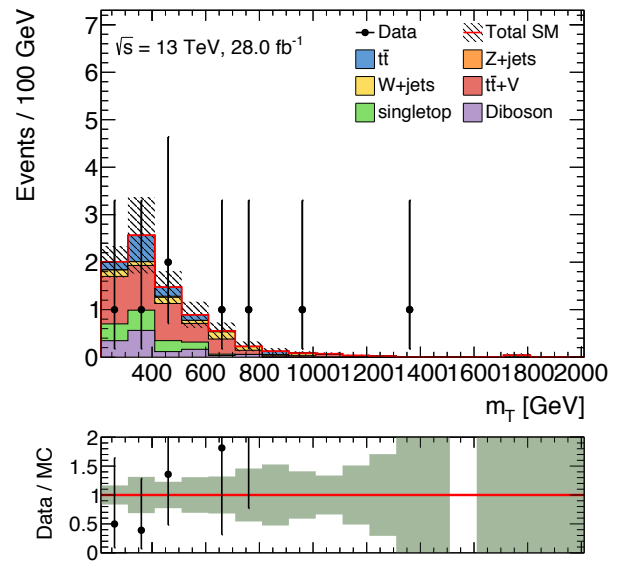
(b) m_T at SR of *Boosted*
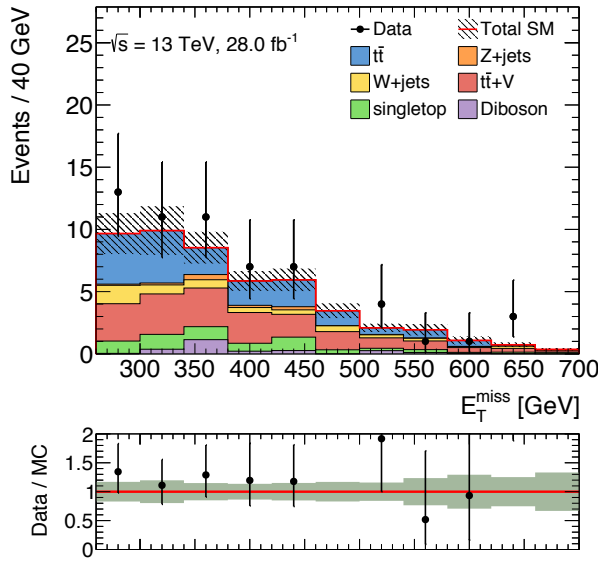
(c) $E_\mathrm{T}^\mathrm{miss}$ at SR of *Resolved*
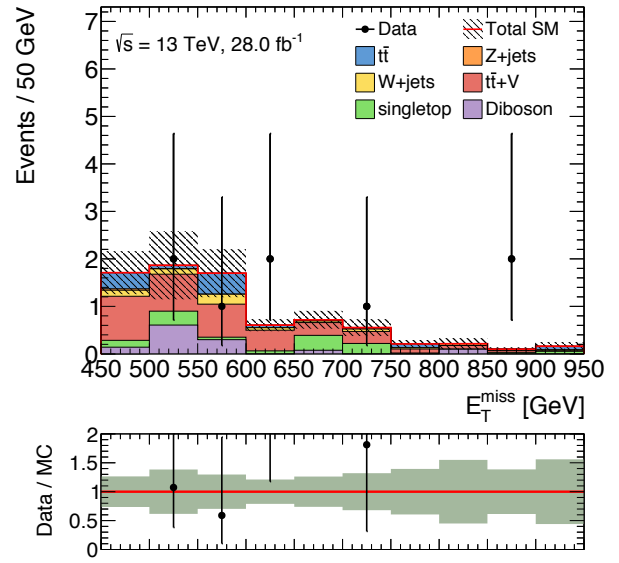
(d) $E_\mathrm{T}^\mathrm{miss}$ at SR of *Boosted*
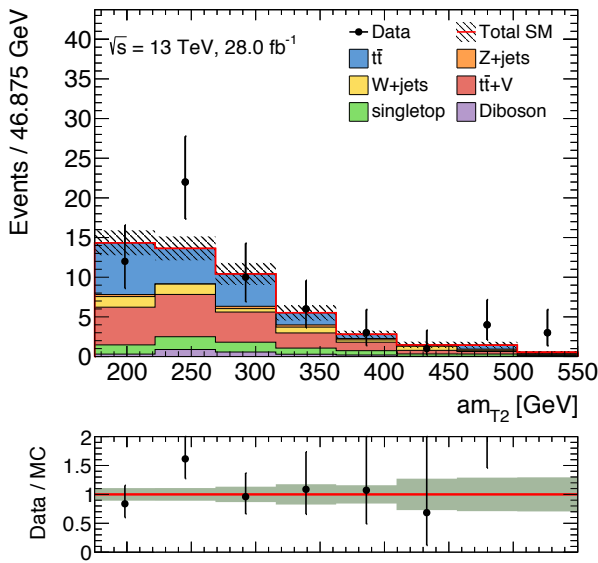
(e) am_T2 at SR of *Resolved*
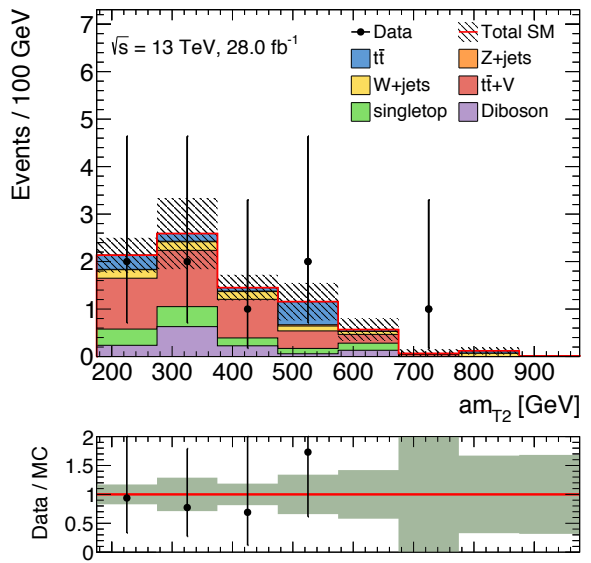
(f) am_T2 at SR of *Boosted*

Figure 9.6: m_T, $E_\mathrm{T}^\mathrm{miss}$, and am_T2 distributions at *Resolved* (left) and *Boosted* (right) SRs. The background-only fit result is propagated to the background models at SR. The uncertainty band includes statistical and systematic error.
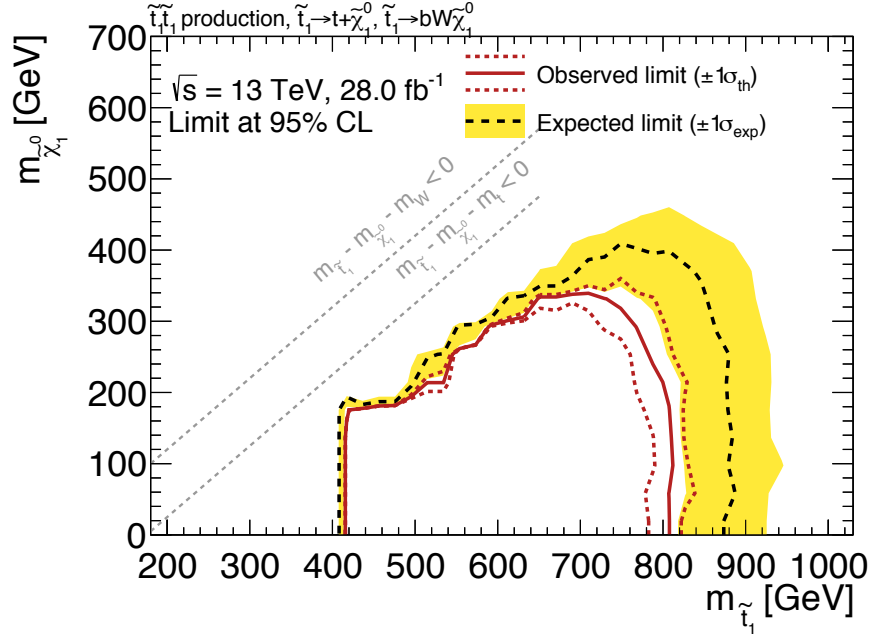
Figure 9.7: *Resolved*: Expected (black dashed) and observed (red solid) CL_s exclusion limits at 95% CL in the plane of $m_{\tilde{t}_1}$ versus $m_{\tilde{\chi}_1^0}$. The dashed red line (σ_{th}) indicates the results with $\pm 1\sigma$ variation of the signal cross section uncertainty (Figure 3.1).
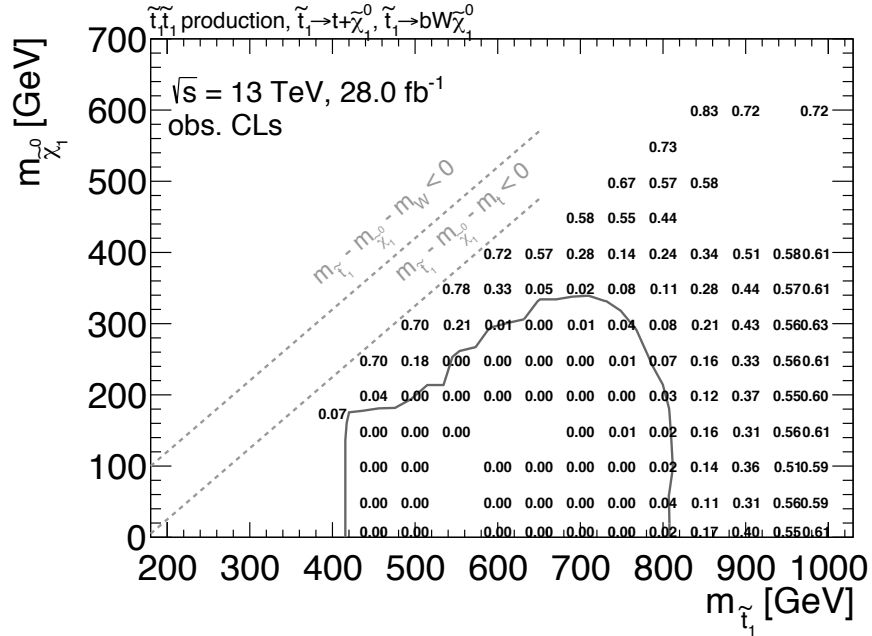
Figure 9.8: *Resolved*: Mass points used to draw the contours in Figure 9.7. Observed CL_s values without variation of the signal cross section uncertainty are shown on the mass points.
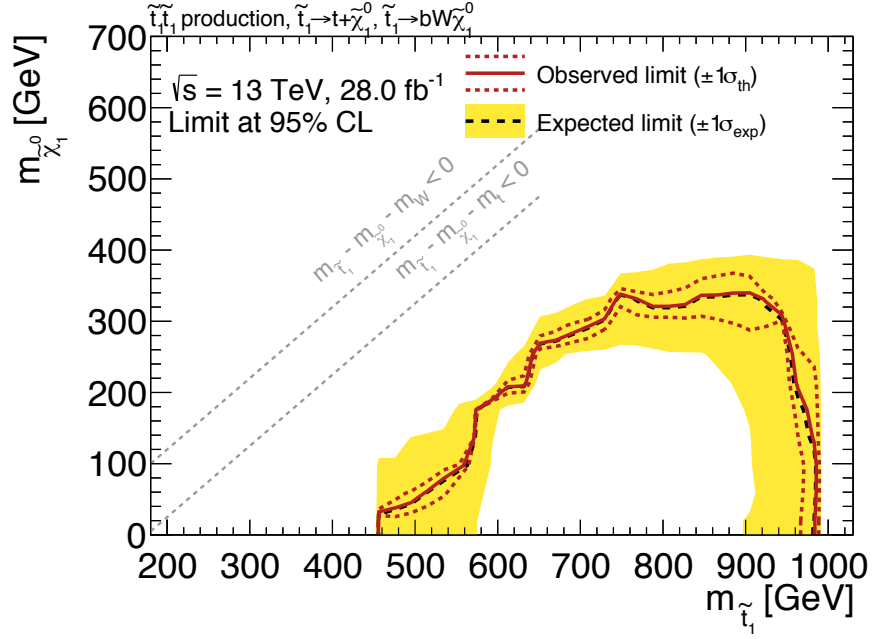
Figure 9.9: *Boosted*: Expected (black dashed) and observed (red solid) CL_s exclusion limits at 95% CL in the plane of $m_{\tilde{t}_1}$ versus $m_{\tilde{\chi}_1^0}$. The dashed red line (σ_{th}) indicates the results with $\pm 1\sigma$ variation of the signal cross section uncertainty (Figure 3.1).
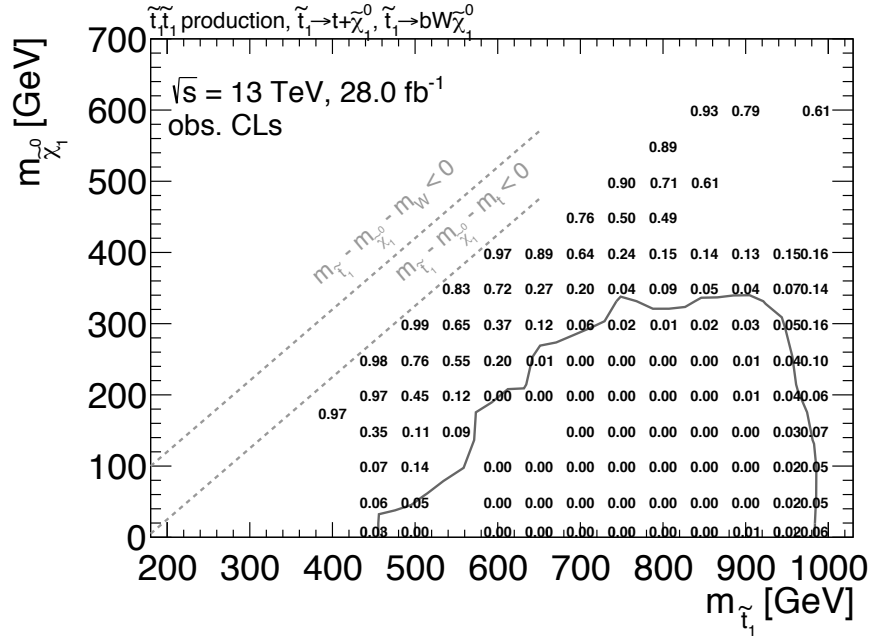
Figure 9.10: *Boosted*: Mass points used to draw the contours in Figure 9.9. Observed CL_s values without variation of the signal cross section uncertainty are shown on the mass points.

9.2 Results from *Diagonal*

Before doing the 2-D shape fit shown in Figure 6.24, a test fit has been done to validate the shape fit, which is described in Appendix A. The result has concluded that there is no significant issue in the fit configuration and modeling, and then the 'unblind' fit was performed.

Figure 9.11 shows the observed m_T shape at each E_T^{miss} slice and TAUCR with the predicted shapes after the background-only fit. The observed shape is within the uncertainties on the prediction of the background-only fit. The other variables not used in the fit are also shown in Figure 9.12−9.23 under the same condition. There is no remarkable issue in the distributions.

The parameters and correlations after the unblind fit are shown in Figure 9.24 and 9.25. There are correlations of 20−50% for $\mu_{ttbarTau}$ with JER, JES, E_T^{miss} soft term, and $t\bar{t}$ and single top theory uncertainties. Since they are relatively large systematic uncertainties as indicated in Table 8.1−8.5 and *Diagonal* analysis exploits the 2-D shape fit with high statistics, those correlations could be stronger than *Resolved* and *Boosted*. However, since all the systematic parameters in *Diagonal* remain within 0.5 σ line and there is no large excess in the observed shape, the correlation effect on $\mu_{ttbarTau}$ is not a significant issue for the fit.

To evaluate how plausible the prediction of the background-only fit is, CL_b and its z-value are calculated by discovery hypothesis test with the benchmark signal model $((m_{\tilde{t}_1}, m_{\tilde{\chi}_1^0}) = (400, 200)$ GeV). The observed CL_b and its z-value obtained by the model independent discovery hypothesis test are 0.221 and 0.770 σ. The other mass points are also tested, but all the z-values are within 1 σ. This concludes that there is no significant deviation from the SM-only model in *Diagonal* analysis.

To evaluate how much the signal models are excluded, CL_s exclusion limits at 95% CL are derived from the *Diagonal* analysis, shown in Figure 9.26. The mass points used to draw the contours are shown with the observed CL_s values in Figure 9.27. For *Diagonal*, the observed CL_s limit is within the $\pm 1\sigma$ band of the expected CL_s. The *Diagonal* result excludes the $\tilde{t}_1 \rightarrow t\tilde{\chi}_1^0$ model with $m_{\tilde{\chi}_1^0} \lesssim 240$ GeV and $\tilde{t}_1 \rightarrow bW\tilde{\chi}_1^0$ model with $m_{\tilde{\chi}_1^0} \lesssim 260$ GeV near the *Diagonal* line.
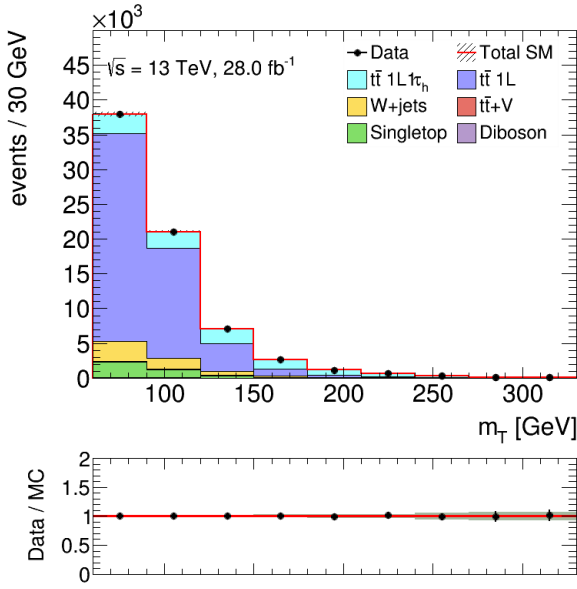
(a) m_{T} at $E_{\mathrm{T}}^{\mathrm{miss}} = [100,\ 150]$ GeV.
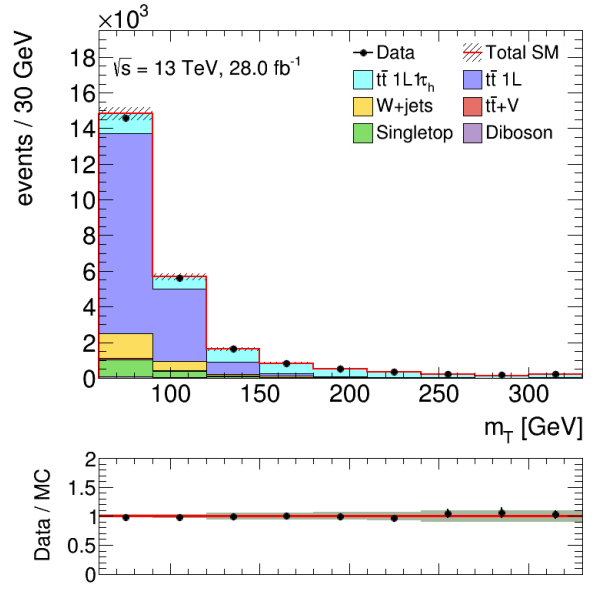
(b) m_{T} at $E_{\mathrm{T}}^{\mathrm{miss}} = [150,\ 200]$ GeV.
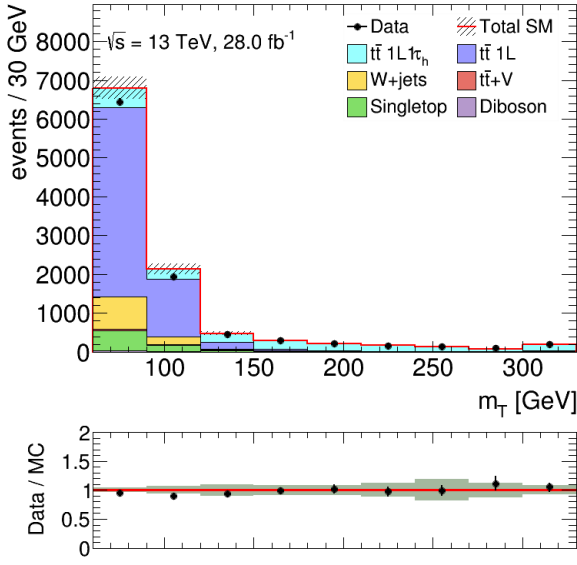
(c) m_{T} at $E_{\mathrm{T}}^{\mathrm{miss}} = [200,\ 250]$ GeV.
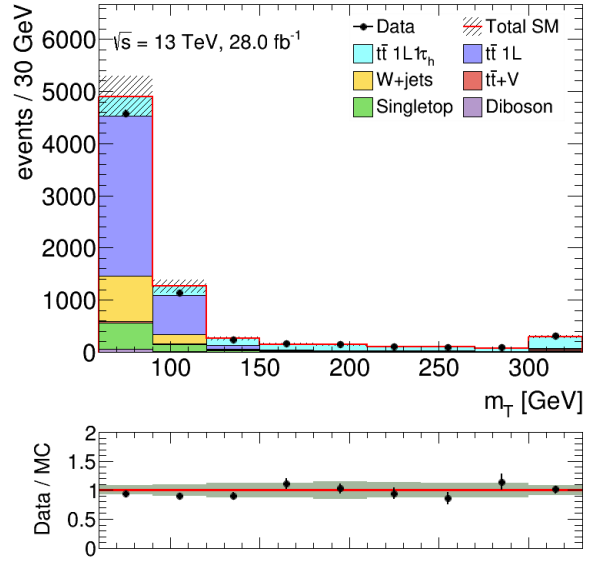
(d) m_{T} at $E_{\mathrm{T}}^{\mathrm{miss}} = [250,\ \mathrm{inf}]$ GeV.
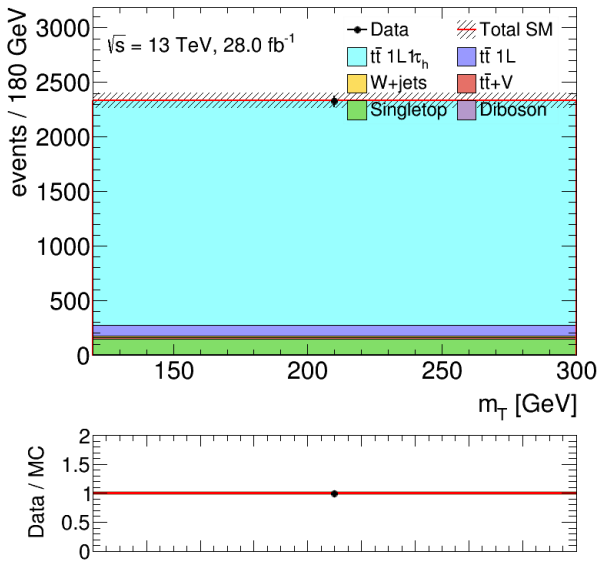
(e) m_{T} at TAUCR.

Figure 9.11: m_{T} distribution at each $E_{\mathrm{T}}^{\mathrm{miss}}$ slice and TAUCR after the background-only fit with unblind. The uncertainty band includes statistical and systematic error.

114
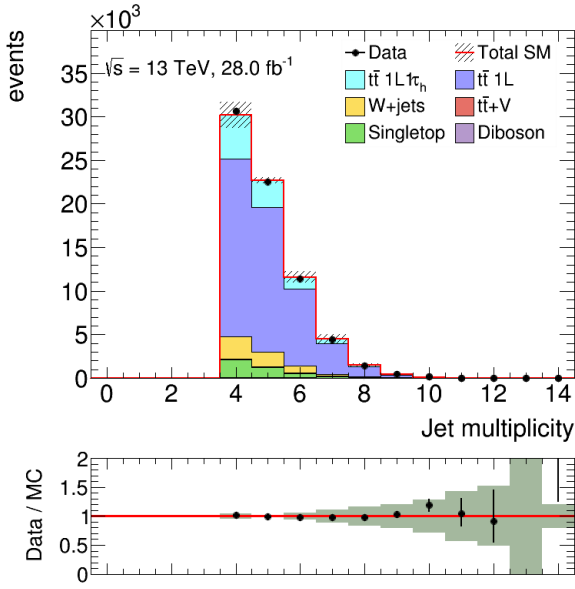
(a) jet multiplicity at $E_T^{miss} = [100, 150]$ GeV.
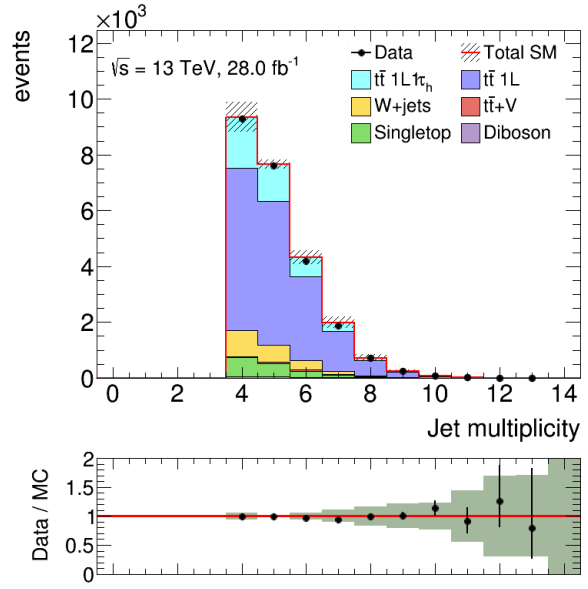
(b) jet multiplicity at $E_T^{miss} = [150, 200]$ GeV.
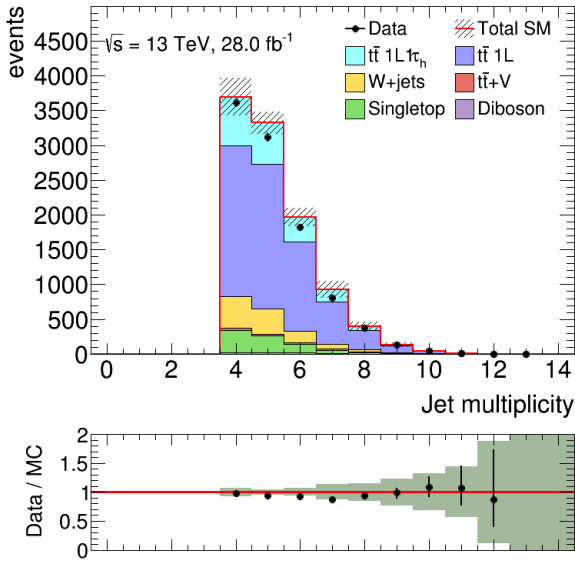
(c) jet multiplicity at $E_T^{miss} = [200, 250]$ GeV.
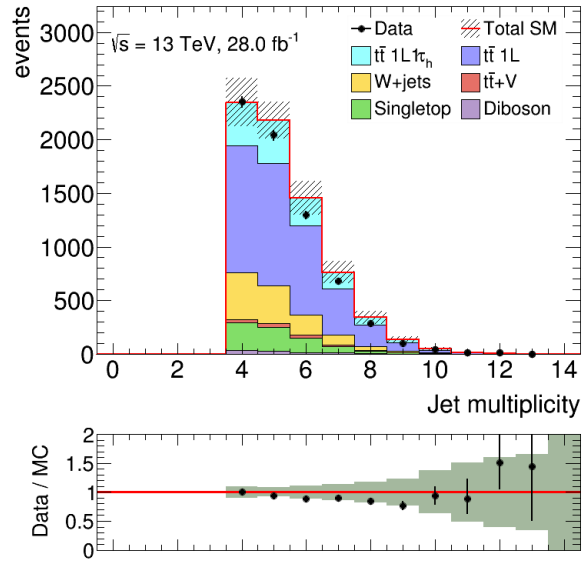
(d) jet multiplicity at $E_T^{miss} = [250, inf]$ GeV.
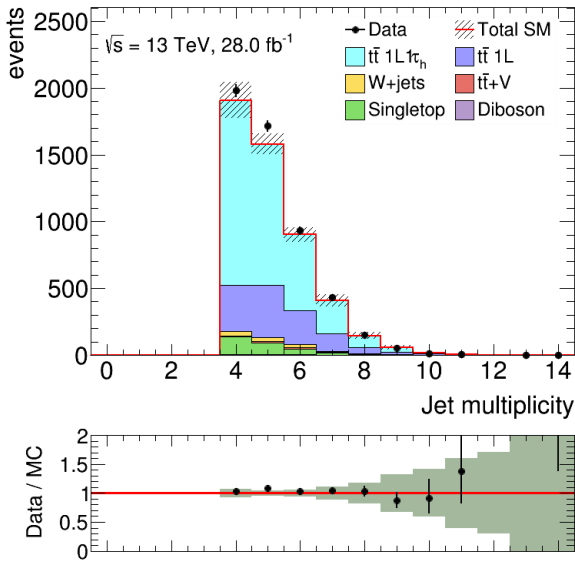
(e) jet multiplicity at TAUCR.

Figure 9.12: jet multiplicity distribution at each E_T^{miss} slice and TAUCR after the background-only fit with unblind. The uncertainty band includes statistical and systematic error.
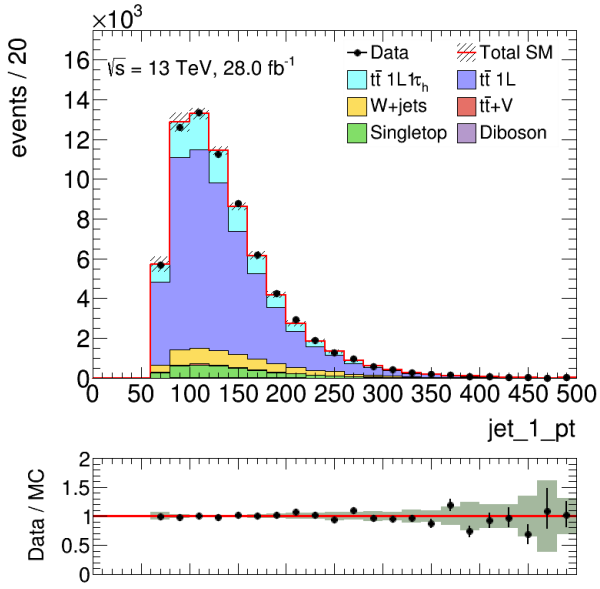
(a) 1st jet p_T at $E_T^{miss} = [100, 150]$ GeV.
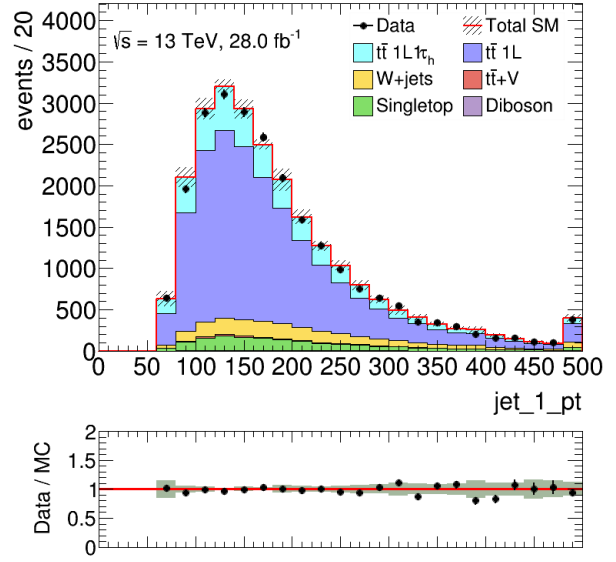
(b) 1st jet p_T at $E_T^{miss} = [150, 200]$ GeV.
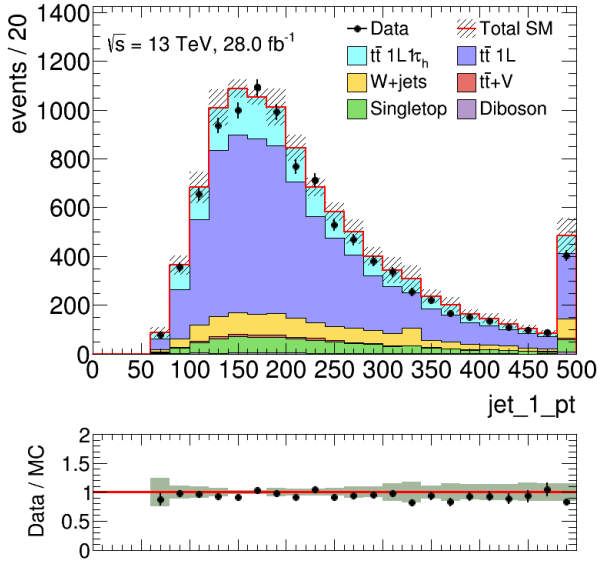
(c) 1st jet p_T at $E_T^{miss} = [200, 250]$ GeV.
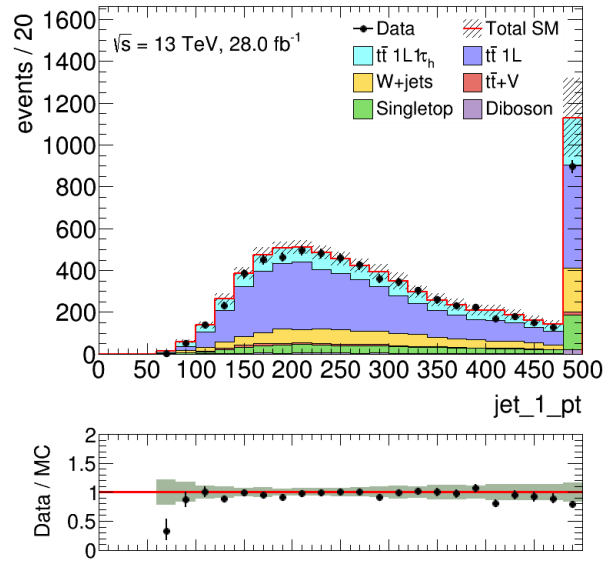
(d) 1st jet p_T at $E_T^{miss} = [250, inf]$ GeV.
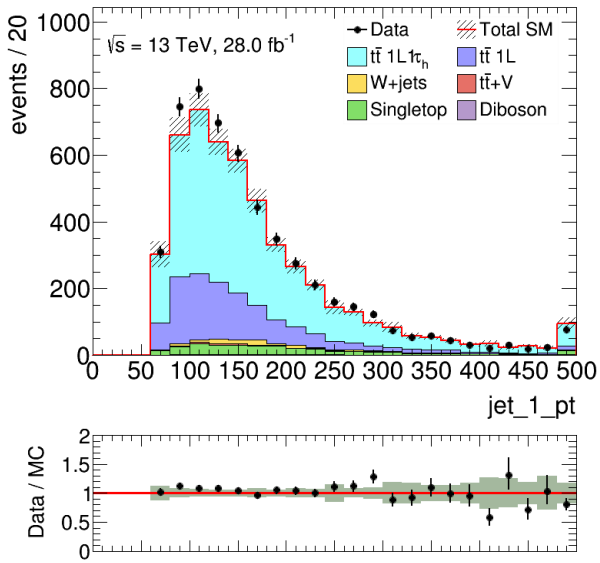
(e) 1st jet p_T at TAUCR.

Figure 9.13: 1st jet p_T distribution at each E_T^{miss} slice and TAUCR after the background-only fit with unblind. The uncertainty band includes statistical and systematic error.
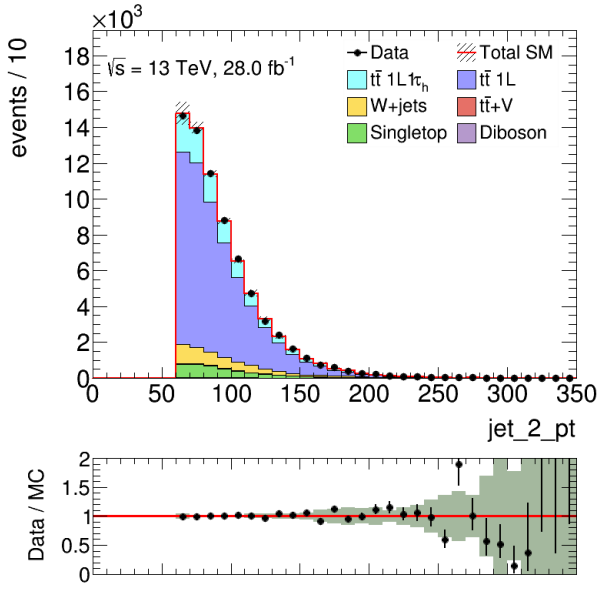
(a) 2nd jet p_T at $E_T^{miss} = [100, 150]$ GeV.
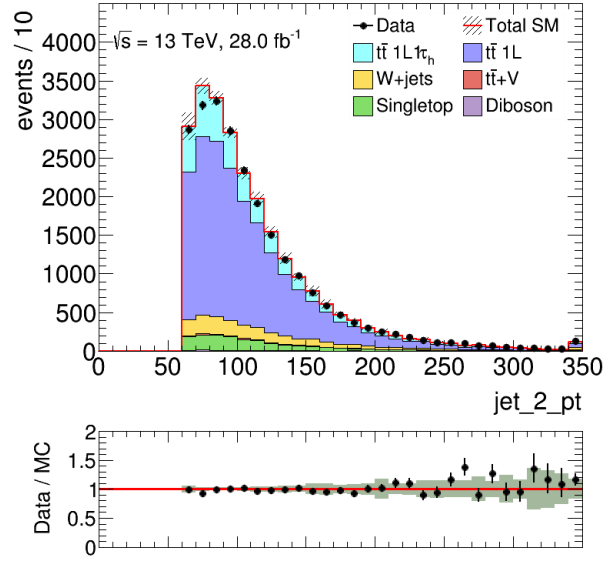
(b) 2nd jet p_T at $E_T^{miss} = [150, 200]$ GeV.
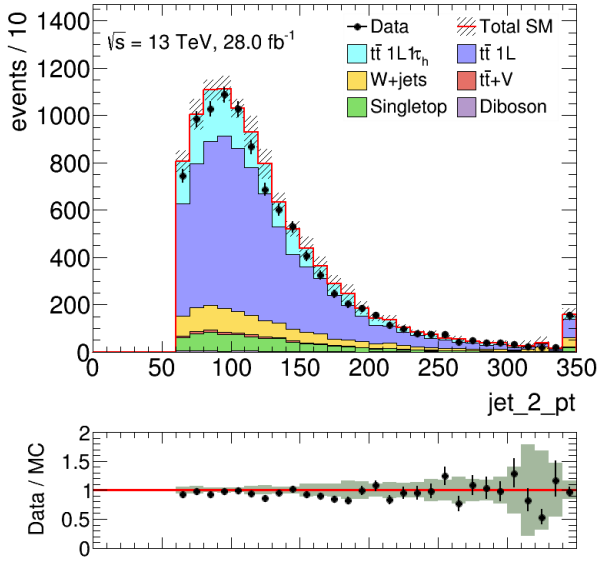
(c) 2nd jet p_T at $E_T^{miss} = [200, 250]$ GeV.
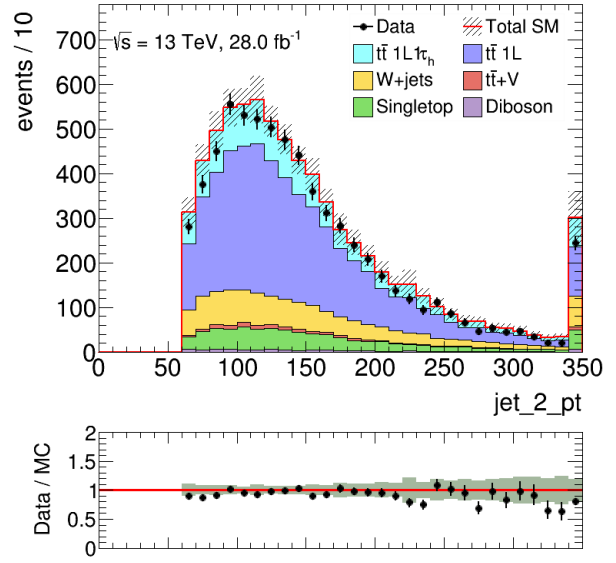
(d) 2nd jet p_T at $E_T^{miss} = [250, inf]$ GeV.
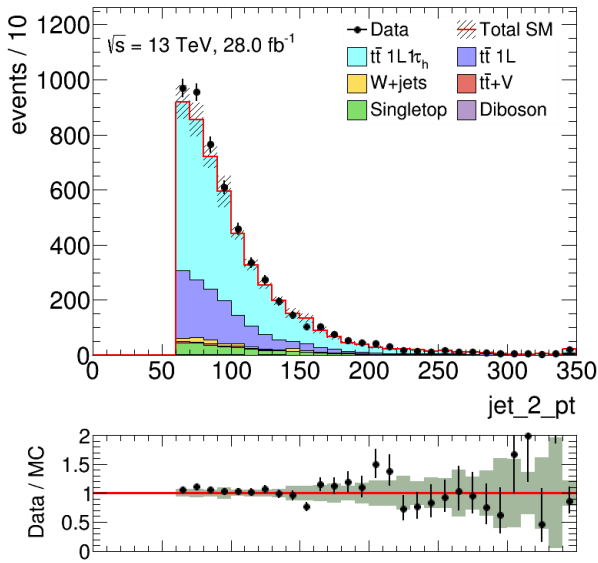
(e) 2nd jet p_T at TAUCR.

Figure 9.14: 2nd jet p_T distribution at each E_T^{miss} slice and TAUCR after the background-only fit with unblind. The uncertainty band includes statistical and systematic error.
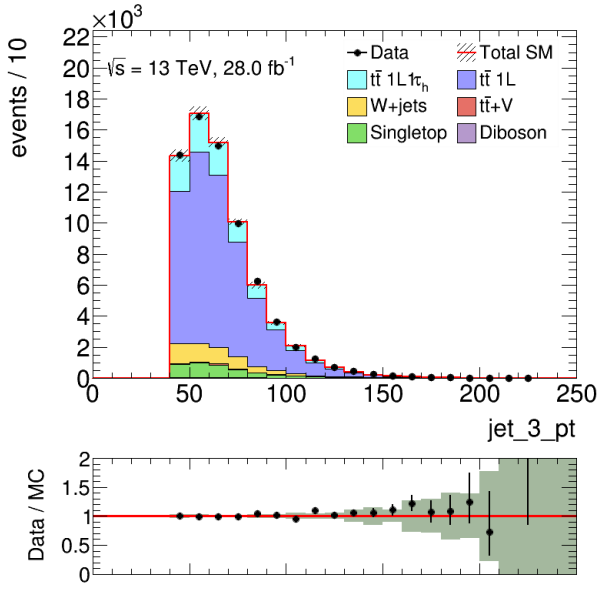
(a) 2nd jet p_T at $E_T^{miss} = [100, 150]$ GeV.
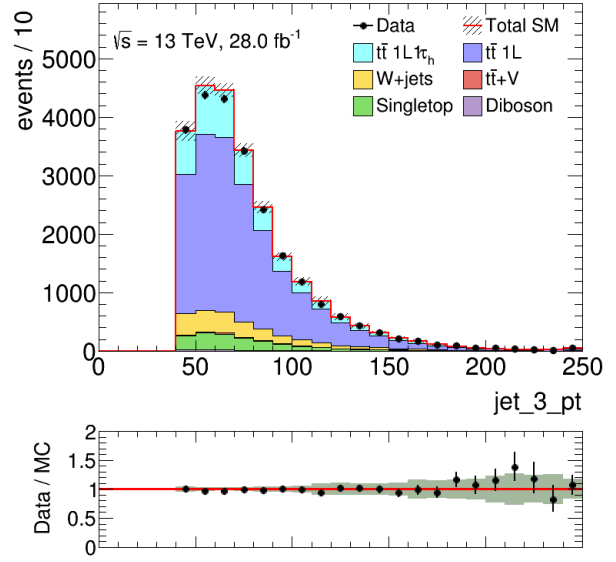
(b) 2nd jet p_T at $E_T^{miss} = [150, 200]$ GeV.
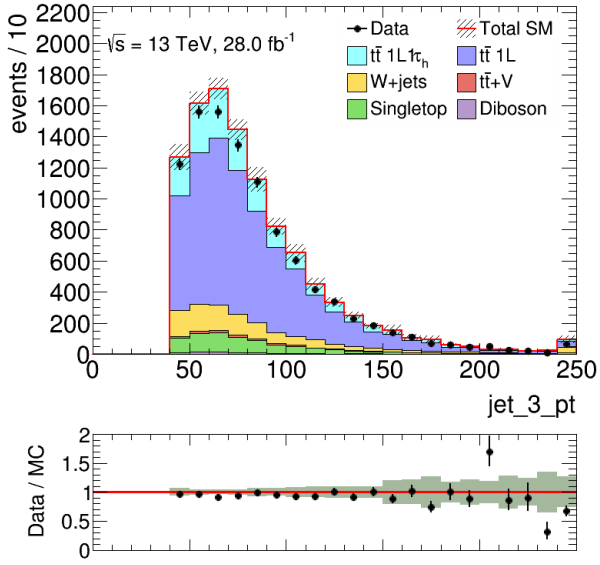
(c) 2nd jet p_T at $E_T^{miss} = [200, 250]$ GeV.
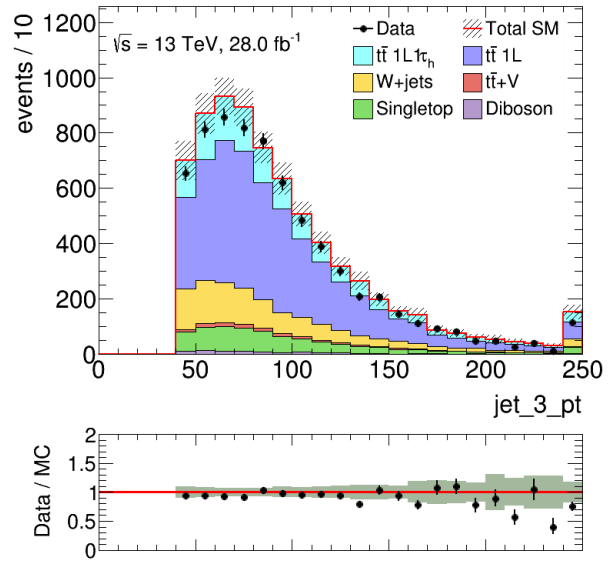
(d) 2nd jet p_T at $E_T^{miss} = [250, inf]$ GeV.
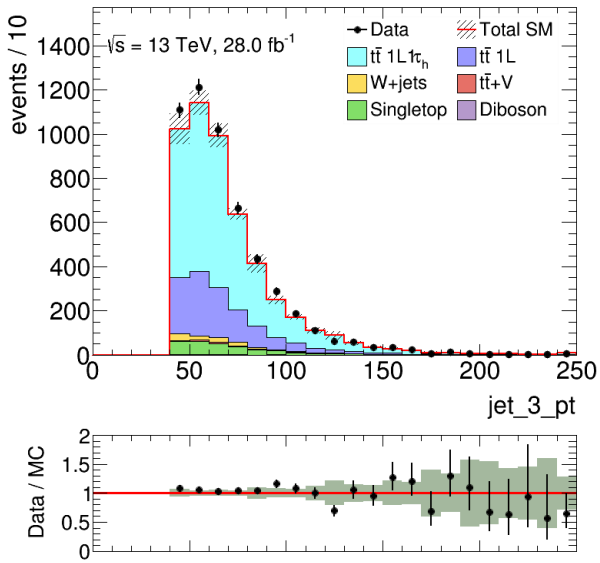
(e) 3rd jet p_T at TAUCR.

Figure 9.15: 3rd jet p_T distribution at each E_T^{miss} slice and TAUCR after the background-only fit with unblind. The uncertainty band includes statistical and systematic error.
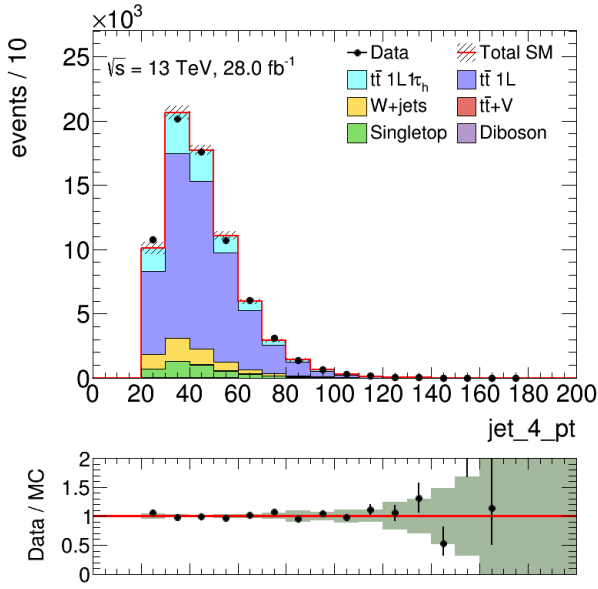
(a) 2nd jet p_T at $E_T^{miss} = [100, 150]$ GeV.
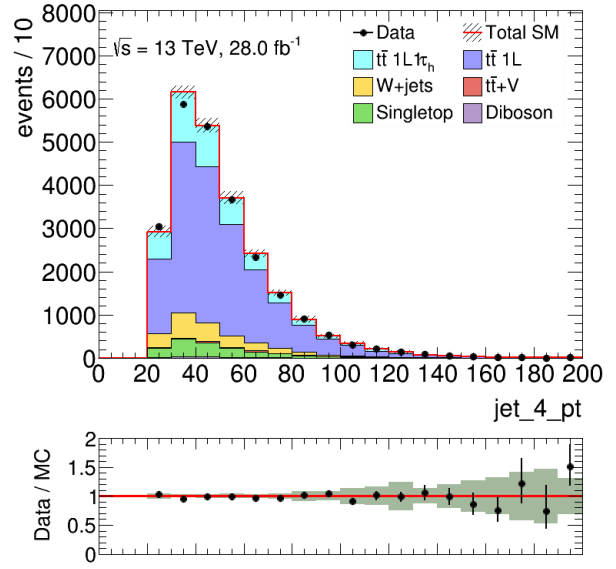
(b) 2nd jet p_T at $E_T^{miss} = [150, 200]$ GeV.
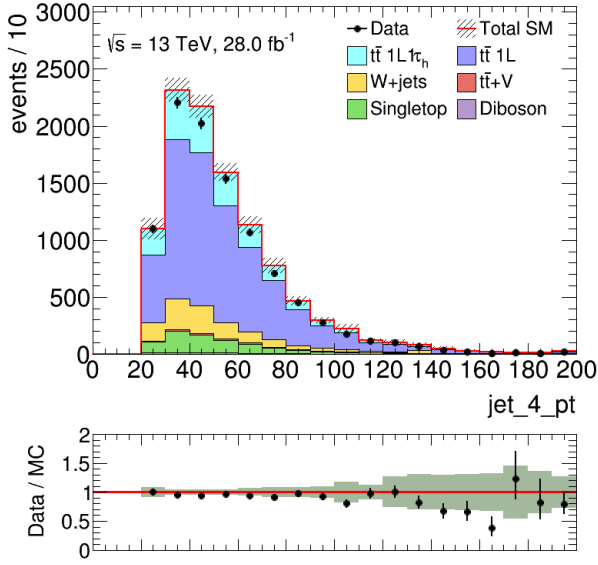
(c) 2nd jet p_T at $E_T^{miss} = [200, 250]$ GeV.
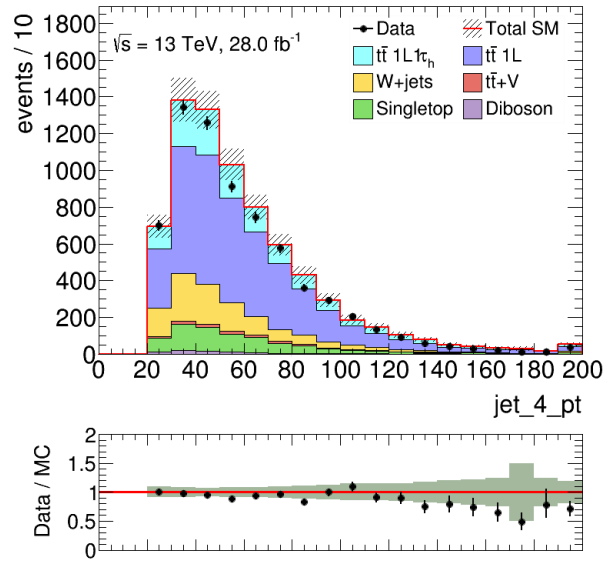
(d) 2nd jet p_T at $E_T^{miss} = [250, inf]$ GeV.
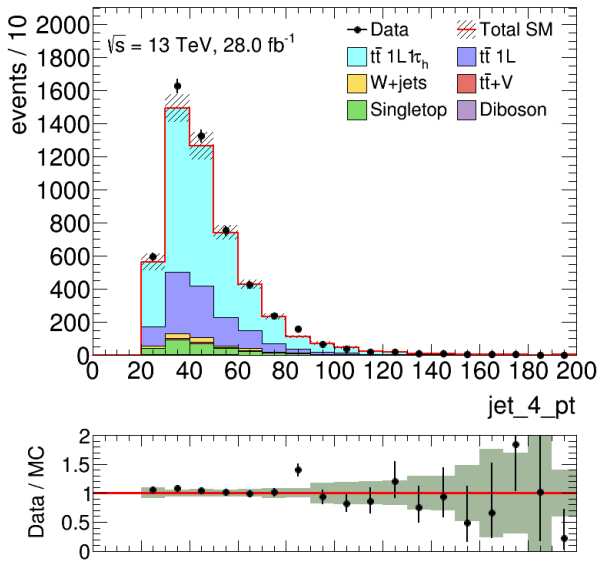
(e) 4th jet p_T at TAUCR.

Figure 9.16: 4th jet p_T distribution at each E_T^{miss} slice and TAUCR after the background-only fit with unblind. The uncertainty band includes statistical and systematic error.

119
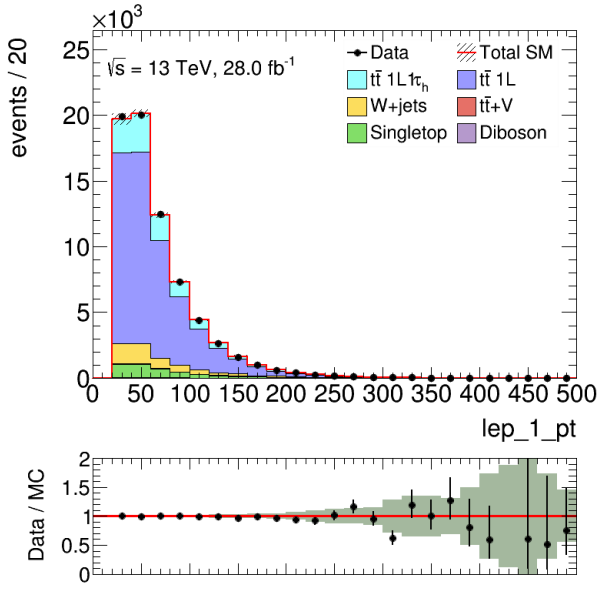
(a) lepton p_T at $E_T^{miss} = [100, 150]$ GeV.
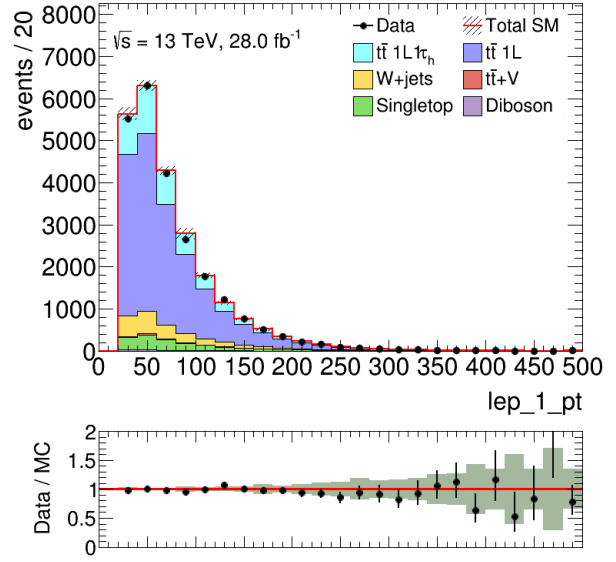
(b) lepton p_T at $E_T^{miss} = [150, 200]$ GeV.
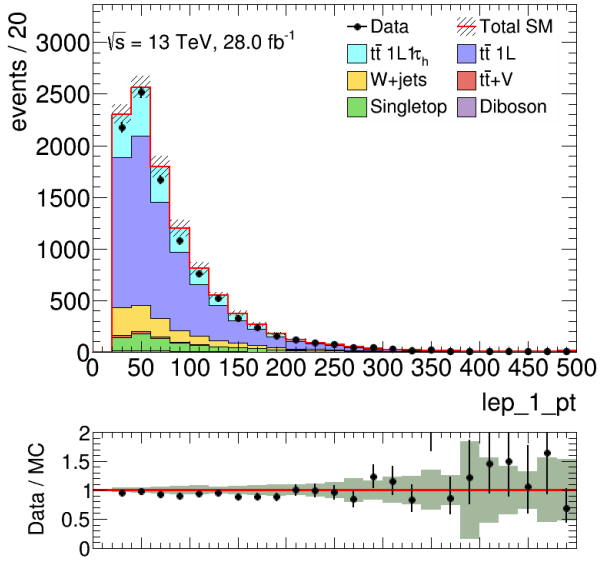
(c) lepton p_T at $E_T^{miss} = [200, 250]$ GeV.
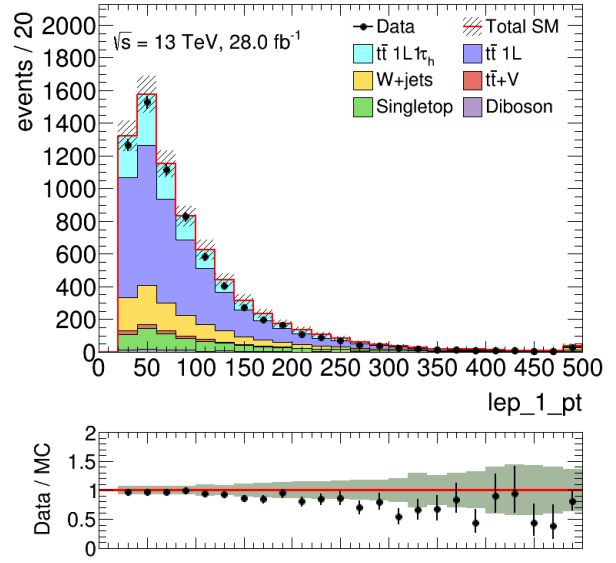
(d) lepton p_T at $E_T^{miss} = [250, inf]$ GeV.
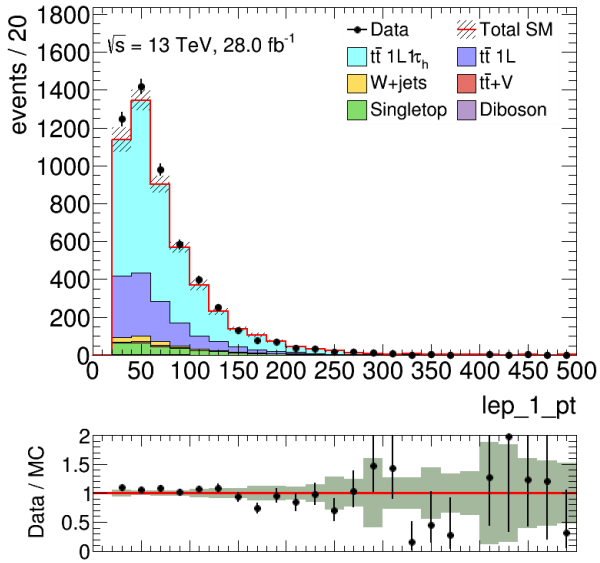
(e) lepton p_T at TAUCR.

Figure 9.17: lepton p_T distribution at each E_T^{miss} slice and TAUCR after the background-only fit with unblind. The uncertainty band includes statistical and systematic error.
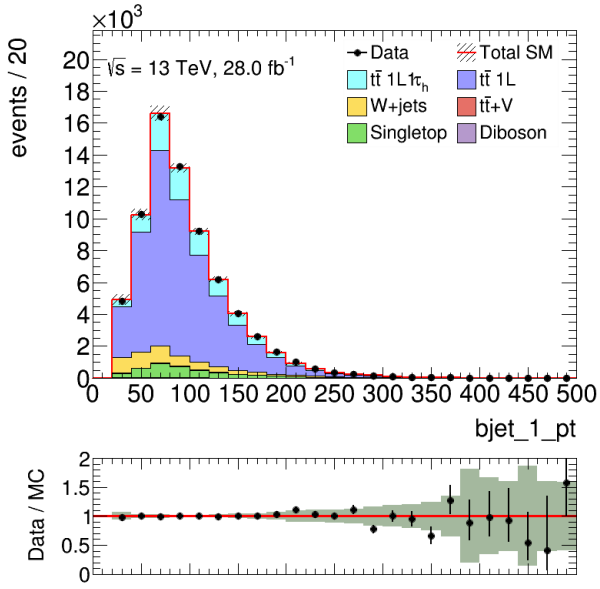
(a) 1st b-jet p_T at $E_T^{miss} = [100, 150]$ GeV.
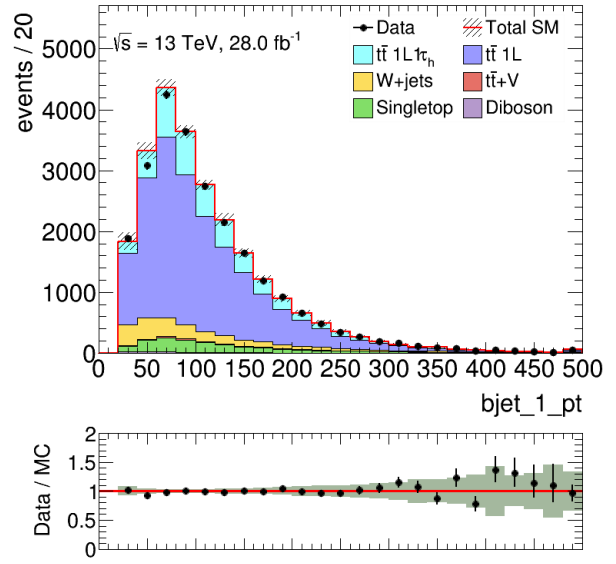
(b) 1st b-jet p_T at $E_T^{miss} = [150, 200]$ GeV.
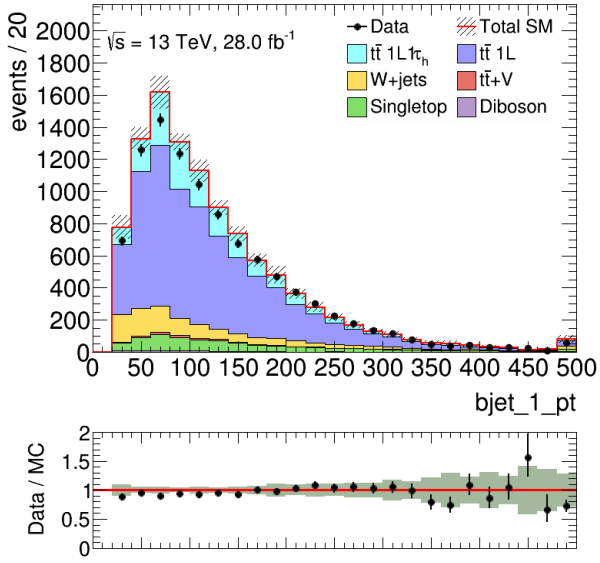
(c) 1st b-jet p_T at $E_T^{miss} = [200, 250]$ GeV.
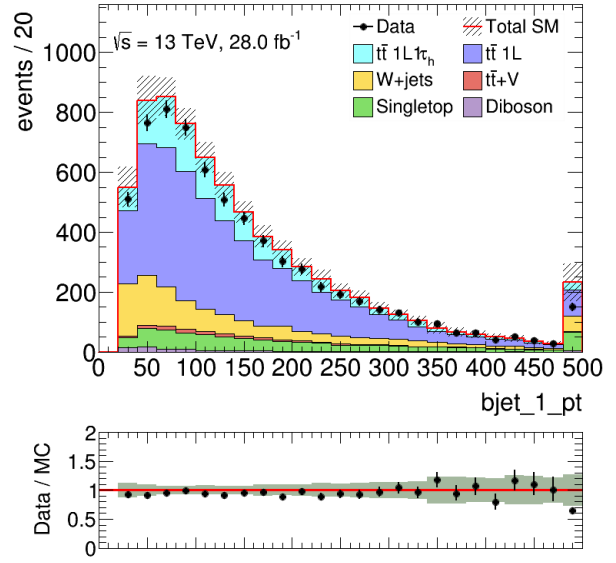
(d) 1st b-jet p_T at $E_T^{miss} = [250, inf]$ GeV.
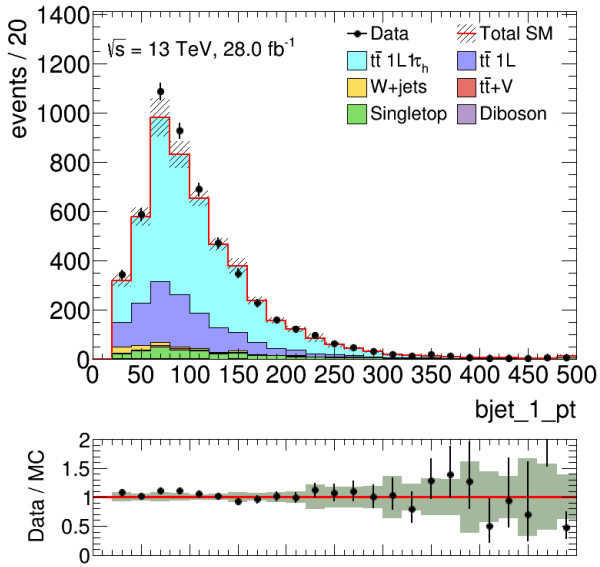
(e) 1st b-jet p_T at TAUCR.

Figure 9.18: 1st b-jet p_T distribution at each E_T^{miss} slice and TAUCR after the background-only fit with unblind. The uncertainty band includes statistical and systematic error.
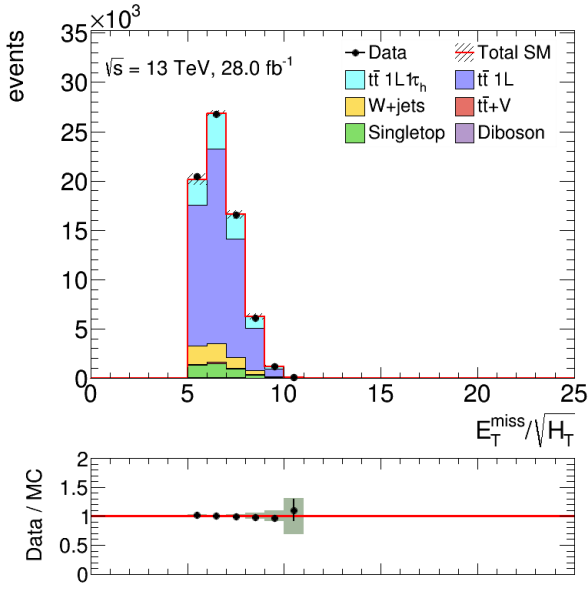
(a) $E_T^{miss}/\sqrt{H_T}$ at $E_T^{miss} = [100, 150]$ GeV.
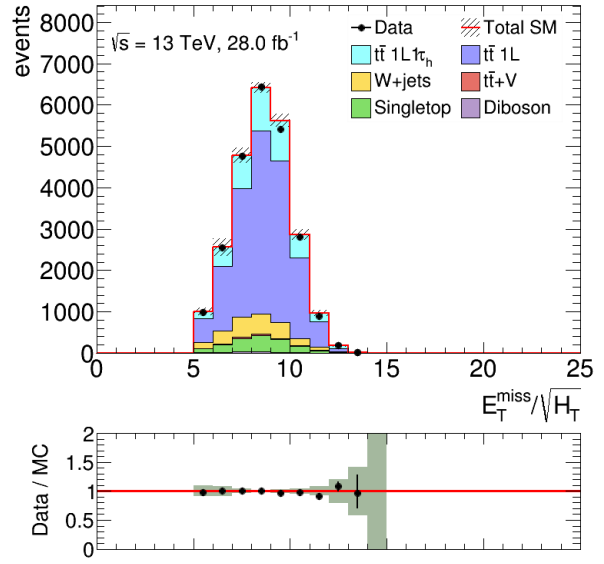
(b) $E_T^{miss}/\sqrt{H_T}$ at $E_T^{miss} = [150, 200]$ GeV.
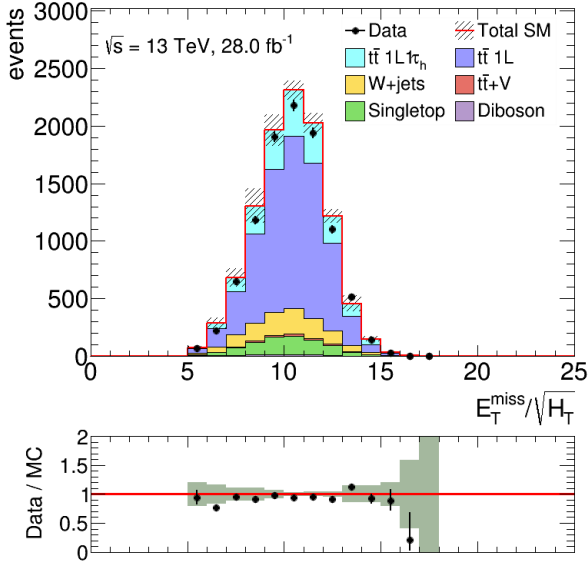
(c) $E_T^{miss}/\sqrt{H_T}$ at $E_T^{miss} = [200, 250]$ GeV.
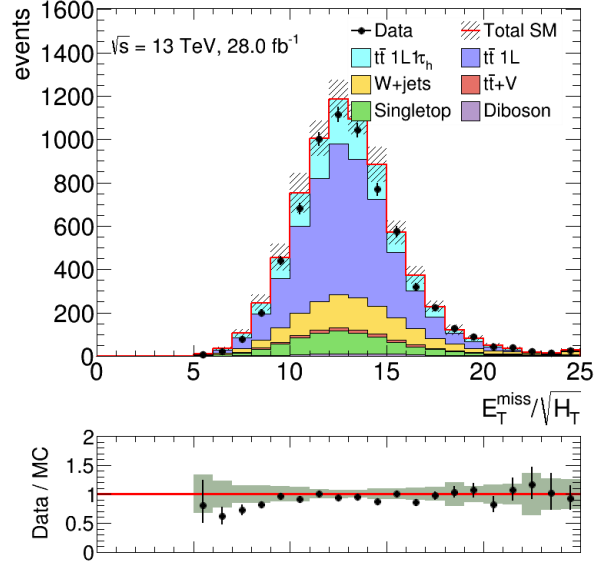
(d) $E_T^{miss}/\sqrt{H_T}$ at $E_T^{miss} = [250, \text{inf}]$ GeV.
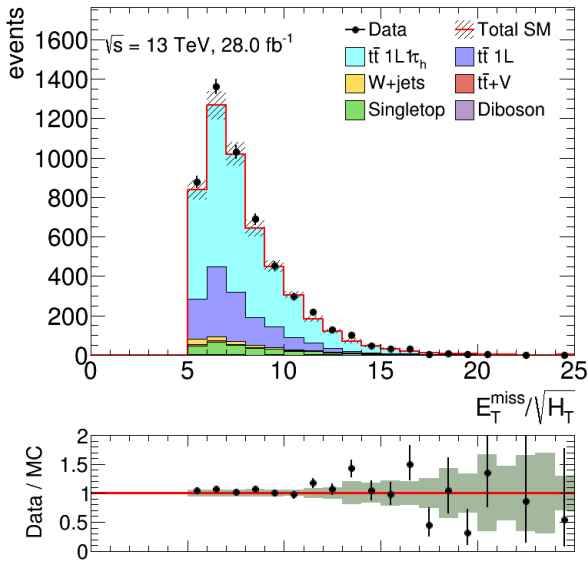
(e) $E_T^{miss}/\sqrt{H_T}$ at TAUCR.

Figure 9.19: $E_T^{miss}/\sqrt{H_T}$ distribution at each E_T^{miss} slice and TAUCR after the background-only fit with unblind. The uncertainty band includes statistical and systematic error.
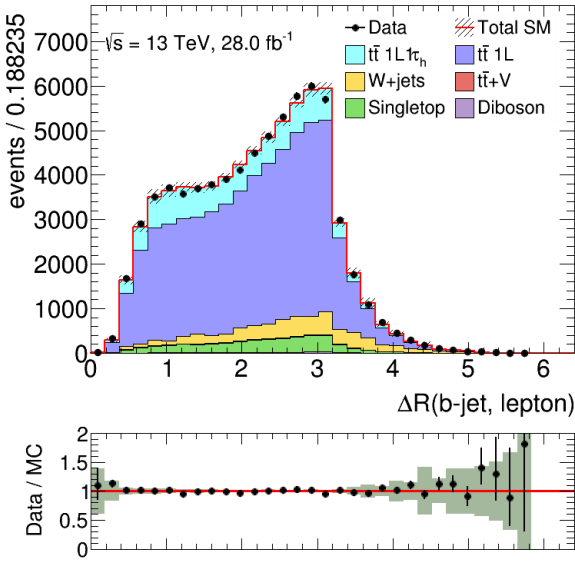
(a) $\Delta R(b, \ell)$ at $E_T^{miss} = [100, 150]$ GeV.
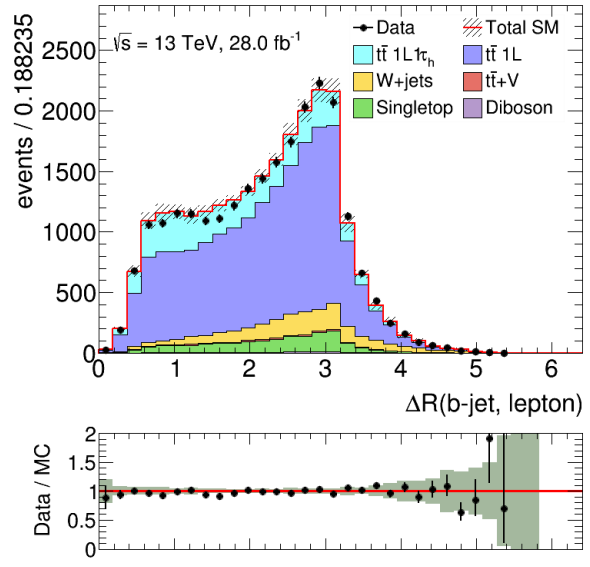
(b) $\Delta R(b, \ell)$ at $E_T^{miss} = [150, 200]$ GeV.
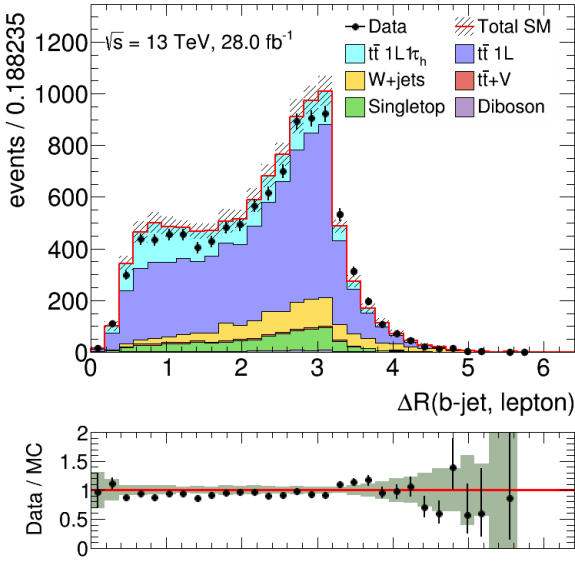
(c) $\Delta R(b, \ell)$ at $E_T^{miss} = [200, 250]$ GeV.
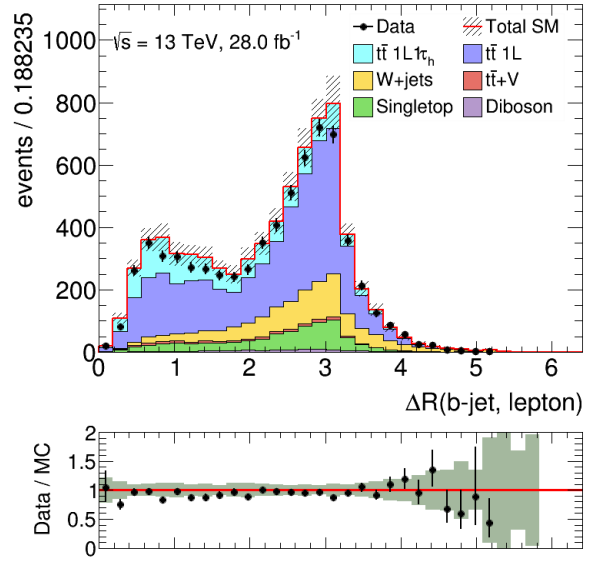
(d) $\Delta R(b, \ell)$ at $E_T^{miss} = [250, \text{inf}]$ GeV.
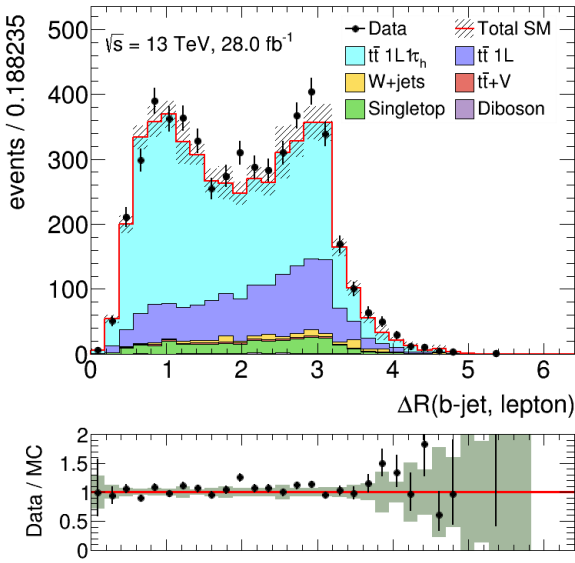
(e) $\Delta R(b, \ell)$ at TAUCR.

Figure 9.20: $\Delta R(b, \ell)$ distribution at each E_T^{miss} slice and TAUCR after the background-only fit with unblind. The uncertainty band includes statistical and systematic error. These plots are just for validations of the 2-D shape fit, and not used in either the event selection or the fit.
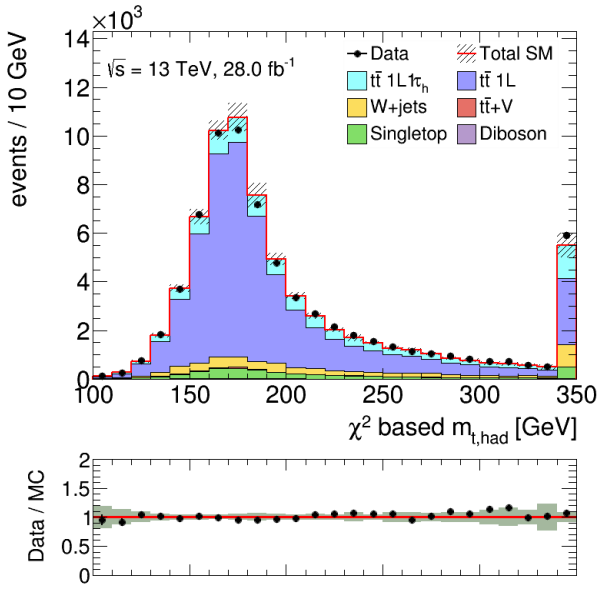
(a) m_{top}^{χ} at $E_T^{miss} = [100, \ 150]$ GeV.
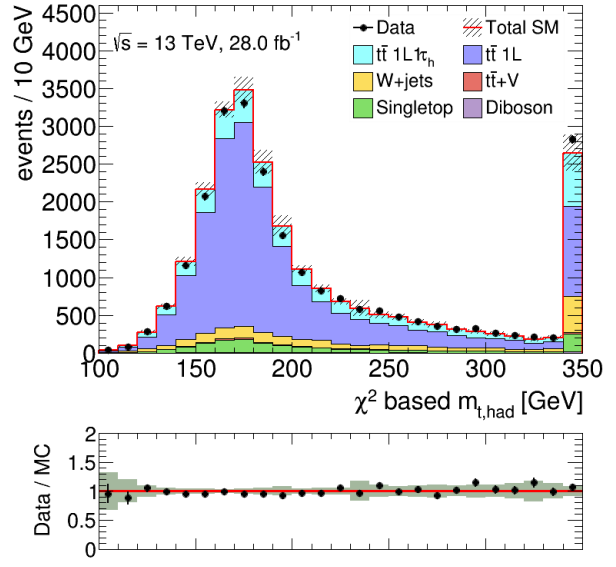
(b) m_{top}^{χ} at $E_T^{miss} = [150, \ 200]$ GeV.
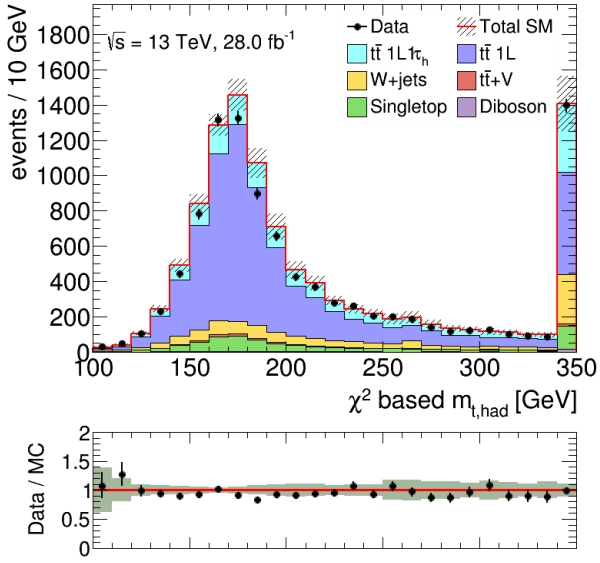
(c) m_{top}^{χ} at $E_T^{miss} = [200, \ 250]$ GeV.
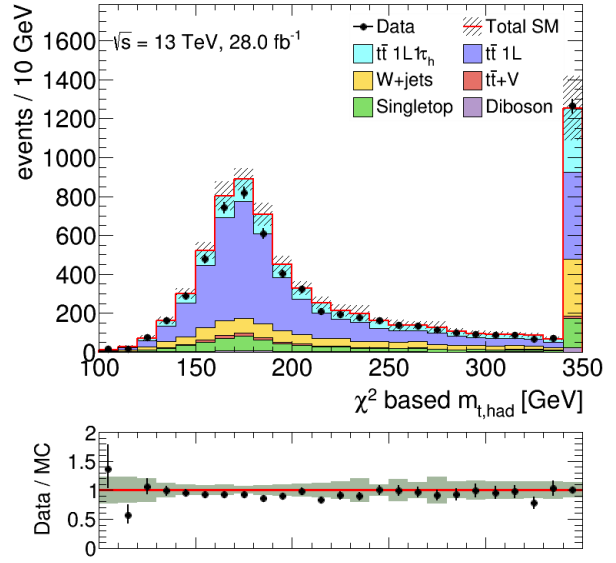
(d) m_{top}^{χ} at $E_T^{miss} = [250, \ \text{inf}]$ GeV.
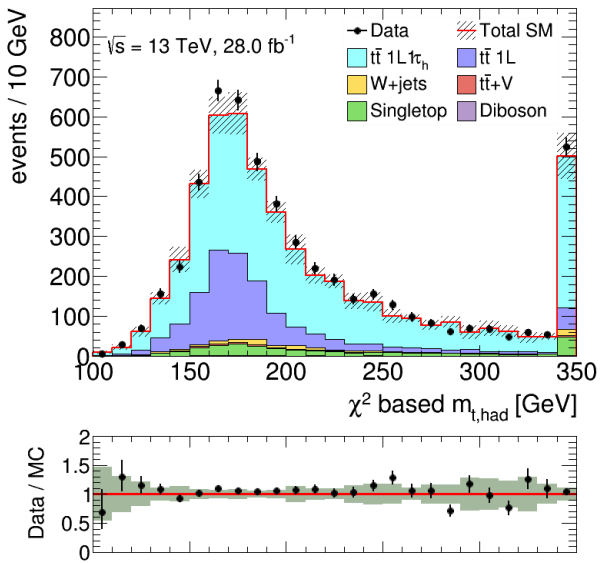
(e) m_{top}^{χ} at TAUCR.

Figure 9.21: m_{top}^{χ} distribution at each E_T^{miss} slice and TAUCR after the background-only fit with unblind. The uncertainty band includes statistical and systematic error. These plots are just for validations of the 2-D shape fit, and not used in either the event selection or the fit.
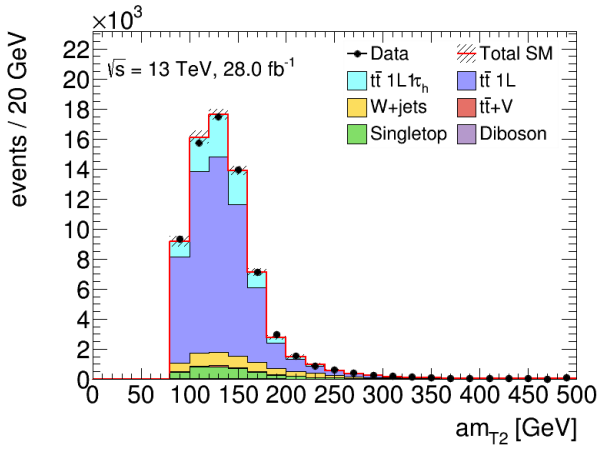
(a) am_{T2} at $E_T^{miss} = [100, 150]$ GeV.
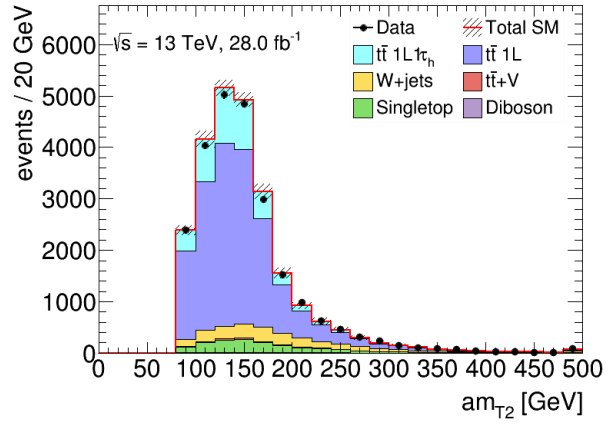
(b) am_{T2} at $E_T^{miss} = [150, 200]$ GeV.
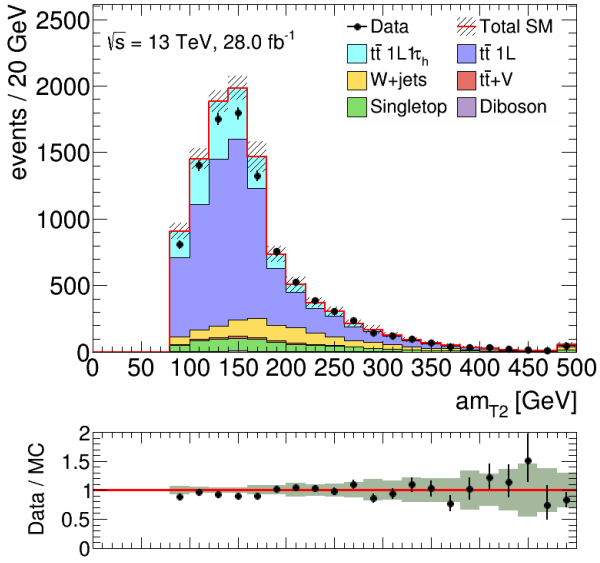
(c) am_{T2} at $E_T^{miss} = [200, 250]$ GeV.
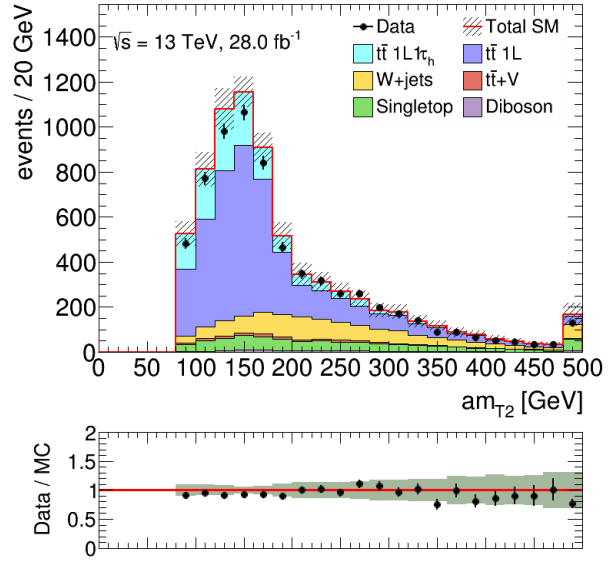
(d) am_{T2} at $E_T^{miss} = [250, inf]$ GeV.
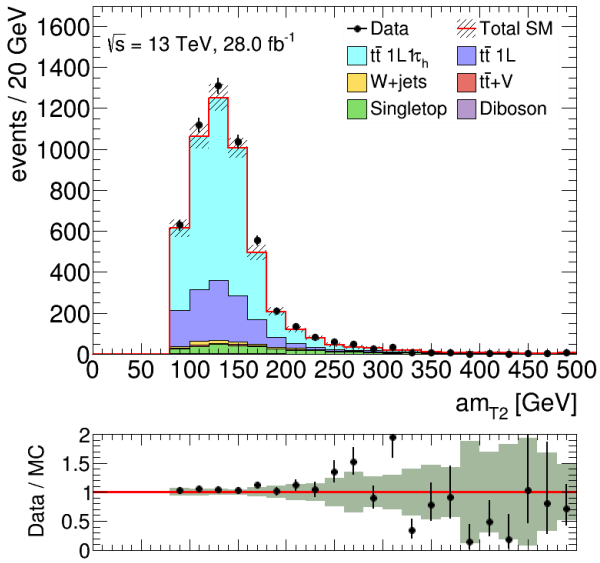
(e) am_{T2} at TAUCR.

Figure 9.22: am_{T2} distribution at each E_T^{miss} slice and TAUCR after the background-only fit with unblind. The uncertainty band includes statistical and systematic error. These plots are just for validations of the 2-D shape fit, and not used in either the event selection or the fit.
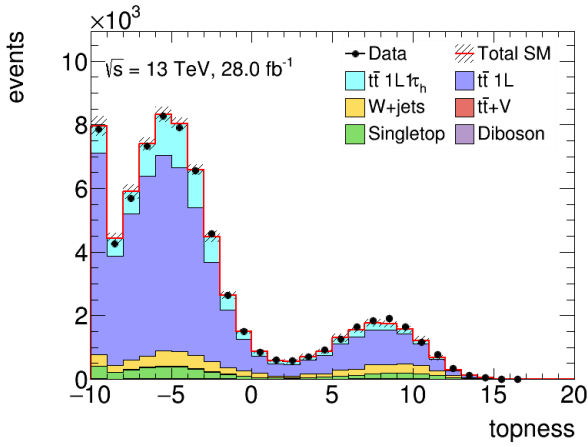
(a) *topness* at $E_T^{miss} = [100, \ 150]$ GeV.
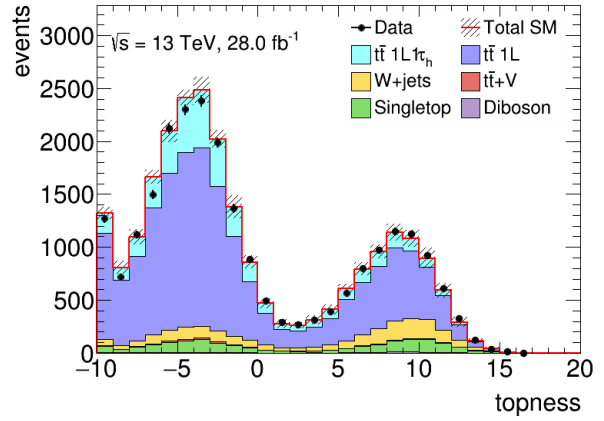
(b) *topness* at $E_T^{miss} = [150, \ 200]$ GeV.
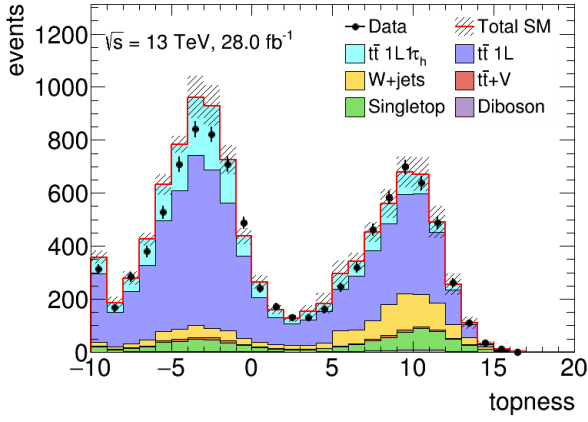
(c) *topness* at $E_T^{miss} = [200, \ 250]$ GeV.
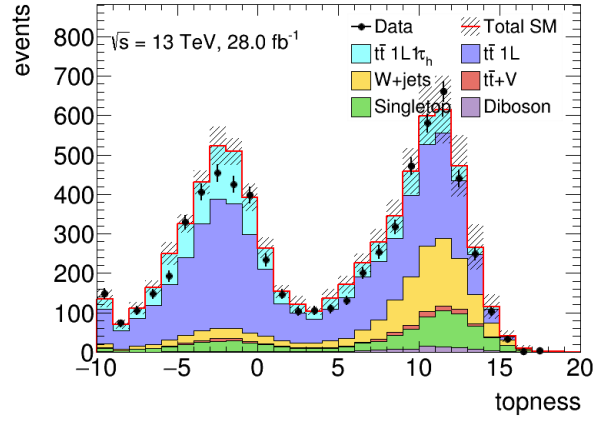
(d) *topness* at $E_T^{miss} = [250, \ inf]$ GeV.
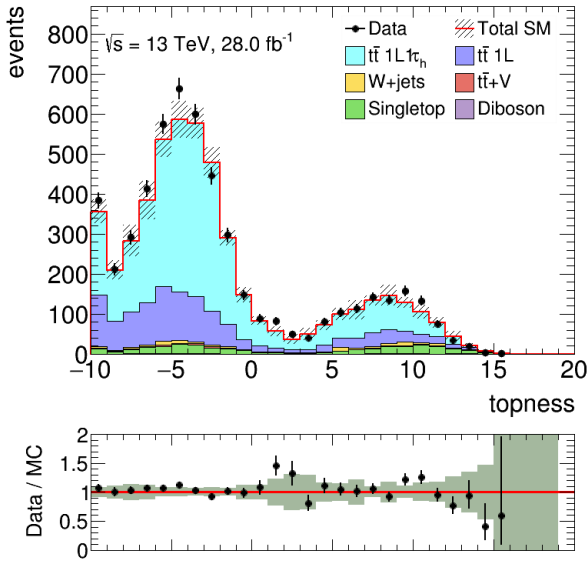
(e) *topness* at TAUCR.

Figure 9.23: *topness* distribution at each E_T^{miss} slice and TAUCR after the background-only fit with unblind. The uncertainty band includes statistical and systematic error. These plots are just for validations of the 2-D shape fit, and not used in either the event selection or the fit.
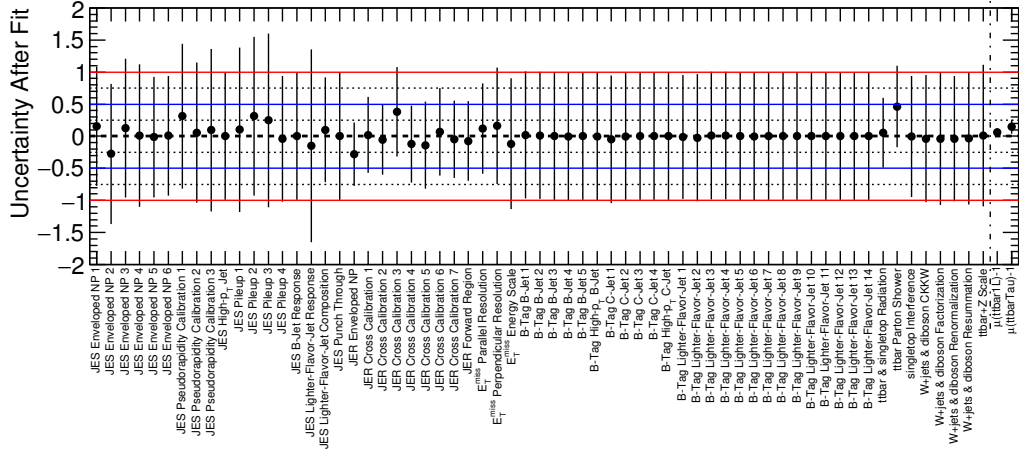
Figure 9.24: Model parameters and their uncertainties after the 2-D shape fit with unblind. The vertical dashed-dotted line divides into two categories: standardized systematic parameters (left) and normalization scale factors (right). The naming rule of systematic parameters follow Table 8.1−8.5. For the detailed explanation on the fit configuration, see section 7.2.
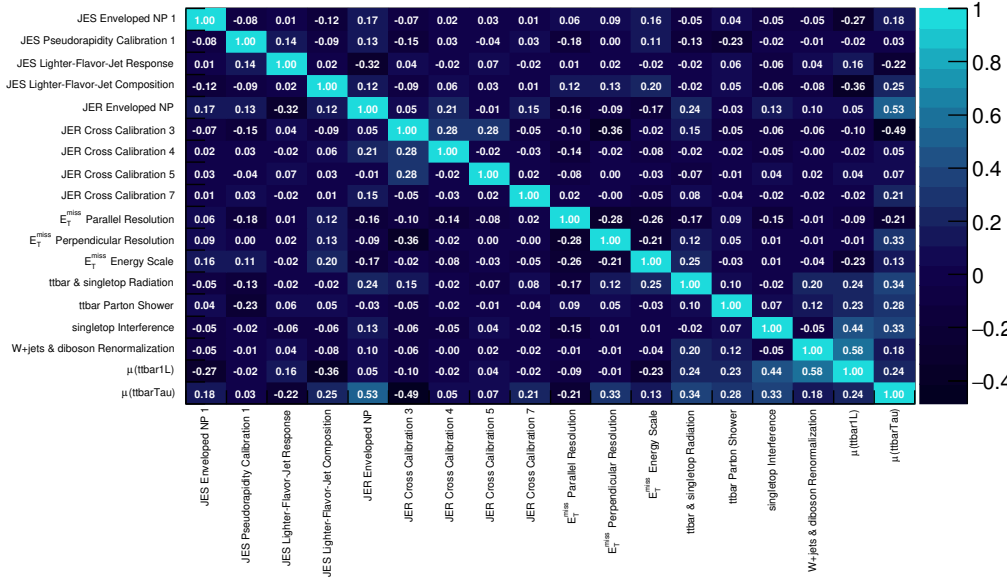
Figure 9.25: Correlations among model parameters after the 2-D shape fit with unblind. Only parameters with at least one correlation of more than 0.2 are shown. The naming rule of systematic parameters follow Table 8.1−8.5. For the detailed explanation on the fit configuration, see section 7.2.
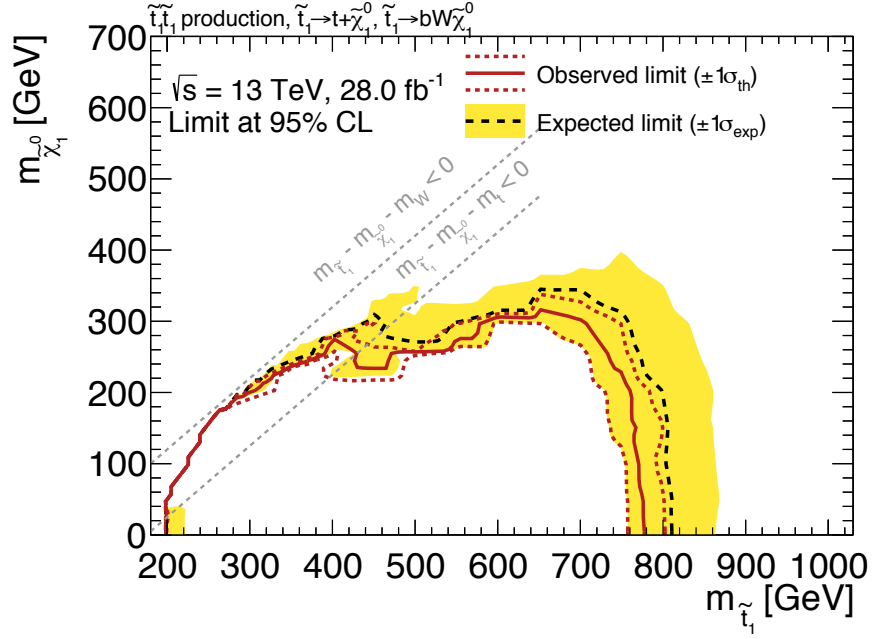
Figure 9.26: *Diagonal*: Expected (black dashed) and observed (red solid) CL_s exclusion limits at 95% CL in the plane of $m_{\tilde{t}_1}$ versus $m_{\tilde{\chi}_1^0}$. The dashed red line (σ_{th}) indicates the results with $\pm 1\sigma$ variation of the signal cross section uncertainty (Figure 3.1).
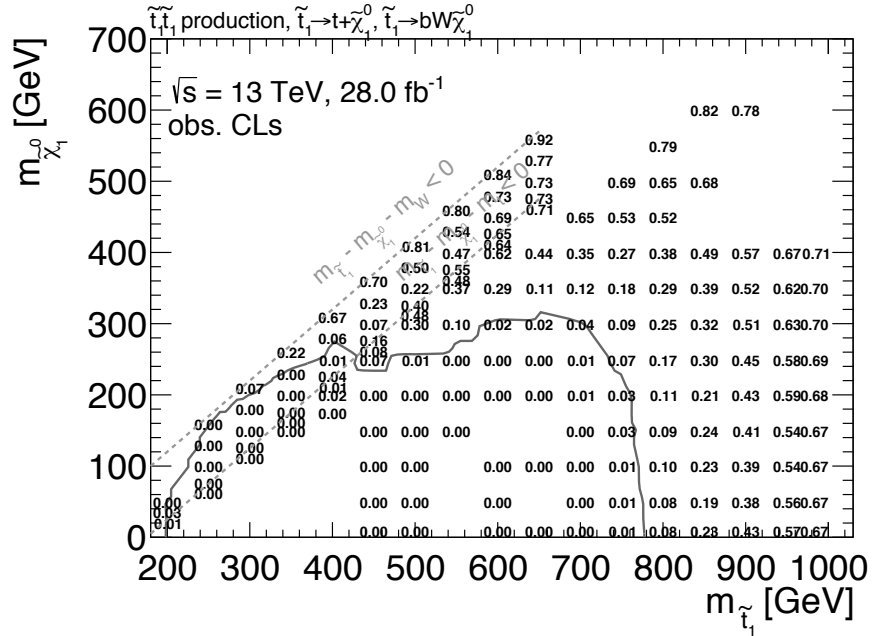
Figure 9.27: *Diagonal*: Mass points used to draw the contours in Figure 9.9. Observed CL_s values without variation of the signal cross section uncertainty are shown on the mass points.

9.3 Combined Results

As shown in Figure 9.7, 9.9, and 9.26, *Resolved*, *Boosted*, and *Diagonal* results exclude their target regions individually. Figure 9.28 shows CL_s exclusion limits at 95% CL obtained by combining *Resolved*, *Boosted*, and *Diagonal* results, where the exclusion limits are obtained by selecting one of the three strategies, which gives the lowest expected CL_s value, for each mass point. As a comparison, Figure 9.29 shows the exclusion limits obtained by the latest search results using 13.2 fb^{-1} of LHC pp collision data collected in the ATLAS and CMS experiments. *Resolved*, *Boosted*, and *Diagonal* results using the data of 28.0 fb^{-1} enlarges the exclusion contours in Figure 9.29 for $\tilde{t}_1 \to t\tilde{\chi}_1^0$ and $\tilde{t}_1 \to bW\tilde{\chi}_1^0$ decay model with 100% $\mathcal{BR}$.

The *Diagonal* result newly excludes the $\tilde{t}_1 \to t\tilde{\chi}_1^0$ and $\tilde{t}_1 \to bW\tilde{\chi}_1^0$ model with $m_{\tilde{t}_1}$ from 200 to 240 GeV and $(m_{\tilde{t}_1}, m_{\tilde{\chi}_1^0}) \sim (430, 250)$ GeV near the *Diagonal* line. The *Resolved* result doesn't newly exclude but enlarges the expected CL_s contour up to $(m_{\tilde{t}_1}, m_{\tilde{\chi}_1^0}) \sim (700 - 800, 400)$ GeV. The *Boosted* result newly enlarges the expected and observed limits up to $m_{\tilde{t}_1} \lesssim 980$ GeV for $m_{\tilde{\chi}_1^0} \lesssim 300$ GeV and $(m_{\tilde{t}_1}, m_{\tilde{\chi}_1^0}) = (900, 350)$ GeV, which is the highest $\tilde{\chi}_1^0$ mass excluded in *Boosted* region.

For a fair comparison of performance, the expected CL_s exclusion limits of the combination of *Resolved*, *Boosted*, and *Diagonal* on the assumption of 13.2 fb^{-1} are evaluated and compared to the ones of ATLAS and CMS analyses with 13.2 fb^{-1} in Figure 9.30. Figure 9.30 indicates that as well as the *Diagonal* analysis with 28.0 fb^{-1}, the analysis with 13.2 fb^{-1} can also provide the best performance at 200 GeV $< m_{\tilde{t}_1} < 240$ GeV and at $(m_{\tilde{t}_1}, m_{\tilde{\chi}_1^0}) \sim (430, 250)$ GeV, compared to the other ATLAS and CMS analyses with 13.2 fb^{-1}.
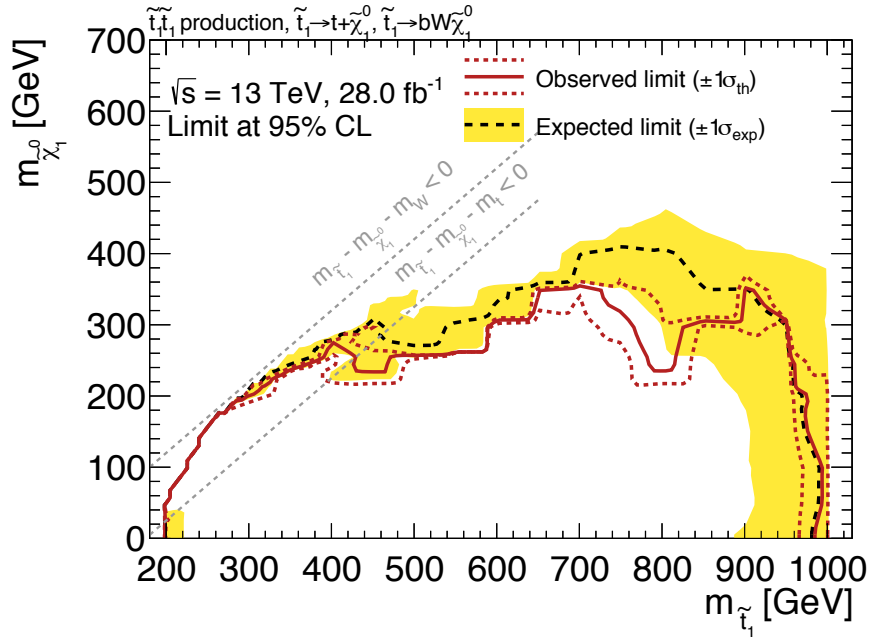
Figure 9.28: The expected (black dashed) and observed (red solid) CL$_s$ exclusion limits at 95% CL in the plane of $m_{\tilde{t}_1}$ versus $m_{\tilde{\chi}_1^0}$ derived by combining *Resolved*, *Boosted*, and *Diagonal* results. The exclusion limits are obtained by selecting one of the three strategies, which gives the lowest expected CL$_s$ value, for each mass point before checking the observed CL$_s$ value.
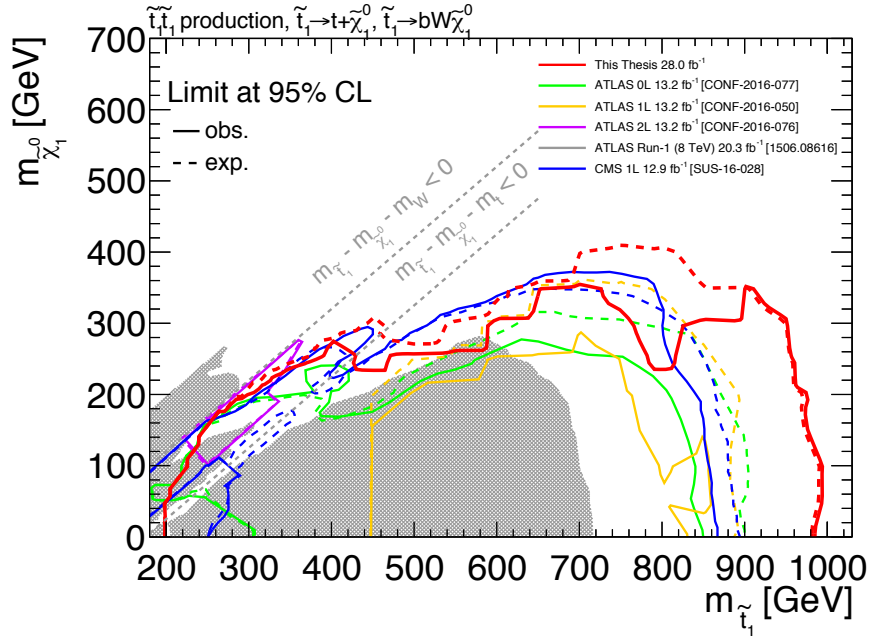
Figure 9.29: Comparison of the combined results of *Resolved*, *Boosted*, and *Diagonal* (red line) to the dedicated ATLAS and CMS searches for stop pair production. The green, orange, and violet lines correspond to searches based on 13.2 fb^{-1} of pp collision data taken by the ATLAS detector at $\sqrt{s} = 13$ TeV using events with no lepton [130], one lepton [27], and two leptons [131], respectively. The blue line corresponds to the CMS result based on 12.9 fb^{-1} data taken at $\sqrt{s} = 13$ TeV using events with one lepton [132]. The observed limit obtained by the ATLAS Run-1 search with 20.3 fb^{-1} at $\sqrt{s} = 8$ TeV [133] is also indicated by the gray region. Exclusion limits at 95% CL are shown in the $(m_{\tilde{t}_1}, m_{\tilde{\chi}_1^0})$ plane. The solid and dashed lines show the observed and expected limits, respectively, which include all uncertainties except the theoretical signal cross section uncertainty.
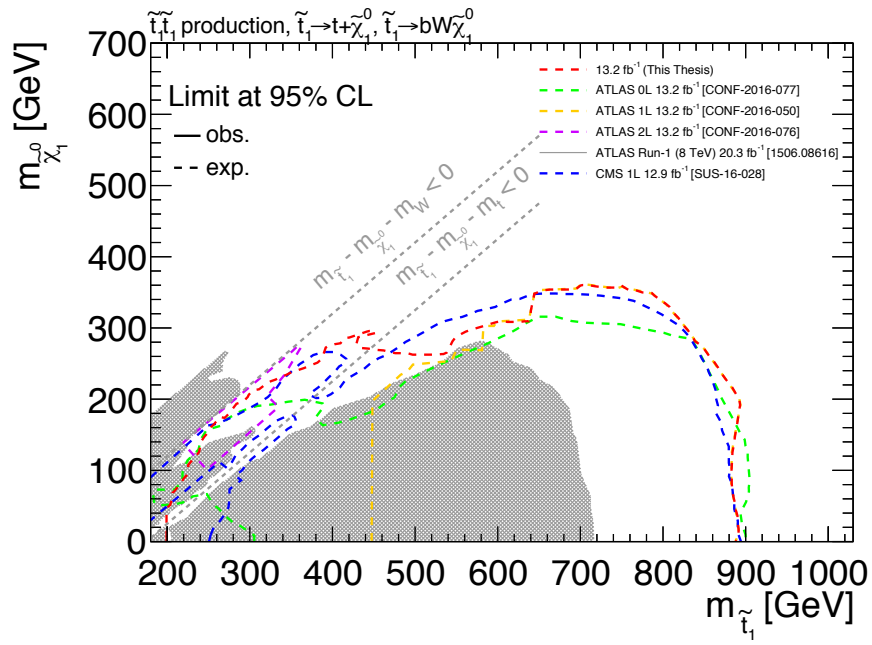
Figure 9.30: Comparison of the expected CL_s exclusion limits obtained by the combination of *Resolved*, *Boosted*, and *Diagonal* on the assumption of 13.2 fb^{-1} (red line) with the ones obtained by the ATLAS results with 13.2 fb^{-1} using events with no lepton [130], one lepton [27], and two leptons [131] and the CMS result with 12.9 fb^{-1} using events with one lepton [132]. As a reference, the observed limit obtained by the ATLAS Run-1 search with 20.3 fb^{-1} at $\sqrt{s} = 8$ TeV [133] is also indicated by the gray region. The expected limits include all uncertainties except the theoretical signal cross section uncertainty.

9.4 Future Prospects

Figure 9.31 shows a schedule of the LHC operation with center-of-mass energy and integrated luminosity indicated. Run-2 is planned to continue until 2018 and provide 100∼150 fb^{-1}. In the shutdown period from 2019 to 2020 (LS2), LHC and some detectors will be upgraded and replaced to increase instantaneous luminosity by a factor of two. Run-3 is planned to operate from 2021 to 2023 and provide 300 fb^{-1}. In the shutdown period from 2024 to mid-2026 (LS3), LHC and several detectors will be upgraded and replaced, and the upgraded LHC is called 'High Luminosity Large Hadron Collider (HL-LHC)'. HL-LHC increases instantaneous luminosity by a factor of 5 to 7 and is planned to operate from mid-2016 to 2037 and provide 3000 fb^{-1}.

As one of future prospects, the expected exclusion limits are evaluated by assuming higher integrated luminosity in the future, which is shown in Figure 9.32, where systematic uncertainties are assumed to be not changed. Run-2 and Run-3 are expected to exclude most of mass points with up to $m_{\tilde{\chi}_1^0} \sim 400$ to 500 GeV[2]. The HL-LHC will reach most of mass points with up to $m_{\tilde{\chi}_1^0} \sim 500$ to 600 GeV. The analysis needs to be improved to search mass points with $m_{\tilde{\chi}_1^0} > 600$ GeV.

As integrated luminosity increases, the larger $E_{\mathrm{T}}^{\mathrm{miss}}$ region will be more important because the signal events tend to provide larger $E_{\mathrm{T}}^{\mathrm{miss}}$ than the backgrounds. Therefore, adding larger $E_{\mathrm{T}}^{\mathrm{miss}}$ bins (for example, $[250, 300]$, $[300, 350]$ GeV) would improve sensitivity.

Focusing on ISR jet from signal event is also interesting. The signal events with one ISR jet can provide larger $E_{\mathrm{T}}^{\mathrm{miss}}$ because the existing of the ISR jet weakens back-to-back state of the stop pair and also the neutralino pair. This characteristics is indirectly exploited in the ($E_{\mathrm{T}}^{\mathrm{miss}}$,$m_{\mathrm{T}}$) shape fit in this thesis, but the direct use of ISR-related variables may improve sensitivity such as the stop analysis with no lepton [130]. Application of multivariate analysis such as machine learning techniques [93] or matrix element likelihood method [134] to the signal events with one ISR jet is also interesting as a longer-term study. There were dedicated studies using matrix element likelihood method where matrix element of the signal event is used at the LO precision without any ISR jets [135, 136] and such studies indicate that the likelihood based on the matrix element without ISR jets are not good enough to improve sensitivity. It indicates that at least matrix element without any ISR jets doesn't work well and therefore considering ISR jets could be one of motivated studies for the further improvement of the analysis.

---

[2] A region of $m_{\tilde{t}_1} > 1$ TeV was not evaluated because samples with such high mass points were unavailable.
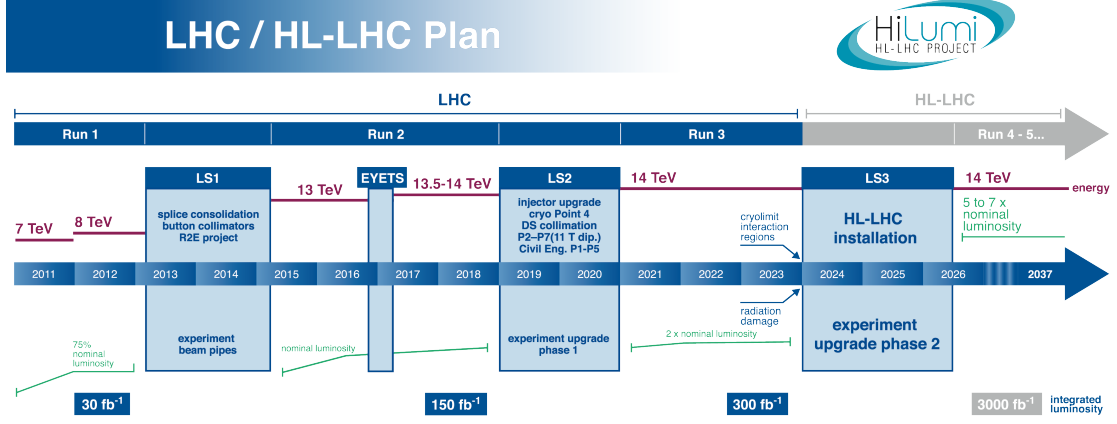
Figure 9.31: A schedule of the LHC and HL-LHC operation [137].
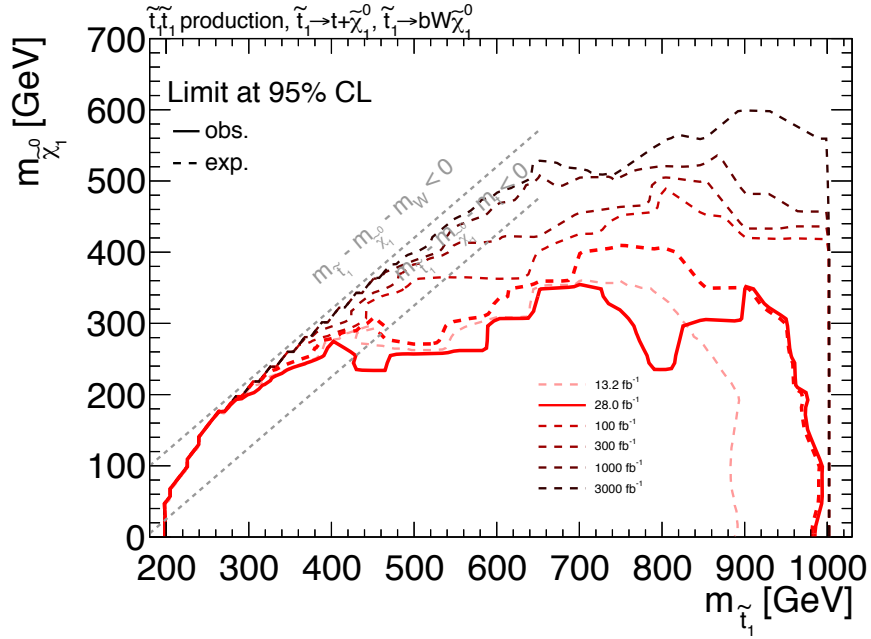
Figure 9.32: Evolution of the expected exclusion limits at 95% CL due to increment of integrated luminosity. The expected limits are evaluated by assuming integrated luminosity of 13.2 (early-Run-2, Moriond 2016), 28.0 (this thesis), 100 (late-Run-2), 300 (Run-3), 1000 (early-HL-LHC), and 3000 (HL-LHC) fb^{-1}. *Resolved*, *Boosted*, and *Diagonal* results are combined as described in Section 9.3. The dashed lines show the expected limits including all uncertainties except the theoretical signal cross section uncertainty. For 28.0 fb^{-1}, the observed limit (solid line) is also shown as a reference. The systematic uncertainties are assumed to be not changed. A region of $m_{\tilde{t}_1} > 1$ TeV was not evaluated because samples with such high mass points were unavailable.

Chapter 10

Conclusion

This thesis presents a search for top squarks in events with one lepton in pp collisions at $\sqrt{s} = 13$ TeV. Top squark (stop) is a new particle predicted by supersymmetry, which is an extension of the SM. Stop is the key particle to naturally solve the hierarchy problem of the Higgs mass correction (naturalness). The analysis targets a direct pair production of stops where each stop decays into the top quark and the lightest neutralino ($\tilde{t}_1 \rightarrow t\tilde{\chi}_1^0$), the W boson from one of the two top quarks decays to an electron or muon (either directly or via a τ lepton), and the W boson from the other top quark decays hadronically. The lightest neutralino is a candidate of dark matter and this is also one of motivations of supersymmetry.

Since the analysis optimized to $\tilde{t}_1 \rightarrow t\tilde{\chi}_1^0$ is also sensitive to a model where stop directly decays into the b-quark, W-boson, and the lightest neutralino ($\tilde{t}_1 \rightarrow bW\tilde{\chi}_1^0$), the analysis result is reinterpreted for $\tilde{t}_1 \rightarrow bW\tilde{\chi}_1^0$ model. The search uses 28.0 fb^{-1} of LHC pp collision data collected in the ATLAS experiment in 2015 and 2016.

Since the signal event topology highly depends on the mass difference between the stop and the lightest neutralino, three analyses are performed which are optimized to *Diagonal*, *Resolved*, and *Boosted* topologies of the signal events. In *Boosted* topology ($\Delta m(\tilde{t}_1, \tilde{\chi}_1^0) \gtrsim 3m_t$), top quarks are highly boosted so that bqq' from hadronic top decay forms one large-R jet. In *Resolved* topology ($\Delta m(\tilde{t}_1, \tilde{\chi}_1^0) \sim 2m_t$), the hadronic top decay products are not merged into one large-R jet but resolved into three smaller-radius jets because p_T of top quark is relatively medium. In *Diagonal* topology ($\Delta m(\tilde{t}_1, \tilde{\chi}_1^0) \sim m_t$), the behavior of hadronic top decay is the same as *Resolved* region but $\tilde{\chi}_1^0$ and t from $\tilde{t}_1$ decay are nearly collinear with respect to $\tilde{t}_1$ momentum.

In a preceding study using the data of 13.2 fb^{-1}, which uses events with one lepton in the final state, there were some excesses of CL$_b = 2.2\ \sigma - 3.3\ \sigma$ in several signal regions which are somewhat kinematically overlapped with each other [27]. The search in this thesis covers a part of the phase spaces with the excesses. For this reason, *Resolved* and *Boosted* analyses in this thesis are similar to those of Ref. [27]. The originality in this thesis is the *Diagonal* analysis which is newly developed and performed to search the *Diagonal* region which is more important from the view of naturalness. The key technique newly developed for *Diagonal* analysis is a background estimation using '2-dimensional shape fit', which greatly expands the search region of *Diagonal*.

The analysis starts from defining physics object, which is a four-momentum reconstructed from the detector signature with a tag such as electron, muon, jet, b-jet, etc. The defined physics

objects are used in the event selection which specifies a phase space named 'signal region (SR)', where the signal events are enhanced and background events are suppressed. Since there is contamination of background events in the SR, they are estimated by using 'control region (CR)' defined as a SR with some key requirements changed to enhance purity and yield of a specific background in the region. Number of events in SR and CRs are used in a simultaneous fit, where the fitted parameters are total normalization scale factors for signal and backgrounds. The total normalization scale factors are determined from the statistical constraint of CRs in the simultaneous fit, and then the background contamination in SR can be estimated from the fitted $\mu_{\mathbf{bkg}}$. Experimental and theoretical uncertainties are also considered by incorporating the systematic parameters with gaussian constraints into likelihood used in the simultaneous fit. Finally, CL_b and CL_s values are calculated in the hypothesis test which compares null-hypothesis (background-only scenario) to alternative-hypothesis (background + signal scenario) using the fit result.

The detector signature of the signal events is similar to that of a top quark pair ($t\bar{t}$) produced in association with large missing transverse momentum, which becomes the main background in the analyses. The event selection and background estimation are optimized to *Diagonal*, *Resolved*, and *Boosted* analyses, individually. *Resolved* and *Boosted* analyses exploit the conventional cut-and-count methods and the dedicated event selections which highly suppress the $t\bar{t}$ events. *Diagonal* analysis exploits the dedicated 2-dimensional ($E_{\mathrm{T}}^{\mathrm{miss}}$,$m_{\mathrm{T}}$) shape fit newly developed in this thesis, which precisely estimates the $t\bar{t}$ events in the signal region.

The analysis concludes that there is no significant excess over the SM background expectation in *Diagonal*, *Resolved*, and *Boosted* signal regions. Exclusion limits at 95% CL are derived for stop pair production models for the assumptions of $\mathcal{BR}(\tilde{t}_1 \to t\tilde{\chi}_1^0) = 100\%$ and $\mathcal{BR}(\tilde{t}_1 \to bW\tilde{\chi}_1^0) = 100\%$ with different hypotheses of the mass splitting between the stop and the lightest neutralino. These results extend the latest ATLAS and CMS exclusion limits with an integrated luminosity of 13.2 fb^{-1} for stop pair production model. The *Diagonal* result newly excludes the $\tilde{t}_1 \to t\tilde{\chi}_1^0$ and $\tilde{t}_1 \to bW\tilde{\chi}_1^0$ models with 200 GeV $< m_{\tilde{\chi}_1^0} <$ 240 GeV and $(m_{\tilde{t}_1}, m_{\tilde{\chi}_1^0}) \sim$ (430, 250) GeV near the *Diagonal* line. The *Resolved* result doesn't newly exclude but enlarges the expected CL_s contour up to $(m_{\tilde{t}_1}, m_{\tilde{\chi}_1^0}) \sim$ (700 − 800, 400) GeV. Although there was the excess of CL_b = 2.2 σ in the *Resolved* analysis with 13.2 fb^{-1} reported in Ref. [27], the excess decreases to CL_b = 1.29 σ in this thesis. The *Boosted* result newly excludes the $\tilde{t}_1 \to t\tilde{\chi}_1^0$ model with the $m_{\tilde{t}_1} \lesssim$ 980 GeV for $m_{\tilde{\chi}_1^0} \lesssim$ 300 GeV and $(m_{\tilde{t}_1}, m_{\tilde{\chi}_1^0}) =$ (900, 350) GeV.

Acknowledgements

Appendix A

Validation Fit for *Diagonal*
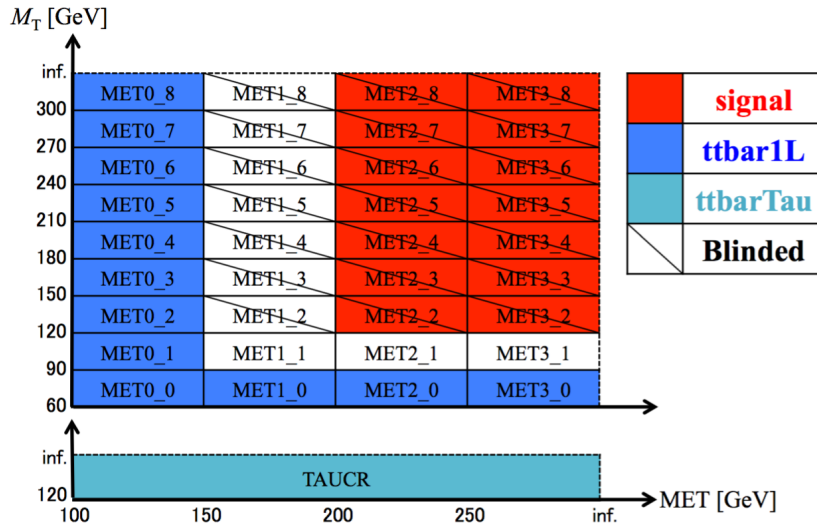
Figure A.1: Binning configuration for the validation fit in *Diagonal*. Slashed bins are 'blinded' bins that had not been either used until this validation fit has confirmed that there is no issue with respect to the $(E_T^{\mathrm{miss}}, m_T)$ shape fit configuration.

In this appendix, results of a validation fit for *Diagonal* are shown. In the context of *Diagonal*, the validation fit means the 2-D shape fit with the blinded bins indicated in Figure A.1 and the signal model dropped away from fit. The purpose of the validation fit is to check how well the background models (or the SM-only model) can explain the observed data and to confirm there is no issue in the fit. Figure A.2 shows variable distributions after validation fit at each E_T^{miss} slice and at TAUCR. The variables not used in the selection, $\Delta R(b, \ell)$, m_{top}^{χ}, am_{T2}, and *topness*, are also checked and shown in Figure A.3-A.14. The parameters and correlations after fit are shown in Figure A.15 and A.16. The observed CL_b obtained by a discovery hypothesis test with the benchmark signal model in *Diagonal* where $(m_{\tilde{t}_1}, m_{\tilde{\chi}_1^0}) = (400, 200)$ is 0.436 (0.160 σ)[1], concluding that there is no significant deviation from the SM-only prediction and thus the SM-only model is plausible.

From the validation fit results, it has been concluded that there is no significant issue in the

---

[1] The terminology of hypothesis test is summarized in Section 7.

2-D shape fit and unblind fit can be done with a confidence in this context. The unblind fit results are shown in Section 9.2.
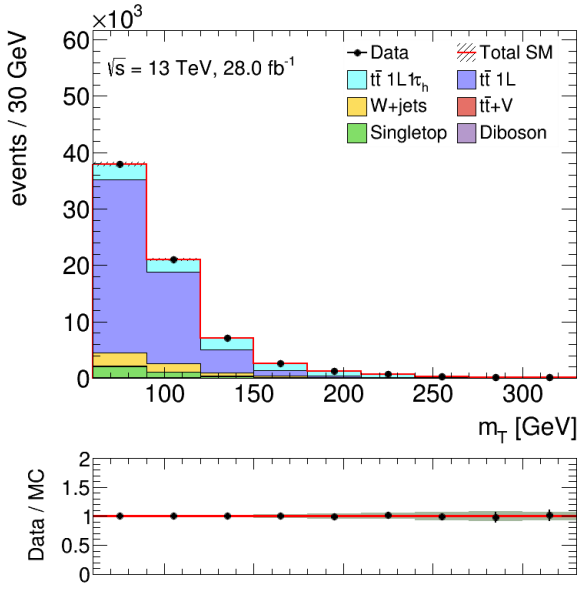
(a) m_T at 1st $E_\mathrm{T}^\mathrm{miss}$ slice [100, 150] GeV.
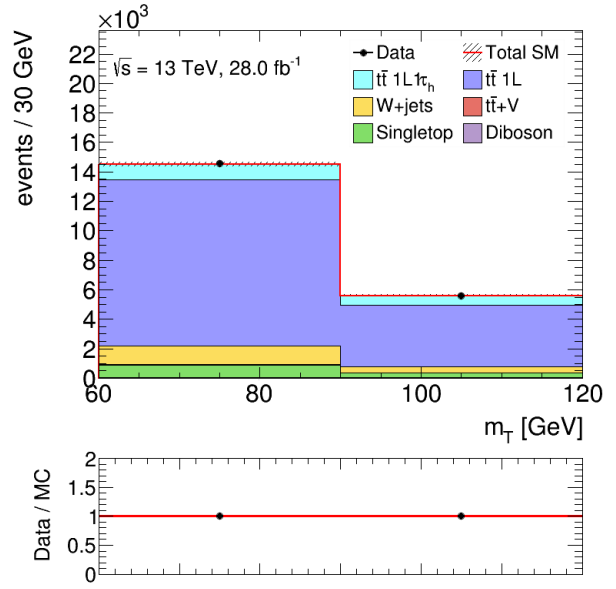
(b) m_T at 2nd $E_\mathrm{T}^\mathrm{miss}$ slice [150, 200] GeV.
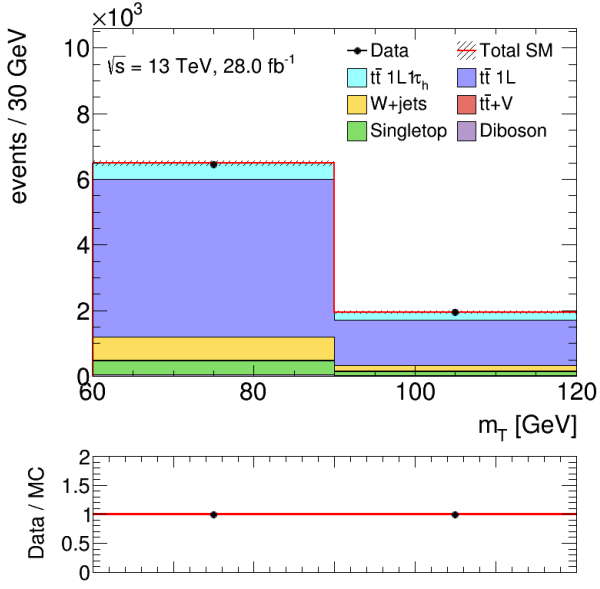
(c) m_T at 3rd $E_\mathrm{T}^\mathrm{miss}$ slice [200, 250] GeV.
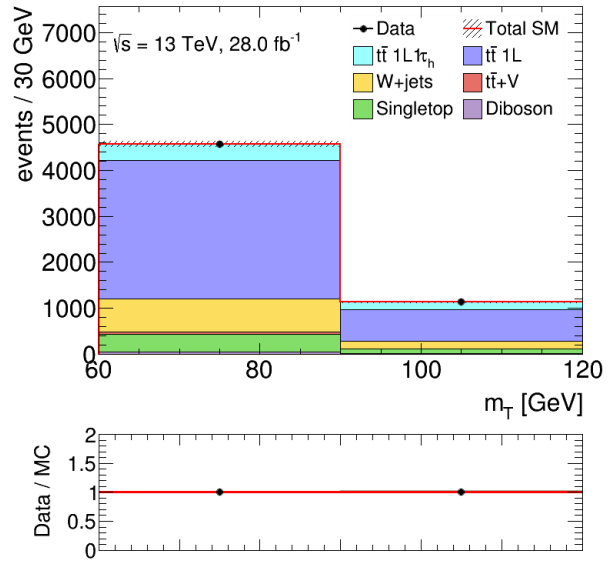
(d) m_T at 4th $E_\mathrm{T}^\mathrm{miss}$ slice [250, inf] GeV.
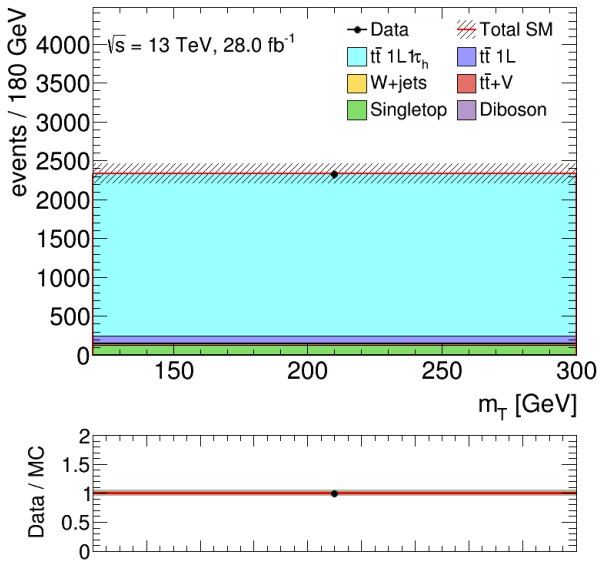
(e) m_T at TAUCR.

Figure A.2: m_T distribution with blind at each $E_\mathrm{T}^\mathrm{miss}$ slice after the validation fit. The uncertainty band includes statistical and systematic error.
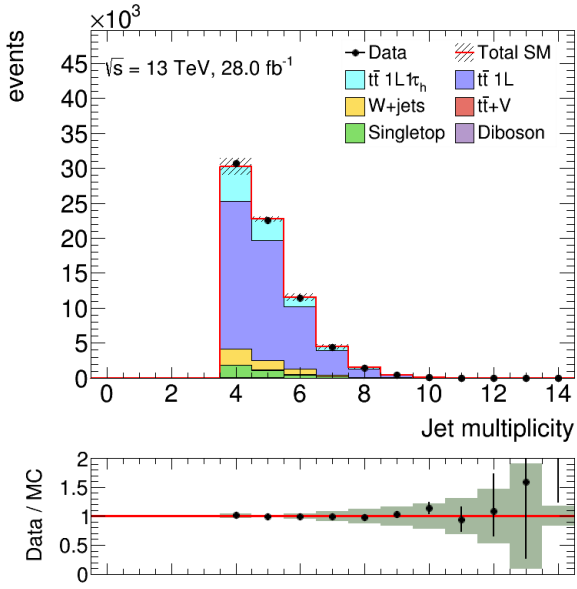
(a) jet multiplicity at 1st E_T^{miss} slice [100, 150] GeV.
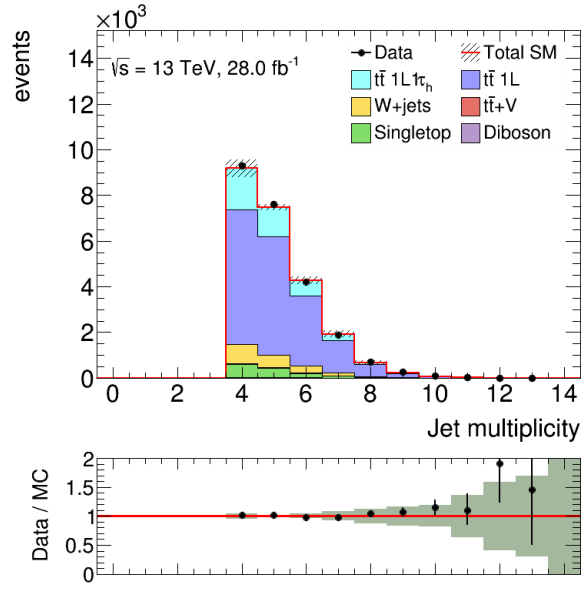
(b) jet multiplicity at 2nd E_T^{miss} slice [150, 200] GeV.
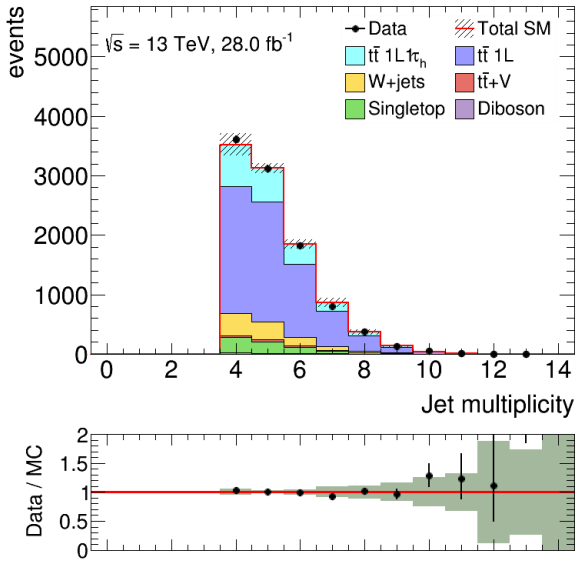
(c) jet multiplicity at 3rd E_T^{miss} slice [200, 250] GeV.
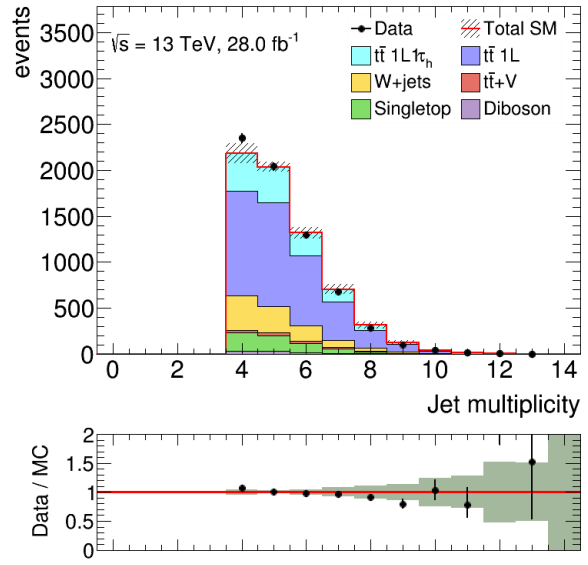
(d) jet multiplicity at 4th E_T^{miss} slice [250, inf] GeV.
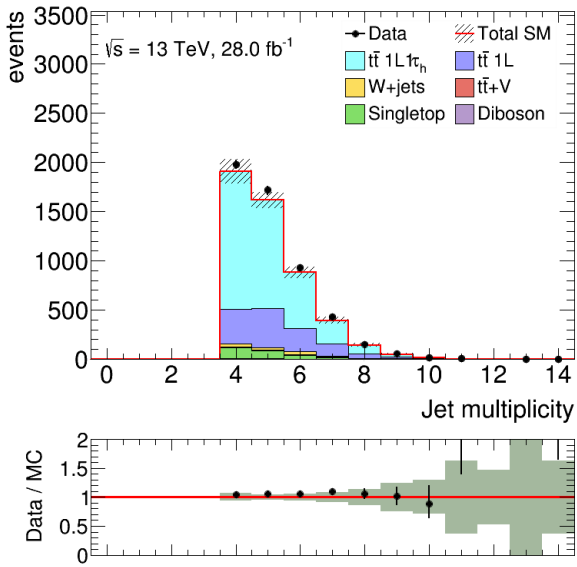
(e) jet multiplicity at TAUCR.

Figure A.3: jet multiplicity distribution at each E_T^{miss} slice after the validation fit. The uncertainty band includes statistical and systematic error.
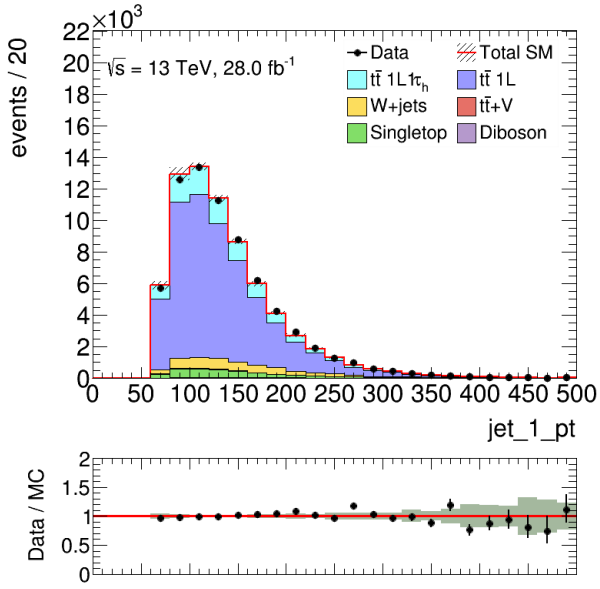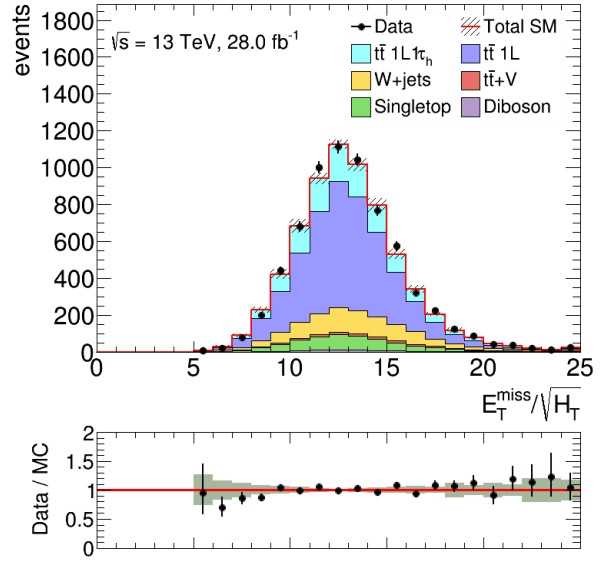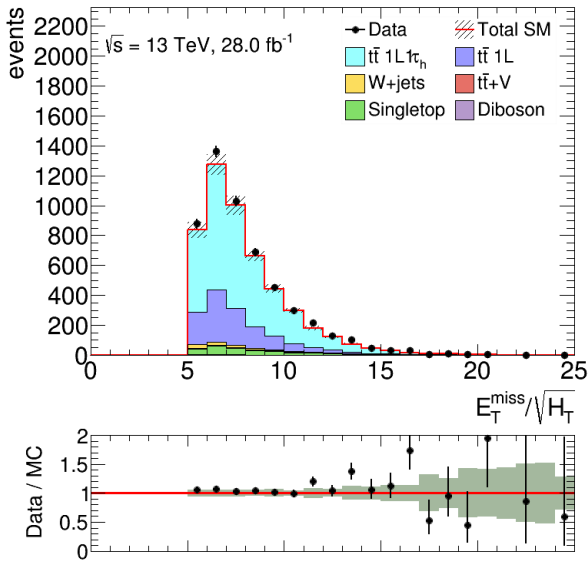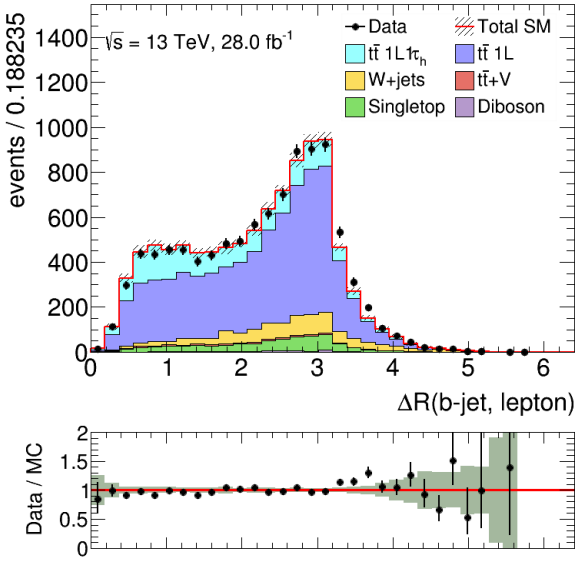
(a) 1st jet p_T at 1st E_T^{miss} slice [100, 150] GeV.
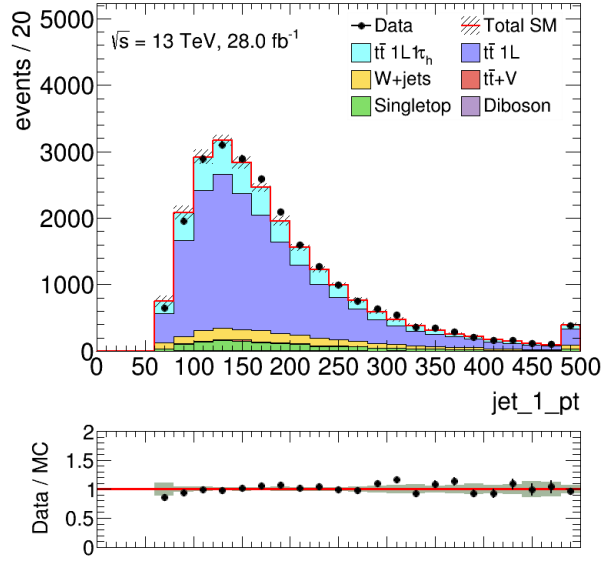
(b) 1st jet p_T at 2nd E_T^{miss} slice [150, 200] GeV.
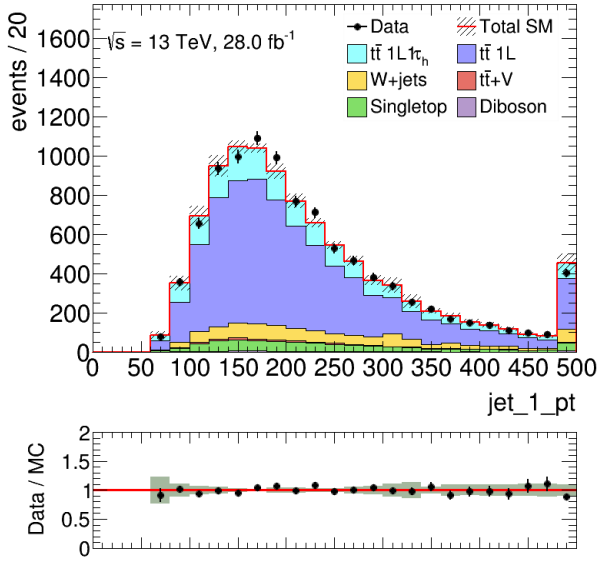
(c) 1st jet p_T at 3rd E_T^{miss} slice [200, 250] GeV.
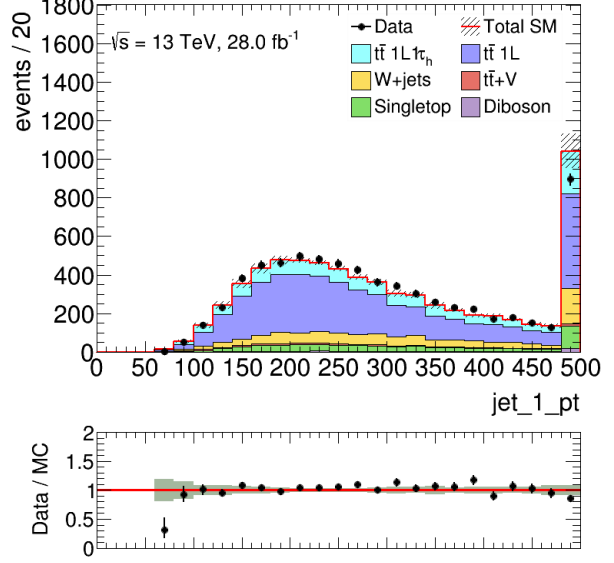
(d) 1st jet p_T at 4th E_T^{miss} slice [250, inf] GeV.
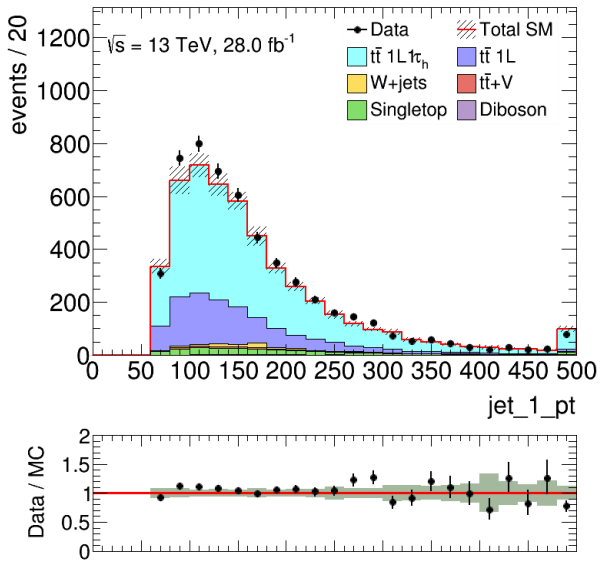
(e) 1st jet p_T at TAUCR.

Figure A.4: 1st jet p_T distribution at each E_T^{miss} slice after the validation fit. The uncertainty band includes statistical and systematic error.
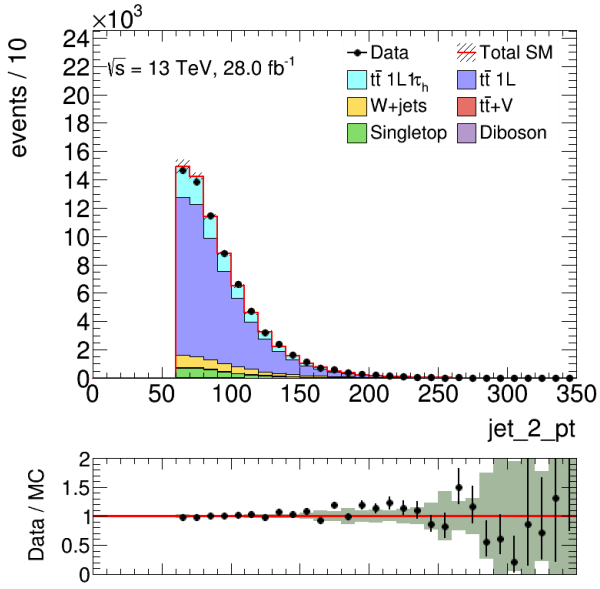
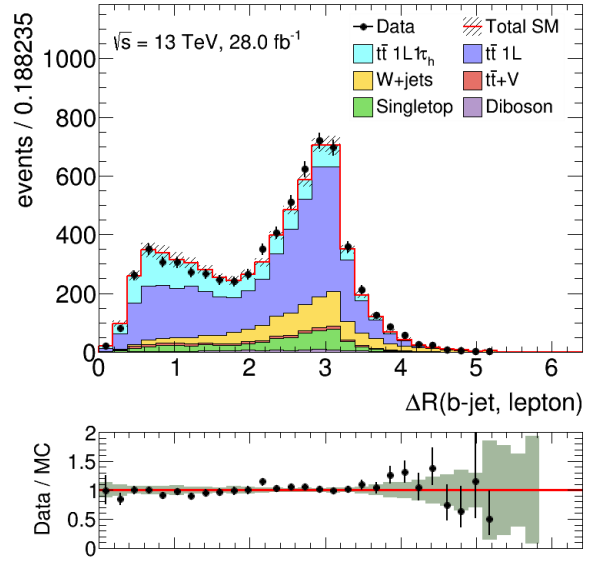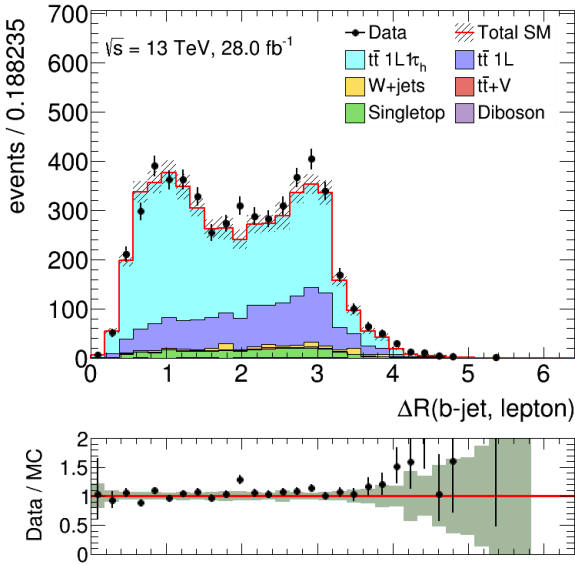(a) 2nd jet p_T at 1st E_T^{miss} slice [100, 150] GeV.
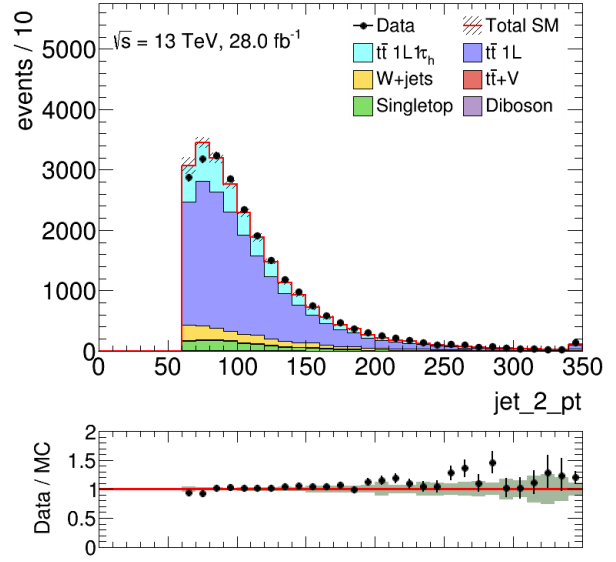
(b) 2nd jet p_T at 2nd E_T^{miss} slice [150, 200] GeV.
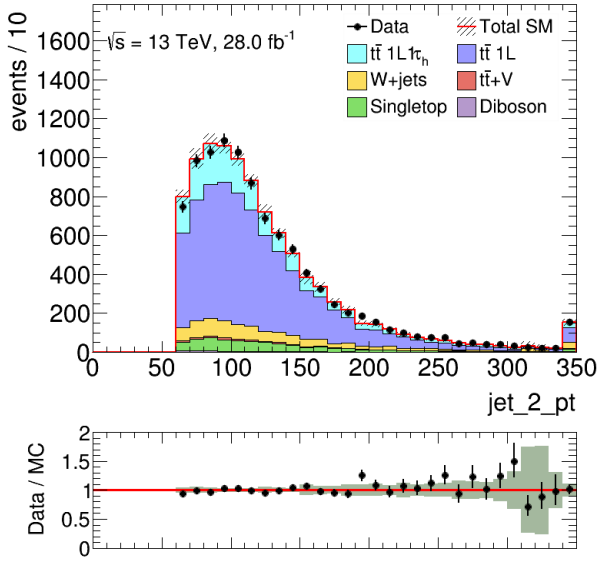
(c) 2nd jet p_T at 3rd E_T^{miss} slice [200, 250] GeV.
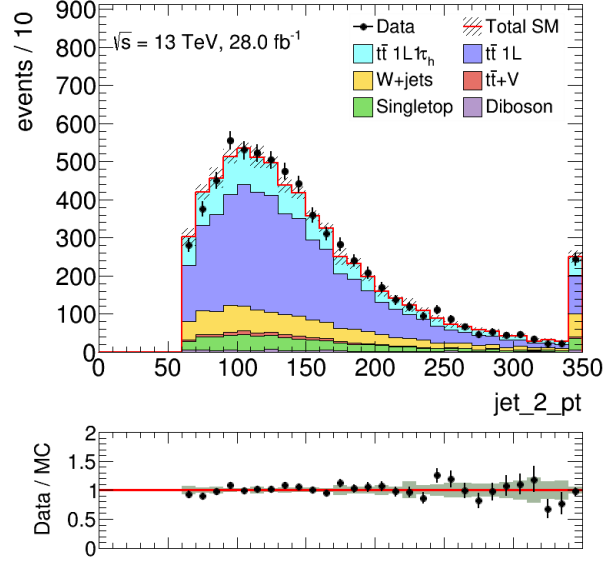
(d) 2nd jet p_T at 4th E_T^{miss} slice [250, inf] GeV.
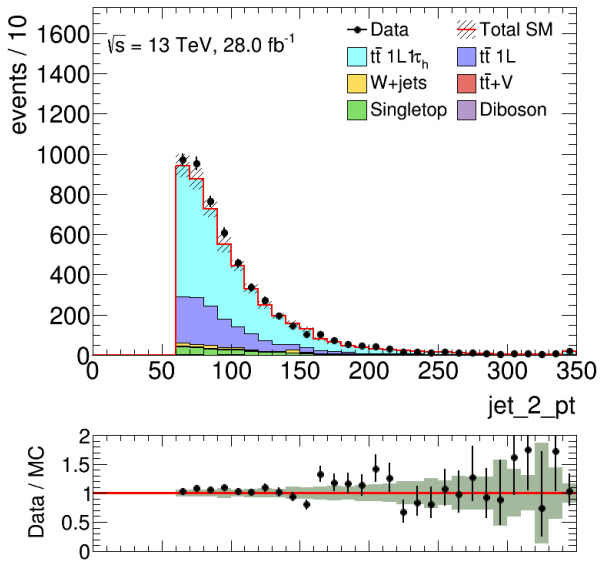
(e) 2nd jet p_T at TAUCR.

Figure A.5: 2nd jet p_T distribution at each E_T^{miss} slice after the validation fit. The uncertainty band includes statistical and systematic error.
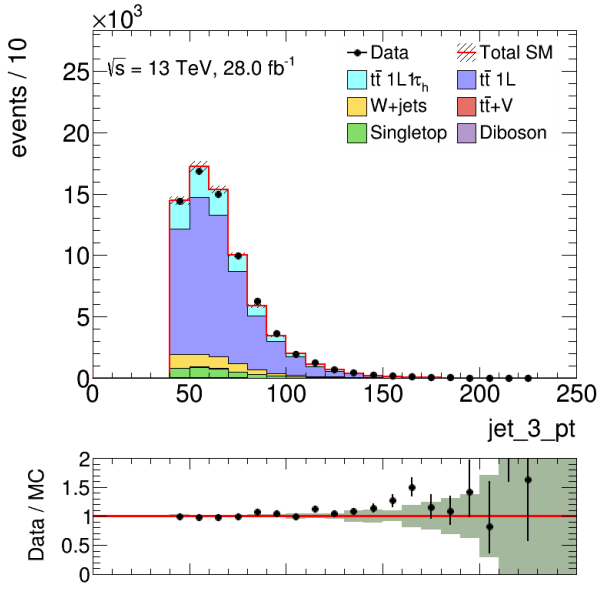
(a) 2nd jet p_T at 1st E_T^{miss} slice [100, 150] GeV.
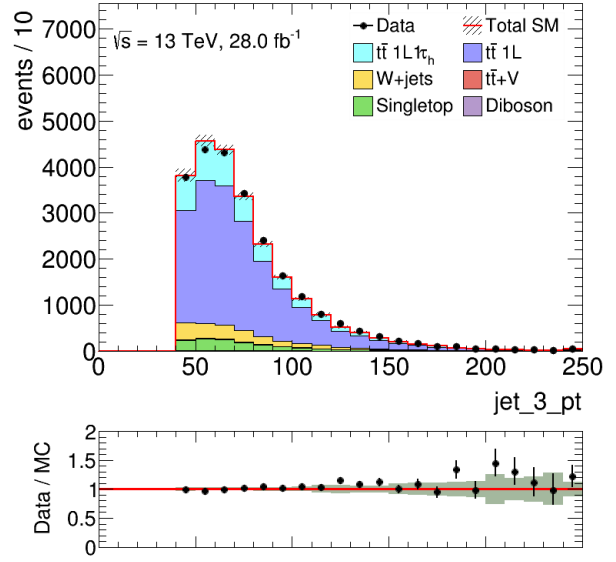
(b) 2nd jet p_T at 2nd E_T^{miss} slice [150, 200] GeV.
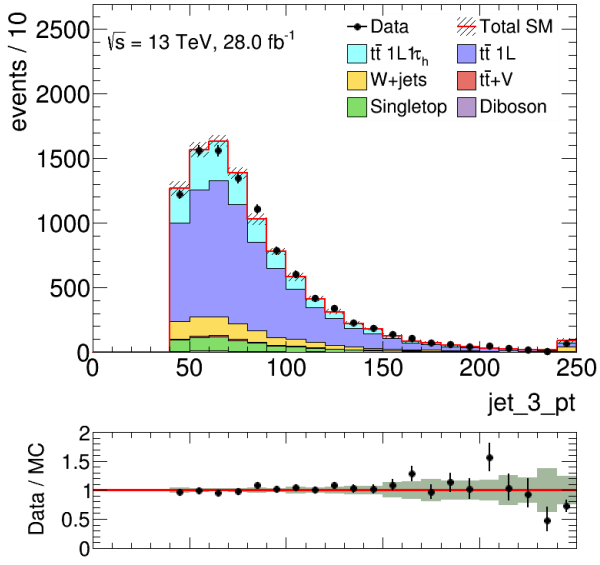
(c) 2nd jet p_T at 3rd E_T^{miss} slice [200, 250] GeV.
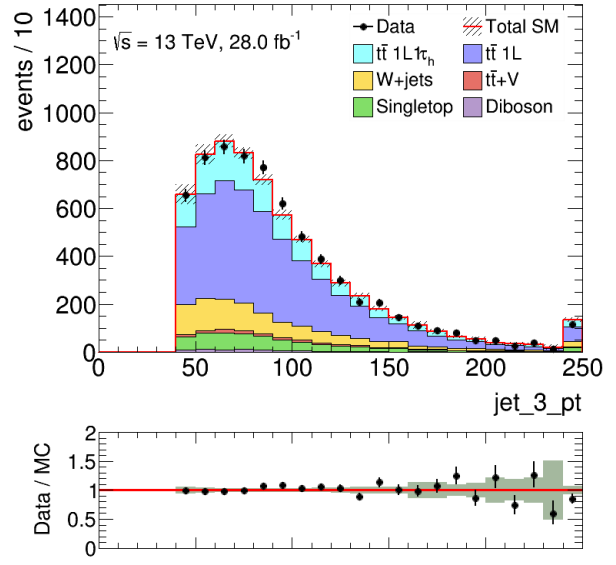
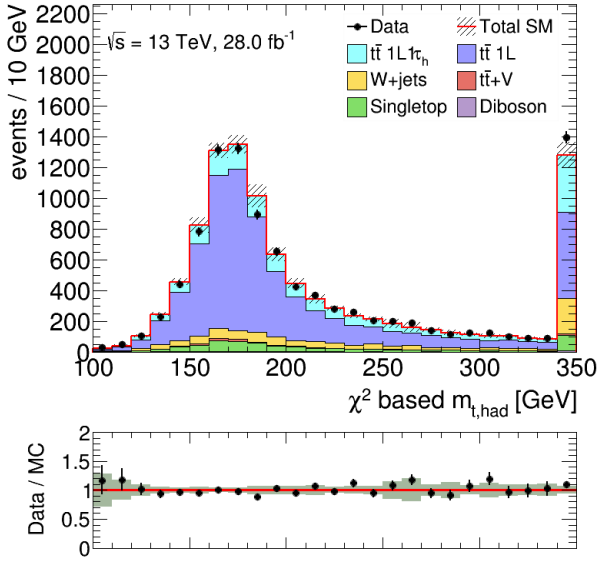(d) 2nd jet p_T at 4th E_T^{miss} slice [250, inf] GeV.
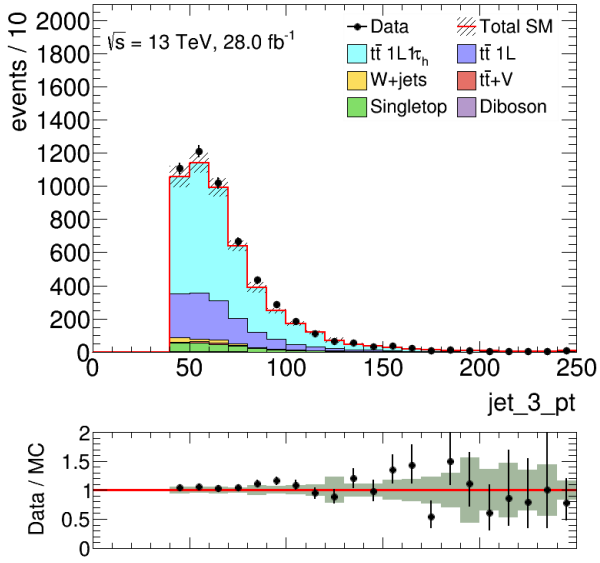
(e) 3rd jet p_T at TAUCR.

Figure A.6: 3rd jet p_T distribution at each E_T^{miss} slice after the validation fit. The uncertainty band includes statistical and systematic error.
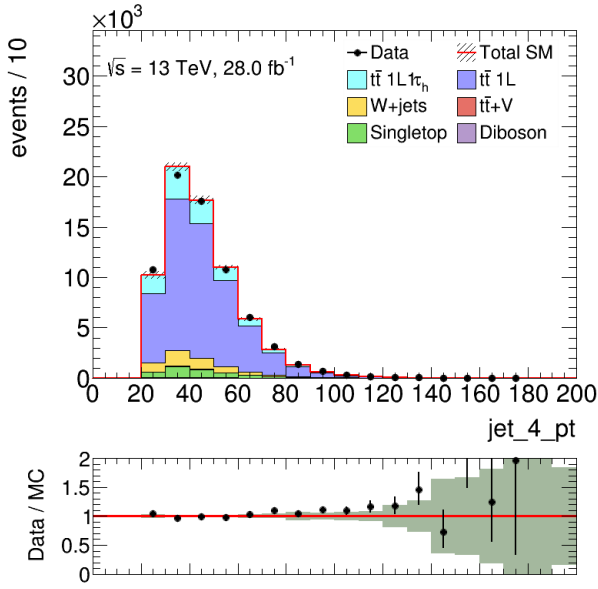
(a) 2nd jet p_T at 1st E_T^{miss} slice [100, 150] GeV.
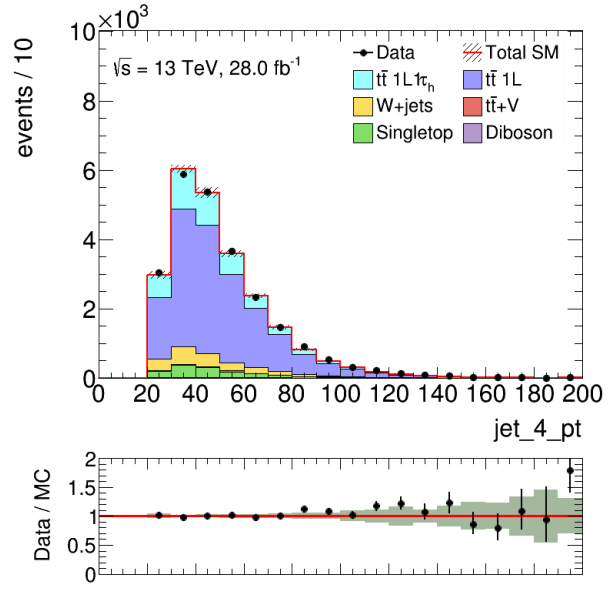
(b) 2nd jet p_T at 2nd E_T^{miss} slice [150, 200] GeV.
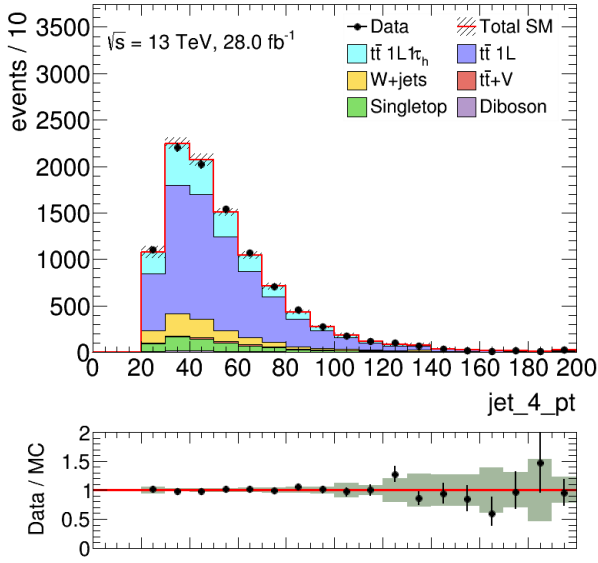
(c) 2nd jet p_T at 3rd E_T^{miss} slice [200, 250] GeV.
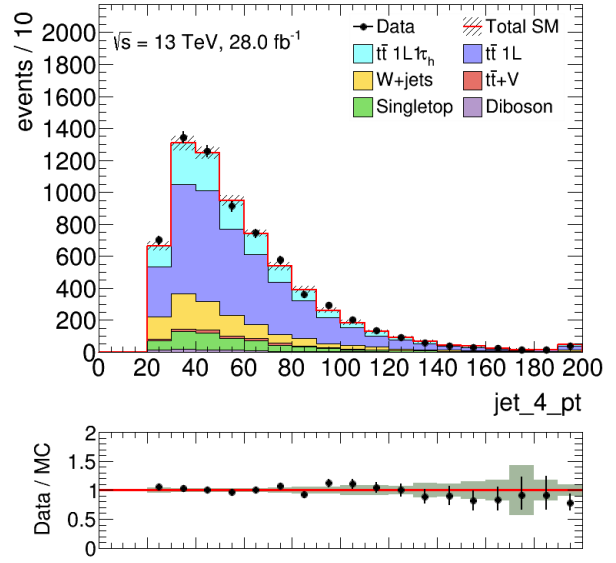
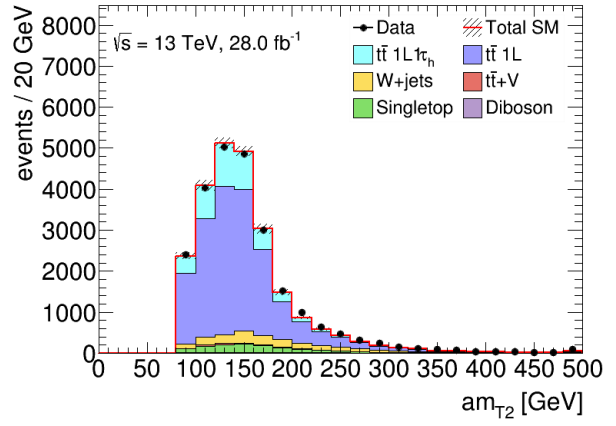(d) 2nd jet p_T at 4th E_T^{miss} slice [250, inf] GeV.
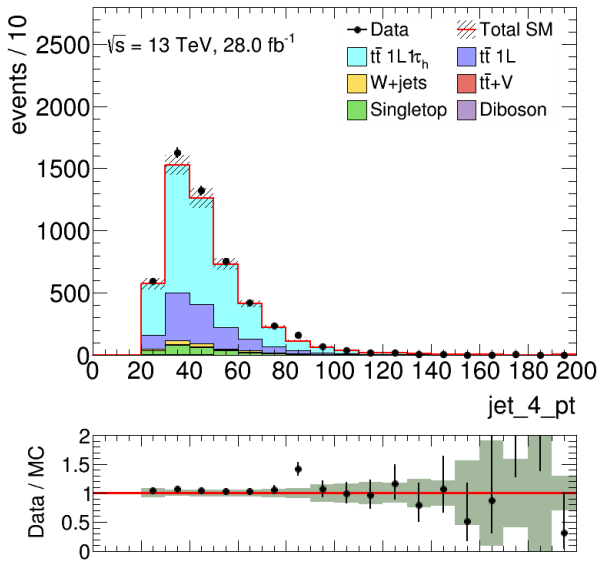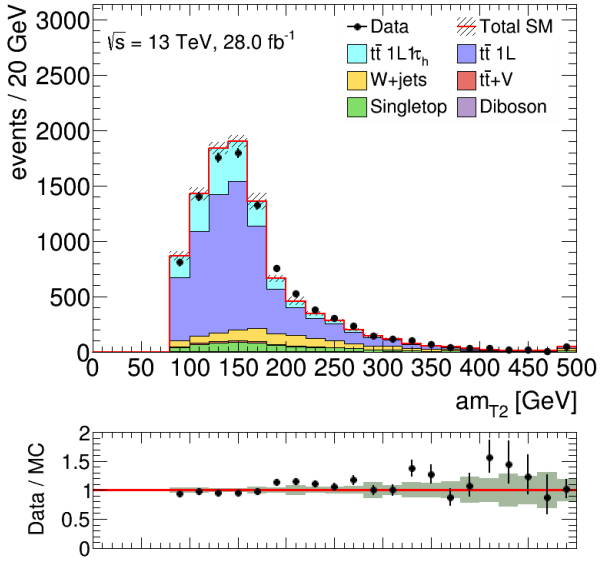
(e) 4th jet p_T at TAUCR.

Figure A.7: 4th jet p_T distribution at each E_T^{miss} slice after the validation fit. The uncertainty band includes statistical and systematic error.

144
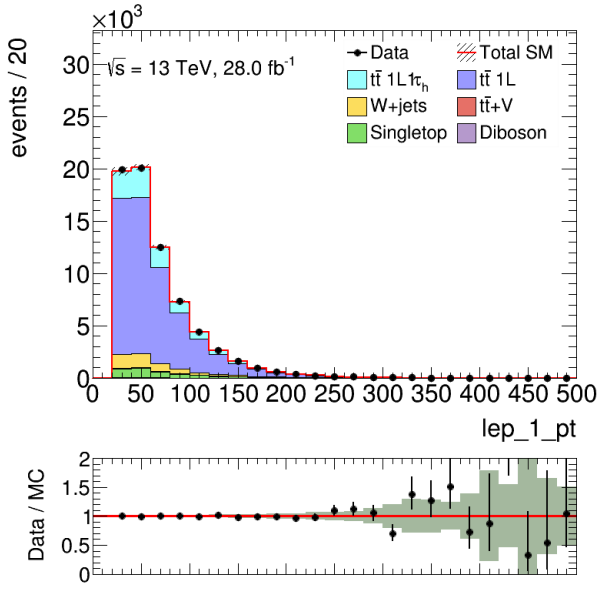
(a) lepton p_{T} at 1st $E_{\mathrm{T}}^{\mathrm{miss}}$ slice [100, 150] GeV.
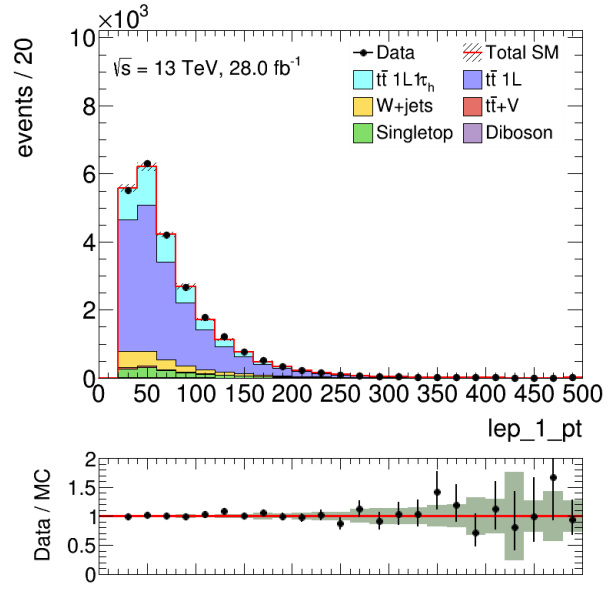
(b) lepton p_{T} at 2nd $E_{\mathrm{T}}^{\mathrm{miss}}$ slice [150, 200] GeV.
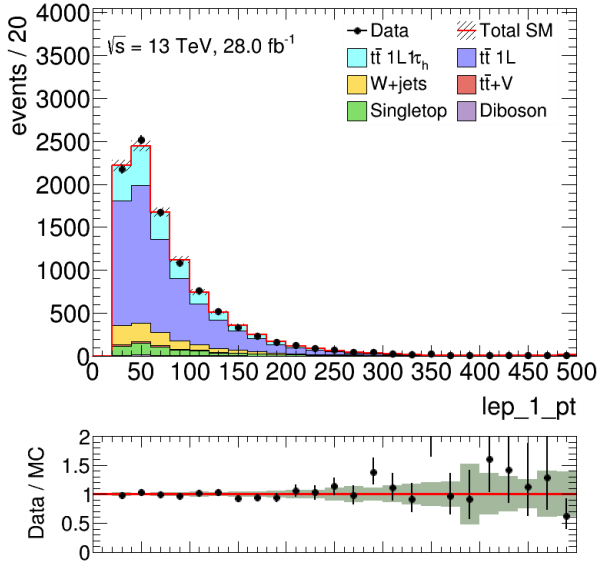
(c) lepton p_{T} at 3rd $E_{\mathrm{T}}^{\mathrm{miss}}$ slice [200, 250] GeV.
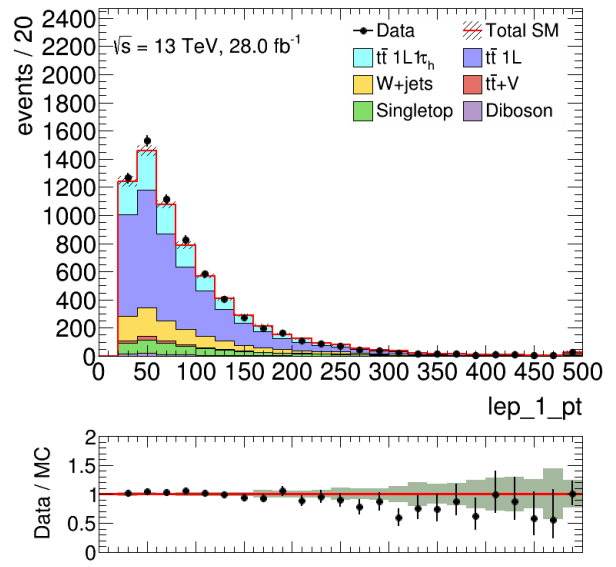
(d) lepton p_{T} at 4th $E_{\mathrm{T}}^{\mathrm{miss}}$ slice [250, inf] GeV.
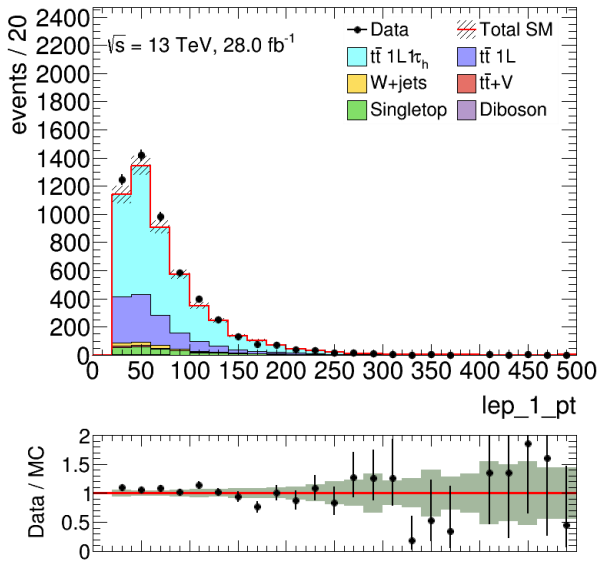
(e) lepton p_{T} at TAUCR.

Figure A.8: lepton p_{T} distribution at each $E_{\mathrm{T}}^{\mathrm{miss}}$ slice after the validation fit. The uncertainty band includes statistical and systematic error.
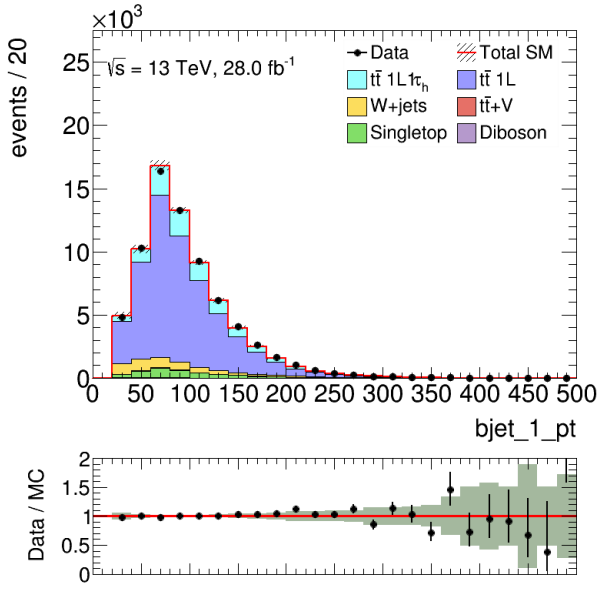
(a) 1st b-jet p_T at 1st E_T^{miss} slice [100, 150] GeV.
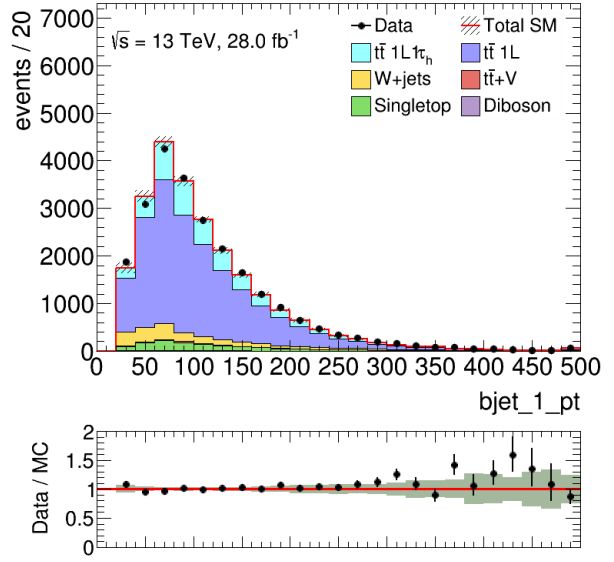
(b) 1st b-jet p_T at 2nd E_T^{miss} slice [150, 200] GeV.
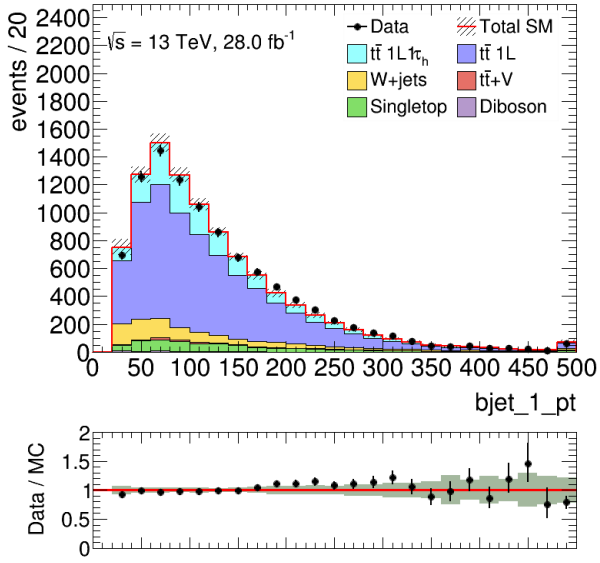
(c) 1st b-jet p_T at 3rd E_T^{miss} slice [200, 250] GeV.
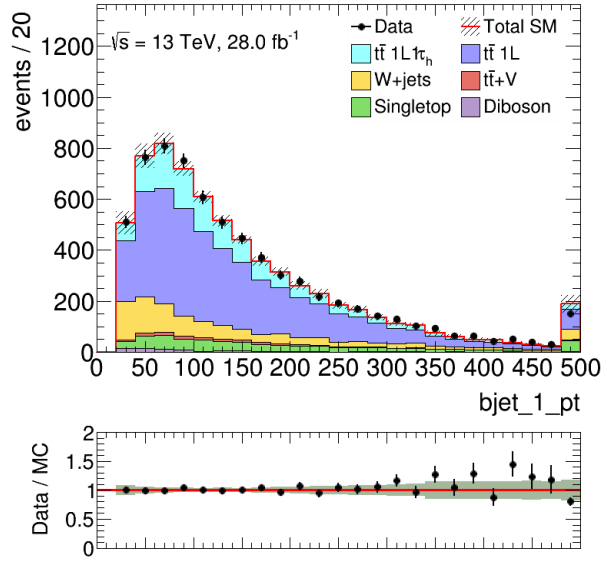
(d) 1st b-jet p_T at 4th E_T^{miss} slice [250, inf] GeV.
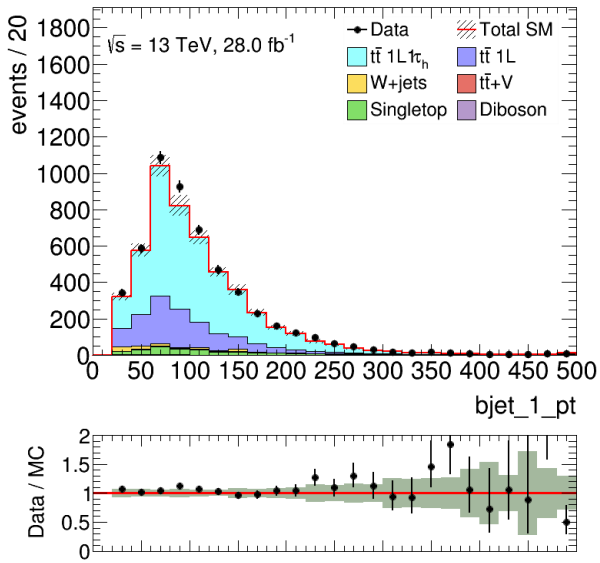
(e) 1st b-jet p_T at TAUCR.

Figure A.9: 1st b-jet p_T distribution at each E_T^{miss} slice after the validation fit. The uncertainty band includes statistical and systematic error.
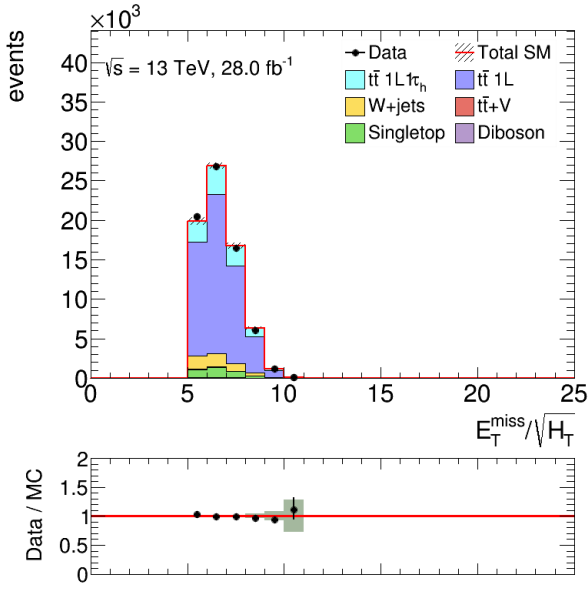
(a) $E_T^{miss}/\sqrt{H_T}$ at 1st E_T^{miss} slice [100, 150] GeV.
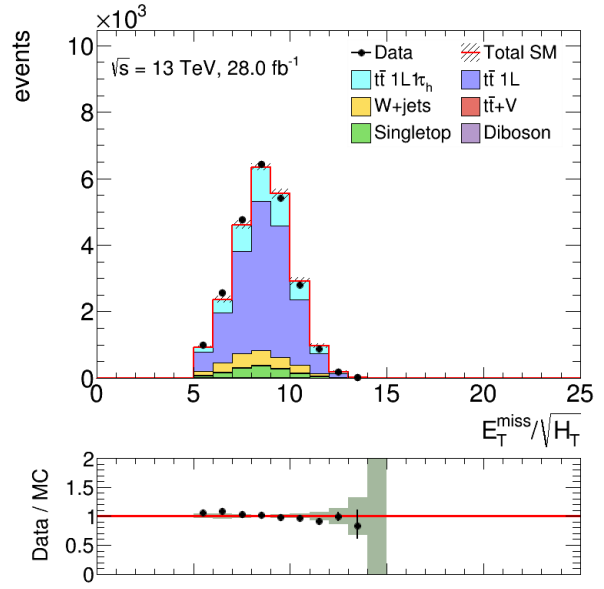
(b) $E_T^{miss}/\sqrt{H_T}$ at 2nd E_T^{miss} slice [150, 200] GeV.
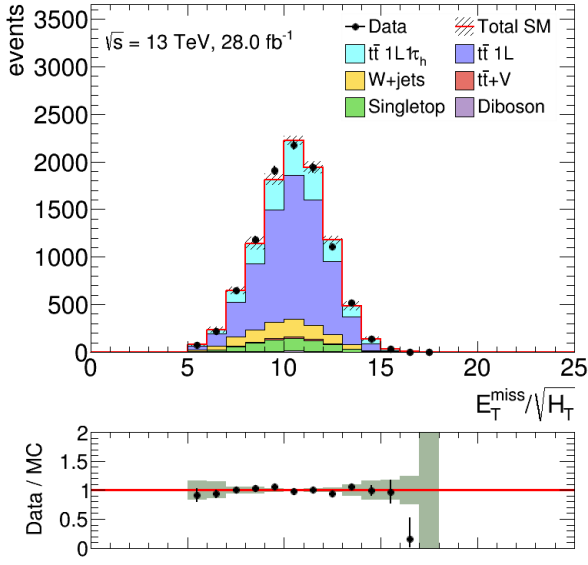
(c) $E_T^{miss}/\sqrt{H_T}$ at 3rd E_T^{miss} slice [200, 250] GeV.

(d) $E_T^{miss}/\sqrt{H_T}$ at 4th E_T^{miss} slice [250, inf] GeV.
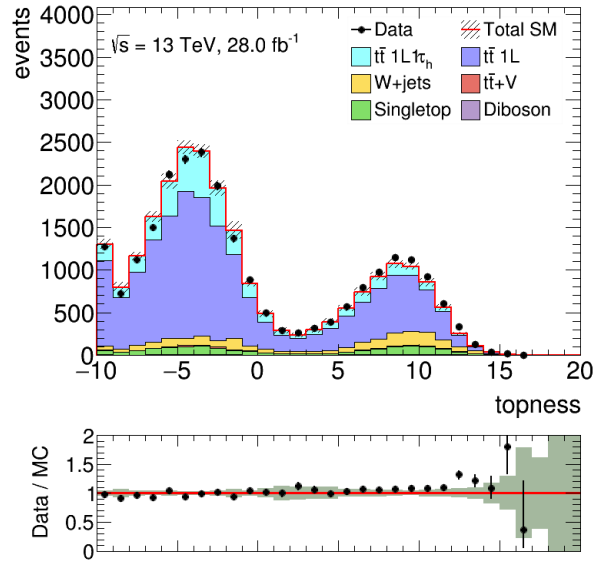
(e) $E_T^{miss}/\sqrt{H_T}$ at TAUCR.

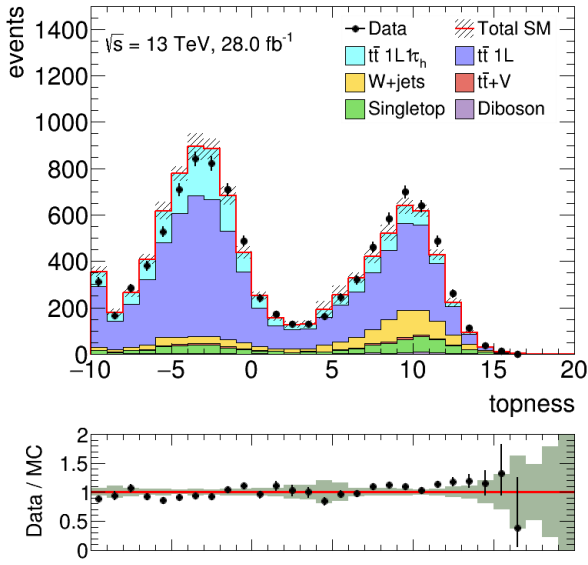Figure A.10: $E_T^{miss}/\sqrt{H_T}$ distribution at each E_T^{miss} slice after the validation fit. The uncertainty band includes statistical and systematic error.
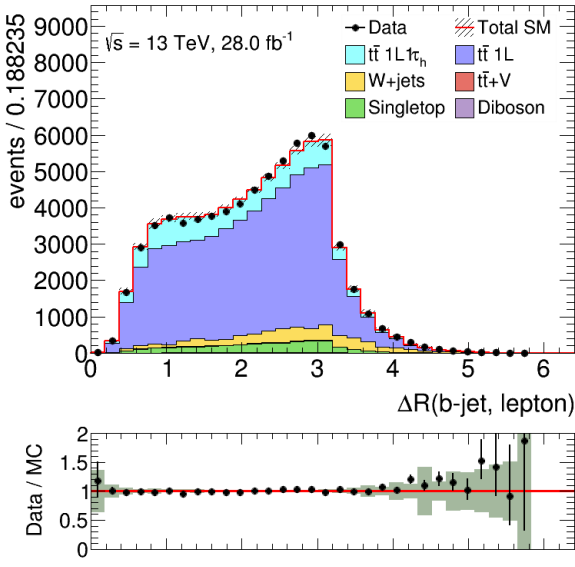
(a) $\Delta R(b, \ell)$ at 1st E_T^{miss} slice [100, 150] GeV.
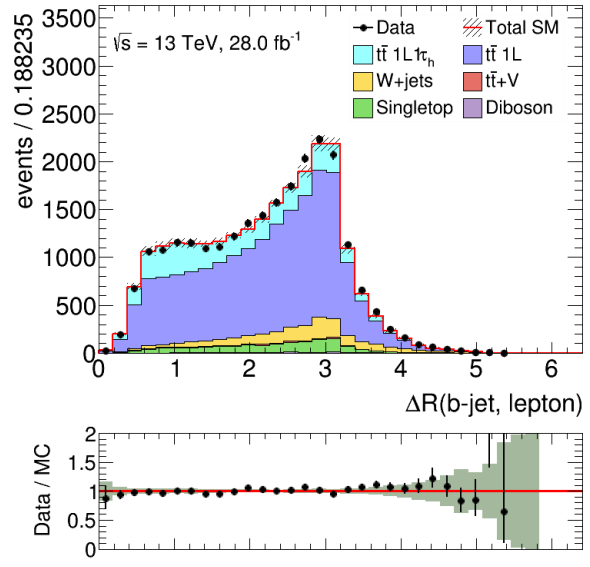
(b) $\Delta R(b, \ell)$ at 2nd E_T^{miss} slice [150, 200] GeV.

(c) $\Delta R(b, \ell)$ at 3rd E_T^{miss} slice [200, 250] GeV.

(d) $\Delta R(b, \ell)$ at 4th E_T^{miss} slice [250, inf] GeV.

(e) $\Delta R(b, \ell)$ at TAUCR.

Figure A.11: $\Delta R(b, \ell)$ distribution at each E_T^{miss} slice after the validation fit. The uncertainty band includes statistical and systematic error. These plots are just for validations of the 2-D shape fit, and not used in either the event selection or the fit.
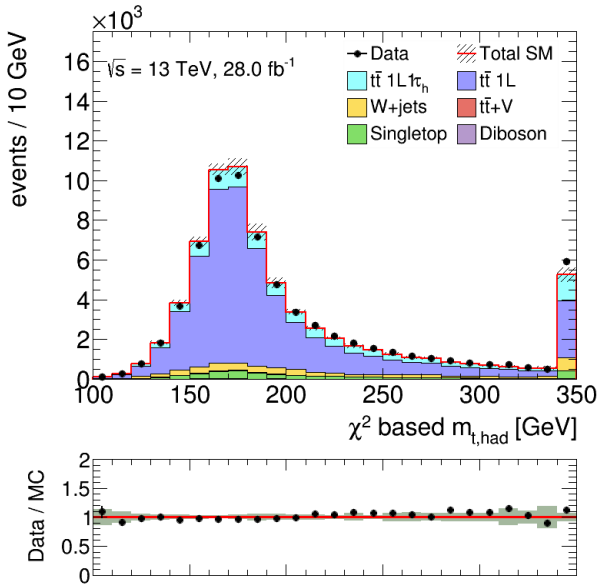
(a) m_{top}^{χ} at 1st E_T^{miss} slice [100, 150] GeV.
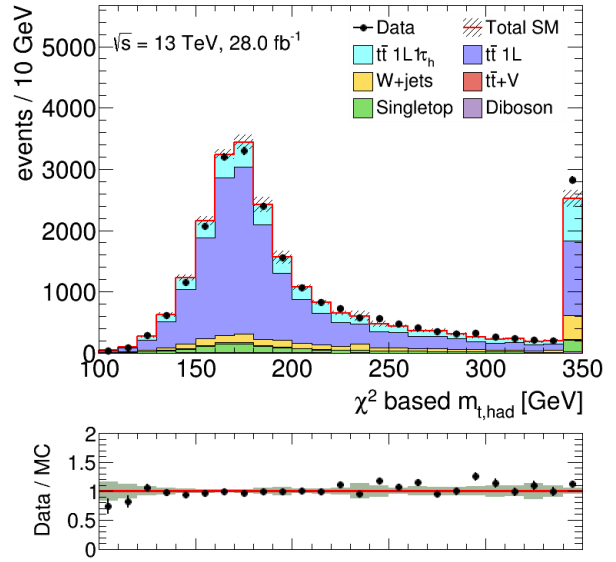
(b) m_{top}^{χ} at 2nd E_T^{miss} slice [150, 200] GeV.

(c) m_{top}^{χ} at 3rd E_T^{miss} slice [200, 250] GeV.
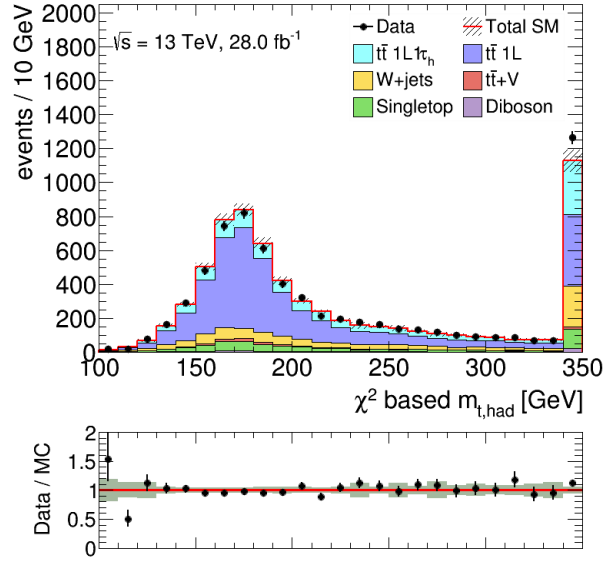
(d) m_{top}^{χ} at 4th E_T^{miss} slice [250, inf] GeV.
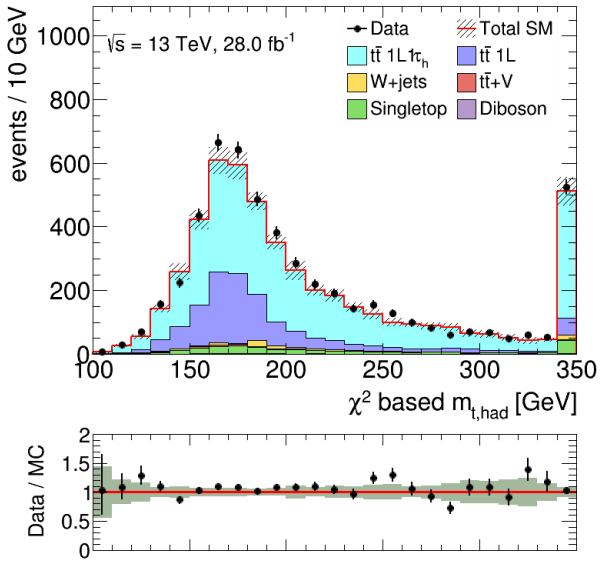
(e) m_{top}^{χ} at TAUCR.

Figure A.12: m_{top}^{χ} distribution at each E_T^{miss} slice after the validation fit. The uncertainty band includes statistical and systematic error. These plots are just for validations of the 2-D shape fit, and not used in either the event selection or the fit.
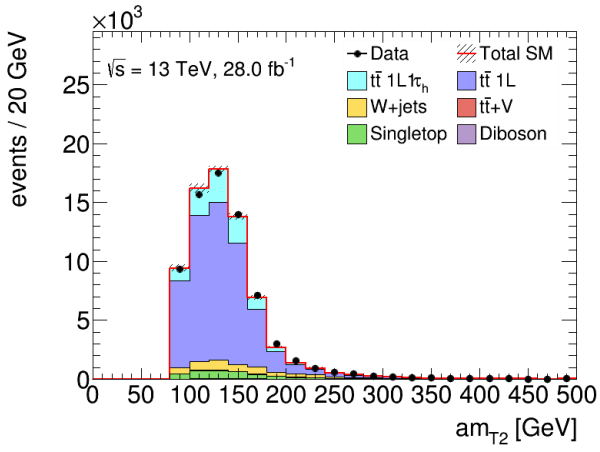
(a) am_{T2} at 1st E_T^{miss} slice [100, 150] GeV.

(b) am_{T2} at 2nd E_T^{miss} slice [150, 200] GeV.

(c) am_{T2} at 3rd E_T^{miss} slice [200, 250] GeV.
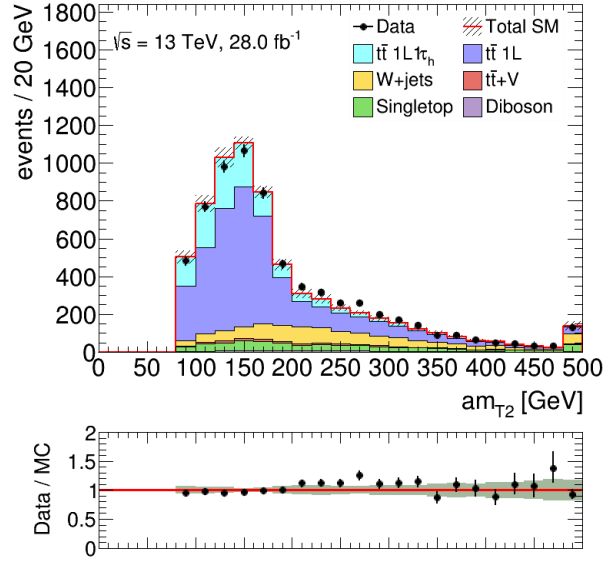
(d) am_{T2} at 4th E_T^{miss} slice [250, inf] GeV.
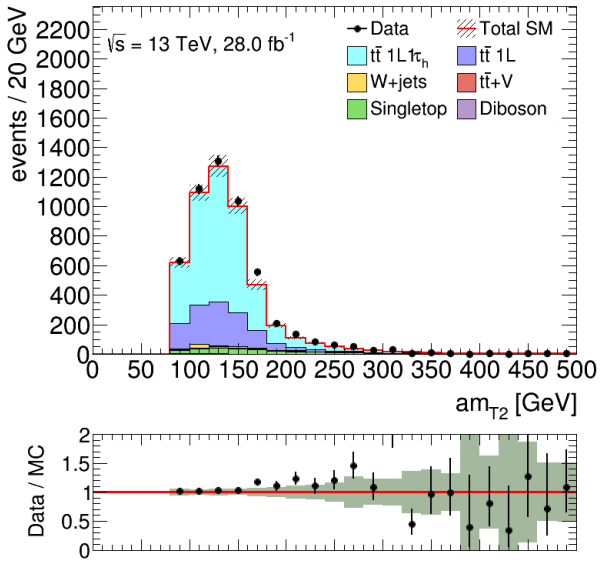
(e) am_{T2} at TAUCR.

Figure A.13: am_{T2} distribution at each E_T^{miss} slice after the validation fit. The uncertainty band includes statistical and systematic error. These plots are just for validations of the 2-D shape fit, and not used in either the event selection or the fit.
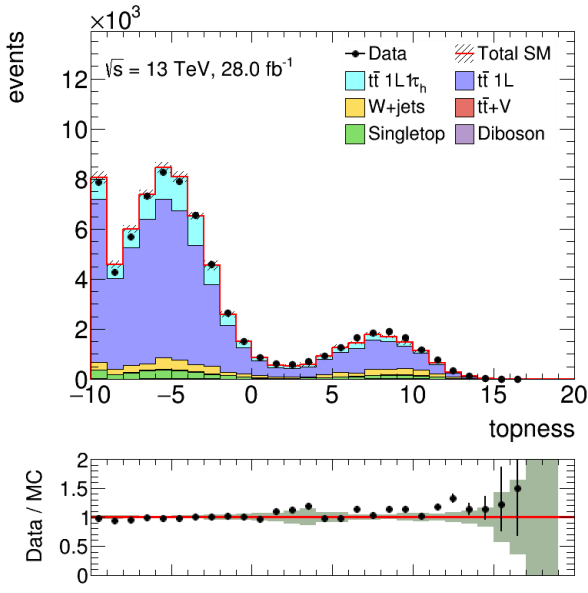
(a) *topness* at 1st E_T^{miss} slice [100, 150] GeV.

(b) *topness* at 2nd E_T^{miss} slice [150, 200] GeV.

(c) *topness* at 3rd E_T^{miss} slice [200, 250] GeV.
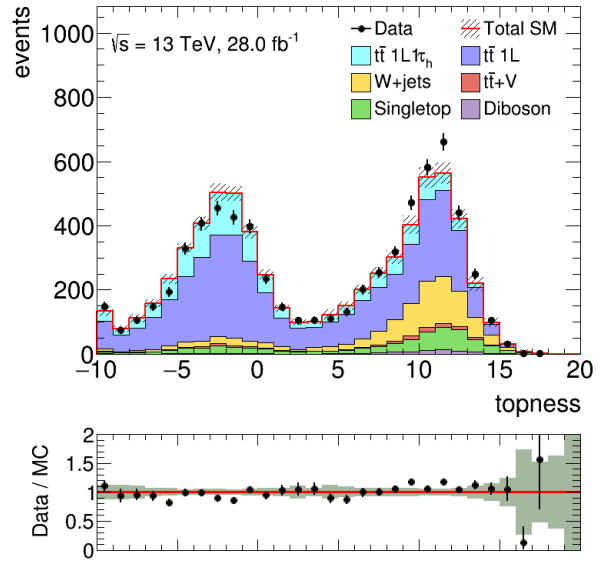
(d) *topness* at 4th E_T^{miss} slice [250, inf] GeV.
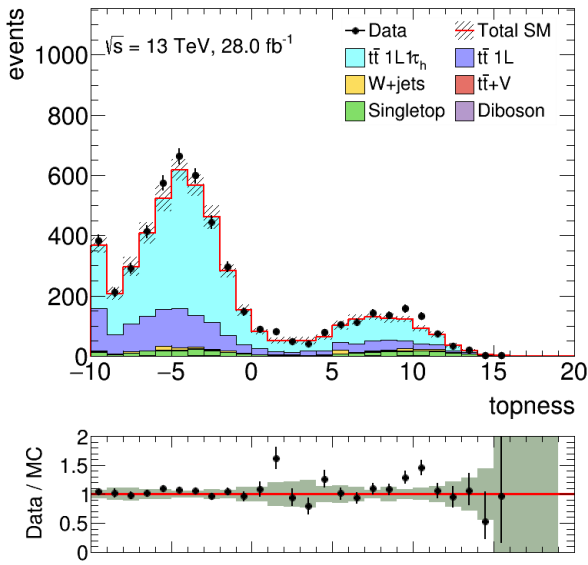
(e) *topness* at TAUCR.

Figure A.14: *topness* distribution at each E_T^{miss} slice after the validation fit. The uncertainty band includes statistical and systematic error. These plots are just for validations of the 2-D shape fit, and not used in either the event selection or the fit.
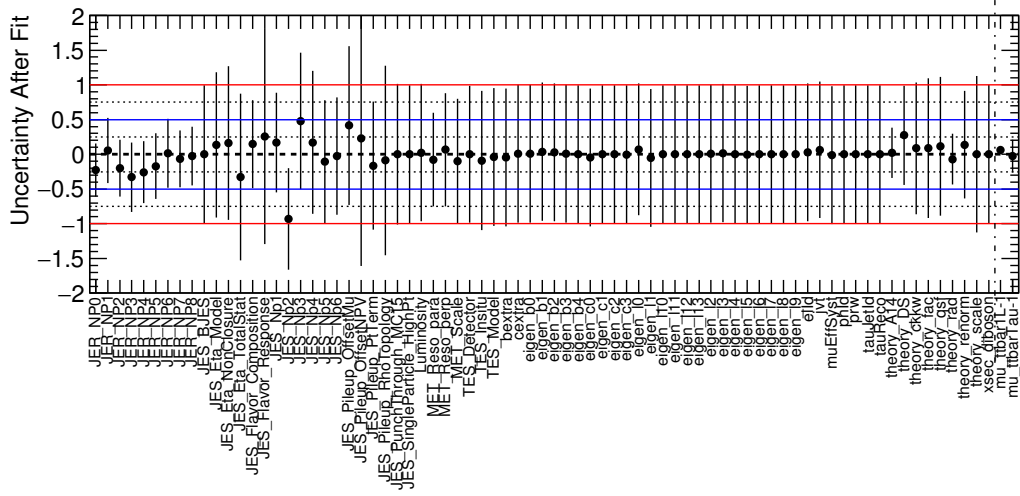
Figure A.15: Model parameters and their uncertainties after the 2-D shape validation fit. The vertical dashed-dotted line divides into two categories; standardized systematic parameters (left) and normalization scale factors (right). The naming rule of systematic parameters follow Table 8.1-8.5. For the detailed explanation on the fit configuration, see Section 7.2.
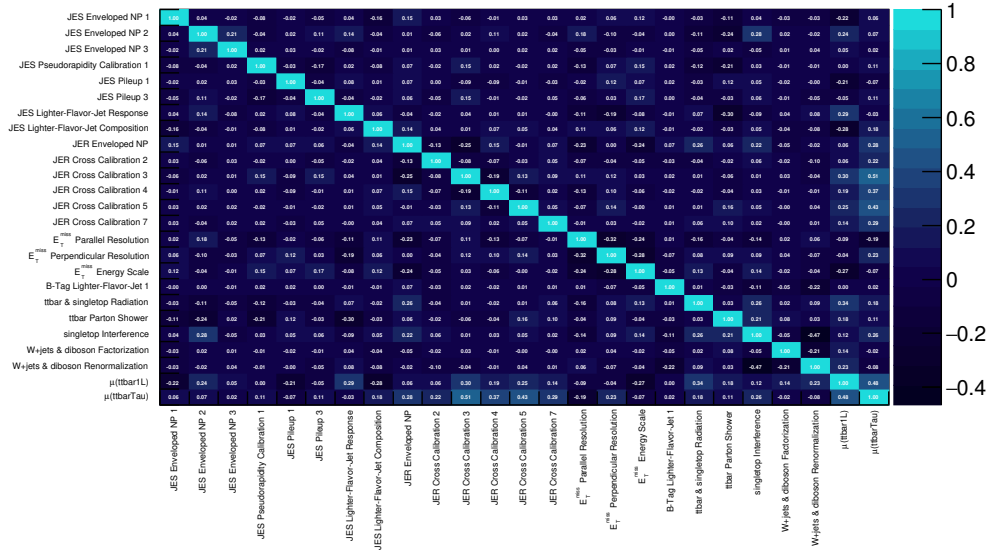
Figure A.16: Correlations among model parameters after the 2-D shape validation fit. Only parameters with at least one correlation of more than 0.2 are shown. The naming rule of systematic parameters follow Table 8.1-8.5. For the detailed explanation on the fit configuration, see Section 7.2.

Appendix B

Asymptotic Formulae for Hypothesis Test

This appendix summarizes the 'asymptotic formulae [120]' that analytically deduces probability distribution of the modified profile likelihood ratio (PLR) in Equation 7.13. The asymptotic formulae can reduce CPU time drastically compared to a traditional MC sampling method, therefore it is matched to the analysis where many nuisance parameters must be included in the model. For usefulness in the later use, two types of test statistics are defined for the purpose of discovery and exclusion declaration respectively. The test statistic used for discovery is defined as:

$$
t_0 = \begin{cases} 0 & (\hat{\mu}_{\mathrm{sig}} < 0) \\ -2 \ln \tilde{\lambda}(0) & (\hat{\mu}_{\mathrm{sig}} \geq 0) \end{cases} \tag{B.1}
$$

And the test statistic used for exclusion is defined as:

$$
t_1 = \begin{cases} 0 & (\hat{\mu}_{\mathrm{sig}} > 1) \\ -2 \ln \tilde{\lambda}(1) & (\hat{\mu}_{\mathrm{sig}} \leq 1) \end{cases} \tag{B.2}
$$

To construct the probability distribution of t_0 (t_1) to calculate p-values for discovery (exclusion), the asymptotic formulae [120] are used in the analysis instead of a traditional MC sampling method. The asymptotic formulae are based on the Wald's theorem [138] where for the case there is just one POI, the following approximation of profile likelihood ratio is derived:

$$
-2 \ln \lambda(\mu_{\mathrm{sig}}) = \frac{(\mu_{\mathrm{sig}} - \hat{\mu}_{\mathrm{sig}})^2}{\sigma^2} + O(1/\sqrt{N}) \tag{B.3}
$$

where N is the number of observed events. From Equation B.3, the test statistic for discovery (Equation B.1) is approximated as:

$$
t_0 = \begin{cases} 0 & (\hat{\mu}_{\mathrm{sig}} < 0) \\ \frac{\hat{\mu}_{\mathrm{sig}}^2}{\sigma^2} & (\hat{\mu}_{\mathrm{sig}} \geq 0) \end{cases} \tag{B.4}
$$

where σ is standard deviation of $\hat{\mu}_{\mathrm{sig}}$. And the probability of the test statistic for discovery can be derived as:

$$
Prob(t_0|\mu'_{\mathrm{sig}}) = \left(1 - \Phi\left(\frac{\mu'_{\mathrm{sig}}}{\sigma}\right)\right) \delta(t_0) + \frac{1}{2} \frac{1}{\sqrt{2\pi}} \frac{1}{\sqrt{t_0}} \exp\left[-\frac{1}{2}\left(\sqrt{t_0} - \frac{\mu'_{\mathrm{sig}}}{\sigma}\right)^2\right] \tag{B.5}
$$

where Φ is standard gaussian, μ'_{sig} indicates which hypothesis is assumed true for the probability ($\mu'_{\text{sig}} = 0$ and $\mu'_{\text{sig}} = 1$ for null- and alternative-hypothesis respectively), and $\hat{\mu}_{\text{sig}}$ is assumed to follow a gaussian distribution with mean μ'_{sig} and standard deviation σ. In the case of the test of null-hypothesis ($\mu'_{\text{sig}} = 0$) to calculate CL_b, this reduces to:

$$Prob(t_0|\mu'_{\text{sig}} = 0) = \frac{1}{2}\delta(t_0) + \frac{1}{2}\frac{1}{\sqrt{2\pi}}\frac{1}{\sqrt{t_0}}e^{-\frac{t_0}{2}} \tag{B.6}$$

In the same way, the test statistic for exclusion (Equation B.2) is approximated as:

$$t_1 = \begin{cases} 0 & (\hat{\mu}_{\text{sig}} > 1) \\ \frac{(1-\hat{\mu}_{\text{sig}})^2}{\sigma^2} & (0 \leq \hat{\mu}_{\text{sig}} \leq 1) \\ \frac{1}{\sigma^2} - \frac{2\hat{\mu}_{\text{sig}}}{\sigma^2} & (\hat{\mu}_{\text{sig}} < 0) \end{cases} \tag{B.7}$$

and the probability of the test statistic for exclusion can be derived as:

$$\begin{aligned} Prob(t_1|\mu'_{\text{sig}}) &= \Phi\left(\frac{\mu'_{\text{sig}} - 1}{\sigma}\right)\delta(t_1) \\ &+ \begin{cases} \frac{1}{2}\frac{1}{\sqrt{2\pi}}\frac{1}{\sqrt{t_1}}\exp\left[-\frac{1}{2}(\sqrt{t_1} - \frac{1-\mu'_{\text{sig}}}{\sigma})^2\right] & (0 < t_1 \leq \frac{1}{\sigma^2}) \\ \frac{1}{\sqrt{2\pi}(2/\sigma)}\exp\left[-\frac{1}{2}\frac{(t_1 - (1-2\mu'_{\text{sig}})/\sigma^2)^2}{(2/\sigma)^2}\right] & (t_1 > \frac{1}{\sigma^2}) \end{cases} \end{aligned} \tag{B.8}$$

For CL_s calculation, CL_b and CL_{s+b} can be calculated by integration of $Prob(t_1|\mu'_{\text{sig}} = 0)$ and $Prob(t_1|\mu'_{\text{sig}} = 1)$. The hypothesis test with the asymptotic formulae and profile calculation are implemented in RooStats [118].

Appendix C

Systematic Uncertainty Plots for *Diagonal*

This appendix shows η modeling for *Diagonal* in detail. Since there are too many η functions ($\sim$84000), relatively important systematic variations for the dominant background $t\bar{t}$ (1L1τ_h) at each E_T^{miss} slice and TAUCR are shown in Figure C.1-C.10.
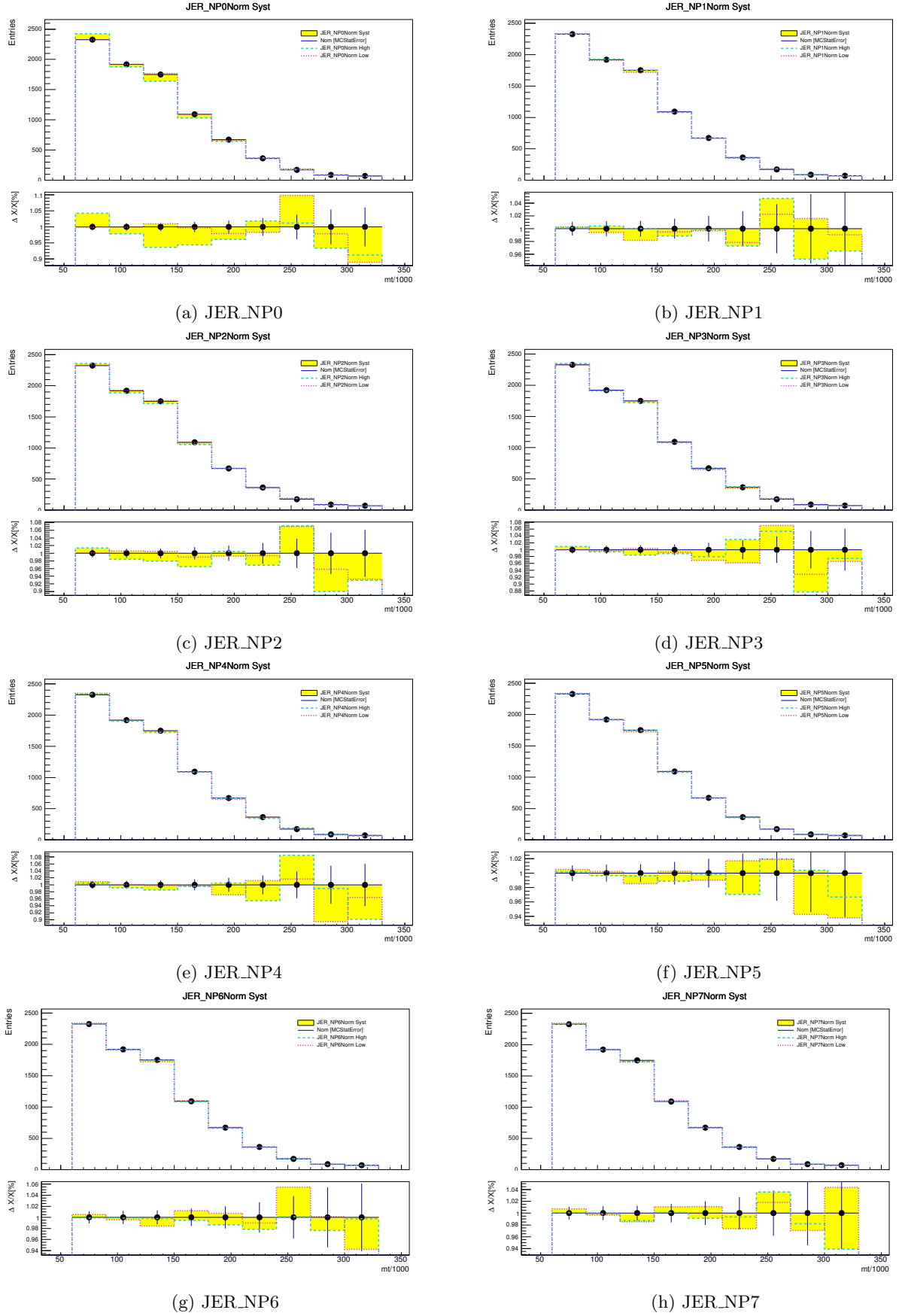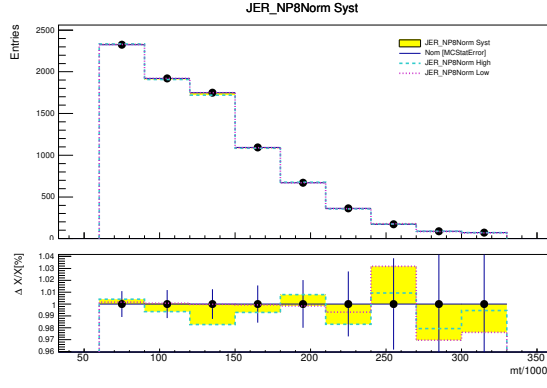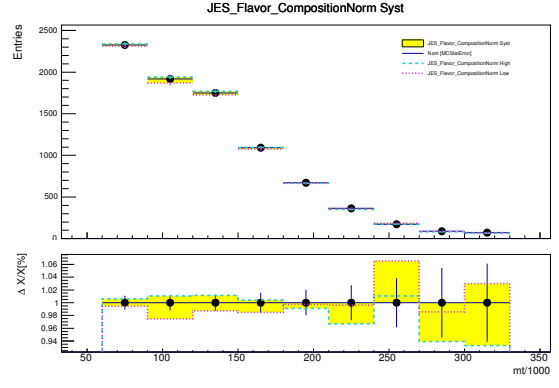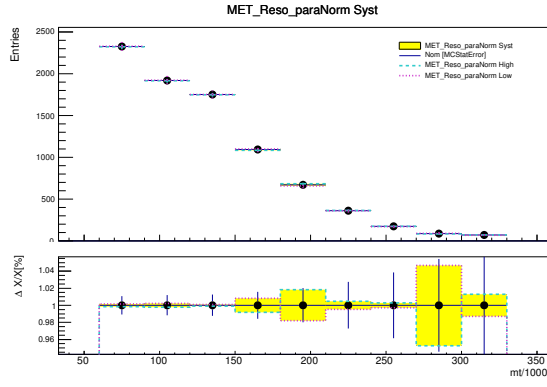
(a) JER_NP0

(b) JER_NP1

(c) JER_NP2

(d) JER_NP3

(e) JER_NP4

(f) JER_NP5

(g) JER_NP6

(h) JER_NP7

Figure C.1: Systematic variations of m_T [GeV] shape at the 1st $E_\mathrm{T}^\mathrm{miss}$ slice ([100, 150] GeV) of *Diagonal* for $t\bar{t}$ (1L1τ_h) (1/2). Each error bar indicates MC statistical error. Green and red lines indicate the $\eta(\alpha = \pm 1)$ values.
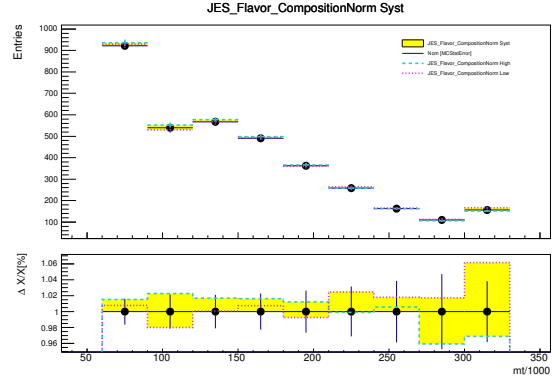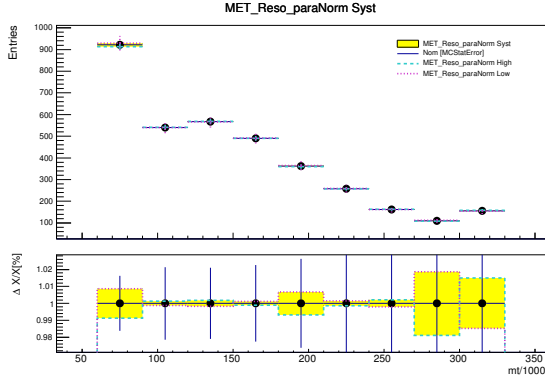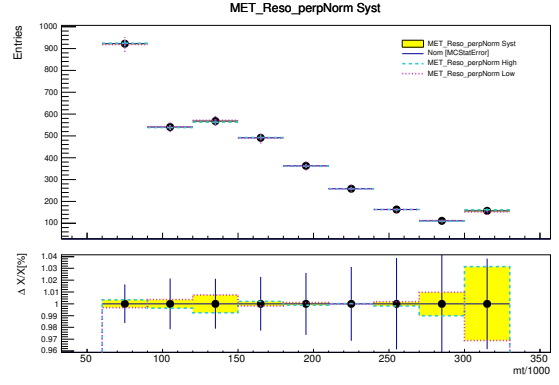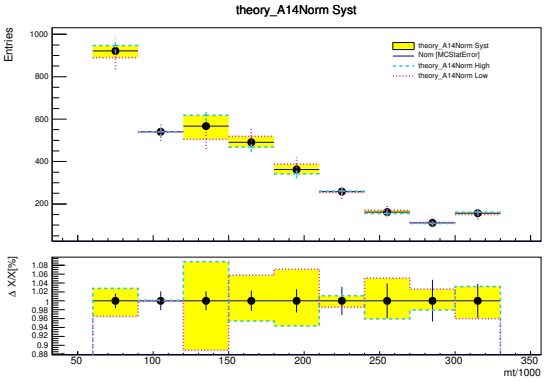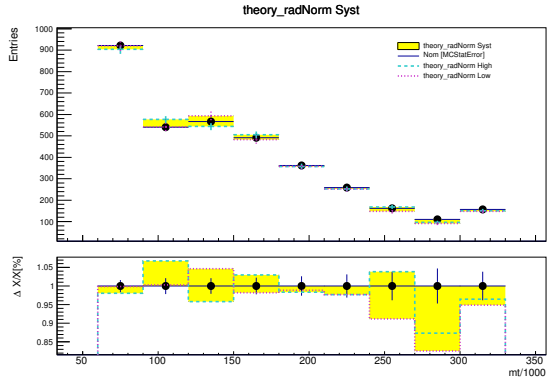
156

(a) JER_NP8

(b) JES_Flavor_Composition

(c) MET_Reso_para
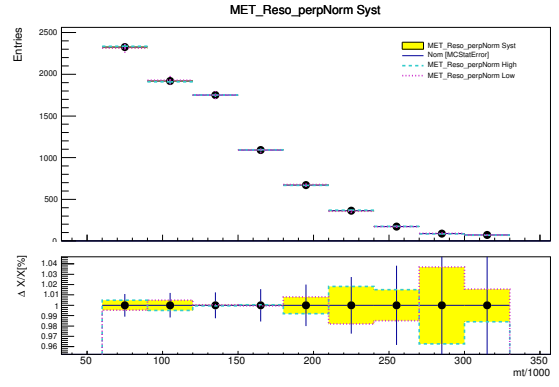
(d) MET_Reso_perp
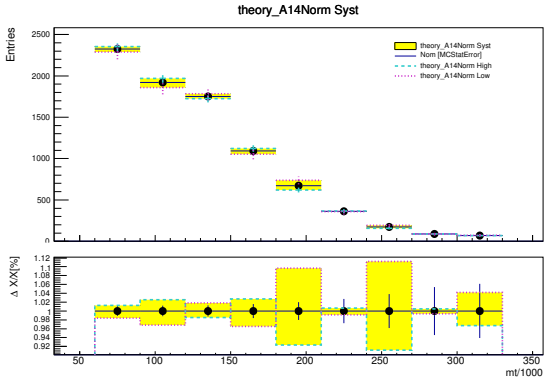
(e) theory_A14
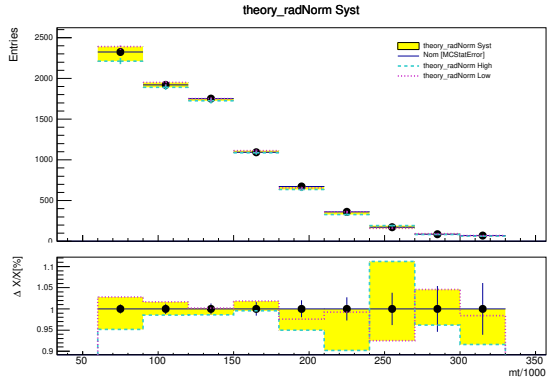
(f) theory_rad

Figure C.2: Systematic variations of m_T [GeV] shape at the 1st E_T^{miss} slice ([100, 150] GeV) of *Diagonal* for $t\bar{t}$ ($1L1\tau_h$) (2/2). Each error bar indicates MC statistical error. Green and red lines indicate the $\eta(\alpha = \pm 1)$ values.

(a) JER_NP0

(b) JER_NP1

(c) JER_NP2

(d) JER_NP3

(e) JER_NP4

(f) JER_NP5

(g) JER_NP6

(h) JER_NP7
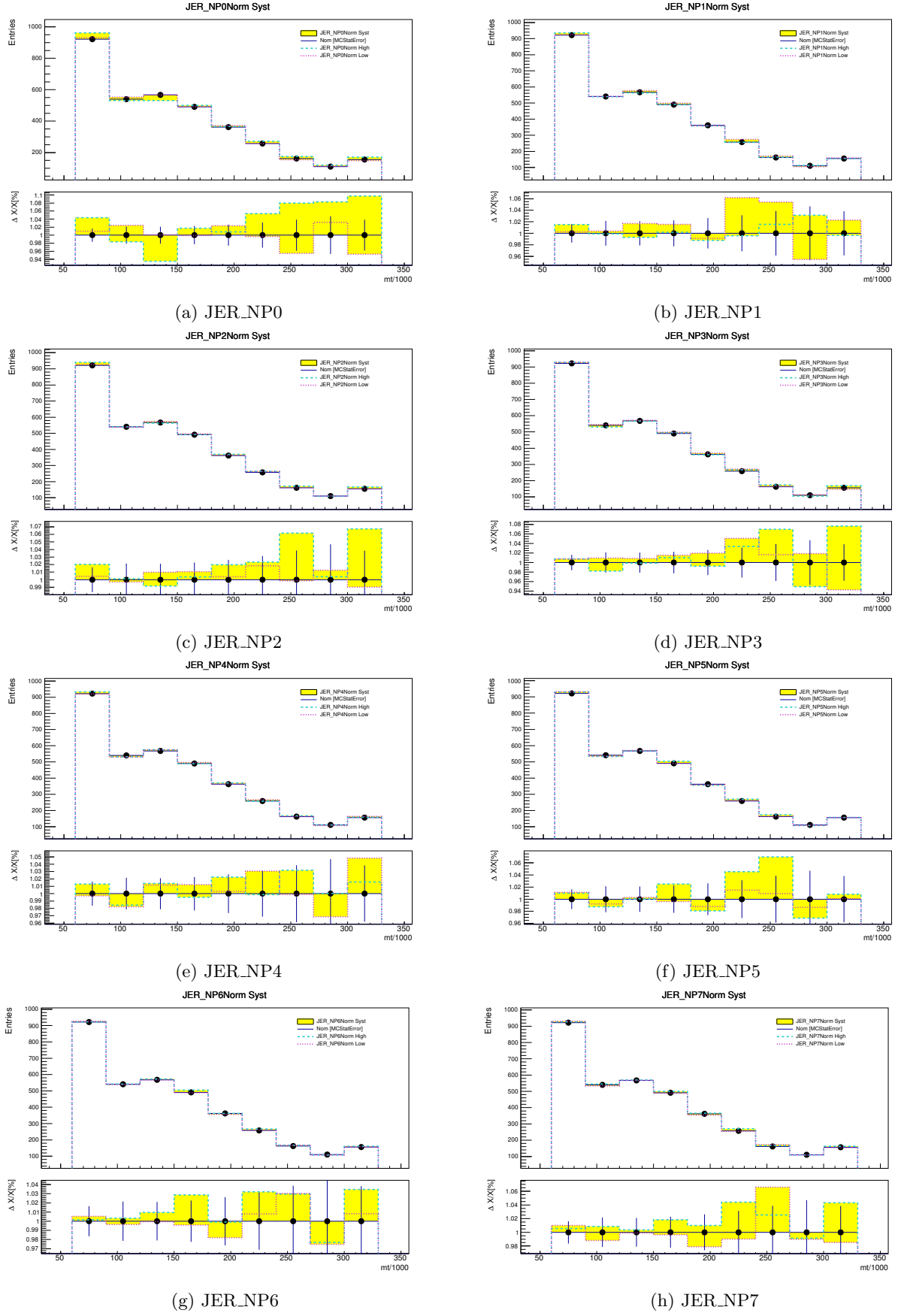
Figure C.3: Systematic variations of m_T [GeV] shape at the 2nd E_T^{miss} slice ([150, 200] GeV) of *Diagonal* for $t\bar{t}$ (1L1τ_h) (1/2). Each error bar indicates MC statistical error. Green and red lines indicate the $\eta(\alpha = \pm 1)$ values.
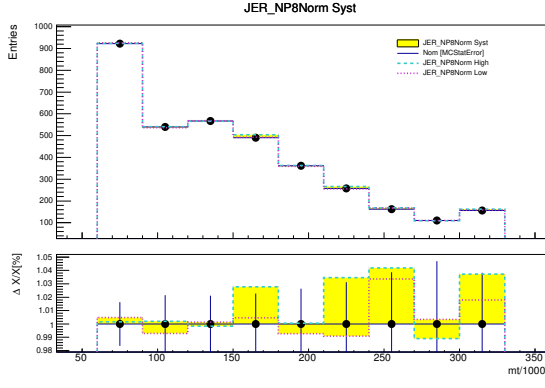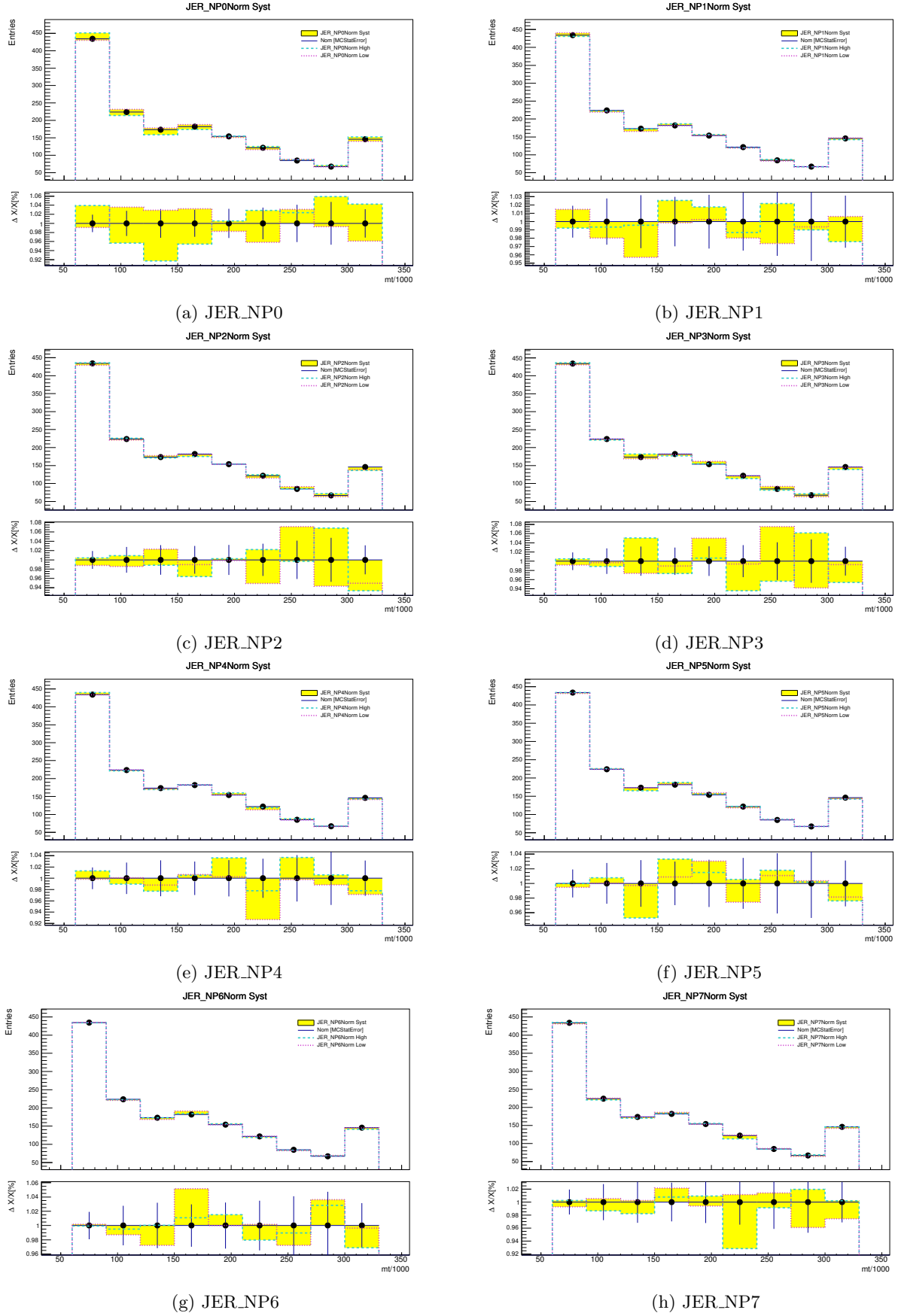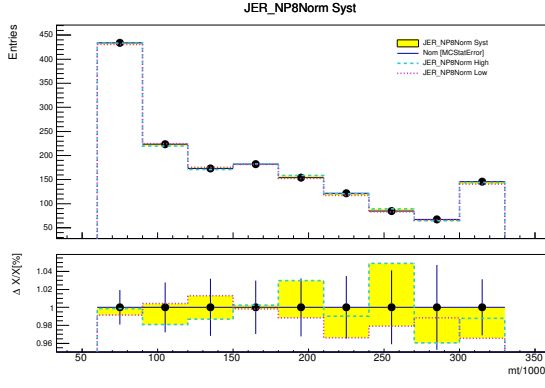
(a) JER_NP8

(b) JES_Flavor_Composition

(c) MET_Reso_para

(d) MET_Reso_perp

(e) theory_A14

(f) theory_rad

Figure C.4: Systematic variations of m_T [GeV] shape at the 2nd E_T^{miss} slice ([150, 200] GeV) of *Diagonal* for $t\bar{t}$ (1L1τ_h) (2/2). Each error bar indicates MC statistical error. Green and red lines indicate the $\eta(\alpha = \pm 1)$ values.
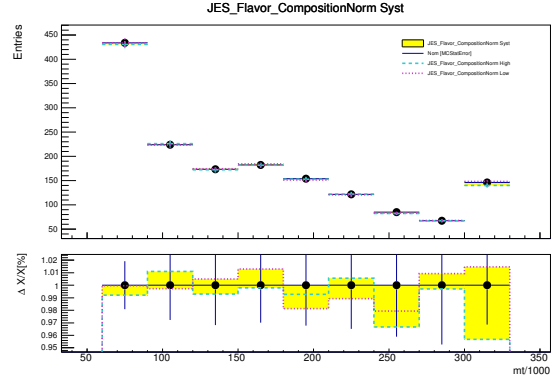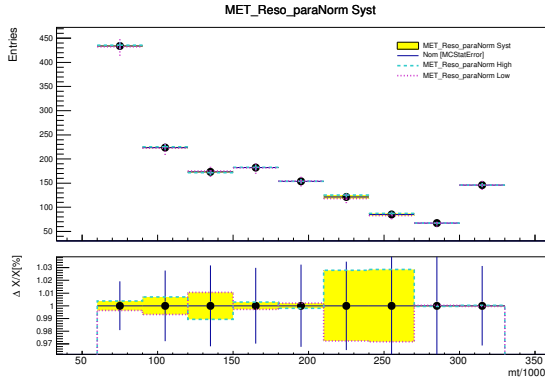
Figure C.5: Systematic variations of m_T [GeV] shape at the 3rd E_T^{miss} slice ([200, 250] GeV) of *Diagonal* for $t\bar{t}$ (1L1τ_h) (1/2). Each error bar indicates MC statistical error. Green and red lines indicate the $\eta(\alpha = \pm 1)$ values.
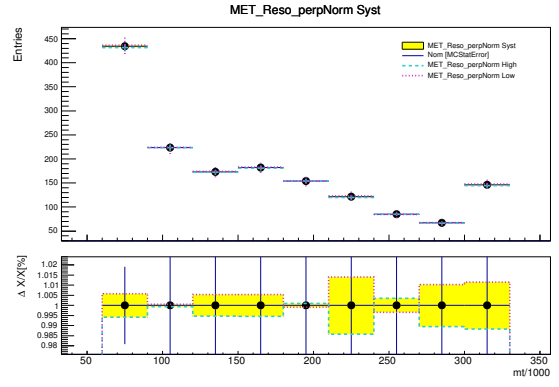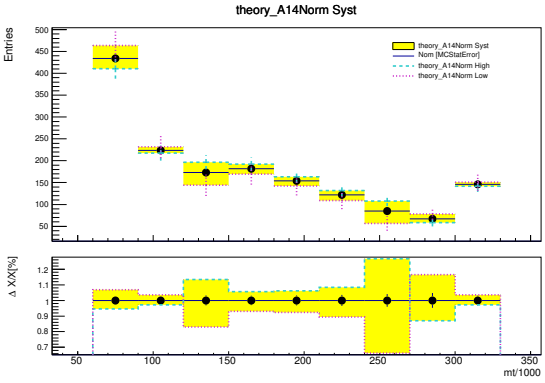
(a) JER_NP8

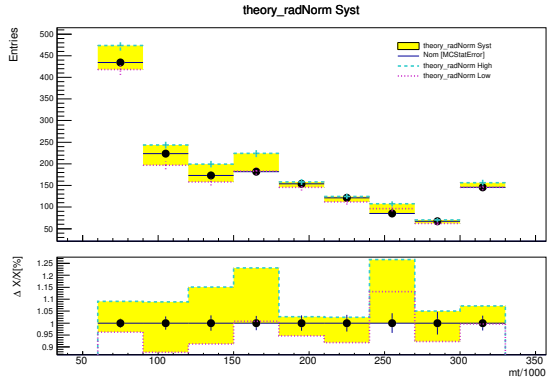(b) JES_Flavor_Composition

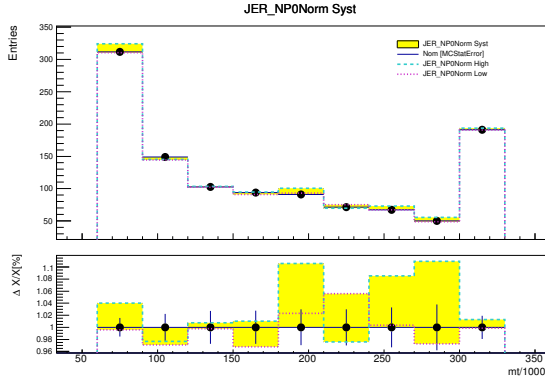(c) MET_Reso_para

(d) MET_Reso_perp

(e) theory_A14

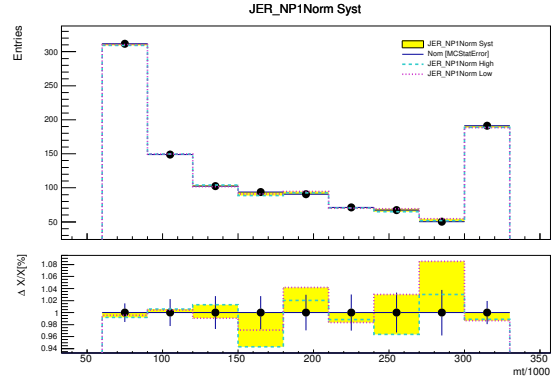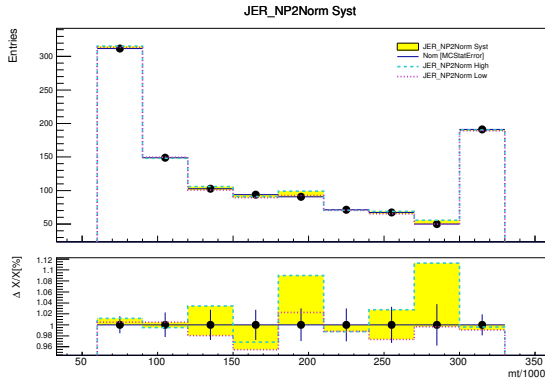(f) theory_rad

Figure C.6: Systematic variations of m_{T} [GeV] shape at the 3rd $E_{\mathrm{T}}^{\mathrm{miss}}$ slice ([200, 250] GeV) of *Diagonal* for $t\bar{t}$ (1L1τ_h) (2/2). Each error bar indicates MC statistical error. Green and red lines indicate the $\eta(\alpha = \pm 1)$ values.
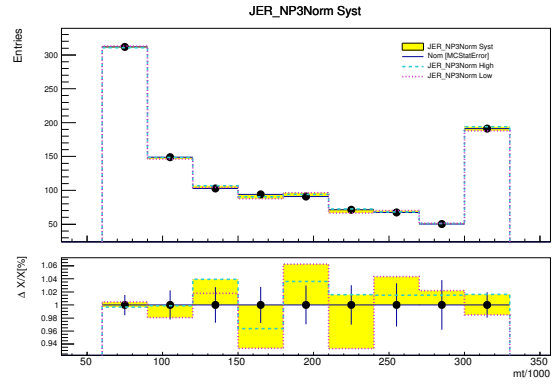
(a) JER_NP0 (b) JER_NP1

(c) JER_NP2 (d) JER_NP3

(e) JER_NP4 (f) JER_NP5

(g) JER_NP6 (h) JER_NP7

Figure C.7: Systematic variations of m_T [GeV] shape at the highest E_T^{miss} slice ([250, inf] GeV) of *Diagonal* for $t\bar{t}$ (1L1τ_h) (1/2). Each error bar indicates MC statistical error. Green and red lines indicate the $\eta(\alpha = \pm 1)$ values.

162
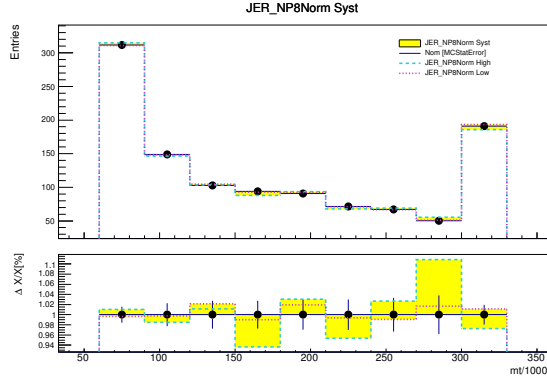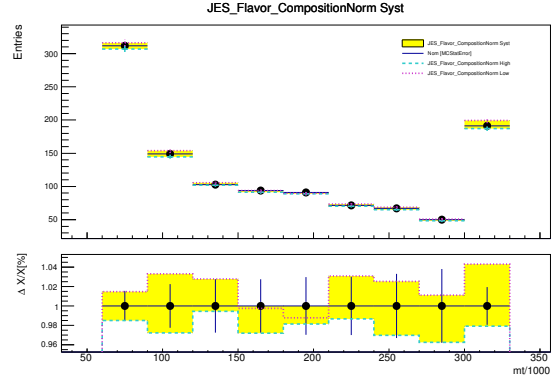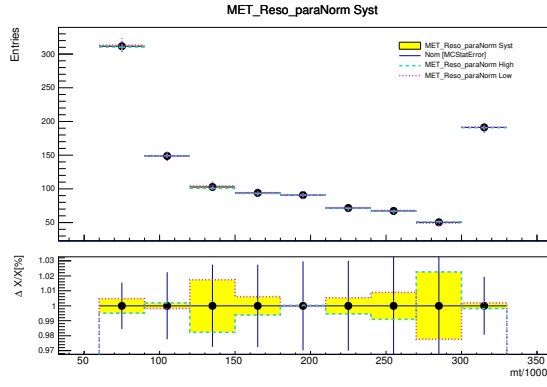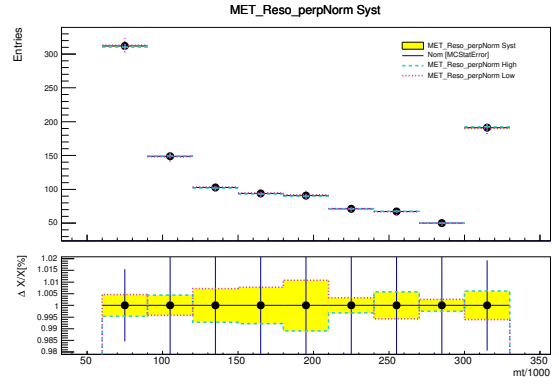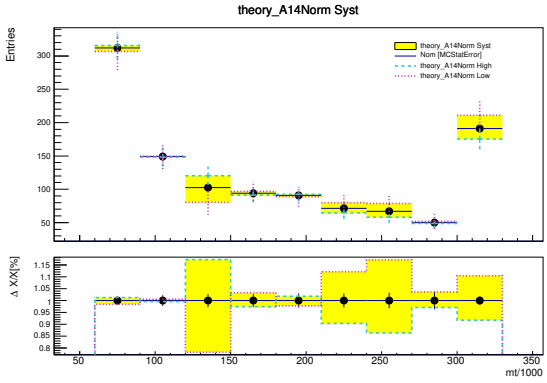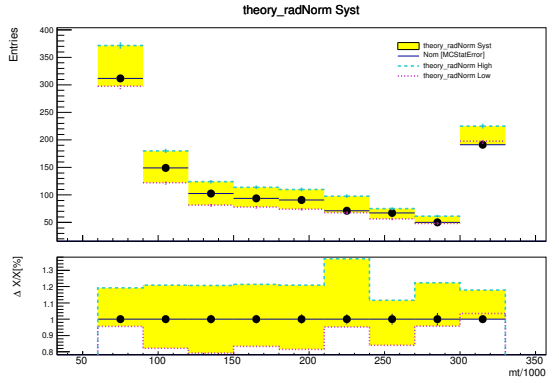
Figure C.8: Systematic variations of m_T [GeV] shape at the highest E_T^{miss} slice ([250, inf] GeV) of *Diagonal* for $t\bar{t}$ (1L1τ_h) (2/2). Each error bar indicates MC statistical error. Green and red lines indicate the $\eta(\alpha = \pm 1)$ values.

Figure C.9: Systematic variations of m_T [GeV] shape at TAUCR of *Diagonal* for $t\bar{t}$ (1L1τ_h) (1/2). Each error bar indicates MC statistical error. Green and red lines indicate the $\eta(\alpha = \pm 1)$ values.
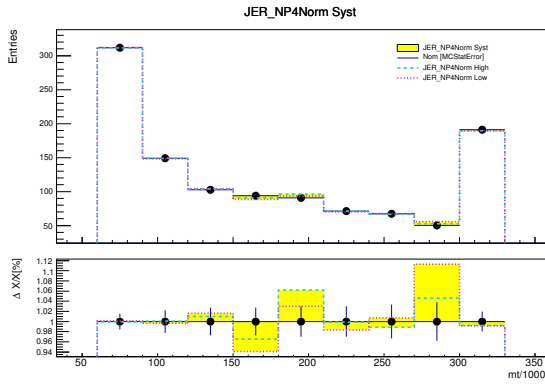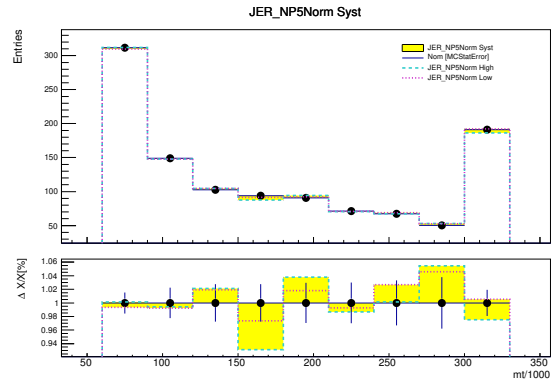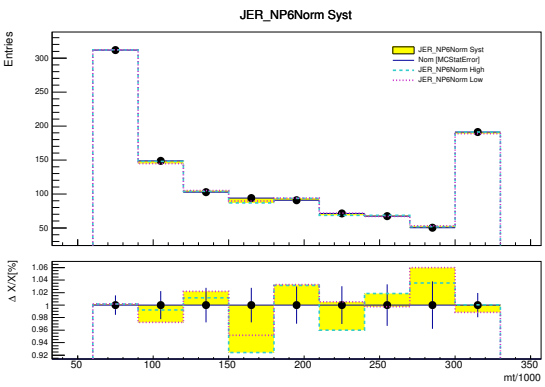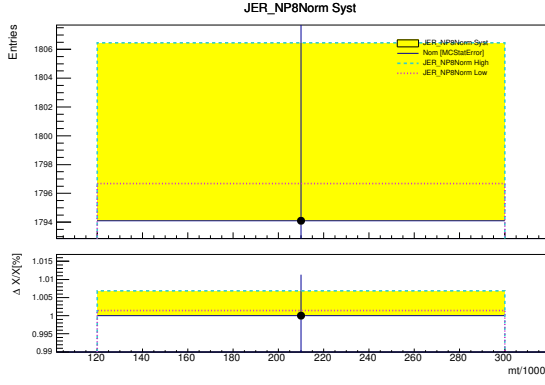
(a) JER_NP8
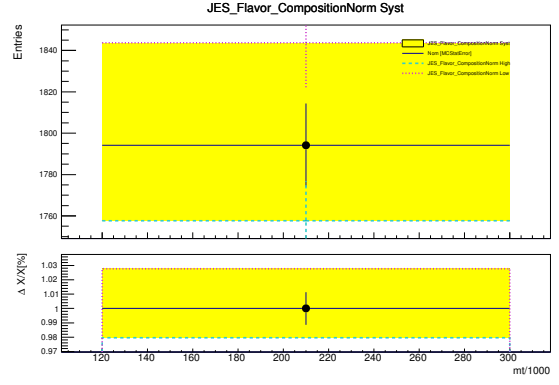
(b) JES_Flavor_Composition
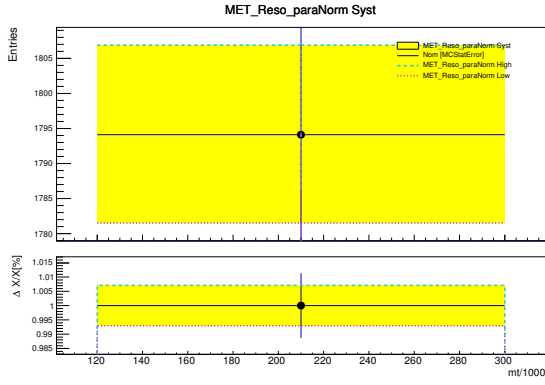
(c) MET_Reso_para
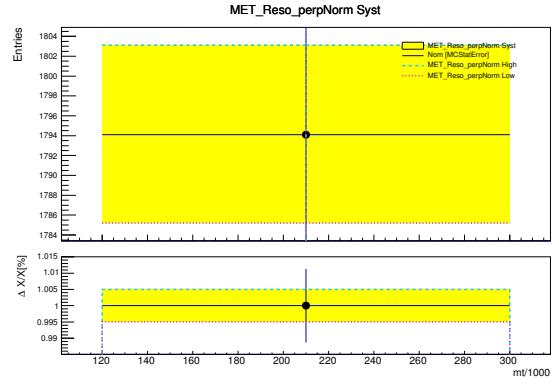
(d) MET_Reso_perp
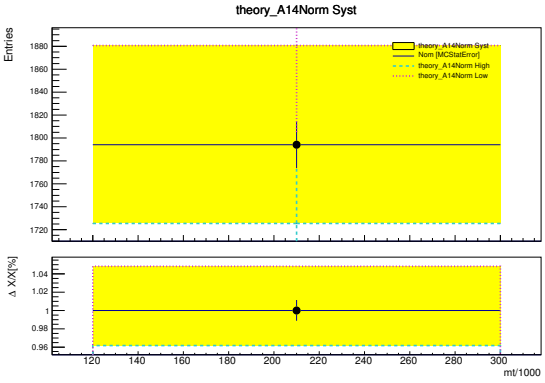
(e) theory_A14
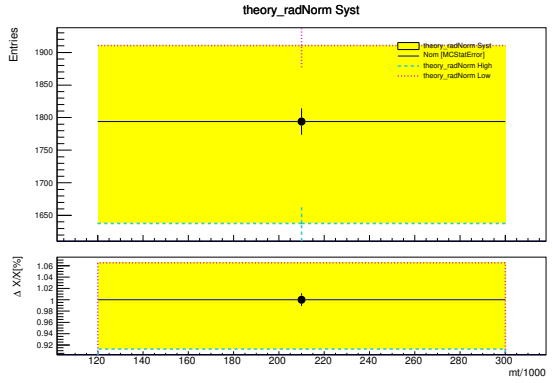
(f) theory_rad

Figure C.10: Systematic variations of m_{T} [GeV] shape at TAUCR of *Diagonal* for $t\bar{t}$ (1L1τ_h) (2/2). Each error bar indicates MC statistical error. Green and red lines indicate the $\eta(\alpha = \pm 1)$ values.

Appendix D

Upgrading Trigger Readout of LAr Calorimeter

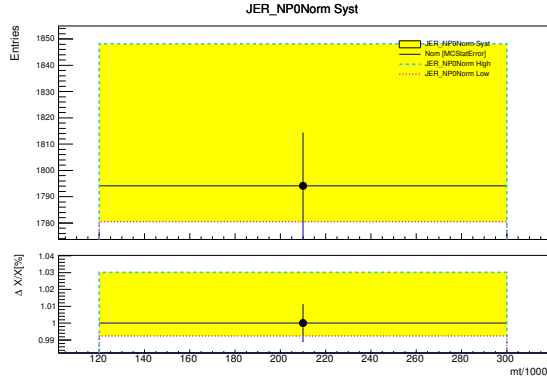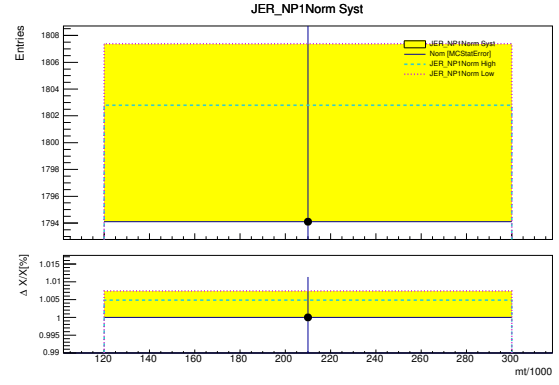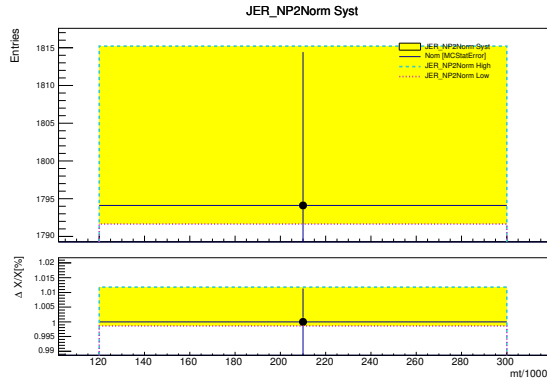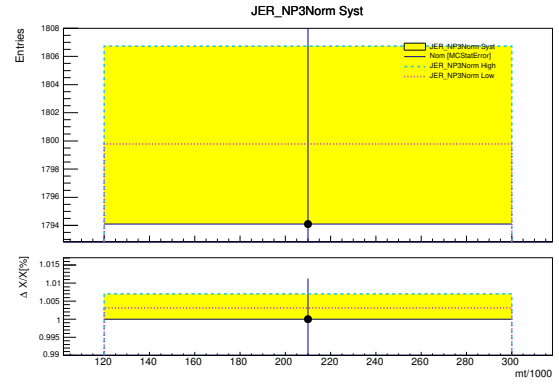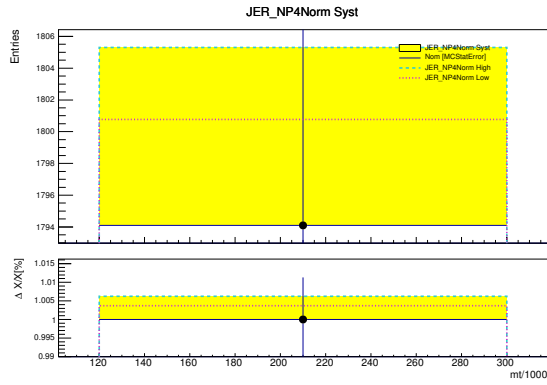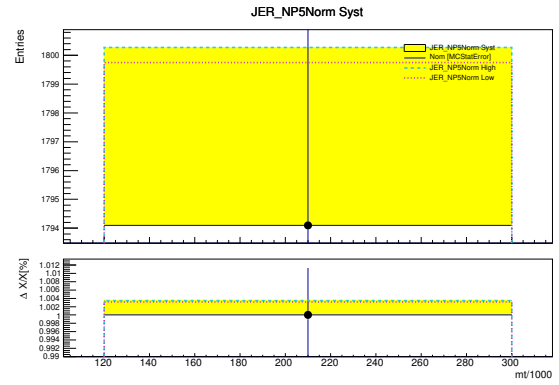This appendix describes upgrade studies of the LAr calorimeter trigger readout. There is a long-term project of upgrading trigger readout of the ATLAS LAr calorimeter, which is aimed at 'High-Luminosity LHC (HL-LHC)' that will start from 2024 with an ultimate peak instantaneous luminosity of $\mathcal{L} \sim 5 \times 10^{34}$ cm^{-2}s^{-1} and will deliver an integrated luminosity of ~ 250 fb^{-1} in a year and up to 3 fb^{-1} after 12 years of running. Due to its very high instantaneous luminosity, keeping L1 trigger rate 100 kHz in HL-LHC requires to replace the current trigger readout electronics with new high-end ones. The new trigger readout system is named 'supercell' that can provide higher-granularity, higher-resolution and longitudinal shower information from the calorimeter to the L1 trigger processors [139].

Appendix D.1 describes supercell design. Appendix D.2 outlines new high-end electronics for supercell. Appendix D.3 introduces 'demonstrator system' to do performance tests of the new high-end electronics and obtain experiences of supercell installation. Appendix D.4 shows results of the performance test with the demonstrator system. My main works were performance tests of 'demonstrator system', described in Appendix D.4. Especially, I contributed to the success of first installation of the demonstrator system by assuring through performance tests that it has no significant problem.

D.1   Supercell

Figure D.1 illustrates how supercell works with comparison of the current trigger readout system named 'trigger tower' and shows the behavior of the supercell and the trigger tower against injection of an electron into the barrel part of LAr calorimeter. Although there are four layers in the barrel part and calorimeter cells with fine granularity as described in section 2.2.2 and Table 2.1, the trigger tower reads out just only sum of energy deposits over a coarser range of $\Delta\eta \times \Delta\phi = 0.1 \times 0.1$ in the four layers all because of limitation of its readout performance. In the case of supercell, new electronics can provide faster readout and thus the supercell can read out each of 10 energy deposits per the range of trigger tower with granularity of $\Delta\eta \times \Delta\phi = 0.1 \times 0.1$(1st and 4th layers) and 0.025×0.1(2nd and 3rd layers) as illustrated in Figure D.1. The new trigger readout electronics will be installed into the LAr calorimeter during two terms;
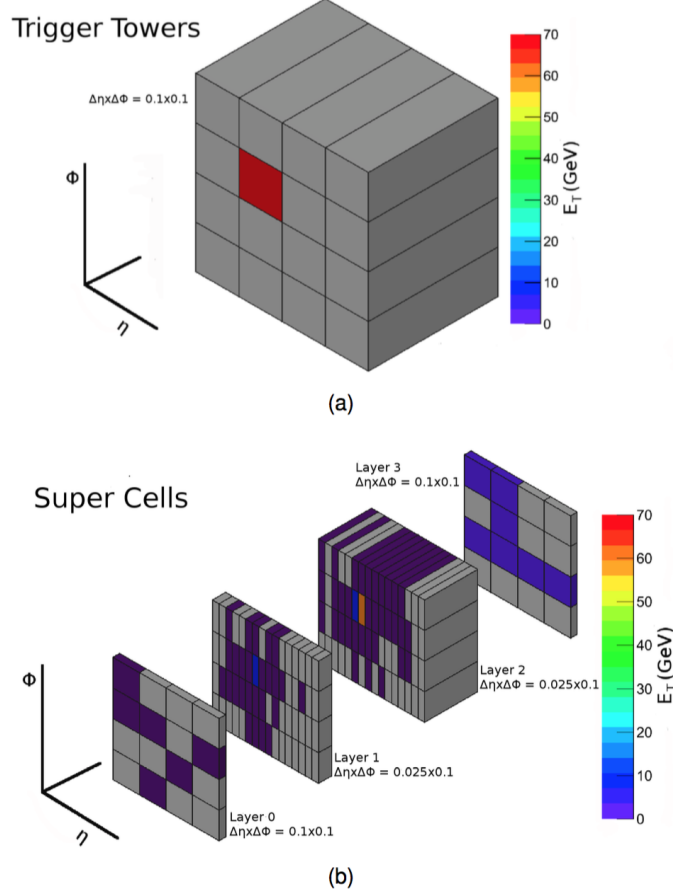
Figure D.1: Comparison of the upgraded and the current trigger readout systems, 'supercell' (a) and 'trigger tower' (b). An electron (with transverse energy of 70 GeV) is injected into the barrel part of LAr calorimeter, and the behavior of supercell and trigger tower is illustrated.

a long shutdown during 2019 - 2020 (Phase-I upgrade) and the next long shutdown during 2024 - mid-2026 (Phase-II upgrade)[137, 139].

D.2 New High-End Electronics for Supercell Toward Phase-I Upgrade

Figure D.2 shows the new readout system in the Phase-I Upgrade that contains the legacy trigger tower readout path and the new supercell readout path will be prepared in parallel in order to keep the legacy trigger path as a fallback. The new high-end electronics for the supercell readout is prepared for purpose of fast real-time data processing and transfer. In this section, four new components, a new baseplane, a new layer sub board, the LAr Trigger Digitizer Board (LTDB), and the LAr Digital Processing System (LDPS) are overviewed.

New Layer Sum Board

The current layer sum board (LSB) provides summation of analog signals of the elementary LAr calorimeter cells over a range of $\Delta\eta \times \Delta\phi = 0.1 \times 0.1$ for a given layer of the calorimeter. During the Phase-I Upgrade, the new LSB processes 4 times finer segments $\Delta\eta \times \Delta\phi =$

167
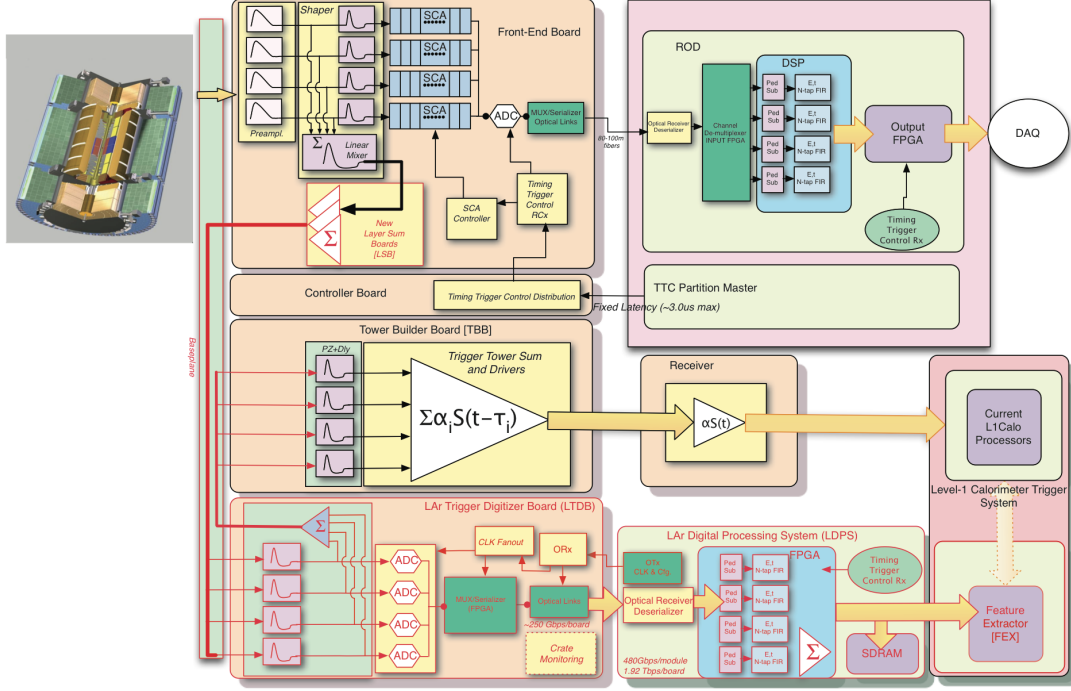
Figure D.2: Schematic diagram of the architecture of the readout electronics after the Phase-I Upgrade [139]. New components are indicated by red-outlined blocks.

0.025×0.1 for the summation in the 2nd and 3rd layers. The new LSBs are mounted on the Front-End Board (see the upper left side of Figure D.2).

New Baseplane

In order to allocate new slot for LTDB and to route the analog signal from Front-End Boards, the current baseplane is replaced. A much larger number of signals can be transferred through the new baseplane. It also routes the legacy trigger signals to the Tower Builder Board, as is done by the current baseplane.

LAr Trigger Digitizer Board

Primary role of LTDB is to digitize the supercell signals from the new LSB. The 40 MHz sampling digitization is realized with custom developed 12-bit SAR ADC in 130 nm CMOS technology, which has a good level of radiation tolerance [140]. The other role is to transmit the digitized signal to the LDPS. LOCx2 serializer and LOCld optical driver [141] are developed to perform the data transfer at 5.44 Gb/s per fibre; 40 fibers are used in total. Each of the 124 LTDBs handles up to 320 Super Cell channels.

LAr Digital Processing System

There are three roles assigned to the LDPS. First, the LDPS receives the digitized data at a total rate of 25 Tb/s. Second, the LDPS reconstructs transverse energies of each Super Cell and also calculate energy sums in real time. Finally, the LDPS transmits data containing the transverse energy information to the L1 trigger processors. For achieving these roles, LDPS in design consists of 32 ATCA carrier blades named LAr digital processing blade (LDPB) (see Figure D.3), which carry 4 Advanced Mezzanine Cards (AMC) each (see Figure D.4). On the AMCs, precise energy reconstruction, pile-up suppression,

and identification of the correct bunch crossing time are performed. Each AMC carries one ALTERA Arria-10 FPGA for the real time processing which handles 320 supercells at maximum.
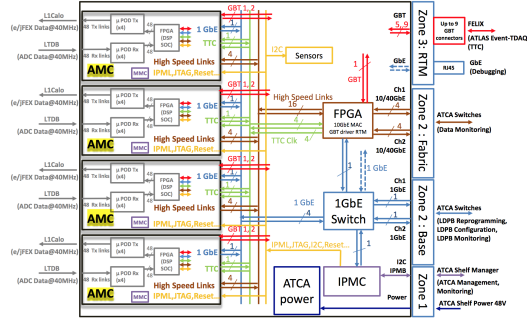
Figure D.3: Schematic diagram of LDPB, which contains four AMCs.
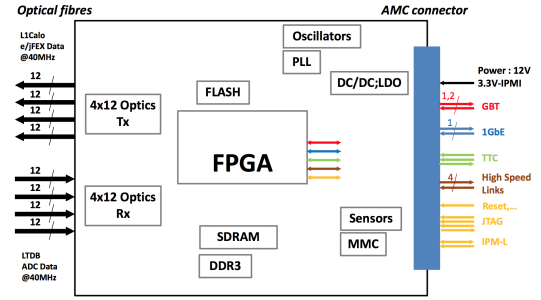
Figure D.4: Schematic diagram of an AMC, with an ALTERA Arria-10 FPGA on the center.

D.3 Demonstrator System
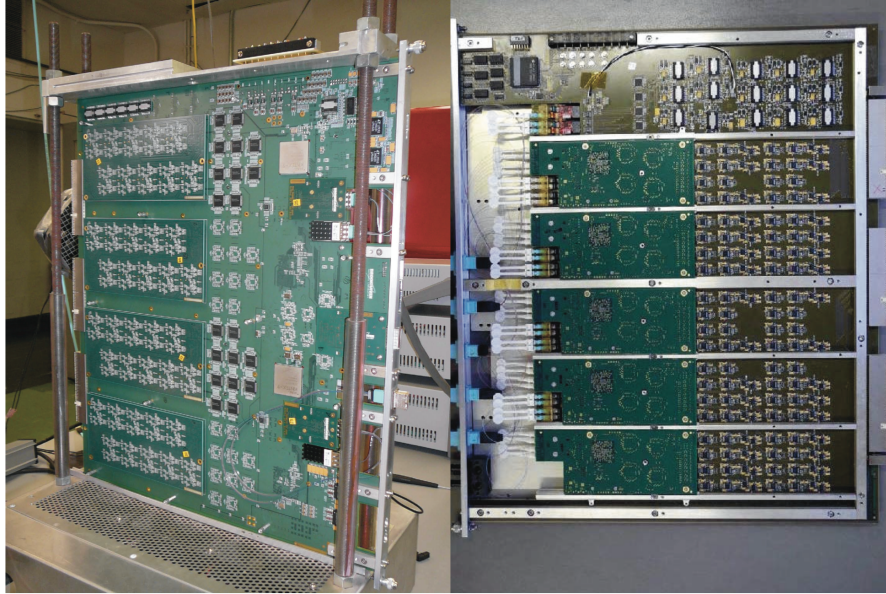
Figure D.5: The two types of LTDB demonstrators, developed by BNL (left) and LAL/Saclay (right) respectively.

For developing hardware, obtaining the installation experience, and testing and validating the performance of the supercell, a 'demonstrator' system has been installed in the ATLAS detector in summer 2014. LTDB prototypes, also called LTDB demonstrators, have been installed in one of front-end crates as shown in Figure D.2. The LTDB demonstrators read out supercells for the region of a barrel part of the LAr calorimeter, $1.767 < \phi < 2.160$, $0 < \eta < 1.4$, and operates in parallel to the regular ATLAS data taking during the LHC Run-2. Figure D.5 shows two types of demonstrators, developed by BNL and LAL/Saclay. The BNL LTDB uses analog mezzanine

and digital main board. The LAL/Saclay LTDB has a design with opposite configuration, digital mezzanine and analog main board. A commercial product, TI ADS5272, is chosen as ADC in both LTDBs.
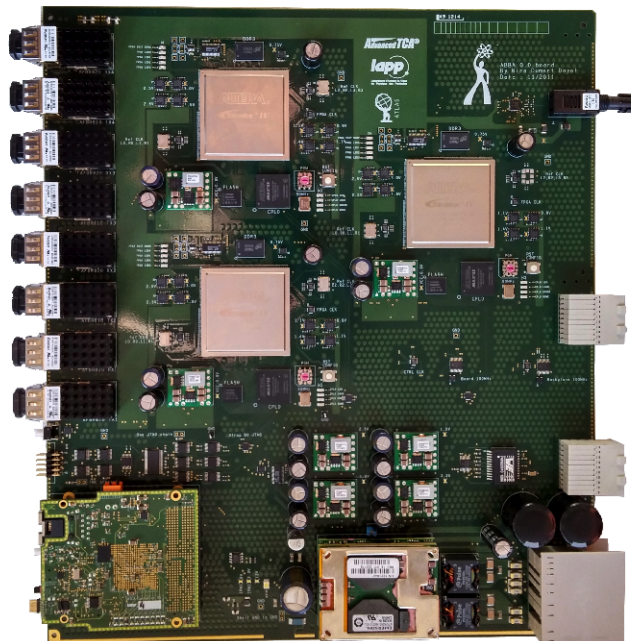
Figure D.6: The pre-prototype LDPB developed in LAPP

The digitized data is transmitted to the pre-prototype LDPB, developed by LAPP (see Figure D.6), which have been installed in USA15 (Backend part of ATLAS). The LDPB is designed along with a commercial Advanced Telecommunications Computing Architecture (ATCA) system. Its core components are ALTERA®Stratix IV FPGAs. The two front FPGAs receive the digitized data and format them in ATLAS RAW Event Format. The formatted event data is transferred through the back FPGA, via ATCA fabric interface with IPbus and Internet Control Message Protocol (ICMP). These three FPGAs are interconnected via XAUI.

D.4 Performance Results from the Demonstrator System

This section shows the results of measurement on the demonstrator system [142]. First, the performance of the legacy readout is discussed, followed by the demonstrator readout.

Measurements with the Legacy Readout

The purpose of measurements with the legacy readout is for assuring that the LTDB demonstrator does not degrade the performance of the energy measurement for the current physics run. First, using a calibration system, we confirmed that there is no dead channel and adjusted the gain level in each channel. The total noise and coherent noise fraction of front-end boards were measured with the legacy readout. Figure D.7 and D.8 are a comparison of the total noise and the coherent noise fraction of front-end boards for the demonstrator crate and for neighboring crates. The noise level of the demonstrator crate is consistent with that of neighboring crates. Figure D.9 shows the total noise on the trigger

tower readout. The observed noise level is consistent with the current system.

Measurements with the Demonstrator Readout

We have evaluated the prototype LTDB performance in terms of noise, pulse and linearity. Figure D.10 shows the RMS of the pedestal run in ADC counts for the LTDB Demonstrator as function of η. The noise level is as expected between 100 and 250 MeV per supercell. Figure D.11 shows the responses of four supercells (one from each layer) from the LTDB demonstrator to injected calibration pulses (DAC = 1000 to each LAr cell). The size and shape of pulses are as expected and vary due to different detector and electronics properties. Figure D.12 shows pulse shapes of a super cell from the demonstrator for injected calibration pulses with different amplitudes. The size and shape of pulses are as expected and show good linearity up to DAC = 8000, while beyond, analog saturation occurs upstream of the demonstrator board as expected by the design. In Figure D.13, the pulse maximum in ADC counts for four different super cells from the demonstrator as function of the amplitude of injected calibration pulse in DAC (left) and transverse energy (right) are shown. The pulse shapes shown in Figure D.12 correspond to blue up triangles in Figure D.13. In the right part of Figure D.13, one can observe that the linearity is kept up to sufficiently large values of E_T.
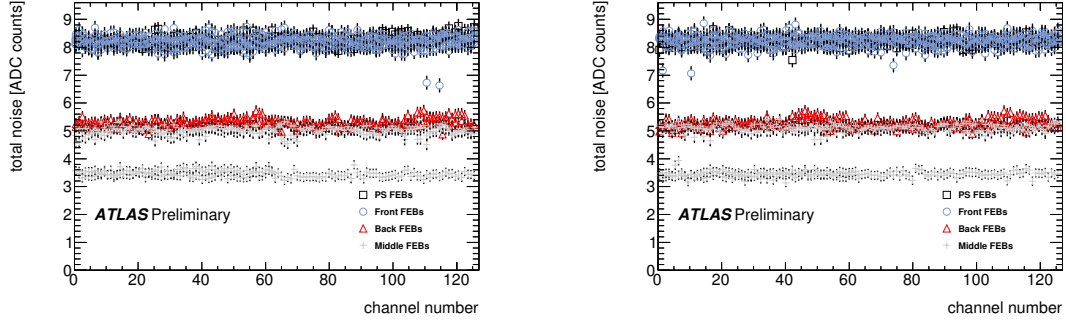
Figure D.7: The RMS of pedestal run for channels of the Front-End Boards in the demonstrator crate (left) and same sets in the neighboring crate (right). There are 28 Front-End Boards per crate, each has 128 channels. The noise levels of the boards vary because different capacitances and gains are applied to their respective cells [142].
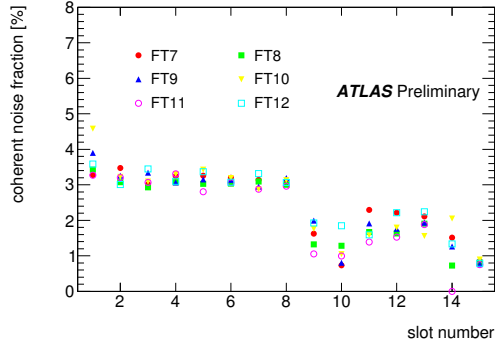
Figure D.8: The fraction of coherent noise per readout channel (Coherent Noise Fraction, CNF) for feedthroughs (FT) 7-12 on the calorimeter. FT9 and 10 belong to the demonstrator crate. FT7, 8, 11, and 12 belong to the neighbor crate. The board in the first slot reads out the presampler, the boards in the following seven slots read out the front layer, the next two boards the back layer and the last four boards the middle layer of the calorimeter. The last entry is the CNF of the whole half crate. The coherent noise fraction was calculated according to the following equation, $\rho_{\mathrm{CNF}} = \frac{\sqrt{\sigma^2_{\sum_{i \in A}} - N_{i \in A} \cdot <\sigma^2_{i \in A}>}}{N_{i \in A} \cdot <\sigma_{i \in A}>}$, where A is a set of channels, $N_{i \in A}$ is the number of channels belong to A [142].
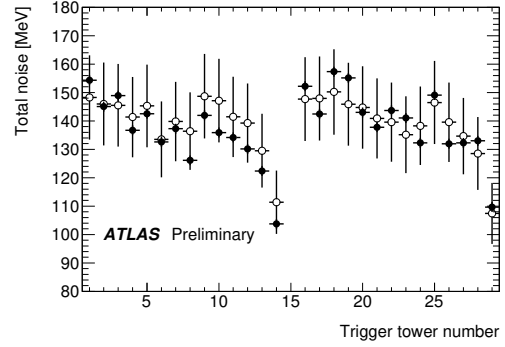
Figure D.9: The total noise in the trigger tower readout path on the demonstrator system in transverse energy in MeV. Trigger tower 1-14 correspond to 0 to 1.4 in η and 16-29 are the same in η, but adjacent in ϕ. The values represented by the full circles were measured by a spectrum analyzer, and the values shown in open circles were measured with Flash ADCs [142].
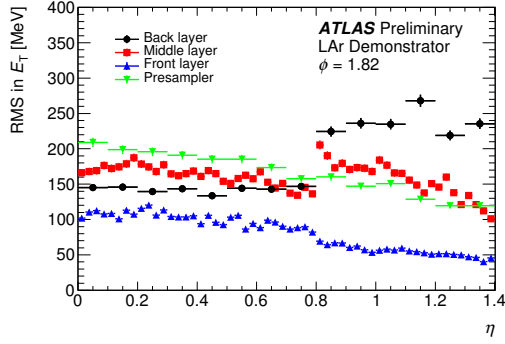
Figure D.10: Pseudo rapidity dependence of the RMS of the transverse energy of the supercells from the demonstrator setup without beam. The jump seen at $\eta = 0.8$ reflects the change of absorber thickness, electrodes and calibration resistors. The noise level is as expected between 100 and 250 MeV per super cell [142].
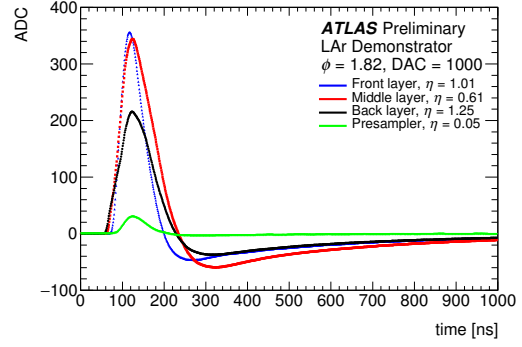
Figure D.11: Responses of four supercells (one from each layer) from the LTDB demonstrator to injected calibration pulses (DAC = 1000 to each LAr calorimeter cell) [142].
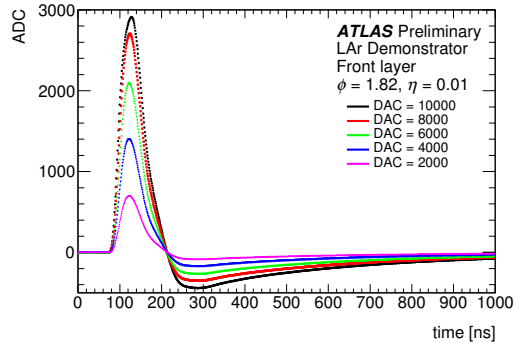
Figure D.12: Pulse shapes of a super cell from the demonstrator for injected calibration pulses with different amplitudes [142].
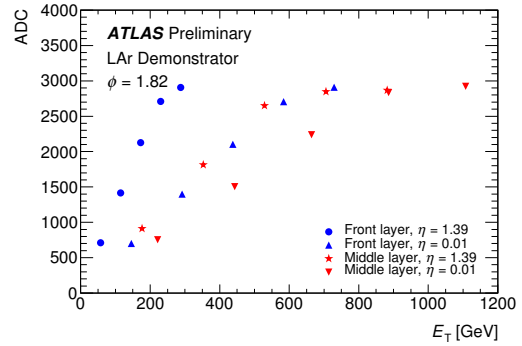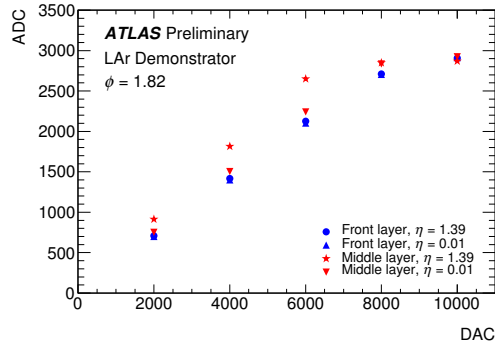
Figure D.13: Pulse maximum in ADC counts for four different super cells from the demonstrator for injected calibration pulses amplitude in DAC (left) and transverse energy (right) [142].

Bibliography

[1] C. Patrignani and P. D. Group, *Review of Particle Physics*,
Chinese Physics C **40** (2016) 100001,
URL: http://stacks.iop.org/1674-1137/40/i=10/a=100001.

[2] N. Sakai, *Naturalness in Supersymmetric Guts*, Z. Phys. C **11** (1981) 153.

[3] S. Dimopoulos, S. Raby, and F. Wilczek, *Supersymmetry and the Scale of Unification*,
Phys. Rev. D **24** (1981) 1681.

[4] L. E. Ibanez and G. G. Ross,
Low-Energy Predictions in Supersymmetric Grand Unified Theories,
Phys. Lett. B **105** (1981) 439.

[5] S. Dimopoulos and H. Georgi, *Softly Broken Supersymmetry and SU(5)*,
Nucl. Phys. B **193** (1981) 150.

[6] S. P. Martin, *A Supersymmetry primer*,
(1997), [Adv. Ser. Direct. High Energy Phys.18,1(1998)], arXiv: hep-ph/9709356.

[7] Yu. A. Golfand and E. P. Likhtman,
Extension of the Algebra of Poincare Group Generators and Violation of p Invariance,
JETP Lett. **13** (1971) 323, [Pisma Zh. Eksp. Teor. Fiz.13,452(1971)].

[8] D. V. Volkov and V. P. Akulov, *Is the Neutrino a Goldstone Particle?*
Phys. Lett. B **46** (1973) 109.

[9] J. Wess and B. Zumino, *Supergauge Transformations in Four-Dimensions*,
Nucl. Phys. B **70** (1974) 39.

[10] J. Wess and B. Zumino, *Supergauge Invariant Extension of Quantum Electrodynamics*,
Nucl. Phys. B **78** (1974) 1.

[11] S. Ferrara and B. Zumino, *Supergauge Invariant Yang-Mills Theories*,
Nucl. Phys. B **79** (1974) 413.

[12] A. Salam and J. A. Strathdee, *Supersymmetry and Nonabelian Gauges*,
Phys. Lett. B **51** (1974) 353.

[13] R. Barbieri and G. F. Giudice, *Upper Bounds on Supersymmetric Particle Masses*,
Nucl. Phys. B **306** (1988) 63.

[14] B. de Carlos and J. A. Casas, *One loop analysis of the electroweak breaking in
supersymmetric models and the fine tuning problem*, Phys. Lett. B **309** (1993) 320,
arXiv: hep-ph/9303291.

[15] K. Abe et al.,
Search for proton decay via $p \to \nu K^+$ *using 260 kiloton-year data of Super-Kamiokande*,
Phys. Rev. D **90** (2014) 072005, arXiv: 1408.1195 [hep-ex].

[16] G. R. Farrar and P. Fayet, *Phenomenology of the Production, Decay, and Detection of New Hadronic States Associated with Supersymmetry*, Phys. Lett. B **76** (1978) 575.

[17] H. Goldberg, *Constraint on the Photino Mass from Cosmology*,
Phys. Rev. Lett. **50** (1983) 1419, [Erratum: Phys. Rev. Lett.103,099905(2009)].

[18] J. R. Ellis et al., *Supersymmetric Relics from the Big Bang*,
Nucl. Phys. B **238** (1984) 453.

[19] S. Dimopoulos, S. Raby, and F. Wilczek, *Supersymmetry and the scale of unification*,
Phys. Rev. D **24** (6 1981) 1681,
URL: http://link.aps.org/doi/10.1103/PhysRevD.24.1681.

[20] L. Ibez and G. Ross, *Low-energy predictions in supersymmetric grand unified theories*,
Physics Letters B **105** (1981) 439 , ISSN: 0370-2693,
URL: http://www.sciencedirect.com/science/article/pii/0370269381912004.

[21] W. J. Marciano and Senjanovi, *Predictions of supersymmetric grand unified theories*,
Phys. Rev. D **25** (11 1982) 3092,
URL: http://link.aps.org/doi/10.1103/PhysRevD.25.3092.

[22] A. Bartl et al., "Impact of SUSY CP phases on stop and sbottom decays in the MSSM,"
2003, arXiv: hep-ph/0306281,
URL: http://alice.cern.ch/format/showfull?sysnb=2381355.

[23] M. Papucci, J. T. Ruderman, and A. Weiler, *Natural SUSY Endures*,
JHEP **09** (2012) 035, arXiv: 1110.6926 [hep-ph].

[24] J. Fan and M. Reece, *A New Look at Higgs Constraints on Stops*, JHEP **06** (2014) 031,
arXiv: 1401.7671 [hep-ph].

[25] G. Aad et al.,
Observation and measurement of Higgs boson decays to WW^* *with the ATLAS detector*,
Phys. Rev. **D92** (2015) 012006, arXiv: 1412.2641 [hep-ex].

[26] ATLAS Collaboration,
Search for top squarks in final states with one isolated lepton, jets, and missing transverse momentum in $\sqrt{s} = 13$ *TeV pp collisions with the ATLAS detector*, (2016),
arXiv: 1606.03903 [hep-ex].

[27] *Search for top squarks in final states with one isolated lepton, jets, and missing transverse momentum in* $\sqrt{s} = 13$ *TeV pp collisions with the ATLAS detector*, (2016),
URL: https://cds.cern.ch/record/2206132.

[28] M. Cacciari, G. P. Salam, and G. Soyez, *The Anti-k_t jet clustering algorithm*,
JHEP **0804** (2008) 063, arXiv: 0802.1189 [hep-ph].

[29] *b-tagging in dense environments*, (2014), URL: https://cds.cern.ch/record/1750682.

[30] L. Evans and P. Bryant, *LHC Machine*, Journal of Instrumentation **3** (2008) S08001,
URL: http://stacks.iop.org/1748-0221/3/i=08/a=S08001.

[31] C. De Melis, *The CERN accelerator complex*, (2016), General Photo,
URL: https://cds.cern.ch/record/2197559.

[32] ATLAS Collaboration, *The ATLAS Experiment at the CERN Large Hadron Collider*,
JINST **3** (2008) S08003.

[33] *Track Reconstruction Performance of the ATLAS Inner Detector at $\sqrt{s} = 13$ TeV*,
(2015), URL: http://cds.cern.ch/record/2037683.

[34] *Studies of the ATLAS Inner Detector material using $\sqrt{s} = 13$ TeV pp collision data*,
(2015), URL: http://cds.cern.ch/record/2109010.

[35] J. Pequenao, "Computer Generated image of the ATLAS calorimeter," 2008,
URL: http://cds.cern.ch/record/1095927.

[36] N. Nikiforou, "Performance of the ATLAS Liquid Argon Calorimeter after three years of
LHC operation and plans for a future upgrade," *Proceedings, 3rd International
Conference on Advancements in Nuclear Instrumentation Measurement Methods and
their Applications (ANIMMA 2013): Marseille, France, June 23-27, 2013*, 2013,
arXiv: 1306.6756 [physics.ins-det],
URL: https://inspirehep.net/record/1240499/files/arXiv:1306.6756.pdf.

[37] G. Aad et al.,
Electron and photon energy calibration with the ATLAS detector using LHC Run 1 data,
Eur. Phys. J. **C74** (2014) 3071, arXiv: 1407.5063 [hep-ex].

[38] G. Aad et al.,
Technical Design Report for the Phase-I Upgrade of the ATLAS TDAQ System,
(2013), Final version presented to December 2013 LHCC.,
URL: https://cds.cern.ch/record/1602235.

[39] *2015 start-up trigger menu and initial performance assessment of the ATLAS trigger
using Run-2 data*, (2016), URL: https://cds.cern.ch/record/2136007.

[40] ATLAS Collaboration, *The ATLAS Simulation Infrastructure*,
Eur. Phys. J. C **70** (2010) 823, arXiv: 1005.4568 [hep-ex].

[41] S. Agostinelli et al. (GEANT4 Collaboration), *GEANT4: A Simulation toolkit*,
Nucl. Instrum. Meth. A **506** (2003) 250.

[42] ATLAS Collaboration, *The simulation principle and performance of the ATLAS fast
calorimeter simulation FastCaloSim*, ATL-PHYS-PUB-2010-013, 2010,
URL: http://cds.cern.ch/record/1300517.

[43] M. Czakon, P. Fiedler, and A. Mitov,
Total Top-Quark Pair-Production Cross Section at Hadron Colliders Through $O(\alpha_S^4)$,
Phys. Rev. Lett. **110** (2013) 252004, arXiv: 1303.6254 [hep-ph].

[44] M. Czakon and A. Mitov,
NNLO corrections to top pair production at hadron colliders: the quark-gluon reaction,
JHEP **1301** (2013) 080, arXiv: 1210.6832 [hep-ph].

[45] M. Czakon and A. Mitov, *NNLO corrections to top-pair production at hadron colliders:
the all-fermionic scattering channels*, JHEP **1212** (2012) 054,
arXiv: 1207.0236 [hep-ph].

[46] P. Baernreuther, M. Czakon, and A. Mitov, *Percent Level Precision Physics at the Tevatron: First Genuine NNLO QCD Corrections to $q\bar{q} \to t\bar{t} + X$*, Phys. Rev. Lett. **109** (2012) 132001, arXiv: 1204.5201 [hep-ph].

[47] M. Cacciari et al., *Top-pair production at hadron colliders with next-to-next-to-leading logarithmic soft-gluon resummation*, Phys. Lett. B **710** (2012) 612, arXiv: 1111.5869 [hep-ph].

[48] M. Czakon and A. Mitov, *Top++: A Program for the Calculation of the Top-Pair Cross-Section at Hadron Colliders*, Comput. Phys. Commun. **185** (2014) 2930, arXiv: 1112.5675 [hep-ph].

[49] N. Kidonakis, *Next-to-next-to-leading-order collinear and soft gluon corrections for t-channel single top quark production*, Phys. Rev. D **83** (2011) 091503, arXiv: 1103.2792 [hep-ph].

[50] N. Kidonakis, *Two-loop soft anomalous dimensions for single top quark associated production with a W- or H-*, Phys. Rev. D **82** (2010) 054018, arXiv: 1005.4451 [hep-ph].

[51] N. Kidonakis, *NNLL resummation for s-channel single top quark production*, Phys. Rev. D **81** (2010) 054028, arXiv: 1001.5034 [hep-ph].

[52] S. Catani et al., *Vector boson production at hadron colliders: a fully exclusive QCD calculation at NNLO*, Phys. Rev. Lett. **103** (2009) 082001, arXiv: 0903.2120 [hep-ph].

[53] J. Alwall et al., *The automated computation of tree-level and next-to-leading order differential cross sections, and their matching to parton shower simulations*, JHEP **1407** (2014) 079, arXiv: 1405.0301 [hep-ph].

[54] C. Borschensky et al., *Squark and gluino production cross sections in pp collisions at $\sqrt{s}$ = 13, 14, 33 and 100 TeV*, Eur. Phys. J. C **74** (2014) 3174, arXiv: 1407.5066 [hep-ph].

[55] M.R. Buckley, D. Feld, and D. Goncalves, *Scalar Simplified Models for Dark Matter*, Phys. Rev. D **91** (2015) 015017, arXiv: 1410.6497 [hep-ph].

[56] U. Haisch and E. Re, *Simplified dark matter top-quark interactions at the LHC*, JHEP **06** (2015) 078, arXiv: 1503.00691 [hep-ph].

[57] R. D. Ball et al., *Parton distributions with LHC data*, Nucl. Phys. B **867** (2013) 244, arXiv: 1207.1303 [hep-ph].

[58] ATLAS Collaboration, *ATLAS Pythia 8 tunes to 7 TeV data*, ATL-PHYS-PUB-2014-021, 2014, URL: http://cdsweb.cern.ch/record/1966419.

[59] T. Sjöstrand, S. Mrenna, and P. Z. Skands, *A Brief Introduction to PYTHIA 8.1*, Comput. Phys. Commun. **178** (2008) 852, arXiv: 0710.3820 [hep-ph].

[60] M. Kramer et al., *Supersymmetry production cross sections in pp collisions at $\sqrt{s} = 7$ TeV*, (2012), arXiv: 1206.2892 [hep-ph].

[61] S. Alioli et al., *A general framework for implementing NLO calculations in shower Monte Carlo programs: the POWHEG BOX*, JHEP **1006** (2010) 043, arXiv: 1002.2581 [hep-ph].

[62] E. Re, *Single-top Wt-channel production matched with parton showers using the POWHEG method*, Eur. Phys. J. C **71** (2011) 1547, arXiv: 1009.2450 [hep-ph].

[63] S. Frixione, P. Nason, and G. Ridolfi, *A Positive-weight next-to-leading-order Monte Carlo for heavy flavour hadroproduction*, JHEP **0709** (2007) 126, arXiv: 0707.3088 [hep-ph].

[64] R. Frederix, E. Re, and P. Torrielli, *Single-top t-channel hadroproduction in the four-flavour scheme with POWHEG and aMC@NLO*, JHEP **1209** (2012) 130, arXiv: 1207.5391 [hep-ph].

[65] S. Alioli et al., *NLO single-top production matched with shower in POWHEG: s- and t-channel contributions*, JHEP **0909** (2009) 111, [Erratum: JHEP02,011(2010)], arXiv: 0907.4076 [hep-ph].

[66] H.-L. Lai et al., *New parton distributions for collider physics*, Phys. Rev. D **82** (2010) 074024, arXiv: 1007.2241 [hep-ph].

[67] P. Z. Skands, *Tuning Monte Carlo Generators: The Perugia Tunes*, Phys. Rev. D **82** (2010) 074018, arXiv: 1005.3457 [hep-ph].

[68] T. Sjöstrand, S. Mrenna, and P. Z. Skands, *PYTHIA 6.4 Physics and Manual*, JHEP **0605** (2006) 026, arXiv: hep-ph/0603175.

[69] *Simulation of top quark production for the ATLAS experiment at sqrt(s) = 13 TeV*, (2016), URL: https://cds.cern.ch/record/2120417.

[70] T. Gleisberg et al., *Event generation with SHERPA 1.1*, JHEP **0902** (2009) 007, arXiv: 0811.4622 [hep-ph].

[71] T. Gleisberg and S. Höche, *Comix, a new matrix element generator*, JHEP **0812** (2008) 039, arXiv: 0808.3674 [hep-ph].

[72] F. Cascioli, P. Maierhofer, and S. Pozzorini, *Scattering Amplitudes with Open Loops*, Phys. Rev. Lett. **108** (2012) 111601, arXiv: 1111.5206 [hep-ph].

[73] F. Siegert, "Scale setting in Sherpa 2.2 V+jets samples," URL: https://indico.cern.ch/event/514684/contributions/2037116/attachments/1249637/1841917/Scale_setting_in_Sherpa_2.2_Vjets_samples.pdf.

[74] R. D. Ball et al., *Parton distributions for the LHC Run II*, JHEP **1504** (2015) 040, arXiv: 1410.8849 [hep-ph].

[75] S. Schumann and F. Krauss, *A Parton shower algorithm based on Catani-Seymour dipole factorisation*, JHEP **0803** (2008) 038, arXiv: 0709.1027 [hep-ph].

[76] ATLAS Collaboration, *Monte Carlo Generators for the Production of a W or Z/γ* Boson in Association with Jets at ATLAS in Run 2*, ATL-PHYS-PUB-2016-003, 2016, URL: http://cdsweb.cern.ch/record/2120133.

[77] ATLAS Collaboration, *Multi-boson simulation for 13 TeV ATLAS analyses*, ATL-PHYS-PUB-2016-002, 2016, URL: http://cdsweb.cern.ch/record/2119986.

[78] J. Pumplin et al.,
New generation of parton distributions with uncertainties from global QCD analysis,
JHEP **0207** (2002) 012, arXiv: hep-ph/0201195.

[79] ATLAS Collaboration, *Studies on the MC generator modelling of ttX
(X=W,Z,gamma,Higgs or heavy flavor jets) processes as used in Run2*,
ATL-PHYS-PUB-2016-005, 2016, URL: http://cds.cern.ch/record/2120826.

[80] "Electron efficiency measurements with the ATLAS detector using the 2015 LHC
proton-proton collision data," tech. rep. ATLAS-CONF-2016-024, CERN, 2016,
URL: https://cds.cern.ch/record/2157687.

[81] ATLAS Collaboration, *Electron identification measurements in ATLAS using*
$\sqrt{s} = 13$ *TeV data with* 50 *ns bunch spacing*, ATL-PHYS-PUB-2015-041, 2015,
URL: http://cdsweb.cern.ch/record/2048202.

[82] ATLAS Collaboration, *Muon reconstruction performance of the ATLAS detector in
proton-proton collision data at* $\sqrt{s} =13$ *TeV*, Eur. Phys. J. **C76** (2016) 292,
arXiv: 1603.05598 [hep-ex].

[83] ATLAS Collaboration, *Expected photon performance in the ATLAS experiment*,
ATL-PHYS-PUB-2011-007, 2011, URL: http://cdsweb.cern.ch/record/1345329.

[84] W. Lampl et al., *Calorimeter Clustering Algorithms: Description and Performance*,
ATL-LARG-PUB-2008-002, 2008, URL: http://cds.cern.ch/record/1099735.

[85] ATLAS Collaboration, *Jet energy measurement with the ATLAS detector in
proton–proton collisions at* $\sqrt{s} = 7$ *TeV*, Eur. Phys. J. C **73** (2013) 2304,
arXiv: 1112.6426 [hep-ex].

[86] M. Cacciari and G. P. Salam, *Pileup subtraction using jet areas*,
Phys. Lett. B **659** (2008) 119, arXiv: 0707.1378 [hep-ph].

[87] M. Cacciari, G. P. Salam, and G. Soyez, *The Catchment Area of Jets*,
JHEP **0804** (2008) 005, arXiv: 0802.1188 [hep-ph].

[88] ATLAS Collaboration, *Performance of pile-up mitigation techniques for jets in pp
collisions at* $\sqrt{s} = 8$ *TeV using the ATLAS detector*,
Nucl. Instrum. Meth. **A824** (2016) 367, arXiv: 1510.03823 [hep-ex].

[89] ATLAS Collaboration, *Jet energy measurement and its systematic uncertainty in
proton–proton collisions at* $\sqrt{s} = 7$ *TeV with the ATLAS detector*,
Eur. Phys. J. C **75** (2015) 17, arXiv: 1406.0076 [hep-ex].

[90] *Jet Calibration and Systematic Uncertainties for Jets Reconstructed in the ATLAS
Detector at* $\sqrt{s} = 13$ *TeV*, (2015), URL: https://cds.cern.ch/record/2037613.

[91] ATLAS Collaboration, *Characterisation and mitigation of beam-induced backgrounds
observed in the ATLAS detector during the 2011 proton–proton run*,
JINST **8** (2013) P07004, arXiv: 1303.0223 [hep-ex].

[92] ATLAS Collaboration,
Selection of jets produced in 13 TeV proton–proton collisions with the ATLAS detector,
ATLAS-CONF-2015-029, 2015, URL: http://cdsweb.cern.ch/record/2037702.

[93] A. Hoecker et al., *TMVA: Toolkit for Multivariate Data Analysis*,
PoS **ACAT** (2007) 040, arXiv: physics/0703039.

[94] ATLAS Collaboration,
"Optimisation of the ATLAS *b*-tagging performance for the 2016 LHC Run,"
tech. rep. ATL-PHYS-PUB-2016-012, CERN, 2016,
URL: https://cds.cern.ch/record/2160731.

[95] *Expected performance of the ATLAS b-tagging algorithms in Run-2*, (2015),
URL: https://cds.cern.ch/record/2037697.

[96] ATLAS Collaboration, *Performance of b-Jet Identification in the ATLAS Experiment*,
JINST **11** (2016) P04008, arXiv: 1512.01094 [hep-ex].

[97] ATLAS Collaboration, *Commissioning of the reconstruction of hadronic tau lepton
decays in ATLAS using pp collisions at $\sqrt{s} = 13$ TeV*, ATL-PHYS-PUB-2015-025, 2015,
URL: http://cdsweb.cern.ch/record/2037716.

[98] ATLAS Collaboration, *Reconstruction, Energy Calibration, and Identification of
Hadronically Decaying Tau Leptons in the ATLAS Experiment for Run-2 of the LHC*,
ATL-PHYS-PUB-2015-045, 2015, URL: http://cds.cern.ch/record/2064383.

[99] ATLAS Collaboration, *Performance of missing transverse momentum reconstruction
with the ATLAS detector in the first proton–proton collisions at $\sqrt{s} = 13$ TeV*,
ATL-PHYS-PUB-2015-027, 2015, URL: http://cdsweb.cern.ch/record/2037904.

[100] ATLAS Collaboration, *Expected performance of missing transverse momentum
reconstruction for the ATLAS detector at $\sqrt{s} = 13$ TeV*, ATL-PHYS-PUB-2015-023,
2015, URL: http://cdsweb.cern.ch/record/2037700.

[101] ATLAS Collaboration, *Search for new phenomena in final states with large jet
multiplicities and missing transverse momentum at $\sqrt{s} = 8$ TeV proton–proton collisions
using the ATLAS experiment*, JHEP **1310** (2013) 130, arXiv: 1308.1841 [hep-ex].

[102] ATLAS Collaboration, *Search for direct pair production of the top squark in all-hadronic
final states in proton–proton collisions at $\sqrt{s} = 8$ TeV with the ATLAS detector*,
JHEP **1409** (2014) 015, arXiv: 1406.1122 [hep-ex].

[103] B. Nachman et al., *Jets from Jets: Re-clustering as a tool for large radius jet
reconstruction and grooming at the LHC*, JHEP **1502** (2015) 075,
arXiv: 1407.2922 [hep-ph].

[104] D. Krohn, J. Thaler, and L.-T. Wang, *Jet Trimming*, JHEP **1002** (2010) 084,
arXiv: 0912.1342 [hep-ph].

[105] C. Lester and D. Summers,
Measuring masses of semi-invisibly decaying particles pair produced at hadron colliders,
Phys. Lett. **B 463** (1999) 99, arXiv: hep-ph/9906349.

[106] *Monte Carlo Calibration and Combination of In-situ Measurements of Jet Energy Scale,
Jet Energy Resolution and Jet Mass in ATLAS*, (2015),
URL: http://cds.cern.ch/record/2044941.

[107] ATLAS Collaboration,
Search for top squark pair production in final states with one isolated lepton, jets, and missing transverse momentum in $\sqrt{s} = 8$ TeV pp collisions with the ATLAS detector,
JHEP **1411** (2014) 118, arXiv: 1407.0583 [hep-ex].

[108] B. Nachman and C. G. Lester, *Significance Variables*, Phys. Rev. D **88** (2013) 075013, arXiv: 1303.7009 [hep-ph].

[109] Y. Bai et al., *Stop the Top Background of the Stop Search*, JHEP **07** (2012) 110, arXiv: 1203.4813 [hep-ph].

[110] A. J. Barr, B. Gripaios, and C. G. Lester,
Transverse masses and kinematic constraints: from the boundary to the crease,
JHEP **11** (2009) 096, arXiv: 0908.3779 [hep-ph].

[111] P. Konar et al., *Dark Matter Particle Spectroscopy at the LHC: Generalizing MT2 to Asymmetric Event Topologies*, JHEP **04** (2010) 086, arXiv: 0911.4126 [hep-ph].

[112] M. L. Graesser and J. Shelton, *Hunting Mixed Top Squark Decays*,
Phys. Rev. Lett. **111** (2013) 121802, arXiv: 1212.4495 [hep-ph].

[113] K. Melnikov, M. Schulze, and A. Scharf, *QCD corrections to top quark pair production in association with a photon at hadron colliders*, Phys. Rev. D **83** (2011) 074013,
arXiv: 1102.1967 [hep-ph].

[114] A. L. Read, *Presentation of search results: The CL(s) technique*,
J. Phys. G **28** (2002) 2693.

[115] F. James and M. Roos, *Minuit: A System for Function Minimization and Analysis of the Parameter Errors and Correlations*, Comput. Phys. Commun. **10** (1975) 343.

[116] K. Cranmer et al.,
HistFactory: A tool for creating statistical models for use with RooFit and RooStats,
Cern-Open-2012-016 (2012).

[117] M. Baak et al., *HistFitter software framework for statistical data analysis*,
European Physical Journal C **75**, 153 (2015) 153, arXiv: 1410.1280 [hep-ex].

[118] L. Moneta et al., "The RooStats project,"
Proceedings of the 13th International Workshop on Advanced Computing and Analysis Techniques in Physics Research. February 22-27, 2010, Jaipur, India. 2010 57,
arXiv: 1009.1003 [physics.data-an].

[119] J. Neyman and E. S. Pearson,
On the Problem of the Most Efficient Tests of Statistical Hypotheses,
Philosophical Transactions of the Royal Society of London Series A **231** (1933) 289.

[120] G. Cowan et al., *Asymptotic formulae for likelihood-based tests of new physics*,
The European Physical Journal C **71** (2011) 1554, ISSN: 1434-6052,
URL: http://dx.doi.org/10.1140/epjc/s10052-011-1554-0.

[121] ATLAS Collaboration, *Calibration of b-tagging using dileptonic top pair events in a combinatorial likelihood approach with the ATLAS experiment*, ATLAS-CONF-2014-004,
2014, URL: http://cdsweb.cern.ch/record/1664335.

[122] ATLAS Collaboration, *Calibration of the performance of b-tagging for c and light-flavour jets in the 2012 ATLAS data*, ATLAS-CONF-2014-046, 2014,
URL: http://cdsweb.cern.ch/record/1741020.

[123] S. Schramm et al., *A method for the construction of strongly reduced representations of ATLAS experimental uncertainties and the application thereof to the jet energy scale*, (2015), URL: https://cds.cern.ch/record/2014656.

[124] S. Frixione et al., *Single-top hadroproduction in association with a W boson*, JHEP **0807** (2008) 029, arXiv: 0805.3067 [hep-ph].

[125] S. Catani et al., *QCD matrix elements + parton showers*, JHEP **11** (2001) 063, arXiv: hep-ph/0109231.

[126] G. Aad et al., *Measurement of the cross-section for W boson production in association with b-jets in pp collisions at $\sqrt{s}$ = 7 TeV with the ATLAS detector*, JHEP **06** (2013) 084, arXiv: 1302.2929 [hep-ex].

[127] D. Geerts, "Theoretical W+jets Heavy Flavour fraction uncertainties," https://indico.cern.ch/event/215583/contributions/436127/, 2012.

[128] J Butterworth et al., *Single Boson and Diboson Production Cross Sections in pp Collisions at $\sqrt{s}$ = 7 TeV*, (2010), URL: https://cds.cern.ch/record/1287902.

[129] S. Dulat et al., *New parton distribution functions from a global analysis of quantum chromodynamics*, Phys. Rev. D **93** (2016) 033006, arXiv: 1506.07443 [hep-ph].

[130] *Search for the Supersymmetric Partner of the Top Quark in the Jets+Emiss Final State at sqrt(s) = 13 TeV*, (2016), URL: http://cds.cern.ch/record/2206250.

[131] *Search for direct top squark pair production and dark matter production in final states with two leptons in $\sqrt{s}$ = 13 TeV pp collisions using 13.3 fb^{-1} of ATLAS data*, (2016), URL: http://cds.cern.ch/record/2206249.

[132] *Search for direct top squark pair production in the single lepton final state at $\sqrt{s}$ = 13 TeV*, (2016), URL: https://cds.cern.ch/record/2205271.

[133] G. Aad et al., *ATLAS Run 1 searches for direct pair production of third-generation squarks at the Large Hadron Collider*, Eur. Phys. J. **C75** (2015) 510, [Erratum: Eur. Phys. J.C76,no.3,153(2016)], arXiv: 1506.08616 [hep-ex].

[134] I. Volobouev, *Matrix Element Method in HEP: Transfer Functions, Efficiencies, and Likelihood Normalization*, ArXiv e-prints (2011), arXiv: 1101.2259 [physics.data-an].

[135] T. Mori, "Studies on Matrix Element Likelihood Method," URL: https://twiki.cern.ch/twiki/bin/view/Main/MatrixElementMethod.

[136] P. Artoisenet et al., *Automation of the matrix element reweighting method*, JHEP **12** (2010) 068, arXiv: 1007.3300 [hep-ph].

[137] CERN, "The HL-LHC project," URL: http://hilumilhc.web.cern.ch/about/hl-lhc-project.

[138] A. Wald, *Tests of Statistical Hypotheses Concerning Several Parameters When the Number of Observations is Large*,
Transactions of the American Mathematical Society **54** (1943) 426, ISSN: 00029947,
URL: http://www.jstor.org/stable/1990256.

[139] M. C. Aleksa et al.,
ATLAS Liquid Argon Calorimeter Phase-I Upgrade Technical Design Report,
(2013), Final version presented to December 2013 LHCC.,
URL: https://cds.cern.ch/record/1602230.

[140] J Kuppambatti et al., *A radiation-hard dual channel 4-bit pipeline for a 12-bit 40 MS/s ADC prototype with extended dynamic range for the ATLAS Liquid Argon Calorimeter readout electronics upgrade at the CERN LHC*,
Journal of Instrumentation **8** (2013) P09008,
URL: http://stacks.iop.org/1748-0221/8/i=09/a=P09008.

[141] "The LOCic Specifications," URL: https://edms.cern.ch/document/1209515/1.0.

[142] "Public Liquid Argon Calorimeter Plots on Upgrade,"
https://twiki.cern.ch/twiki/bin/view/AtlasPublic/LArCaloPublicResultsUpgrade.